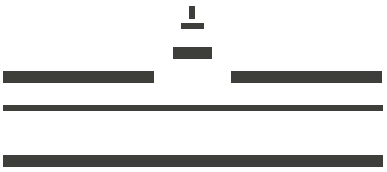

Westfälische
Wilhelms-Universität
Münster

Fach: Mathematik

New Finite Element Methods to Solve the EEG/MEG Forward Problem

Inaugural Dissertation

zur Erlangung des Doktorgrades der Naturwissenschaften
– Dr. rer. nat. –
im Fachbereich Mathematik und Informatik
der Mathematisch-Naturwissenschaftlichen Fakultät
der Westfälischen Wilhelms-Universität Münster

eingereicht von
Johannes Vorwerk
aus Warendorf

– 2016 –

Dekan:	Prof. Dr. Martin Stein
Erster Gutachter:	Priv.-Doz. Dr. Carsten Wolters (Universität Münster)
Zweiter Gutachter:	Prof. Dr. Christian Engwer (Universität Münster)
Dritter Gutachter:	Prof. Dr. Sampsa Pursiainen (Tampere University of Technology)
Tag der mündlichen Prüfung:	3. Februar 2016
Tag der Promotion:	3. Februar 2016

Abstract

Electroencephalography (EEG) and magnetoencephalography (MEG) have become important tools for non-invasive functional neuroimaging due to their unique time resolution. This comes at the cost of an ill-posed inverse problem that has to be solved to reconstruct the active brain areas underlying a measured signal. For accurate EEG/MEG source analysis, it is necessary to precisely simulate the electric and magnetic fields generated by a minimal patch of active brain tissue, represented by the model assumption of a current dipole. This leads to the so-called forward problem of EEG/MEG, which has to be solved numerically when aiming to consider the individual shape and conductivity distribution of the subject's head as it is recommendable. A possible method to achieve this goal is the finite element method (FEM). In this thesis, two important aspects influencing the accuracy achieved in solving the EEG/MEG forward problem using FEM are studied. On the one hand, the numerical accuracy achieved by both established and newly presented FEM approaches is evaluated for EEG/MEG forward solutions, where both spherical and realistic head models are considered as evaluation scenarios. On the other hand, the influence of differently detailed distinctions of the conductive compartments in the human head in the setup of an individual head model is investigated.
Key contributions are:

- Different source modeling approaches to solve the EEG/MEG forward problem based on a conforming FEM formulation (CG-FEM) are evaluated in both spherical and realistic multi-compartment head models and it is shown that these achieve high accuracies in the considered scenarios. The Venant approach is found to achieve the best compromise of numerical accuracy and computational effort for both EEG and MEG. It is further shown that in many cases the effects of simplifications in the model creation exceed the numerical errors.

- On this basis, the influence of the modeling of different conductive features of the human head on topography and magnitude of EEG/MEG forward simulations and on inverse solutions is investigated. The most important conductive compartments to be modeled are identified and a guideline for EEG/MEG head volume conductor modeling is derived. It is concluded that starting from the common three-layer scenario (skin, skull, and brain) especially the additional distinction of the homogeneous brain compartment into CSF, gray matter, and white matter is highly recommendable, particularly for the EEG forward problem.

- Theoretical derivations and evaluations of two newly presented FEM approaches to solve the EEG/MEG forward problem, discontinuous Galerkin (DG)- and Mixed-FEM, are presented. It is shown that, while matching the accuracy of the CG-FEM in common sphere models, these approaches allow to prevent numerical errors, so-called leakage effects, that occur in certain geometries for CG-FEM and that they achieve a higher accuracy than CG-FEM in a realistic six-layer head model. For the regular hexahedral meshes used in this thesis, the projected Mixed-FEM achieved the highest accuracies.

Keywords: EEG, MEG, forward problem, source analysis, finite element method, discontinuous Galerkin, mixed finite elements, realistic head modeling, volume conductor generation, volume conduction effects, tissue conductivity anisotropy

Acknowledgments

I want to thank everyone who made this thesis possible, especially:

- Carsten H. Wolters for giving me the opportunity to work in his group, his invaluable advice, his support, and of course for being supervisor of this thesis.
- Christian Engwer for his scientific input and for refereeing this thesis.
- Sampsa Pursiainen for the fruitful cooperations and for refereeing this thesis.
- Ümit Aydin, Felix Lucka, Andreas Nüßing, Maria Carla Piastra, and Sven Wagner for proofreading this thesis and many scientific and non-scientific discussions.
- The student assistants and/or master students Florian Grüne, Jakob Ludewig, and Tobias Trame for their excellent work.
- Pia Lau and Robert Wunderlich for getting me into juggling and recreative cake breaks in the final weeks of writing this thesis.
- All colleagues at the IBB for a nice time with a great working atmosphere.
- All cooperation partners, especially from Leipzig (Jae-Hyun Cho, Thomas Knösche), Erlangen (Stefan Rampp, Martin Bauer), and Nijmegen (Robert Oostenveld, Lilla Magyari).
- My parents for their support at all times.

Furthermore, I am grateful to the German Research Foundation (DFG) and Carsten H. Wolters for funding this research through the project WO1425/2-1 and the DFG Priority Program 1665, project WO1425/5-1.

Contents

List of Figures

List of Tables

Notation and Abbreviations

As most of the notation and abbreviations are introduced in the corresponding chapters, this listing serves as a reference for later look-up and does not claim to be complete.

General notation

Ω	open set in $\mathbb{R}^n$; usually the head domain
Γ	$= \partial\Omega$
d	dimension, usually $d = 3$
$\partial f / \partial x_i$	partial derivative
$\partial^\alpha f$	$= \partial^{\lvert\alpha\rvert} f / (\partial x_1^{\alpha_1} \dots \partial x_n^{\alpha_n})$
$\mathbf{n}$	normal vector, usually on Γ
$\mathbf{n}_F$, $\mathbf{n}_{e,f}$	normal vector on face F, normal vector pointing from element e to f
∇f	$= (\partial f/\partial x_1, \dots, \partial f/\partial x_d) = \operatorname{grad} f$
$\nabla \cdot \mathbf{q}$	$= \sum_{i=1}^d \partial q_i / \partial x_i = \operatorname{div} \mathbf{q}$
$\partial_{\mathbf{n}} f$	$= \langle \mathbf{n}, \nabla f \rangle$, normal derivative
∇_h	element-wise gradient
Δ	Laplace operator
$\langle a, b \rangle$	$a, b \in \mathbb{R}^d$, vector scalar product
$\lVert \mathbf{x} \rVert_2$	$= \langle \mathbf{x}, \mathbf{x} \rangle^{1/2}$, cartesian norm
$\lvert V \rvert$	volume of V
$a \times b$	vector product
A^t	transpose of a matrix
$A_{i\cdot}$, $A_{\cdot j}$	i-th row/j-th column of matrix A
$\mathbf{I}$	identity matrix
$\delta_{i,j}$	Kronecker delta

$L^2(\Omega)$	space of square-integrable functions on Ω
$L^p(\Omega)$	space of p-integrable functions on Ω
$L^\infty(\Omega)$	space of essentially bounded functions on Ω
$C^m(\Omega)$	space of functions with continuous derivatives of order m
$C_0^\infty(\Omega)$	space of infinitely often continuously differentiable functions with trace zero
$W^{k,p}(\Omega)$	Sobolev space of $L^p(\Omega)$ functions with weak derivatives of order k
$H^k(\Omega)$	$= W^{k,2}(\Omega)$
$H^k_{loc}(\Omega)$	space of locally H^k functions
H'	dual space of H
$H^{-k}(\Omega)$	dual space of $H^k(\Omega)$ with respect to the $L^2(\Omega)$-scalar product
$H(\mathrm{div};\Omega)$	cf. Definition 3
$L^2(\Omega)^3$	$= [L^2(\Omega)]^3$, correspondingly $L^\infty(\Omega)^3$, $H^k(\Omega)^3$, ...
$(\cdot,\cdot)_V$	V-scalar product
$(f,g)_{L^2(\Omega)}$	$= \int_\Omega fg\,\mathrm{d}x$, $f,g \in L^2(\Omega)$, $L^2(\Omega)$-scalar product
$(\mathbf{p},\mathbf{q})_{L^2(\Omega)^d}$	$= \int_\Omega \langle \mathbf{p},\mathbf{q}\rangle\,\mathrm{d}x$, $L^2(\Omega)^d$-scalar product
$\|\cdot\|_V$	norm on V induced by the scalar-product
$\|\cdot\|_{H^k(\Omega)}$	$H^k(\Omega)$-seminorm, cf. (1.19)
$\langle l, v\rangle \coloneqq l(v)$	$l \in V'$, $v \in V$, dual pair
$f * g$	$f * g(\mathbf{x}) = \int f(\mathbf{x}')g(\mathbf{x}-\mathbf{x}')\,\mathrm{d}x'$, folding of functions f and g
$\mathrm{supp}\, f$	support of a function f
$\delta_{\mathbf{x}}(\mathbf{y})$	Dirac delta distribution
$\mathbb{1}_T(\mathbf{x})$	indicator function on T

$\mathcal{T}$, $\mathcal{T}_h$, $\mathcal{T}_h(\Omega)$	(admissible) decomposition of Ω, cf. Definition 2
$V(\mathcal{T})$, $E(\mathcal{T})$, $F(\mathcal{T})$	sets of all vertices, edges, and faces of an element $T \in \mathcal{T}$
$P_k(T)$	space of polynomials of degree k on an element $T \in \mathcal{T}$, cf. (2.1)
$\tilde{P}_k(T)$	space of homogeneous polynomials of degree k, cf. (2.2)
$Q_k(T)$	space of polynomials of degree $\leq k$, cf. (2.3)
$\mathcal{M}_k(\mathcal{T})$	space of elementwise P_k functions, cf. (2.4)
$\mathcal{M}_k^0$	$\mathcal{M}^k \cap C^0(\Omega)$, cf. (2.5)
P_1	$= \mathcal{M}_1^0$
P_0	$= \mathcal{M}_0$
$Q_k(\mathcal{T})$	space of elementwise Q_k functions, cf. (2.6)
$RT_k(T)$, $RT_k(\mathcal{T})$	Raviart-Thomas space of order k, cf. Definition 4
S_h	set of finite element basis functions
$R_k(\partial T)$	cf. Proposition 7
Γ_{int}	internal skeleton, cf. (4.2)
$W^{k,p}(\mathcal{T}_h)$, $H^k(\mathcal{T}_h)$	broken Sobolev-spaces, cf. (4.3)
V_h^k	broken polynomial space, cf. 4.25
$[\![\cdot]\!]_{e,f}$, $[\cdot]_{e,f}$, $\{\cdot\}_{e,f}$	jump and average operators, cf. (4.6)
$\mathcal{O}(h^{1/2})$	Landau symbol

Specific notations and abbrevations

u	electric potential
$\mathbf{j}$	electric current
$\mathbf{j}^p$	primary current, dipole source
σ	electric conductivity distribution, $\sigma : \mathbb{R}^3 \to \mathbb{R}^+$ or $\sigma : \mathbb{R}^3 \to \mathbb{R}^{3\times 3}$,
Φ	magnetic flux
Φ_p, Φ_s	primary and secondary magnetic flux, respectively
G	fundamental solution of the Poisson problem, cf. Section 1.4
RDM	relative difference measure, cf. (2.63)
$lnMAG$	logarithmic magnitude error, cf. (2.63)
$lnMAG_{\mathbf{j},loc}$	local logarithmic magnitude error, cf. (4.39)
$totDIFF_{\mathbf{j},loc}$	local current difference, cf. (4.40)
IQR	inter-quartile range
spread	difference between minimal and maximal error
SNR	signal-to-noise ratio
CDT	constrained Delaunay tetrahedralization
$LCMV$	linear constrained minium variance beamformer, cf. Section 3.1.5
$ICoh$	imaginary coherence, cf. Section 3.1.5
$GPDC$	generalized partial directed coherence, cf. Section 3.1.5
$ln(Z^2)$	output SNR, cf. Section 3.1.5
CG-FEM	continuous Galerkin finite element method, cf. Chapter 2
DG-FEM	discontinuous Galerkin finite element method, cf. Chapter 4
SIPG	symmetric interior penalty Galerkin method, cf. Chapter 4
SWIPG	symmetric weighted interior penalty Galerkin method, cf. Chapter 4
NIPG	non-symmetric interior penalty Galerkin method, cf. Chapter 4
LDG	local discontinuous Galerkin method, cf. Chapter 4
M-FEM	mixed finite element method, cf. Chapter 5

Introduction

Understanding the functioning of the human brain is an important goal of research, involving many areas of science. Common examples are psychology, where for example the emergence of emotions or the origin of mental diseases are topics of research, or medicine, where such research is necessary for a better understanding and treatment of neurological diseases, e.g., epilepsy. Prior to the development of modern neuroimaging techniques, brain research was dependent on indirect evidence such as behavioral experiments and lesion studies or on post-mortem analysis of the brain structure. Nowadays, neuroimaging techniques have become powerful tools that allow insight into functioning and pathology of the live human brain on a macroscopic level.

The used technologies can roughly be separated into those to depict the anatomical structure of the brain on the one hand and those for imaging the functioning of the brain on the other hand. Frequently used technologies to generate structural images of the human brain are, e.g., *X-ray computed tomography* (CT) or *magnetic resonance imaging* (MRI), the functioning of the brain can, e.g., be investigated by analyzing the characteristics of metabolism using techniques such as *positron emission tomography* (PET), *single photon emission computed tomography* (SPECT), or *functional magnetic resonance imaging* (fMRI); amongst these tools *electroencephalography* (EEG) and *magnetoencephalography* (MEG) are unique due to their time resolution in the range of milliseconds and the comparably direct relation between brain activity and measured signal. These features motivate the frequent use of EEG and MEG in cognitive science, but also in clinical applications, e.g., in pre-surgical epilepsy diagnosis or in sleep medicine.

To reconstruct the positions of the sources inside the brain volume that underlie a measured signal, it is necessary to solve the ill-posed inverse problem of EEG/MEG. This requires to simulate the electric/magnetic field caused by a point-like source in the brain volume: the so-called forward problem of EEG/MEG (Brette and Destexhe, 2012). The exactness that can be achieved in solving the inverse problem strongly depends on the accuracy with which the forward problem is solved. An important aspect in order to increase this accuracy is the use of realistic volume conductor models of the subject's head. As the forward problem of EEG/MEG cannot be solved analytically in such geometries, this necessitates the use of numerical methods; amongst the proposed methods to solve the forward problem are *boundary*

element methods (BEM) (Akalin-Acar and Makeig, 2010; Gramfort et al., 2011; Mosher and Leahy, 1999; Stenroos and Sarvas, 2012), *finite difference methods* (FDM) (Montes-Restrepo et al., 2014; Vatta et al., 2009; Wendel et al., 2008), *finite volume methods* (FVM) (Cook and Koles, 2006), and *finite element methods* (FEM) (Bertrand et al., 1991; Drechsler et al., 2009; Marin et al., 1998; Pursiainen et al., 2011; Ramon et al., 2006; Schimpf et al., 2002).

This thesis focuses on the evaluation and application of FEM to solve the EEG and MEG forward problem. FE methods were shown to achieve high numerical accuracies in solving the EEG forward problem (Drechsler et al., 2009; Vorwerk et al., 2012), while the computational burden could be clearly reduced by the introduction of transfer matrices and fast solver methods (Gencer and Acar, 2004; Weinstein et al., 2000; Wolters et al., 2004). To apply FEM in solving the EEG/MEG forward problem, an important task that has to be solved is the modeling of the highly irregular source distribution introduced by the assumption of a current dipole as fundamental source. Amongst the most frequently used approaches to deal with this task are the Venant (Buchner et al., 1997; Schönen et al., 1994; Toupin, 1965; Vorwerk et al., 2012), the partial integration (Vallaghé and Papadopoulo, 2010; Vorwerk et al., 2012; Weinstein et al., 2000; Yan et al., 1991), the Whitney or Raviart-Thomas (Pursiainen et al., 2011; Tanzer et al., 2005), and the subtraction approach (Bertrand et al., 1991; Drechsler et al., 2009; Marin et al., 1998; Schimpf et al., 2002; Vorwerk et al., 2012; Wolters et al., 2007c). Until recently, all of these approaches were exclusively formulated in the context of Continuous Galerkin FEM (CG-FEM), also called Lagrange- or conforming FEM. While the thereby achievable accuracy in most scenarios is, as previously mentioned, high, scenarios exist, where the accuracy of the CG-FEM is clearly diminished. To tackle this problem, two new FEM formulations are introduced and evaluated in this thesis. The partial integration and subtraction approach are formulated in the framework of the discontinuous Galerkin FEM (DG-FEM) (Arnold et al., 2002; Di Pietro and Ern, 2011) and a new approach to model the dipole source is introduced on the basis of a Mixed-FEM formulation (Brezzi and Fortin, 1991; Raviart and Thomas, 1977). It is shown that these approaches lead to similar accuracies as CG-FEM in common sphere geometries, but achieve better results for some special geometries and in a realistic six-compartment head model.

A second possible source of error besides the modeling of the highly irregular source distribution, are simplifications made in the generation of the volume conductor model. The BEM depends on representations of the surfaces between compartments of different conductivity and is often used in combination with realistically shaped three-layer head models consisting of skin, skull, and a homogeneous brain compartment inside the skull. In contrast, FEM, FDM, and FVM depend on 3d-discretizations of the volume and principally allow the distinction of arbitrarily many compartments of different conductivity. Possible refinements of three-layer head models are, e.g., the separation of the homogeneous compartment inside the skull into cerebrospinal fluid (CSF) and gray and white matter (Lanfer et al., 2012a; Ramon et al., 2004; Wendel et al., 2008). Furthermore, the different tissues of the skull, skull compacta and spongiosa, can be distinguished (Akhtari et al., 2002; Dannhauer et al., 2011; Sadleir and Argibay, 2007) or the anisotropic structure of the white matter can be taken into account (Güllmar et al., 2010;

Ramon et al., 2004). In this thesis the influence of modeling/not modeling these different conductive compartments and features of the human head – skull compacta, skull spongiosa, CSF, gray matter, white matter, and white matter anisotropy – in the creation of a volume conductor on both EEG and MEG forward solutions is investigated. Therefore, statistical evaluations and visualizations of the effects on signal topography and magnitude are generated. On this basis the high importance of accurate volume conductor modeling for EEG and, to a lesser degree, for MEG forward solutions is shown. As most important modeling steps the consideration of the highly conductive CSF and the distinction of gray/white matter conductivity differences is found. Subsequently, also the influence on the inverse problem is studied and a MATLAB-pipeline allowing the simple generation of FEM forward solutions using five-compartment head models is presented.

The structure of this thesis is as follows: After deriving the forward problems of EEG and MEG and indicating quasi-analytical solutions for sphere models in Chapter 1, the CG-FEM is introduced to solve the forward problems of EEG and MEG in Chapter 2. On this basis, different approaches to model the dipole source are presented and their numerical accuracy for both sphere and realistic head models is evaluated for EEG and MEG. In Chapter 3 the numerical errors are set in relation to the effects of simplifications in the modeling of the head volume conductor and the most important conductive compartments to be modeled are identified. Motivated by a scenario in which the CG-FEM achieves insufficient accuracies, the so-called skull leakage, the DG- and Mixed-FEM are introduced in Chapters 4 and 5, respectively. It is shown that both approaches achieve a similar numerical accuracy as the CG-FEM in common geometries, while effectively preventing the numerical inaccuracies caused by leakage effects.

1

The EEG/MEG Forward Problem

In this chapter, the *partial differential equation* (PDE) that is known as the *forward problem of EEG* and, employing the law of Biot-Savart, subsequently also the *forward problem of MEG* is derived. Starting point is a short description of the physiology underlying the generation of electrical fields in the human brain. Subsequently, a simplification of *Maxwell's equations* is introduced, the so-called *quasi-static approximation*, and a *Poisson equation* with *Neumann boundary conditions* for the electric potential is deduced, which defines the forward problem of EEG. After presenting an adequate source model and deriving the forward problem of MEG, analytical solutions in sphere models for both EEG and MEG are noted.

1.1. Physiological Background

The electrical potential differences at the head surface measured with the EEG as well as the magnetic fields measured with the MEG are an effect of electromagnetic fields induced by *ion currents* inside the brain. To understand the sources of this *bioelectromagnetism*, the basic structures and elementary processes inside this highly complex organ are shortly explained in the following. The human brain is composed out of 10^{11} up to 10^{12} elementary cells, the so-called *neurons* (Thompson, 1992). Neurons are electrically excitable cells that communicate amongst each other using electrochemical signaling. A typical neuron in the brain consists of three parts, the *soma*, which represents the cell body, the *dendrites*, and

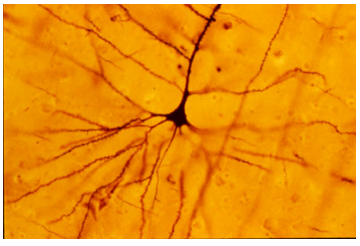

Figure 1.1.: A human neocortical pyramidal neuron stained via Golgi technique. *Source: Bob Jacobs, Wikimedia Commons, CC BY-SA-2.5; released under the GNU Free Documentation License.*

one *axon* arising at the *axon hillock* (cf. Figure 1.1). Each cell builds only one axon, which can reach a length between 1 μm (in the brain) up to 1 m (in the spinal chord) and branch several times, whereas several dendrites having a length of some hundred micrometers may develop. The neurons connect to each other cultivating (complex) networks, communicating via chemical transmitters at the *synapses*, where typically signals from the axon of one neuron are passed to a dendrite of another. Each neuron has about 7,000 synaptic connections to other neurons (Drachman, 2005).

The process of signal transmission between neurons is based on the rise and fall of electric potentials at the cell membranes, established by the diffusion of ions through *ion-channels*. These potential differences cause intra- and extracellular ion currents, i.e., currents flowing in- and outside the neurons, respectively. According to Maxwell's equations of electrodynamics, the movement of electric charges gives rise to electromagnetic fields propagating through the human body. Two major patterns of membrane potentials appear in the signal transmission between neurons: *action potentials* and *post-synaptic potentials*.

When a certain threshold potential at the axon hillock of the *pre-synaptic* neuron is exceeded, the neuron "fires", i.e., a sudden change of the membrane potential consisting in an abrupt rise followed by a fall of the same amplitude occurs. This action potential propagates along the axon, inducing the dumping of neurotransmitters at the pre-synaptic membrane of the affiliated synapses. The diffusion of these transmitters through the neighboring *post-synaptic* membrane causes a potential change – the post-synaptic potential – in the post-synaptic neuron. This (or the sum of various) potential changes may, again, initiate an action potential in the post-synaptic neuron, i.e., the signal is passed on.

Since action potentials are too short (0.5-2 ms), insufficiently synchronized, and their far-field induced by the resulting ion currents is dominated by the quadrupole term, they do not evoke an exploitable EEG signal (Jackson et al., 2006; Plonsey, 2005). In contrast, the simultaneous generation of post-synaptic potentials with a duration of tens of milliseconds by some ten-thousand neighboring and similarly oriented neurons, corresponding to a patch of few square millimeters of cortex surface, results in a measurable, dipolar electromagnetic field (Murakami and Okada, 2006; Okada, 1993). The potential difference between the particular dendrite and the soma induces a balancing flow of ions in the liquid between the neurons. The highest concentration of similarly oriented neurons is given for the approximately 10^9 *pyramidal cells* that are mainly found in the cortex, but also in the hippocampus and the amygdala. Thus, the major contribution to the EEG/MEG signals originates from these areas.

1.2. Quasi-Static Approximation of the Maxwell Equations

In this section, a quasi-static approximation of Maxwell's equations following Hämäläinen et al. (1993) is derived. As a first step we note that the permeability of the head's tissue is

that of free space, i.e., $\mu = \mu_0$. Then, Maxwell's equations read

$$\nabla \cdot \mathbf{E} = \frac{\rho}{\epsilon_r \epsilon_0}, \tag{1.1}$$

$$\nabla \cdot \mathbf{B} = 0, \tag{1.2}$$

$$\nabla \times \mathbf{E} = -\frac{\partial \mathbf{B}}{\partial t}, \tag{1.3}$$

$$\nabla \times \mathbf{B} = \mu_0 \mathbf{j} + \mu_0 \epsilon_r \epsilon_0 \frac{\partial \mathbf{E}}{\partial t}, \tag{1.4}$$

where $\mathbf{E}$ denotes the electric field, $\mathbf{B}$ the magnetic field, ρ the charge density, $\mathbf{j}$ the current density, ϵ_0 and ϵ_r the permittivity of free space and the relative permittivity, respectively, and μ_0 the permeability of free space. In the following, it is shown that the quasi-static approximation, i.e., neglecting the temporal derivatives in Maxwell's equations, is a reasonable assumption for modeling EEG/MEG signals. Using Ohm's law, $\mathbf{j} = \sigma \mathbf{E}$, in (1.4), we have

$$\nabla \times \mathbf{B} = \mu_0 (\sigma \mathbf{E} + \epsilon_r \epsilon_0 \frac{\partial \mathbf{E}}{\partial t}), \tag{1.5}$$

where σ represents the underlying isotropic or anisotropic conductivity distribution, respectively.

Since one can apply a Fourier decomposition to a general time dependent electric field, one has no loss of generality when assuming a harmonic time dependency with angular frequency ω, i.e., $\mathbf{E}(t) = \mathbf{E}_0 e^{-i\omega t}$, in (1.5):

$$\nabla \times \mathbf{B} = \mu_0 (\sigma \mathbf{E} - i \epsilon_r \epsilon_0 \omega \mathbf{E}). \tag{1.6}$$

Thus, for the quasi-static approximation to be valid, it is needed that $|\epsilon_r \epsilon_0 \omega| \ll |\sigma|$, i.e., $|\epsilon_r \epsilon_0 \omega / \sigma| \ll 1$. With $\sigma \approx 0.3$ S/m, $\epsilon_r \approx 10^5$ and a frequency $f = \omega / 2\pi \approx 100$ Hz, which is assumed to be an upper bound for frequencies in neuromagnetism (Hämäläinen et al., 1993), we have $\epsilon_r \epsilon_0 \omega / \sigma \approx 2 \cdot 10^{-3} \ll 1$.

To show that $\partial \mathbf{B} / \partial t$ in (1.3) can be neglected, the rotation of (1.3) is taken and with (1.4) we have

$$\nabla \times \nabla \times \mathbf{E} = -\frac{\partial}{\partial t}(\nabla \times \mathbf{B}) = -\mu_0 \frac{\partial}{\partial t}(\sigma \mathbf{E} + \epsilon_r \epsilon_0 \frac{\partial \mathbf{E}}{\partial t}) = \mu_0 (i\sigma\omega - \epsilon_r \epsilon_0 \omega^2)\mathbf{E}. \tag{1.7}$$

The solutions of this equation have a characteristic wavelength of $\lambda_c = |\mu_0 \sigma \omega (1 - \epsilon_r \epsilon_0 \omega / \sigma)|^{-1/2}$ ≈ 65 m, which is much larger then the diameter of the human head, so that the contribution to $\mathbf{E}$ can be neglected.

1.3. The Forward Problem of EEG

Since $\nabla \times \mathbf{E} = 0$ as a consequence of (1.3), $\mathbf{E}$ is a gradient field and can be related to a scalar potential u:

$$\mathbf{E} = -\nabla u. \tag{1.8}$$

Next, the current density $\mathbf{j}(x)$ is separated into two parts to simplify the following calculations. We define the primary current $\mathbf{j}^p(x)$, which represents the neural activity and is commonly spatially limited to a small volume; the *passive volume* or *return current*, $\mathbf{j}^v(x) = \sigma(x)\mathbf{E}(x)$, flows in the whole medium as an effect of the macroscopic electric field:

$$\mathbf{j}(x) = \mathbf{j}^p(x) + \mathbf{j}^v(x) = \mathbf{j}^p(x) + \sigma(x)\mathbf{E}(x) = \mathbf{j}^p(x) - \sigma(x)\nabla u(x). \tag{1.9}$$

The macroscopic conductivity σ is either a non-negative scalar (isotropic case) or a symmetric positive definite tensor (anisotropic case), i.e., $\sigma : \Omega \to \mathbb{R}^+$ or $\sigma : \Omega \to \mathbb{R}^{3\times 3}$, depending on whether the anisotropic conductivity of, e.g., the white matter is taken into account or not. Ω denotes the head domain.

Remark 1. *We assume that the head domain Ω is open and connected. We further assume that $\Gamma := \partial\Omega$ is sufficiently regular, e.g., Lipschitz continuous or $\Gamma \in C^1$.*

Taking the divergence of (1.4), where the temporal derivative is neglected following Section 1.2 and $\nabla \cdot \nabla \times B = 0$ is exploited, this can be combined with (1.9) and a system of two first order partial differential equations can be formulated:

$$\begin{aligned} \mathbf{j} + \sigma\nabla u &= \mathbf{j}^p \\ \nabla \cdot \mathbf{j} &= 0 \end{aligned} \quad \text{in } \Omega, \tag{1.10a}$$

$$\langle \mathbf{j}, \mathbf{n} \rangle = 0 \quad \text{on } \partial\Omega = \Gamma. \tag{1.10b}$$

This formulation is later used in Chapter 5. However, it is also possible to directly eliminate the unknown $\mathbf{j}$, gaining the second order PDE

$$\nabla \cdot (\sigma\nabla u) = f = \nabla \cdot \mathbf{j}^p \quad \text{in } \Omega, \tag{1.11a}$$

$$\sigma\partial_{\mathbf{n}} u = 0 \quad \text{on } \partial\Omega = \Gamma. \tag{1.11b}$$

This is a Poisson equation with (homogeneous) Neumann boundary conditions. f is introduced as an abstract source term here, the actual definition of f later depends on the choice of the source model.

The forward problem of EEG now consists in finding a solution u or $(\mathbf{j}, u)$ to the equivalent equation systems (1.11) or (1.10), respectively. Classical solutions to the problem in the strong formulation, i.e., solutions that are sufficiently often differentiable for example $u \in C^2(\Omega)$ or similar, are only existing under restrictive assumptions, such as a sufficiently regular source term f and a continuous conductivity σ. These assumptions turn out to be too restrictive in the present scenario, as usually only piecewise constant conductivities can be assumed, i.e., $\sigma \in L^\infty(\Omega)$. Thus, we instead search for a solution of the weak formulation of (1.11). Using a linear test function space V, which needs to be chosen to be a Hilbert space to show existence and uniqueness of a solution as it is shown later, this reads:

$$\text{Find } u \in V \text{ such that } \int_\Omega \langle \sigma \nabla u, \nabla v \rangle \, \mathrm{d}x = \int_\Omega f v \, \mathrm{d}x \text{ for all } v \in V. \tag{1.12}$$

The weak formulation can be derived by multiplying (1.11) with a test function v, integration over the domain Ω, applying Gauss's theorem (multi-dimensional integration by parts), and exploiting the boundary condition (1.11b). Introducing the notation

$$a(u, v) = (\sigma u, v)_{L^2(\Omega)^3} = \int_\Omega \langle \sigma \nabla u, \nabla v \rangle \, \mathrm{d}x \text{ for } u, v \in V, \tag{1.13a}$$

$$l(v) = (f, v)_{L^2(\Omega)} = \int_\Omega f v \, \mathrm{d}x \text{ for } v \in V. \tag{1.13b}$$

(1.12) can be reformulated to

$$\text{Find } u \in V \text{ such that } a(u, v) = l(v) \text{ for all } v \in V. \tag{1.14}$$

One can now show (cf. Braess, 2007, 2.2) that under the assumption that a is a symmetric, positive linear form, i.e., $a(u, u) > 0$ for all $u \in V \backslash \{0\}$, solving (1.14) is equivalent to finding a solution to the variational problem

$$u = \arg\min_{v \in V} J(v), \quad J(v) \coloneqq \frac{1}{2} a(v, v) - l(v). \tag{1.15}$$

Furthermore, the problem (1.14) is consistent with the strong formulation (1.11):

Remark 2 (Consistency)**.** *Every solution of the classical problem* (1.11) *is also a solution of the weak formulation* (1.12)/(1.14)*. This is of course also true for general problems of this kind.*

Proof. Braess (2007, 2.2 and 2.3) □

To show existence and uniqueness of a solution for (1.15) and thereby of course also for (1.12), one would like to apply the *Lemma of Lax-Milgram*:

Lemma 1 (Lax-Milgram)**.** *Let H be a Hilbert space, $a : H \times H \to \mathbb{R}$ an elliptic bilinearform, i.e., symmetric positiv-definite and $a(v, v) > \alpha \|v\|_H^2$ for $v \in H$, $\alpha > 0$. Then, for every $l \in H'$ the variational problem*

$$J(v) \coloneqq \frac{1}{2} a(v, v) - l(v) \to \min \tag{1.16}$$

admits a unique solution in H.

Proof. Braess (2007, 2.5) □

This implies that it is necessary to find a fitting function space V such that a as defined in (1.13a) is V-elliptic. As mentioned, one would desire to find a solution in $C^2(\Omega)$, however this is in most scenarios not mathematically feasible. Instead, V is chosen to be the Sobolev

space $H^1(\Omega)$ in the following. The Neumann boundary condition (cf. Equation 1.11b) only determines the solution u up to a constant; a is therefore not $H^1(\Omega)$-elliptic. This can be solved by restricting $H^1(\Omega)$ to the subspace

$$H^1_*(\Omega) \coloneqq \{v \in H^1(\Omega) : \int_\Omega v \,\mathrm{d}x = 0\}. \tag{1.17}$$

$H^1_*(\Omega)$ is the quotient of $H^1(\Omega)$ taken by the space of constant functions supported on Ω, i.e., the resulting solution is up to a constant unique in $H^1(\Omega)$.
Now, existence and uniqueness of a solution for (1.15)/(1.12) can be shown.

Lemma 2. *For every $l \in H^{-1}(\Omega)$ the variational problem* (1.15) *admits a unique solution in the space $H^1_*(\Omega)$.*

Proof. To apply the Lax-Milgram lemma (Lemma 1) one has to show that $a(v, v)$ is $H^1_*(\Omega)$-elliptic. This is easily done, as

$$a(v,v) = \int_\Omega \langle \sigma \nabla v, \nabla v \rangle \,\mathrm{d}x = \sigma |v|^2_{H^1(\Omega)} \geq \min_{\mathbf{x}\in\Omega} \sigma(\mathbf{x}) \|v\|^2_{L^2(\Omega)}, \tag{1.18}$$

where it is exploited that $\|v\|_{L^2(\Omega)} \leq |v|_{H^1(\Omega)}$ for all $v \in H^1_*(\Omega)$ Braess (cf. 2007, p. 32). $|\cdot|_{H^m(\Omega)}$ is the seminorm

$$|v|^2_{H^m(\Omega)} \coloneqq \sum_{|\alpha|=m} \|\partial^\alpha v\|_{L^2(\Omega)}, \tag{1.19}$$

and ∂^α indicates the partial derivative with multi-index $\alpha = (\alpha_1, \ldots, \alpha_d)$. □

Remark 3. *$l \in H^{-1}(\Omega)$ demands $f \in L^2(\Omega)$ and in terms of $\mathbf{j}^p$ we have $\partial(\mathbf{j}^p)_i/\partial x_i \in L^2(\Omega)$.*

Remark 4. *The condition $\int_\Omega v dx = 0$ is advantageous for the proof of uniqueness, but is mostly not feasible in the implementation of solvers for the equation systems that occur for the numerical methods used to solve the EEG forward problem, e.g., BE or FE methods. However, this problem can be avoided by replacing the pure Neumann boundary conditions by mixed boundary conditions, i.e., introducing Dirichlet boundary conditions on $\Gamma_D \subset \Gamma$, $|\Gamma_D| \neq \emptyset$. It is actually sufficient if Γ_D consists of a single point, $\Gamma_D = \mathbf{x}_D \in \partial\Omega$, to uniquely determine u.*

Remark 5. *If we additionally assume $\sigma \in C^1(\Omega)$ and $f \in L^2(\Omega)$, we find $u \in H^2_{loc}(\Omega)$ for a solution $u \in H^1(\Omega)$ of* (1.14) *and for each open $V \subset\subset \Omega$ we have the estimate*

$$\|u\|_{H^2(V)} \leq C(\|f\|_{L^2(V)} + \|u\|_{L^2(V)}) \tag{1.20}$$

with a constant C only depending on V, Ω, and σ (Evans, 1998). For $f \in H^m(\Omega)$, we even find $u \in H^{m+2}_{loc}(\Omega)$ (Evans, 1998). If a classical solution u of (1.11) *exists, we even have $u \in C^2(\Omega) \cap C^1(\bar{\Omega})$ (Hackbusch, 2003).*
However, these estimates do not take the discontinuous conductivity distribution σ and the possibly singular source term f (cf. Section 1.4) into account. For a jumping conductivity distribution $\sigma \notin C^1(\Omega)$ that is constant/continuous on the disjunct subsets $\Omega_i \subset \Omega$, $\Omega_i \cap \Omega_j =$

$\emptyset$ for $i \neq j$, $\cup_i \bar{\Omega}_i = \bar{\Omega}$ one can at least still expect to have $u \in H^2_{loc}(\Omega_i)$, while the derivative of u is usually not continuous at the boundaries $\Gamma_{i,j} = \bar{\Omega}_i \cup \bar{\Omega}_j, i \neq j$ (Hackbusch, 2003). For problems with a Dirac source term, but sufficiently regular conductivity distribution, e.g., σ Lipschitz continuous, and Ω convex and polyhedral it can be shown that $u \in W^{1,p}(\Omega)$, $1 \leq p < 1.5$ (Casas, 1985; Köppl and Wohlmuth, 2014). A further loss of regularity has to be expected when a source term that has a stronger singularity than a delta function is chosen as it is the case for the choice of a current dipole, though, it can be approximated through the limit case of two approaching Dirac distributions.

Next, the already mentioned and commonly assumed source model of a current dipole is introduced, which has the consequence that even the assumption $f \in L^2(\Omega)$ is not fulfilled.

1.4. The Current Dipole as a Source Model

The source term f has to be chosen so that it adequately represents the generators of measured EEG/MEG signals in the brain, i.e., the electrical currents generated by brain activity. A widely used concept in bioelectromagnetism is the mathematical or *current dipole*, which represents an infinitesimally small source of electrical current. This is a good approximation to the neural generators of EEG/MEG seen from a relatively far distance (de Munck et al., 1988; Hämäläinen et al., 1993; Sarvas, 1987), since the far-field of such a source is mainly dipolar (cf. Section 1.1). Furthermore, it can be shown that any further source of electrical current can be decomposed into a distribution of current dipoles, as this is the fundamental solution of the Poisson problem in the strong formulation (1.11). A current dipole is defined by its position $\mathbf{x}_0$ and its moment $\mathbf{p}$:

$$\mathbf{j}^p(\mathbf{x}) = \mathbf{p}\delta_{\mathbf{x}_0}(\mathbf{x}), \tag{1.21}$$

where $\delta_{\mathbf{x}_0}$ is the Dirac delta distribution and $\mathbf{p}$ the dipole moment (cf. Jackson et al., 2006). It can be illustrated as the limit case of two *electrical monopoles*, a current source and a sink with charge q and distance vector $\mathbf{d}$, that come infinitely close together in $\mathbf{x}_0$, while the dipole moment $\mathbf{p} = q\mathbf{d}$ remains constant:

$$\mathbf{p} = \lim_{\substack{\|\mathbf{d}\|_2 \to 0 \\ q \to \infty}} \int \mathbf{x}(q\delta_{\mathbf{x}_0 + \mathbf{d}/2}(\mathbf{x}) - q\delta_{\mathbf{x}_0 - \mathbf{d}/2}(\mathbf{x}))\,\mathrm{d}x = \lim_{\substack{\|\mathbf{d}\|_2 \to 0 \\ q \to \infty}} q\mathbf{d}. \tag{1.22}$$

$\mathbf{p}$ can then be related to the dipole term in the *multipole expansion* of a source distribution (Jackson et al., 2006). The corresponding source term f in (1.11) is given by $f = \nabla \cdot \mathbf{j}^p = \langle \mathbf{p}, \nabla \delta_{\mathbf{x}_0} \rangle$. However, since we have

$$\delta(\mathbf{x}) \in H^{-3/2-\epsilon} \qquad \text{and} \qquad \partial^\alpha \delta(\mathbf{x}) \in H^{-3/2-|\alpha|-\epsilon} \text{ for } \epsilon > 0 \text{ (cf. Taylor, 1996)}, \tag{1.23}$$

the requirements of Lemma 2 are not fulfilled. This is possibly problematic with regard to the convergence of the numerical solutions as it gets clear in the following chapters.

Furthermore, it is unclear how to evaluate $\nabla\delta_{\mathbf{x}_0}$. Dealing with this singularity is the main task to solve when one would like to apply finite element methods to solve the EEG/MEG forward problem. The derivation and evaluation of different approaches to resolve this are a main topic of this thesis and content of Chapters 2, 4, and 5.

However, the choice $\mathbf{j}^p = \mathbf{p}\delta_{\mathbf{x}_0}$ has some advantages in the analytical treatment of the Poisson equation, since $\delta_{\mathbf{x}_0}$ occurs naturally in the context of *fundamental solutions* and choosing $f = \nabla\mathbf{j}^p$ allows to derive analytical formulas to calculate EEG/MEG forward solutions in some simple scenarios. Therefore, the fundamental solution of the Poisson problem is needed.

Definition 1. *We define*

$$G(x) \coloneqq \frac{1}{4\pi\|\mathbf{x}\|_2} \qquad \text{for } \mathbf{x} \in \mathbb{R}^3. \tag{1.24}$$

Remark 6. *For $n \geq 3$, G is the fundamental solution of the Poisson equation, i.e., it fulfills the property $-\Delta G(\mathbf{x}) = \delta(\mathbf{x})$ in a distributive sense.*

Proof. Jackson et al. (2006); Nédélec (2001). □

Fundamental solutions allow to easily derive solutions of linear partial differential equations via convolution. For example, in an unbounded volume conductor with isotropic conductivity σ, the solution of the Poisson problem is given by convolution of the source term f with G:

$$u = -\frac{1}{\sigma} f * G. \tag{1.25}$$

In the case of a mathematical dipole at position $\mathbf{x}_0$ one obtains (Sarvas, 1987)

$$\begin{aligned} u(\mathbf{x}) = -\frac{1}{\sigma}(\nabla\cdot\mathbf{j}^p) * G(\mathbf{x}) = \frac{1}{\sigma}\int_{\mathbb{R}^3} \langle \mathbf{p}, \nabla\delta_{\mathbf{x}_0}(\mathbf{x}-\mathbf{y})\rangle G(\mathbf{y})\,\mathrm{d}y = \\ -\frac{1}{\sigma}\int_{\mathbb{R}^3} \langle \mathbf{p}\delta_{\mathbf{x}_0}(\mathbf{x}-\mathbf{y}), \nabla G(\mathbf{y})\rangle\,\mathrm{d}y = -\frac{\langle \mathbf{p}, \nabla G(\mathbf{x}-\mathbf{x}_0)\rangle}{\sigma} = \frac{\langle \mathbf{p}, \mathbf{x}-\mathbf{x}_0\rangle}{4\pi\sigma\|\mathbf{x}-\mathbf{x}_0\|_2^3}. \end{aligned} \tag{1.26}$$

The solution of the Poisson equation in an unbounded volume conductor is the basis to introduce the subtraction approach in Section 2.6 (Drechsler et al., 2009; Wolters et al., 2007c).

Also for more general domains Ω, the fundamental solution can often be used to derive a solution of the Poisson problem with boundary conditions such as problem (1.11) (Hackbusch, 2003). However, this is a rather theoretical possibility, since this function can usually only be evaluated explicitly in few special cases, mainly those with a high symmetry. A scenario in which an analytical solution can be derived is the multi-layer sphere model. This is topic of Section 1.6.

The fundamental solution also plays an important role in the numerical solution of (1.11) using *boundary element methods* (BEM) (Adde et al., 2003; Geselowitz, 1967; Kybic et al., 2005; Zanow, 1997), which are applied in Section 2.11.

1.5. The Forward Problem of MEG

In the following, the basic equations of magnetostatics that are needed to solve the forward problem of MEG are stated, for a more general overview on magnetostatics we refer to Jackson et al. (2006). The solution to the forward problem of MEG follows directly from the solution of the respective EEG forward problem via the *law of Biot-Savart*. For a general current distribution $\mathbf{j} : \Omega \to \mathbb{R}^3$ this reads

$$\mathbf{B}(\mathbf{x}) = \frac{\mu_0}{4\pi} \int_\Omega \mathbf{j}(\mathbf{x}') \times \frac{\mathbf{x} - \mathbf{x}'}{\|\mathbf{x} - \mathbf{x}'\|_2^3} \, \mathrm{d}x' \tag{1.27}$$

in the formulation for the magnetic field $\mathbf{B}$. Introducing the vector potential $\mathbf{A}$ in *Coulomb's gauge*, defined through the equations $\mathbf{B}(\mathbf{x}) = \nabla \times \mathbf{A}(\mathbf{x})$ and $\nabla \cdot \mathbf{A} = 0$, (1.27) can be rewritten to

$$\mathbf{A}(\mathbf{x}) = \frac{\mu_0}{4\pi} \int_\Omega \frac{\mathbf{j}(\mathbf{x}')}{\|\mathbf{x} - \mathbf{x}'\|_2} \, \mathrm{d}x'. \tag{1.28}$$

In MEG, the current flow induced in the measurement coil can be calculated when knowing the magnetic flux Φ through the surface enclosed by the coil. With F being this surface and $\gamma \coloneqq \partial F$ its boundary, the magnetic flux is given by

$$\Phi_F = \int_F \mathbf{B}(\mathbf{x}) \, \mathrm{d}F = \oint_\gamma \mathbf{A}(\mathbf{x}) \, \mathrm{d}\mathbf{x}, \tag{1.29}$$

where the equality follows from Stokes' theorem. Only the equations for the vector potential $\mathbf{A}$ are derived here, however, the representation in terms of $\mathbf{B}$ follows accordingly. Again splitting the current $\mathbf{j}$ into primary current $\mathbf{j}^p$ and volume currents $\sigma \nabla u$ following (1.9), the current distribution is given by $\mathbf{j}(\mathbf{x}) = \mathbf{j}^p(\mathbf{x}) - \sigma(\mathbf{x}) \nabla u(\mathbf{x})$ and from (1.28) and (1.29) we have

$$\Phi_F = \oint_\gamma \frac{\mu_0}{4\pi} \int_\Omega \frac{\mathbf{j}^p(\mathbf{x}') - \sigma(\mathbf{x}') \nabla u(\mathbf{x}')}{\|\mathbf{x} - \mathbf{x}'\|_2} \, \mathrm{d}x' \, \mathrm{d}x. \tag{1.30}$$

This expression can be simplified by applying *Fubini's theorem* and defining

$$\mathbf{C}(\mathbf{x}') \coloneqq \oint_\gamma \frac{1}{\|\mathbf{x} - \mathbf{x}'\|_2} \, \mathrm{d}x. \tag{1.31}$$

If one furthermore assumes a dipolar source $\mathbf{j}^p = \mathbf{p}\delta_{\mathbf{x}_0}$ as introduced in Section 1.4, the so-called primary and secondary magnetic flux, Φ_p and Φ_s, can be defined:

$$\Phi_p = \frac{\mu_0}{4\pi} \langle \mathbf{p}, \mathbf{C}(\mathbf{x}_0) \rangle, \tag{1.32a}$$

$$\Phi_s = -\frac{\mu_0}{4\pi} \int_\Omega \langle \sigma(\mathbf{x}') \nabla u(\mathbf{x}'), \mathbf{C}(\mathbf{x}') \rangle \, \mathrm{d}x', \tag{1.32b}$$

$$\Phi_F = \Phi_p + \Phi_s \tag{1.32c}$$

The primary flux Φ_p represents the magnetic field directly caused by the current dipole $\mathbf{j}^p$,

while the secondary flux Φ_s can be identified with the volume currents $\sigma\nabla u$ (Hämäläinen et al., 1993). When the coil integral $\mathbf{C}$ is known, the primary flux can be directly evaluated analytically.

1.6. Analytical Solutions to the EEG/MEG Forward Problem

Besides the unbounded homogeneous volume conductor, some further geometries exist for which the forward problems of EEG/MEG (1.11)/(1.32) can be solved (quasi-)analytically. One of these is the multi-layer sphere model. The analytical formulas allow for an easy calculation of the electric potentials under the constraint to model the human head by nested spheres of different conductivities, i.e., the compartment boundaries are spheres with a common origin. In practice, analytical solutions were (and still are) used to solve the forward problem of EEG and especially MEG due to the fast computation and the omission of the model generation. Obviously, a major drawback is that the assumption of a multi-layer sphere as a model for the human head is rather inexact. Thereby, especially for the EEG, but also for the MEG, the model error exceeds the numerical errors of methods being able to solve the forward problem for realistic head models, such as the finite element method that is introduced in the following chapter. Nevertheless, analytical solutions are still useful as a tool to compute reference solutions to evaluate the accuracy of the numerical approaches.

We first concentrate on solutions for the EEG forward problem. Different formulas to obtain an analytical solution for the EEG forward problem have been derived. While first solutions were only valid for a constant number of spheres with isotropic conductivities (Geselowitz, 1967; Hosek et al., 1978), solutions that are able to handle arbitrarily many spheres and to a certain extent even anisotropic conductivities have later been developed (de Munck, 1988; de Munck and Peters, 1993; Mosher et al., 1999; Zhang, 1995). The solution derived in de Munck and Peters (1993) is used throughout this thesis, which allows to treat arbitrarily many spheres and even radial symmetric anisotropy. The necessary formulas are noted in the following.

The assumed model consists of N nested shells with radii $r_1 < r_2 < \ldots < r_N$ and constant radial and tangential conductivities $\sigma^{rad}(\mathbf{x}) = \sigma_j^{rad} \in \mathbb{R}^+$ and $\sigma^{tan}(\mathbf{x}) = \sigma_j^{tan} \in \mathbb{R}^+$ in each shell, $r_j < x^r < r_{j+1}$, where $x^r \in \mathbb{R}$ is the radial coordinate of $\mathbf{x}$, i.e., the distance to the sphere origin. It is further assumed that the source is in a more interior layer than the measurement electrodes at positions $\mathbf{y}_i$, $i = 1, \ldots, s$ with s being the number of electrodes, with radial coordinate $y_i^r \in \mathbb{R}$. Then, the potential evoked at $\mathbf{y}_i$ by a source at position $\mathbf{x}$ with dipole moment $\mathbf{p}$ is given by

$$u(\mathbf{x}, \mathbf{p}, \mathbf{y}_i) = \frac{1}{4\pi} \langle \mathbf{p}, \frac{S_0}{y_i^r}\mathbf{y}_i + \left(\frac{S_1}{x^r} - \cos\omega_{x,y_i} \frac{S_0}{x^r} \right) \mathbf{x} \rangle \tag{1.33}$$

with ω_{x,y_i} being the angular distance between $\mathbf{x}$ and $\mathbf{y}_i$, i.e., for spheres with center in the

origin $\omega_{x,y_i} = \arccos\langle \mathbf{x}/\|\mathbf{x}\|_2, \mathbf{y}_i/\|\mathbf{y}_i\|_2 \rangle$, and

$$S_0 = \frac{F_0}{x^r} \frac{\Lambda}{(1 - 2\Lambda\cos\omega_{x,y_i} + \Lambda^2)^{3/2}} + \frac{1}{x^r} \sum_{n=1}^{\infty} \left[(2n+1)R_n(x^r, y_i^r) - F_0\Lambda^n\right] P_n'(\cos\omega_{x,y_i}), \tag{1.34}$$

$$S_1 = F_1 \frac{\Lambda\cos\omega_{x,y_i} - \Lambda^2}{(1 - 2\Lambda\cos\omega_{x,y_i} + \Lambda^2)^{3/2}} + \sum_{n=1}^{\infty} \left[(2n+1)R_n'(x^r, y_i^r) - F_1 n\Lambda^n\right] P_n(\cos\omega_{x,y_i}). \tag{1.35}$$

P_n and P_n' are the Legendre polynomial and its derivative, respectively, and can be computed recursively; the coefficients R_n and their derivatives R_n' can be computed analytically. The computation of the infinite series is stopped when a stopping criterion is fulfilled. The definitions of F_0, F_1, and Λ are given by de Munck and Peters (1993), as well as the exact derivation of the above formulas. This results in the vector of electrode potentials $(u^{ana})_i = u(\mathbf{x}, \mathbf{p}, \mathbf{y}_i)$, $i = 1, \ldots, s$.

Also for the forward problem of MEG several analytic solutions in sphere models were derived (Grynszpan and Geselowitz, 1973; Sarvas, 1987). In the same notation as before, i.e., source position $\mathbf{x}$, dipole moment $\mathbf{p}$, and evaluation position $\mathbf{y}_i$, and the center of the spheres in the origin, the formula of Sarvas (1987) reads

$$\mathbf{B}(\mathbf{x}, \mathbf{p}, \mathbf{y}_i) = \frac{\mu_0}{4\pi F} \left(F\mathbf{p} \times \mathbf{x} - \langle \mathbf{y}_i, \nabla F\rangle \mathbf{p} \times \mathbf{x}\right), \tag{1.36}$$

$F(\mathbf{x}, \mathbf{y}_i) = \|\mathbf{y}_i - \mathbf{x}\|_2(\|\mathbf{y}_i\|_2\|\mathbf{y}_i - \mathbf{x}\|_2 + \|\mathbf{y}_i\|_2^2 - \langle \mathbf{x}, \mathbf{y}_i\rangle)$ and $\nabla F = \nabla F(\mathbf{y}_i)$ the gradient of F with respect to $\mathbf{y}_i$. The magnetic flux through the MEG sensors can now be calculated by integrating the normal component of $\mathbf{B}$ over the sensor face. Formula (1.36) does not depend on the actual conductivity distribution σ and is thus identical for any sphere with spherically symmetric conductivity profile. Furthermore, (1.36) is zero for radial dipole orientations $\mathbf{p}$, as the expression $\mathbf{p} \times \mathbf{x}$ vanishes in this case. This relation is also important in the case of realistically shaped volume conductors. Due to the roughly spherical head shape, source orientations to which the MEG is only weakly sensitive exist in many areas of the brain, so-called *quasi-radial* sources. If desired, these can be identified by a *singular-value decomposition* (SVD) of the magnetic leadfield $L = (\mathbf{e}_i, \Phi_j)$ with $\mathbf{e}_i$ being the cartesian basis vectors and Φ_j the forward solution for the respective MEG sensor, $j = 1, \ldots, s$. Furthermore, every source becomes nearly radial when approaching the center of the sphere, resulting in a weak magnetic field for deep sources in spherical geometries.

When aiming to evaluate only the results for the secondary magnetic flux, as it is done in Section 2.10.4, an analytic solution for Φ_s can be calculated by subtracting the contribution of the primary flux defined in (1.32a) from the result for the full $\mathbf{B}$-field gained from (1.36).

2

The Continuous Galerkin Finite Element Method

In this chapter, the continuous Galerkin finite element method (CG-FEM) and different approaches to deal with the singular source distribution are introduced; namely the *Venant*, *partial integration*, *subtraction approach*, and *Whitney approach*. First, a mathematical framework is derived on which the discretization of the unknowns, i.e., the electric potential u, is based. This is the same for each method. Subsequently, the different ways of dealing with the, due to the assumption of a current dipole as introduced in Section 1.4, singular source function f are presented, which are characteristic for each method. As the source is thereby represented by an infinitesimally small current, i.e., with a limit extent of zero, no natural way to handle this problem in the FEM formulation exists. The presented approaches can be divided into two classes. The Venant, partial integration, and Whitney approach rely on the representation of the current dipole as a blurred/smoothed current distribution, i.e., a current distribution with a non-zero extent is derived that approximates the original current distribution in certain aspects. These approaches are in the following called *direct approaches*. In contrast, for the subtraction approach the solution in the homogeneous volume conductor (1.26) is used as a basis and only a correction potential u^c is calculated numerically to account for the specific conductivity distribution.

First of all, the basics of CG-FEM are presented. This method is also known as conforming or Lagrange FEM, since it is based on *Lagrange Ansatz functions*, i.e., *hat functions*. As these basis functions define a subspace of $H^1(\Omega)$ in which the solution for the problem (1.15) lives, this is a conforming FEM formulation. Subsequently, the respective approaches to deal with the source singularity are derived and a selection of error estimates for the numerical solutions is stated. Finally, the accuracy of these approaches is evaluated in a variety of test scenarios.

2.1. Basic Derivation

The basic idea of the finite element method is not to search for a solution in the usually infinite-dimensional function space in which the variational problem is posed, i.e., in our case $H^1(\Omega)$ or $H^1_*(\Omega)$, but rather in a finite dimensional function space, which is usually chosen to be a subspace of the original function space.
In the following, the notation mainly follows Braess (2007). To construct such a finite dimensional subspace, the volume Ω is subdivided and approximated by a set of simple geometrical objects, the so-called triangulation. In two dimensions these objects are typically triangles or quadrilaterals, in three dimensions usually tetrahedra or hexahedra are chosen. Here, tetrahedra allow a better approximation of the underlying geometry. However, hexahedra may have advantages in practical applications as they allow for a very simple model construction (cf. Chapter 3). For the sake of simplicity, such a subdivision of Ω into either tetrahedra or hexahedra is frequently just called a triangulation $\mathcal{T} = \{T_1, T_2, T_3, ..., T_m\}$ in the following, especially when it is not important whether it is a tetrahedralization or hexahedralization in the specific context.

Definition 2. *A decomposition $\mathcal{T}$ of Ω is called admissible, iff*

1. $\bar{\Omega} = \bigcup_i T_i$,
2. $T_i \neq \emptyset$ *for all* i,
3. *for* $i \neq j$, $T_i \cap T_j = \partial T_i \cap \partial T_j$ *and is (depending on the dimension) either a vertex, an edge, or a face, i.e.,* $\operatorname{codim}(T_i \cap T_j, \Omega) > 0$.

Remark 7.

- *We write $\mathcal{T}_h$ instead of $\mathcal{T}$, if each element $T \in \mathcal{T}$ has a diameter of maximally $2h$.*
- *A family of triangulations $\{\mathcal{T}_h\}$ is called* shape regular*, if there exists $\kappa > 0$, such that for every $T \in \mathcal{T}_h$ with radius ρ_T of the inscribed circle*

$$\rho_T \geq h_T/\kappa$$

  holds true, where h_T is half the diameter of T.
- *Though any considered triangulation $\mathcal{T}_h$ is assumed to be a decomposition of the head domain Ω in the following, we sometimes explicitly refer to it as $\mathcal{T}_h(\Omega)$.*

Some scenarios that may not occur in an admissible triangulation are depicted as 2d-examples in Figure 2.1. In the following, it is implicitly assumed that all decompositions $\mathcal{T}_h$ fulfill Definition 2 and are shape regular. We denote by $V(T)$ the set of vertices of an element $T \in \mathcal{T}$, by $E(T)$ the set of edges $e_i = T \cup U$, $U \in \mathcal{T}$, $U \neq T, e_i \neq \emptyset$, $\operatorname{codim}(e_i, T) = 2$, and by $F(T)$ the set of faces $f_i = T \cup U$, $U \in \mathcal{T}$, $U \neq T, f_i \neq \emptyset$, $\operatorname{codim}(f_i, T) = 1$. Accordingly, $V(\mathcal{T})$, $E(\mathcal{T})$, and $F(\mathcal{T})$ are the sets of all vertices, edges, and faces of $\mathcal{T}$. Furthermore, we denote by

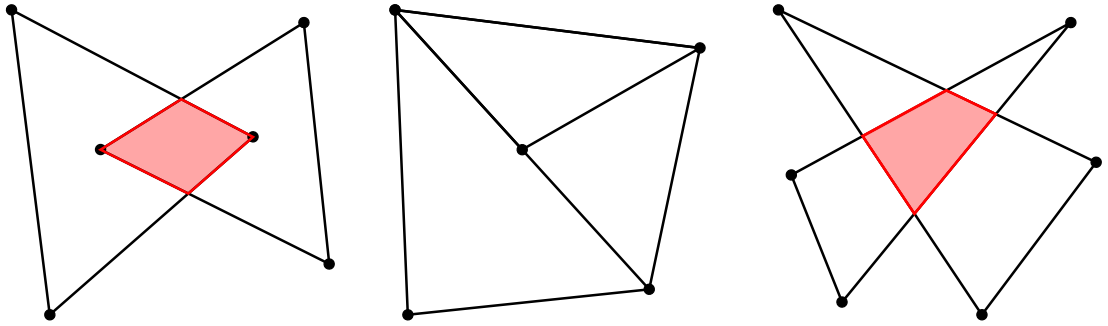

Figure 2.1.: Examples of triangle intersections that may not occur in an admissible triangulation.

$v(\mathbf{x})$ the identification between a point $\mathbf{x}$ and a vertex of a decomposition and by $E(v(\mathbf{x}))$ or $E(\mathbf{x})$ the set of edges the vertex/point is contained in. The same notation is also used for faces.

Next, based on a decomposition $\mathcal{T}_h$, a discrete space V_h to approximate $H^1(\Omega)$ is introduced. We denote by P_k the space of polynomials in $d = \dim \Omega$ variables of degree $p \leq k$, by $\tilde{P}_k$ the space of homogeneous polynomials of degree k, and by Q_k those of partial degree $\leq k$, i.e.:

$$P_k(T) \coloneqq \operatorname{span}\{\Pi_{i=1}^d x_i^{\alpha_i} : \mathbf{x} \in T,\, \alpha \in \mathbb{N}^d, \textstyle\sum \alpha_i \leq k\} \tag{2.1}$$

$$\tilde{P}_k(T) \coloneqq \operatorname{span}\{\Pi_{i=1}^d x_i^{\alpha_i} : \mathbf{x} \in T,\, \alpha \in \mathbb{N}^d, \textstyle\sum \alpha_i = k\} \tag{2.2}$$

$$Q_k(T) \coloneqq \operatorname{span}\{\Pi_{i=1}^d x_i^{\alpha_i} : \mathbf{x} \in T,\, \alpha \in \mathbb{N}^d, \max \alpha_i \leq k\} \tag{2.3}$$

For a tetrahedralization $\mathcal{T}_h(\Omega)$, we introduce the polynomial spaces

$$M^k = \mathcal{M}_k(\mathcal{T}) \coloneqq \{v \in L^2(\Omega) : v|_T \in P_k(T) \text{ for all } T \in \mathcal{T}_h\} \tag{2.4}$$

$$M_0^k \coloneqq \mathcal{M}^k \cap C^0(\Omega) = \mathcal{M}^k \cap H^1(\Omega). \tag{2.5}$$

M_0^1 is also known as the space of P_1-elements. The elements of P_1 are piecewiese linear and continuous functions. Similarly, we define

$$Q_k \coloneqq \{v \in L^2(\Omega) : v|_T \in Q_k(T) \text{ for all } T \in \mathcal{T}_h\} \cap H^1(\Omega). \tag{2.6}$$

In the following, the space $V_h = P_1$ is chosen for tetrahedralizations, while $V_h = Q_1$ is applied for hexahedral decompositions. In both cases, a basis of the space V_h is given by Lagrange Ansatz-functions, which are due to their shape also called hat-functions, and can be defined through the relations

$$h_k \in P_1 \text{ or } Q_1 \quad \text{and} \quad h_k(\mathbf{x}_i) = \delta_{i,k} \text{ for all } \mathbf{x}_i \in V(\mathcal{T}_h). \tag{2.7}$$

We refer to the set of basis functions as $S_h \coloneqq \{h_k,\, k = 1, \ldots, |V(\mathcal{T}_h)|\}$. The set of Lagrange functions S_h is unisolvent, i.e., any function $v \in V_h$ can be uniquely represented in terms of

the h_k, $v(\mathbf{x}) = \sum_k v_k h_k(\mathbf{x})$. The v_k are called the *degrees of freedom* of V_h. If one replaces the space $H^1(\Omega)$ by its approximation $V_h = \operatorname{span} S_h$ in (1.12), it suffices to use the elements of S_h as test functions since this is a linear space. u can now be replaced by its approximation $u_h \in V_h$,

$$u_h(\mathbf{x}) = \sum_j u_j h_j(\mathbf{x}), \tag{2.8}$$

and one has to solve the problem

$$\text{Find } u_h \in V_h, \text{ such that} \quad \int_\Omega \langle \sigma \nabla u_h, \nabla h_k \rangle \, \mathrm{d}x = \int_\Omega f h_k \, \mathrm{d}x \quad \text{for all } h_k \in S_h. \tag{2.9}$$

The approach of approximating u in the space defined by the test functions S_h is called the *Ritz-Galerkin method* (Braess, 2007). Our operators change to

$$a_h(u_h, h_k) = \sum_i u_i \int_\Omega \langle \sigma \nabla h_i, \nabla h_k \rangle \, \mathrm{d}x \text{ for } u_h \in V_h,\ h_k \in S_h, \tag{2.10}$$

$$l_h(h_k) = \int_\Omega f h_k \, \mathrm{d}x \text{ for all } h_k \in S_h. \tag{2.11}$$

Defining

$$A_{ij} = a_h(h_i, h_j) \coloneqq \int_\Omega \langle \sigma \nabla h_i, \nabla h_j \rangle \, \mathrm{d}x \tag{2.12}$$

$$b_i \coloneqq l_h(h_i) = \int_\Omega f h_i \, \mathrm{d}x, \tag{2.13}$$

we obtain a discrete version of (1.14) that can be expressed as a linear equation system

$$Au = b. \tag{2.14}$$

For now, the resulting matrix A is only positive semidefinite, as the additional condition to achieve uniqueness of the weak formulation introduced in Lemma 2 was not considered in the construction of V_h. Thus, the potential u is only fixed up to a constant. However, if the elements S_h define a *partition of unity*, i.e., $\sum_k h_k \equiv 1$, the null space of A is one-dimensional (namely the space of functions $v = \sum_k v_k h_k \in V_h$ with constant coefficients $v_k = \omega \in \mathbb{R}$). Following Remark 4, positive definiteness can then be achieved by introducing mixed boundary conditions and fixing the potential at a single node $\mathbf{x}_D \in \partial\Omega$.

The dimension of A is usually large. Thus, it is not efficient to calculate the inverse matrix A^{-1} to solve for the solution vector u. However, A is sparse, so that (2.14) can be efficiently solved with preconditioned conjugate gradient solvers, e.g., using incomplete Cholesky preconditioning with zero fill-in (IC(0)) or algebraic multigrid (AMG) preconditioning. The efficiency of different solvers was evaluated by Lew et al. (2009b); Wagner (2015); Wolters et al. (2002); in accordance with these results the AMG-CG solver implemented in the SimBio-toolbox

(https://www.mrt.uni-jena.de/simbio/) is used to solve (2.14) throughout this thesis.
When defining $b_i = \int_\Omega f h_i \, \mathrm{d}x$, the choice of $\mathbf{j}^p$ to be a current dipole – as defined in Section 1.4 – was neglected, resulting in $f = \nabla \cdot \mathbf{j}^p = \langle \mathbf{p}, \nabla \delta_{\mathbf{x}_0} \rangle$. Thus, it is not at all clear if the integral $\int_\Omega f h_i \, \mathrm{d}x$ is well-defined and how it should be evaluated, since it is not known how to integrate the singular function $\nabla \delta_{\mathbf{x}_0}$. In the following, different approaches to circumvent this problem are derived, followed by an excursus on error estimates to estimate the accuracy of the discrete solutions of (2.14).

2.2. The Partial Integration (PI) Direct Approach

An intuitive way to overcome the problem of the derivative applied to the δ-distribution is to apply multi-dimensional *partial integration*, i.e., Gauss's theorem, to shift the derivative to the test functions h_k (Gramfort et al., 2011; Lew et al., 2009b; Weinstein et al., 2000; Yan et al., 1991). Thereby, the singularity of the source term can be lowered by one degree and the integration of $\delta_{\mathbf{x}_0}$ is well-known and very simple.

$$b_i^{pi} = \int_\Omega (\nabla \cdot \mathbf{j}^p) h_i \, \mathrm{d}x = \int_\Omega \langle \mathbf{j}^p, \nabla h_i \rangle \, \mathrm{d}x = \begin{cases} \langle \mathbf{p}, \nabla h_i(\mathbf{x}_0) \rangle \text{ if } \mathbf{x}_0 \in \operatorname{supp} h_i, \\ 0 \text{ otherwise.} \end{cases} \tag{2.15}$$

The integration by parts should not be understood in the classical sense here, due to the singularity of $\mathbf{j}^p$, however, it corresponds to the definition of the distributional derivative of $\delta_{\mathbf{x}_0}$. Since the h_i are piecewise linear functions, they are differentiable almost everywhere, so that b^{pi} is well-defined. $\nabla h_k(\mathbf{x})$ is piecewise constant for $V_h = P_1$, i.e., b^{pi} is constant on each element $T \in \mathcal{T}_h$. Thereby, no spatial resolution inside a mesh element is given. For the Q_1-elements used with hexahedra and for higher order polynomial elements this is not the case. The influence of the constant right-hand side inside a mesh element on the accuracy of the solution was evaluated in detail by Vorwerk (2011). Experimentally, the highest accuracies were found for sources placed in the center of the mesh element as one might naively expect (Bauer et al., 2015; Vorwerk, 2011). Practically, this does not lead to any limitations, since the used meshes usually have a sufficient resolution, so that never more than one source per element is set when constructing a source space. This source can then consequently be placed at a position where the resulting error is minimal.

2.3. The Venant Direct Approach

The Venant approach applies *St. Venant's principle*, originally established for elasticity theory, to electrostatics. It is founded on the idea that complicated stress distributions can be locally simplified without notable influence in a relatively large distance when obeying certain restrictions. Thus, Venant's principle allows to replace a point dipole by a distribution of electrical monopoles with very local extent and specific strength, if the moments of the original distribution are conserved. Then, the influence of this approximation on the electric field in a relatively far distance, e.g., at the EEG electrodes, is assumed to be negligible. The

derivation for the approach implemented in the SimBio-toolbox was described by Buchner et al. (1997); Schönen et al. (1994); Wolters et al. (2007a); the basic ideas are recited in the following.

The goal is to represent the dipolar source by a distribution of electrical monopoles $\rho(\mathbf{x})$ that optimally reproduces the moments of this source. Here, the moments of the source distribution are defined to be ${}^kT = \int_\Omega (\mathbf{x} - \mathbf{x}_0)^k \rho(\mathbf{x})\,\mathrm{d}x$. This definition is not equivalent to the coefficients of the multipole expansion as it is known from physics, which is obtained by a multi-dimensional Taylor expansion of the electric potential u (Jackson et al., 2006), which reads

$$u(\mathbf{x}) = \frac{1}{4\pi\epsilon_0}\left(\frac{q}{r} + \frac{\langle \mathbf{p}, \mathbf{x}\rangle}{r^3} + \frac{1}{2}\sum_{ij} Q_{ij}\frac{x_i x_j}{r^5} + \dots\right) \tag{2.16}$$

in cartesian coordinates, where $r = \|\mathbf{x}\|_2$ and the x_i are the entries of $\mathbf{x}$. q is the sum of charges, i.e., $q = 0$ in our case, and $\mathbf{p}$ and Q_{ij} are the dipole and quadrupole moment, respectively:

$$\mathbf{p} = \int \mathbf{x}'\rho(\mathbf{x})\,\mathrm{d}x',$$
$$Q_{ij} = \int (3x_i' x_j' - r'^2\delta_{ij})\rho(\mathbf{x}')\,\mathrm{d}x'.$$

While the dipole moment obviously corresponds to ${}^1T$ after a transformation to a common orign, the quadrupole moment differ from the moment ${}^2T$. This choice is a consequence of the historical derivation of the Venant approach. In some scenarios, e.g., for irregular tetrahedral meshes, this leads to non-optimal simulation results, the differences are nevertheless usually negligible (Hanrath et al., in prep.). Due to the choice of Lagrange functions as test functions as described in Section 2.1, each basis function can be uniquely identified with a mesh vertex. Thus, only the mesh vertices are considered as possible monopole positions; monopoles of strength q_i are placed on the vertex $\mathbf{x}_1 \in V(\mathcal{T})$ closest to the dipole position $\mathbf{x}_0$ and the $n-1$ further vertices $x_2, x_3, \dots, x_n \in E(\mathbf{x}_1)$ that belong to an element $\mathbf{x}_1$ is also part of. In the case of a tetrahedral geometry, this means that they share an edge with $\mathbf{x}_1$. The number of considered vertices is thus 27 for cubic meshes and usually about 16 for tetrahedral meshes (Buchner et al., 1997). To simplify the computation of the moments ${}^kT$, point-like monopole sources are assumed; the source distribution is now given by the sum of monopoles, $\rho = \sum_{i=1}^n q_i \delta_{\mathbf{x}_i}$. The possible consequences of this simplification are discussed later in this section. The discrete moments ${}^kT$, $k \geq 0$, then read

$${}^kT = \sum_{i=1}^n (\mathbf{x}_i - \mathbf{x}_0)^k q_i = \sum_{i=1}^n \Delta\mathbf{x}_i^k q_i, \qquad \Delta\mathbf{x}_i \coloneqq \mathbf{x}_i - \mathbf{x}_0. \tag{2.17}$$

To improve the numerical stability of the resulting equation system, it is rescaled with a suitable reference length a^{ref}, chosen larger than the mesh width h of $\mathcal{T}_h$, so that

$\Delta\mathbf{x}_i/a^{ref} < 1$ for all $i = 1, \ldots, n$. This modifies (2.17) to

$$({}^k\bar{T})_j = \sum_{i=1}^{n} (\Delta\bar{\mathbf{x}}_i)_j^k \, q_i, \qquad j = 1, 2, 3. \tag{2.18}$$

A bar is indicating scaled variables. If the distance $\Delta\bar{\mathbf{x}}_i$ between a vertex $\mathbf{x}_i$ and $\mathbf{x}_0$ is too small, the load q_i can become very high. This might lead to numerical instabilities. Thus, $q_i = 0$ is set for $\Delta\bar{\mathbf{x}}_i < 10^{-3}$. The use of higher order moments ${}^k\bar{T}$ was suggested by Rienäcker et al. (1994). As mentioned previously, these moments should not be confused with the higher moments of the common multipole expansion, only zeroth and first order moment are identical (Jackson et al., 2006). For $k = 0$, (2.18) is the sum of charges $\sum_{i=1}^{n} q_i$, which must be zero since the resulting far-field does not contain any monopole contributions. With the zeroth, all other odd moments vanish, too. The first order moment is exactly the dipole moment, this implies ${}^1T = \mathbf{p}$. We obtain the equation system

$$\underbrace{\begin{bmatrix} ({}^0\bar{T})_j \\ ({}^1\bar{T})_j \\ \vdots \\ ({}^k\bar{T})_j \end{bmatrix}}_{\bar{t}_j} = \underbrace{\begin{bmatrix} (\Delta\bar{\mathbf{x}}_1)_j^0 & (\Delta\bar{\mathbf{x}}_2)_j^0 & \ldots & (\Delta\bar{\mathbf{x}}_n)_j^0 \\ (\Delta\bar{\mathbf{x}}_1)_j^1 & (\Delta\bar{\mathbf{x}}_2)_j^1 & \ldots & (\Delta\bar{\mathbf{x}}_n)_j^1 \\ \vdots & \vdots & \ddots & \vdots \\ (\Delta\bar{\mathbf{x}}_1)_j^k & (\Delta\bar{\mathbf{x}}_2)_j^k & \ldots & (\Delta\bar{\mathbf{x}}_n)_j^k \end{bmatrix}}_{\bar{X}_j} \cdot \underbrace{\begin{bmatrix} q_1 \\ q_2 \\ \vdots \\ q_n \end{bmatrix}}_{q} \tag{2.19}$$

One can compute the ${}^k\bar{T}$ up to $l = 2$ for the given dipole moment $\mathbf{p}$ via

$${}^k\bar{T} = \frac{1 - (-1)^k}{\left(2a^{ref}\right)^k}\mathbf{p}. \tag{2.20}$$

In the case of a point dipole, all higher order moments are automatically zero due to the limit case $\|\mathbf{d}\|_2 \to 0$ in the derivation of the mathematical dipole. We define the matrix $\bar{W}_j$ through $(\bar{W}_j)_{m,s} = (\Delta\bar{\mathbf{x}}_m)^r \, \delta_{m,s}$ for $r = 0$ or $r = 1$. Then, the load vector q is the result of minimizing the functional

$$F_\lambda(q) = \|\bar{t}_j - \bar{X}_j q\|_2^2 + \lambda\|\bar{W}_j q\|_2^2, \tag{2.21}$$

with $\bar{X}_j$ and $\bar{t}_j$ defined as in (2.19). The first term measures the difference between the moments of the original source and the approximation, the second term penalizes loads of large absolute value $|q_i|$ in a least square sense and ensures the uniqueness of the solution when minimizing F_λ. Furthermore, by choosing λ large enough, one avoids sources with large values that do not contribute to the far-field, so-called *blind sources*. Differentiation with respect to the q_i yields the solution of the minimization problem

$$\left(\bar{X}_j^T \bar{X}_j + \lambda \bar{W}_j^T \bar{W}_j\right) q = \bar{X}_j^T \bar{t}_j \tag{2.22}$$

and as result for the vector q

$$q = \left[\sum_{j=1}^{3} \left(\bar{X}_j^T \bar{X}_j + \lambda \bar{W}_j^T \bar{W}_j\right)\right]^{-1} \cdot \sum_{j=1}^{3} \bar{X}_j^T \bar{t}_j. \tag{2.23}$$

The approximation order k is commonly not chosen larger than two. Buchner et al. (1997) suggest that choosing order two results in a spatial concentration of loads in the dipole axis compared to order one. The choice $r = 1$ in the calculation of $\bar{W}_j$ causes a spatial concentration of loads around the dipole position, as large values of $\Delta\bar{x}_i q_i$ are penalized. The parameter λ should be chosen as small as possible to approximate the desired moments accurately, but large enough to avoid indetermination of the equation system.

Though an individual optimization of λ for each dipole position $\mathbf{x}_0$ and the corresponding set of monopole positions $\mathbf{x}_1, \ldots, \mathbf{x}_n$ is possible, the choice of λ is not assumed to be critical and fixing $\lambda = 10^{-6}$ has established in praxis. For the following computations furthermore $a^{ref} = 20$ mm, $k = 2$, $r = 1$ are fixed. These values are rather conservatively chosen, e.g., a value of $a^{ref} = 20$ mm is clearly overestimated as h is rather in the range of a few millimeters for the meshes commonly used nowadays.

If $v_{glo}(i)$ defines the unique mapping between the local indices of the $\mathbf{x}_k$ and the global indices and v_{glo}^{-1} its inverse, the Venant right-hand side vector is given by

$$b_i^{ven} = \begin{cases} q_{v_{glo}^{-1}(i)} \text{ if } i \in v_{glo}^{-1}(\{0, \ldots, n\}), \\ 0 \text{ otherwise.} \end{cases} \tag{2.24}$$

Figuratively speaking, the approach performs a blurring of the previously point-like source current. From a physical point of view, the term $f = \nabla \cdot \mathbf{j}^p$ corresponds to the sinks and sources of the current $\mathbf{j}^p$. The idea of choosing $f = \sum_i q_i \delta_{\mathbf{x}_i}$ is to introduce a current density with sources at the positions $\mathbf{x}_i$ that matches the original distribution in the previously noted properties. In the derivation it was assumed that these sources are point-like. However, due to the used Ritz-Galerkin approach as introduced in Section 2.1, the source term actually corresponds to the function $f = \sum_i q_i h_{v^{-1}(i)}$. This is not considered when computing the moments of the source distribution. Since $\mathbf{x}_i$ corresponds to $\arg\max h_i$ and also to the center of mass of h_i, this is not assumed to have any significant effects. The consequences of the resulting singular right-hand side f on the convergence of the discrete solution are further discussed in Section 2.7.

2.4. The Whitney Approach

In the derivation of Venant and partial integration approach the idea is to replace the singular source distribution $\mathbf{j}^p$ by a blurred distribution that is in a certain sense similar to the original one. Instead, for the Whitney approach directly a source term f with a higher regularity is chosen. Thus, it is necessary to search vector-valued functions, such that the term $\nabla \cdot \mathbf{j}^p$ is well-defined (at least in a weak sense), i.e., $\nabla \cdot \mathbf{j}^p \in L^2(\Omega)$. This is guaranteed if our primary

current $\mathbf{j}^p$ is contained in the space $H(\mathrm{div};\Omega)$:

Definition 3.

$$H(\mathrm{div};\Omega) \coloneqq \left\{\mathbf{q} \in L^2(\Omega)^3 : \nabla \cdot \mathbf{q} \in L^2(\Omega)\right\} \tag{2.25}$$

As discrete approximation of $H(\mathrm{div};\Omega)$ one can choose the space RT_0 of *lowest-order Raviart-Thomas elements* (Nédélec, 1980; Raviart and Thomas, 1977). The normal component of these functions is by definition continuous on element boundaries, they are thus conforming in $H(\mathrm{div};\Omega)$.

Definition 4 (Raviart-Thomas elements)**.** *Let $\mathcal{T}_h(\Omega)$ be a tetrahedralization. We introduce the Raviart-Thomas elements of order k by defining them on each element $T \in \mathcal{T}_h$,*

$$\begin{aligned} RT_k(T) \coloneqq& (P_k(T))^d + \mathbf{x}\tilde{P}_k(T), \\ RT_k(\mathcal{T}_h) \coloneqq& \left\{\mathbf{q} \in L^2(\Omega)^3 : \mathbf{q}|_T \in RT_k(T) \text{ and } \langle \mathbf{q}, \mathbf{n}\rangle \text{ is continuous over } \partial T \text{ for all } T \in \mathcal{T}_h\right\}, \\ =& \left\{\mathbf{q} \in L^2(\Omega)^3 : \mathbf{q}|_T \in RT_k(T) \text{ for all } T \in \mathcal{T}_h\right\} \cap H(\mathrm{div};\Omega). \end{aligned} \tag{2.26}$$

The lowest order space $RT_0(T)$ can also simply be written as

$$RT_0(T) \coloneqq \left\{\mathbf{a} + b\mathbf{x} : \mathbf{a} \in \mathbb{R}^3, b \in \mathbb{R}, \mathbf{x} \in T\right\} \subset H(\mathrm{div}, T).$$

For a hexahedralization $\mathcal{H}_h$ and $H \in \mathcal{H}_h$, the definition of $RT_k(\mathcal{H}_h)$ follows accordingly (Brezzi and Fortin, 1991; Nédélec, 1980):

$$\begin{aligned} RT_k(H) \coloneqq& (Q_k(H))^d + \mathbf{x}Q_k(H) \\ RT_k(\mathcal{H}_h) \coloneqq& \left\{\mathbf{q} \in L^2(\Omega)^3 : \mathbf{q}|_H \in RT_k(H) \text{ and } \langle \mathbf{q}, \mathbf{n}\rangle \text{ is continuous over } \partial H \text{ for all } H \in \mathcal{H}_h\right\} \end{aligned} \tag{2.27}$$

Raviart-Thomas elements are also used and analyzed in more detail in Chapter 5. For now, it suffices to define a basis of the space RT_0 for both tetrahedral and hexahedral elements. For tetrahedral elements, a finite dimensional basis of RT_0 is defined by the vector-valued functions supported on two adjacent elements T_1 and T_2 sharing a common face $f_{1,2} = \bar{T}_1 \cap \bar{T}_2 \in \mathcal{F}_h$, so that the normal derivative is continuous across this face and zero on all other faces. With the $\mathbf{v}_i$ defined as in Figure 2.2 (left), we have

$$\mathbf{w}_k(\mathbf{x}) \coloneqq \begin{cases} \dfrac{|f_{1,2}|}{3|T_1|}\dfrac{\mathbf{v}_4 - \mathbf{x}}{\|\mathbf{v}_4 - \mathbf{v}_1\|_2} & \text{if } \mathbf{x} \in T_1, \\ \dfrac{|f_{1,2}|}{3|T_2|}\dfrac{\mathbf{x} - \mathbf{v}_1}{\|\mathbf{v}_4 - \mathbf{v}_1\|_2} & \text{if } \mathbf{x} \in T_2, \\ 0 \text{ otherwise.} \end{cases} \tag{2.28}$$

$|T_1|$ and $|T_2|$ indicate the volume of the tetrahedra T_1 and T_2, respectively, and $|f_{1,2}|$ the surface area of the face $f_{1,2}$. For $\mathbf{x} \in \partial T_1 \cup \partial T_2$, we have $\langle \mathbf{w}_k(\mathbf{x}), \mathbf{n}_{f_{1,2}}\rangle = \mathbb{1}_{f_{1,2}}(\mathbf{x})$.

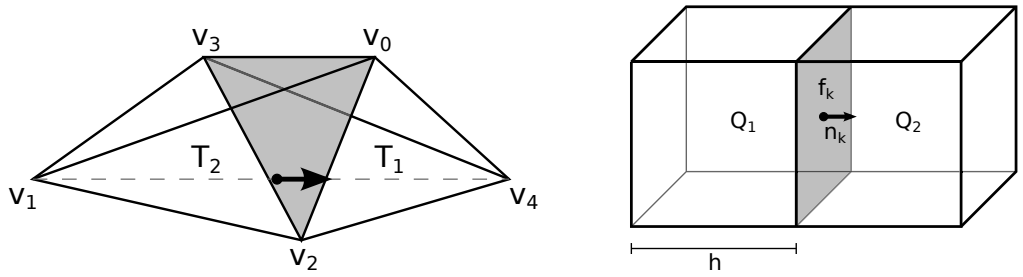

Figure 2.2.: Zeroth order Raviart-Thomas basis function supported on two tetrahedra T_1 and T_2 (left) and on two hexahedra Q_1 and Q_2 (right). Resulting synthetic dipole indicated by the arrow.

For a regular, hexahedral mesh with edge length h, a RT_0 basis function $\mathbf{w}_k$ is supported on the two hexahedra $Q_1, Q_2 \in \mathcal{T}_h$ sharing the face $f_k = \bar{Q}_1 \cap \bar{Q}_2$ with normal vector $\mathbf{n}_k$ and centroid $\bar{\mathbf{x}}_k$ and can be defined by

$$\mathbf{w}_k(\mathbf{x}) = \begin{cases} \left(1 + \frac{\langle \mathbf{x} - \bar{\mathbf{x}}_k, \mathbf{n}_k \rangle}{h}\right) \mathbf{n}_k \text{ if } \mathbf{x} \in \bar{Q}_1 \cup \bar{Q}_2, \\ 0 \text{ otherwise.} \end{cases} \tag{2.29}$$

This definition can be transferred to non-degenerated parallelepipeds using a *Piola transformation* to preserve the normal components (Brezzi and Fortin, 1991; Nédélec, 1980).

One can now write $\mathbf{j}^p$ in terms of $\mathbf{w}_k$, i.e., $\mathbf{j}^p_{rt} = \sum_k j_k \mathbf{w}_k$. To compare the results obtained using Raviart-Thomas elements as source model with those of the other approaches, Pursiainen et al. (2011) derived a relation of the so-called Whitney-type sources to a point dipole of a certain moment and position. Furthermore, it is possible to compute solutions for arbitrary source distributions using different interpolation techniques (Bauer et al., 2015).

Inserting $\mathbf{j}^p_{rt}$ in the FEM right-hand side b_i as defined in (2.13), we have

$$(b^{rt})_i = \int_\Omega \nabla \cdot \mathbf{j}^p_{rt} h_i \, \mathrm{d}x = \sum_k j_k \int_\Omega \nabla \cdot \mathbf{w}_k h_i \, \mathrm{d}x. \tag{2.30}$$

The matrix $G_{ij} = \int_\Omega \nabla \cdot \mathbf{w}_j h_i \, \mathrm{d}x$ defines a mapping from the RT_0 basis functions to the Lagrange basis functions S_h. In the tetrahedral case, G has two non-zero entries per column, for hexahedral meshes the number of non-zero entries per column is eight. In both cases, the contributions from the two elements $\mathbf{w}_k$ is supported on sum up to 0 for the vertices on the shared face f. Thus, for a locally supported source current $\mathbf{j}^p$, b^{rt} is sparse.

Pursiainen et al. (2011) have shown that in the tetrahedral case each basis function $\mathbf{w}_k$ can optimally be identified with a dipole at position $\mathbf{x}_k = (\mathbf{v}_1 + \mathbf{v}_4)/2$ and moment $\mathbf{q}_k = \int_\Omega \mathbf{w}_k \, \mathrm{d}x$ (cf. Figure 2.2, left). This fits to the intuitive choice, since $G_{\cdot k}$ has non-zero entries only at the positions corresponding to $\mathbf{v}_1$ and $\mathbf{v}_4$, i.e., according to the interpretation of the entries of the right-hand side vector b as current sinks and sources, a current from $\mathbf{v}_1$ to $\mathbf{v}_4$ is simulated here. Thus, it seems reasonable to identify this current with a dipole in its midpoint. Accordingly, for a (regular) hexahedral mesh, each $\mathbf{w}_k$ can be identified with a dipole in the center of the shared face (corresponding to the center of gravity $\bar{\mathbf{x}}_k$) and with the dipole moment again

devined via $\mathbf{q}_k = \int_\Omega \mathbf{w}_k \, \mathrm{d}x$ (cf. Figure 2.2, right).
To simulate arbitrary dipolar sources using the Whitney approach, it is necessary to introduce interpolation techniques that define a linear combination of different Whitney elements that represents the original source with position $\mathbf{x}_0$ and moment $\mathbf{p}$.
An intuitive choice is to define the weights j_k for each basis function $\mathbf{w}_k$ via

$$j_k \coloneqq \int \langle \mathbf{j}^p, \mathbf{w}_k \rangle \, \mathrm{d}x = \int \langle \mathbf{p}, \mathbf{w}_k \rangle \delta_{\mathbf{x}_0} \, \mathrm{d}x = \langle \mathbf{p}, \mathbf{w}_k(\mathbf{x}_0) \rangle. \tag{2.31}$$

This interpolation is easy to implement and stable for (regular) hexahedral meshes, where the directions of the $\mathbf{w}_k$ are either orthogonal or parallel to each other. However, this interpolation strategy leads to 32 non-zero entries in the right-hand side b^{rt}, since it utilizes all six basis functions that are supported on the source element. One could also think of other interpolation strategies that are limited to only three of the basis functions, so that the $\mathbf{n}_k$, i.e., the normal vectors of the faces f_k associated to the $\mathbf{w}_k$, form an orthogonal basis. For tetrahedral meshes, it is possible that due to badly shaped tetrahedra the basis functions are not as nicely oriented as in the hexahedral case. To account for this, different interpolation strategies have been presented and evaluated (Bauer et al., 2015; Pursiainen et al., 2011). In the following, the *position based optimization scheme* (PBO) is chosen that was introduced by Bauer et al. (2015). The goal is to approximate a given dipole at position $\mathbf{x}_0 \in T$ and with moment $\mathbf{p}$ through the four basis functions $\mathbf{w}_l$, $l = 1, 2, 3, 4$, that are supported on T and can be associated to the four faces of T, $\mathbf{p}\delta_{\mathbf{x}_0} \approx \sum_l c_l \mathbf{w}_l$. Using the position $\mathbf{x}_l$ and direction $\mathbf{q}_l$ that can be associated to each $\mathbf{w}_l$, the task is to find a solution to the optimization problem

$$\min_c \sum_l c_l^2 \omega_l^2 \text{ subject to } Qc = \mathbf{p}, \tag{2.32}$$

where $c = (c_1, c_2, c_3, c_4)$ are the weights given to each basis function, $\omega_l = \|\mathbf{x}_l - \mathbf{x}_0\|_2$ is a further weighting coefficient, and $Q = (\mathbf{q}_1, \mathbf{q}_2, \mathbf{q}_3, \mathbf{q}_4)$. Due to the convexity of $\sum_l c_l^2 \omega_l^2$, (2.32) has a unique solution that can be obtained via the method of Lagrangian multipliers. It is given by the linear system

$$\begin{pmatrix} D & Q^T \\ Q & 0 \end{pmatrix} \begin{pmatrix} c \\ d \end{pmatrix} = \begin{pmatrix} 0 \\ p \end{pmatrix} \tag{2.33}$$

with diagonal matrix $D = \mathrm{diag}(\omega_1^2, \omega_2^2, \omega_3^2, \omega_4^2)$ and an auxiliary vector of Lagrangian multipliers $d = (\lambda_1, \lambda_2, \lambda_3)$.

2.5. Monopole Distribution for Direct Approaches

As mentioned in Section 2.3, the non-zero entries of the right-hand side vector b can be interpreted as electrical monopoles at the respective vertex positions. Knowing that monopoles placed outside or on the boundary of the source compartment may lead to numerical inaccuracies (Medani et al., in prep.; Vorwerk, 2011), a focal monopole distribution consisting of as few as possible monopoles seems desirable. However, with respect to the approximation of

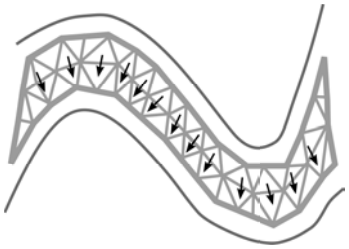

Figure 2.3.: Sketch of sources fixed with a normal constraint in tetrahedral model. *Source: Bauer et al. (2015)*

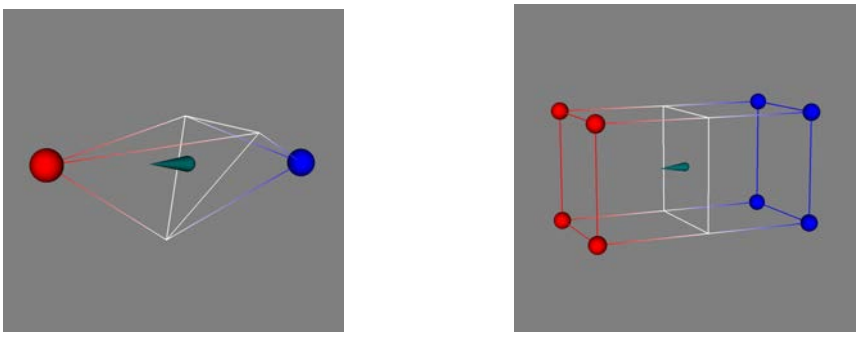

Figure 2.4.: Monopole distribution for the Whitney FE approach for optimized dipole position in tetrahedral and regular hexahedral mesh.

the original dipole, a too small amount of monopoles might also lead to inacurrate solutions. Before evaluating the accuracy of the different approaches to approximate the dipole source, the extent and distribution of the monopole loads are discussed in this section.

Table 2.1.: Number of monopoles considered to model the dipole source (tetrahedral/hexahedral model). Data for Venant approach calculated in model *4layer-802k* (cf. Section 2.10.2).

Source Position/Orientation	Partial Integration	Venant	Whitney
optimized	4/8	≈ 16, (≤ 23) / 27	2 / 8
random	4/8	≈ 16, (≤ 23) / 27	8 / 32

The tetrahedral case is considered first, the hexahedral case follows accordingly. For a source with position and orientation chosen such that it can be represented by a single Raviart-Thomas basis function, the mapping matrix G in Section 2.4 only has two non-zero entries per column and thereby also the right-hand side vector b only has two non-zero entries. These are the two nodes belonging to two tetrahedra that share a common face but are no element of this face. This monopole distribution corresponds to the natural idea of a dipole consisting of a current source and sink of the same strength (cf. Figure 2.4). This scenario might, e.g., occur when the source space is based on a discretized brain surface and a normal constraint, i.e., source orientations perpendicular to this surface, is chosen (cf. Figure 2.3). When applying the interpolation scheme to account for arbitrary source positions and orientations, the number of right-hand side entries grows to 8, since all basis functions supported on the element containing

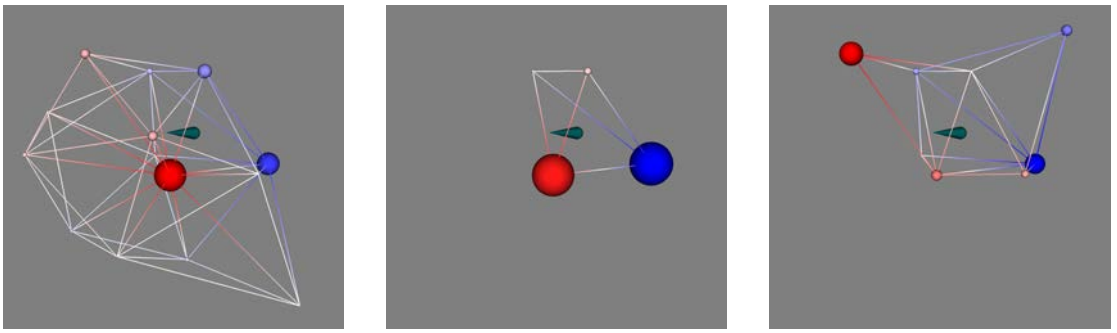

Figure 2.5.: Monopole distribution for the direct FE approaches Venant (left), partial integration (middle) and Whitney (right) in tetrahedral model.

the dipole position are taken into account.

For the partial integration approach the number of monopoles simply corresponds to the number of vertices per mesh element, as it is obvious from the derivation (cf. Section 2.2), while for the Venant approach the number of non-zero right-hand side entries depends on the number of edges the vertex $\mathbf{x}_0$ shares with other vertices. Thus, it depends on the local mesh structure in the tetrahedral case (cf. Section 2.3).

The distributions of the monopoles for a source with random position and orientation in a tetrahedral mesh are shown in Figure 2.5. To give an idea of the extent of the monopole cloud, the displayed detail is not changed for the different approaches. The different extents of the set of monopoles are obvious. For all three approaches, the main contribution to the representation of the dipole is rendered by one large positive and negative load. The value of the other monopole loads is considerably smaller, they mainly contribute a correction to better approximate the desired dipole orientation. Besides the different extent, a major difference between the distributions is the positioning of the two strong monopoles. While these are very close for Venant and partial integration approach, as they share a common edge, they are two nodes on the opposing sides of a face for the Whitney approach. Thereby, they have a clearly larger distance if the mesh is well-shaped. As the PBO interpolation scheme assigns different weights to the respective basis functions, this shows that the dipole representation is dominated by a single Whitney basis function. However, this is just an illustrative single case example, the actual consequences of these differences for the accuracy in solving the EEG/MEG forward problem are investigated in the remainder of this chapter.

In a hexahedral model, as mentioned in Section 2.4, six Whitney basis functions are supported on each element and each of them can be identified with a dipole in the center of an element face. Thus, a dipole whose position and direction are chosen suitably is represented by 8 monopoles (cf. Figure 2.4). For arbitrary positions and orientations, different interpolation techniques are conceivable, the output of the one indicated in Section 2.4 is shown here, leading to a distribution consisting of 32 monopoles. This distribution is depicted in Figure 2.6 (right) together with the distributions for Venant (left) and partial integration approach (middle). The source is the same as in the tetrahedral case and a 2 mm regular hexahedral mesh was used, again the displayed detail is the same for all approaches.

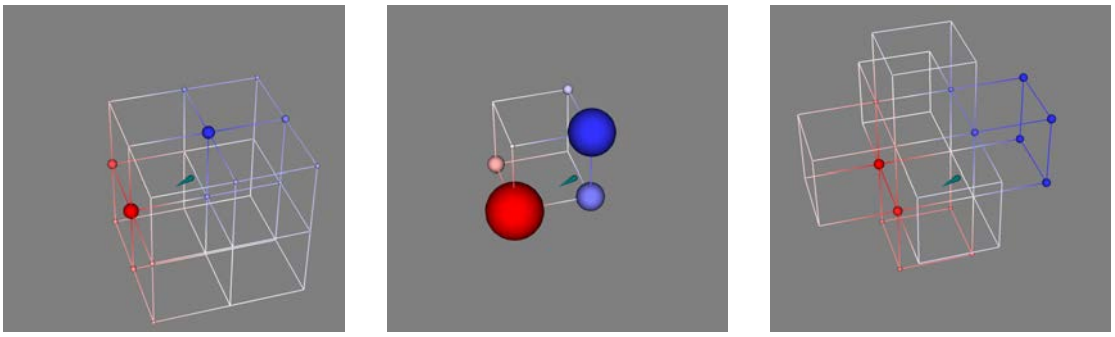

Figure 2.6.: Monopole distribution for the direct FE approaches Venant (left), partial integration (middle), and Whitney (right) in regular hexahedral model.

2.6. The Subtraction Approach

Though founding on different ideas how to approximate the dipole source, all of the previously presented approaches finally ended up at replacing the dipolar source by a distribution of electrical monopoles to circumvent the problem of the singular source term. The basic idea of the subtraction approach is fundamentally different. Under the assumption that there exists a non-empty open neighborhood $\Omega^\infty \subset \Omega$ of the source with constant, isotropic conductivity σ^∞, one can make use of the fundamental solution (1.25)/(1.26) to model the source singularity and rewrite (1.10) into an equation for a correction potential u^c. The correction potential u^c accounts for the specific conductivity profile and can be calculated akin to (2.9) (Bertrand et al., 1991; Drechsler et al., 2009; Wolters et al., 2007c). Anisotropic conductivities in the source area can be modeled similarly, but this case is skipped here and it is referred to (Drechsler et al., 2009; Wolters et al., 2007c) instead. The derivation is essentially identical to the one presented here, only (1.25) has to be adjusted to the anisotropic case.

The main idea is to split up potential u and conductivity σ into two parts:

$$u = u^\infty + u^c, \tag{2.34a}$$

$$\sigma = \sigma^\infty + \sigma^c. \tag{2.34b}$$

u^∞ is defined as the potential in an unbounded, homogeneous volume conductor with conductivity σ^∞ and can thus be calculated analytically applying (1.25): $\sigma^\infty u^\infty = -(\nabla \cdot \mathbf{j}^p) * G$. As previously, $f = \nabla \cdot \mathbf{j}^p = \langle \mathbf{p}, \nabla \delta_{\mathbf{x}_0} \rangle$. Inserting the decomposition of u into (1.11), one can subtract the homogeneous solution, since $\sigma^\infty \Delta u^\infty = -\Delta((\nabla \cdot \mathbf{j}^p) * G) = \nabla \cdot \mathbf{j}^p$, and we obtain a Poisson equation with inhomogeneous Neumann boundary conditions for the correction potential:

$$\nabla \cdot (\sigma \nabla u^c) = f \text{ in } \Omega, \qquad f := -\nabla \cdot (\sigma^c \nabla u^\infty), \tag{2.35a}$$

$$\sigma \partial_{\mathbf{n}} u^c = g \text{ on } \Gamma, \qquad g := -\sigma \partial_{\mathbf{n}} u^\infty. \tag{2.35b}$$

Similarly to Section 1.3, one can derive a weak formulation for the correction potential u^c.

Find $u^c \in H^1_*(\Omega)$, such that

$$\int_\Omega \langle \sigma \nabla u^c, \nabla v \rangle \,\mathrm{d}x = -\int_\Omega \nabla \cdot (\sigma^c \nabla u^\infty) v \,\mathrm{d}x - \int_{\partial\Omega} (\sigma \partial_{\mathbf{n}} u^\infty) v \,\mathrm{d}x \tag{2.36}$$

for all $v \in H^1_*(\Omega)$.

Again, the weak formulation can be derived from (2.35) using partial integration and the identity (2.34b). For the equation system (2.36), existence and uniqueness of a solution can be directly proven in the same fashion as done for the general problem in Section 2.1 (Drechsler et al., 2009; Wolters et al., 2007c). On the left-hand side we have the bilinear form a known from (1.13), thus Lemma 2 still applies. We define the linear form

$$l^c(v) = -\int_\Omega \nabla \cdot (\sigma^c \nabla u^\infty) v dx - \int_{\partial\Omega} \sigma \partial_{\mathbf{n}} u^\infty v \,\mathrm{d}x \tag{2.37}$$

and conclude

Lemma 3. *The linear form l^c is well-defined and bounded on $H^1(\Omega)$, particularly $l^c \in H^1_*(\Omega)'$.*

Proof. Wolters et al. (2007c). □

Thus, the Lemma of Lax-Milgram (Lemma 1) can be applied to prove existence and uniqueness of a solution. Using partial integration and the Neuman boundary condition (2.35b), we have

$$l^c(v) = \int_\Omega \langle \sigma^c \nabla u^\infty, \nabla v \rangle \,\mathrm{d}x - \int_{\partial\Omega} \sigma^\infty \partial_{\mathbf{n}} u^\infty v \,\mathrm{d}x. \tag{2.38}$$

The space $H^1(\Omega)$ is now replaced by its discrete approximation V_h and the representation of $u^c_h \in V_h$ in terms of the basis functions S_h, $u^c_h(\mathbf{x}) = \sum_j (u^c)_j h_j(\mathbf{x})$, is inserted, so that we obtain the equation system

$$Au^c = b^c. \tag{2.39}$$

A is the same stiffness matrix as previously (Section 2.1) and the right-hand side b^c is given by

$$(b^c)_i = \int_\Omega \langle \sigma^c \nabla u^\infty, \nabla h_i \rangle \,\mathrm{d}x - \int_{\partial\Omega} \sigma^\infty \partial_{\mathbf{n}} u^\infty h_i \,\mathrm{d}x. \tag{2.40}$$

This equation system can be solved in the same way as it was done for the direct approaches. The full potential is then computed via (2.34a), $u_h(\mathbf{x}) = u^\infty(\mathbf{x}) + u^c_h(\mathbf{x})$. Since both u^∞ and u^c_h are only determined up to a constant, it has to be made sure that they fulfill a compatibility condition, e.g., $\int_\Omega u^\infty \,\mathrm{d}x = -\int_\Omega u^c \,\mathrm{d}x$, before adding them up.
Since the expression for the right-hand side b^c cannot be further simplified, it needs to be calculated using numerical integration (Drechsler et al., 2009). Especially for superficial

sources the numerical accuracy can decrease strongly (Wolters et al., 2007c). Furthermore, in contrast to the direct approaches, where the right-hand side vectors are generally sparse, b^c is dense. This causes the setup of the right-hand side b^c to be computationally way more expensive for the subtraction approach than for the direct approaches. While this is negligible when solving only few forward problems, it becomes significant when solving many forward problems at a time and applying the transfer matrix approach that is introduced in Section 2.9. A projected subtraction approach that allows for a faster computation of b^c was proposed by Wolters et al. (2007c), but did not lead to satisfying accuracies (Drechsler et al., 2009).

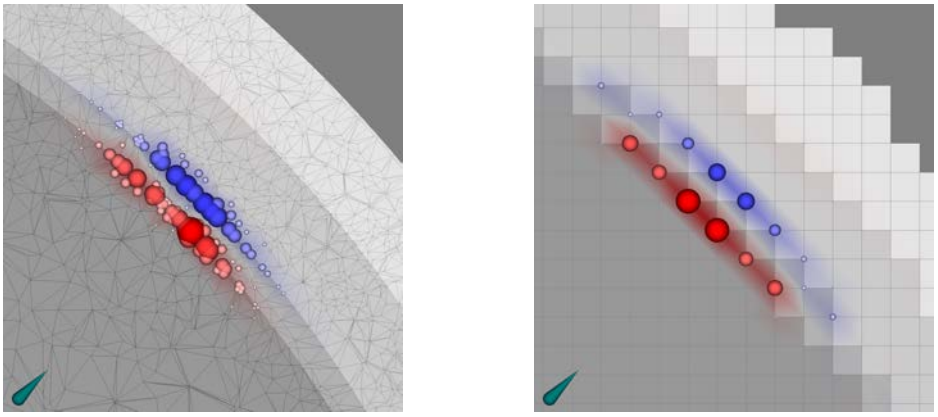

Figure 2.7.: Visualization of volume term of subtraction right-hand side b^c, $\int_\Omega \langle \sigma^c \nabla u^\infty, \nabla h_i \rangle \, \mathrm{d}x$, for a dipole at position $(1, 47, 47)$ and direction $(0, 1, 1)$ in models *4layer-519k* and *seg_2_res_2*. Slice is taken in the $x = 1$ plane, gray values indicate the compartments brain, CSF, skull, and skin (from interior to exterior), dark gray is air.

Remark 8. *If the head model consists of compartments of constant conductivities, $\Omega_1, \ldots, \Omega_n$, as assumed in the numerical experiments in Sections 2.10 and 2.11, $f^c = \nabla \cdot \sigma^c \nabla u^\infty$ is non-zero only at the compartment interfaces $\bar{\Omega}_e \cap \bar{\Omega}_f$, $e \neq f$. For $\mathbf{x} \in \mathring{\Omega}_e$ and any $e = 1, \ldots, n$, $f^c(\mathbf{x}) = \nabla \cdot (\sigma^c(\mathbf{x}) \nabla u^\infty(\mathbf{x})) = \sigma^c(\mathbf{x}) \nabla \cdot \nabla u^\infty(\mathbf{x}) = 0$, since either $\sigma^c(\mathbf{x}) = 0$ or $\nabla \cdot \nabla u^\infty(\mathbf{x}) = \Delta u^\infty(\mathbf{x}) = 0$. Thus, one can also expect that $\int_\Omega \langle \sigma^c \nabla u^\infty, \nabla h_i \rangle \, \mathrm{d}x$ admits the highest absolute values if the vertex $\mathbf{x}_i$ that can be identified with h_i is on a compartment interface. This explains, why the choice of meshes with inhomogeneous resolution, i.e., with smaller mesh elements at compartment interfaces, leads to higher accuracies for the subtraction approach in comparison to homogeneous meshes (cf. Chapter 2; Lew et al., 2009b). In Figure 2.7, $\int_\Omega \langle \sigma^c \nabla u^\infty, \nabla h_i \rangle \, \mathrm{d}x$ is visualized for a dipole at position $(1, 47, 47)$ and direction $(0, 1, 1)$ using the tetrahedral and hexahedral models* 4layer-519k *and seg_2_res_2 from Sections 2.10 and 4.2, respectively.*

2.7. Error Estimates for the Discrete Solution

This section is devoted to the approximation properties of the discrete solution u_h contained in the space $V_h = P_1$ or Q_1. The goal is to derive a priori error estimates of type $\|u - u_h\| \leq Ch^p$ for a solution of the continuous problem u, some norm $\|\cdot\|$, mesh width h, convergence order

p, and a constant C that might depend on u, f, σ, or the shape of Ω, but is independent of h. Commonly, such estimates are derived under the assumption $u \in H^2(\Omega)$, which requires at least $f \in L^2(\Omega)$ and $\sigma \in H^1(\Omega)$. Also assumptions on the shape of the domain Ω are usually necessary, e.g., Ω convex and $\Gamma = \partial\Omega$ (piecewise) C^2-smooth.
This leads to at least two obvious problems when aiming to derive error estimates for FEM EEG forward solutions:

- In multi-compartment head models σ is usually assumed to be piecewise constant on each conductive compartment and jumping on compartment interfaces, i.e., $\sigma \notin H^1(\Omega)$
- For Venant and partial integration approach $f \notin L^2(\Omega)$, while this is uncritical for Whitney and subtraction approach

Finally, a frequent assumption in the derivation of error estimates are homogeneous Dirichlet boundary conditions in (1.11), i.e., $u = 0$ on $\partial\Omega$, so that it is not always clear if these results can be directly transferred to problems with Neumann boundary conditions.
As a consequence, it is necessary to restrict to a simplified setting to be able to easily apply standard error estimates to the EEG forward problem, e.g., a (convex) one-layer model, i.e., σ constant on Ω, as done by Wolters et al. (2007c). This simplification allows to derive error estimates using standard methods for subtraction and Whitney approach, while more work is necessary for partial integration and Venant approach or when willing to consider the piecewise constant conductivity distribution σ.
These thoughts in mind, we note a basic estimate for many scenarios, the *Cea-Lemma*, which states (Braess, 2007; Hackbusch, 2003)

$$\|u - u_h\|_V \leq C \inf_{v \in V_h} \|u - v_h\|_V. \tag{2.41}$$

This estimate is rather unsatisfying as the infimum is neither easily accessible nor demonstrative. However, on this basis meaningful error estimates can be obtained by finding upper bounds for this infimum, optimally with an explicit dependency on the mesh width h. The derivations of the estimates are skipped in the following, for details it is referred to Braess (2007); Hackbusch (2003) if not differently indicated.
Sticking to the naturally occuring H^1-norm and for $u \in H^2(\Omega)$, i.e., $\sigma \in H^1(\Omega)$ and $f \in L^2(\Omega)$, fixing the polynomial degree $k = 1$ we obtain the estimates

$$\|u - u_h\|_{H^1(\Omega)} \leq C_1 h \|u\|_{H^2(\Omega)}, \tag{2.42}$$
$$\|u - u_h\|_{H^1(\Omega)} \leq C_2 h \|f\|_{L^2(\Omega)}. \tag{2.43}$$

In the L^2-norm instead of the H^1-norm, the convergence order in h is one degree higher; still assuming $u \in H^2(\Omega)$, we have

$$\|u - u_h\|_{L^2(\Omega)} \leq C_3 h^2 \|u\|_{H^2(\Omega)}, \tag{2.44}$$

$$\|u - u_h\|_{L^2(\Omega)} \leq C_4 h^2 \|f\|_{L^2(\Omega)}, \tag{2.45}$$

while for $u \in H^1(\Omega)$ one can only assume

$$\|u - u_h\|_{L^2(\Omega)} \leq C_5 h \|u\|_{H^1(\Omega)}. \tag{2.46}$$

These estimates can directly be applied to the Whitney or subtraction approach:

Theorem 1 (Quantitative error estimate for the subtraction approach in a one-layer model; Hackbusch, 2003; Wolters et al., 2007c)**.** *Let u^c be a sufficiently regular solution of* (2.35)*, $u^c \in H^2(\Omega)$. For an appropriate triangulation (tetrahedralization/hexahedralization), linear (trilinear) FE-trial functions, and a continuous and elliptic bilinearform a, we find constants C_1, C_2 independent of u^c and h with*

$$\|u^c - u_h^c\|_{H^1(\Omega)} \leq C_1 h \|u^c\|_{H^2(\Omega)}, \tag{2.47a}$$

$$\|u^c - u_h^c\|_{L^2(\Omega)} \leq C_2 h^2 \|u^c\|_{H^2(\Omega)}. \tag{2.47b}$$

Proof. Hackbusch (2003); Wolters et al. (2007c) □

When applying these estimates to the Whitney approach, it has to be kept in mind that only the convergence of u_h towards a solution u for the Whitney right-hand side $f_{rt} = \nabla \cdot \mathbf{j}_{rt}^p$ is estimated here, while the goodness with which f_{rt} approximates a current dipole is not considered.

The above estimates do no longer hold if the assumption of $\sigma \in H^1(\Omega)$ is dropped. In this case, only general estimates of the type $\|u - u_h\|_{H^1(\Omega)} = \mathcal{O}(h^{1/2})$ and $\|u - u_h\|_{L^2(\Omega)} = \mathcal{O}(h)$ can be directly achieved. Possibly sharper estimates can be reobtained by improving the representation of the domain boundaries Γ_i, e.g., using isoparametric finite elements (Barrett and Elliott, 1987; Hackbusch, 2003; Wolters et al., 2007c).

Other options to achieve (optimal) error estimates for jumping coefficients σ are, e.g., considering the convergence towards a solution u of the weak formulation instead of a strong solution (Li et al., 2010) and the use of weighted-norms (Plum and Wieners, 2003). Due to the less restrictive requirements on the disjunct domains Ω_i of constant conductivity σ_i, we choose to adapt the results of Plum and Wieners (2003) here. It is necessary to assume that u fulfills the (physically reasonable) jump conditions

$$[u]_{i,j} = 0 \qquad \text{and} \qquad [\sigma \partial_{\mathbf{n}} u]_{i,j} = 0$$

on the interfaces $\Gamma_{i,j} = \bar{\Omega}_i \cap \bar{\Omega}_j$. The jump operator is defined as the difference between the limits of a function x on $\Gamma_{i,j}$ taken from Ω_i and Ω_j, respectively, $[x]_{i,j} \coloneqq x|_{\partial\Omega_i} - x|_{\partial\Omega_j}$. It is further introduced and excessively used in Chapter 4.

Theorem 2 (Plum and Wieners, 2003)**.** *Let Ω and the Ω_i be Lipschitz domains with piecewise C^2 boundaries $\partial\Omega_i$, $\cup\bar{\Omega}_i = \Omega$, $\Omega_i \cap \Omega_j = \emptyset$ for $i \neq j$, and $\sigma(\mathbf{x}) = \sigma_i > 0$ for $\mathbf{x} \in \Omega_i$. Let $u \in H^1(\Omega)$ be a solution of the Poisson problem* (1.14) *with homogeneous Dirichlet boundary conditions for $f \in L^2(\Omega)$ and fulfilling the jump conditions. Then, we have the weighted L^2-estimate*

$$\left(\sum_i \sigma_i \|u - u_h\|^2_{L^2(\Omega_i)}\right)^{1/2} \leq Ch^2 \left(\sum_i \sigma_i^{-1} \|f\|^2_{L^2(\Omega_i)}\right)^{1/2} \tag{2.48}$$

for a constant $C > 0$ possibly depending on σ_i.

Proof. Plum and Wieners (2003) □

Corollary 1 (Quantitative error estimate for the subtraction and Whitney approach in a multi-compartment model)**.** *Let Ω and the Ω_i be domains that fulfill the requirements of Theorem 2 and $\sigma(\mathbf{x}) = \sigma_i > 0$ for $\mathbf{x} \in \Omega_i$. Let $u/u^c \in H^1(\Omega)$ be a solution of the Poisson problem* (1.14)*/*(2.36) *with homogeneous Dirichlet boundary conditions and subtraction/Whitney right-hand side $f \in L^2(\Omega)$ and fulfilling the jump conditions. Then, the estimate* (2.48) *holds.*

The previous estimates guarantee that the solution u_h converges against the exact solution u globally in $L^2(\Omega)$. This does not rule out the possibility that the approximate solution still strongly differs from the exact solution in single points. The convergence in single points, which is of interest for the EEG forward problem due to the evaluation of the solution only at the electrode positions, can be guaranteed by error estimates using the L^∞-norm (Braess, 2007):

$$\|u - u_h\|_{L^\infty(\Omega)} \leq Ch\|u\|_{H^2(\Omega)}. \tag{2.49}$$

Again, this estimate is directly applicable to Whitney and subtraction approach in the one-layer scenario. Stricter estimates in the L^∞-norm were, e.g., derived by Ciarlet (1978).
Even when assuming such a simplified scenario, the derivation of error estimates for partial integration and Venant approach is still complicated when interpreting the source term as a distribution of electrical monopoles. Here, two sources of error occur. The error due to the approximation of the source by a monopole distribution and the numerical error of the solution u_h for the monopole right-hand side $f = \sum q_i \delta_{\mathbf{x}_i}$.
The first source of error was experimentally evaluated by Hanrath et al. (in prep.) for Venant and partial integration approach. In the considered setting (one-layer model, Dirichlet boundary conditions) a convergence rate of $\mathcal{O}(h^2)$ was found for the Venant approach in a 2d-scenario, while the partial integration approach showed maximally linear convergence. For the 3d-case, approximately linear convergence was found for both approaches. A theoretical estimate of this error has not been reached yet.
To assess the numerical error of u_h, a priori error estimates for singular right-hand sides f are necessary. First results were, e.g., obtained by Casas (1985); Scott (1973). Therefore, a further simplification is necessary, this time concerning the shape of the domain Ω. Under the

assumption of Ω convex, σ Lipschitz-continuous, homogeneous Dirichlet boundary conditions on $\partial\Omega$, and f being a real and regular Borel measure μ on Ω, possibly $\mu = f = \sum q_i \delta_{\mathbf{x}_i}$, Casas (1985) showed that $u \in W^{1,s}(\Omega)$, $1 \leq s < \frac{d}{d-1}$, and derived the error estimate

$$\|u - u_h\|_{L^2(\Omega)} \leq Ch^{1/2}\|\mu\|_{M(\Omega)} = Ch^{1/2}\sum_i |q_i|. \tag{2.50}$$

Especially for cases where one is not interested in the error at the singularity, such as the EEG forward problem, Köppl and Wohlmuth (2014) derived estimates for the convergence of the FEM solution towards a weak solution in L^2-seminorms that exclude a neighborhood of the singularity. Therefore, the test space $W_0^{1,q}(\Omega)$ is defined:

$$W_0^{1,q}(\Omega) \coloneqq \{v \in W^{1,q}(\Omega) : v|_{\partial\Omega} = 0\}. \tag{2.51}$$

Theorem 3 (Köppl and Wohlmuth, 2014)**.** *Let Ω be a bounded, open, convex, and polyhedral domain. Let further $u \in W^{1,p}(\Omega)$, $p \in (1, 3/2)$, be a solution of the weak formulation of the Poisson problem (1.14) with $V = W_0^{1,q}(\Omega)$, $\frac{1}{p} + \frac{1}{q} = 1$, singular right-hand side $f = \delta_{\mathbf{x}_0}$, and constant conductivity $\sigma \equiv 1$. For an open subset $B \subsetneq \Omega$, such that $\mathbf{x}_0 \in B$, we have the estimate*

$$\|u - u_h\|_{L^2(\Omega\setminus B)} \leq \begin{cases} Ch^2|\ln h|, \text{ if } k = 1, \\ Ch^{k+1}, \text{ if } k > 1 \end{cases} \tag{2.52}$$

for a constant $C > 0$ and k the polynomial degree. C is independent of h, but may depend on $\operatorname{dist}(\mathbf{x}_0, \partial B)$, $\operatorname{dist}(B, \partial\Omega)$, the solution u, and the polynomial degree k.

Proof. Only the main ideas of the proof are exposed here, for the full proof it is referred to Köppl and Wohlmuth (2014).
We assume two subdomains $\mathbf{x}_0 \in B \subsetneq \tilde{B} \subsetneq \Omega$. The main idea of the proof is to use the fundamental solution of the Poisson equation G (cf. Section 1.4) and a cutoff function $\eta \in C^\infty(\Omega)$, $\eta = 1$ on B, $\eta = 0$ on $\Omega\setminus\tilde{B}$, and $0 \leq \eta \leq 1$ on Ω, to construct an auxiliary right-hand side $f_0 = 2\langle\nabla\eta, \nabla G\rangle + \Delta\eta G$ on $\tilde{B}\setminus B$ and consider the weak formulation of $-\Delta v = f_0 + \delta_{\mathbf{x}_0}$ with test space $W_0^{1,q}(\Omega)$. The main task is to show that an inequality of type (2.52) holds for v and the corresponding finite element solution v_h, so that (2.52) follows as a corollary.
To prove this inequality, a series of balls $B_{r_0'} \subset B_{r_0} \subset \ldots \subset B_{r_k'} \subset B_{r_k} \subset B$ is considered and for each of these balls the L^2-error $\|v - v_h\|_{L^2(\Omega\setminus B_{r_l})}$ is estimated depending on the estimatle of the interior ball $B_{r_{l-1}}$. Therefore, the dual problem of the Poisson equation is considered, $-\Delta w_l = (v - v_h)\mathbb{1}_{\Omega\setminus B_{r_l}}$. Upper bounds for the resulting terms are estimated exploiting the properties of the fundamental solution and the main result is proven by induction. □

Remark 9. *Since (1.14) is a linear problem, (2.52) also holds true for a constant conductivity $\sigma \neq 1$. This results in a constant C also depending on σ.*

Theorem 3 now provides the possibility to derive error estimates for the finite element error in partial integration and Venant approach. We denote by q_i the non-zero entries of the

right-hand side vector b^{ven} or b^{pi} and by $\mathbf{x}_i$ the position of the corresponding vertices. Thus, the source term f is given by $f = \sum q_i \delta_{\mathbf{x}_i}$. Assuming linear Ansatz-functions, i.e., $k = 1$, we conclude:

Corollary 2 (Quantitative error estimate for the partial integration and Venant approach in a one-layer model)**.** *Let Ω fulfill the requirements of Theorem 3 and let $u \in W^{1,p}(\Omega)$, $p \in (1, 3/2)$ be a solution of the weak formulation of the Poisson problem* (1.14) *with $V = W_0^{1,q}(\Omega)$, $\frac{1}{p} + \frac{1}{q} = 1$, singular right-hand side $\sum q_i \delta_{\mathbf{x}_i}$, constant conductivity σ, and homogeneous Dirichlet boundary condition $u = 0$ on $\partial\Omega$. For an open subset $B \subsetneq \Omega$, such that $\cup \mathbf{x}_i \in B$, we have the estimate*

$$\|u - u_h\|_{L^2(\Omega \setminus B)} \leq C h^2 |\ln h| \sum_i |q_i| \tag{2.53}$$

for a constant $C > 0$; C is independent of h, but possibly depending on $\operatorname{dist}(\mathbf{x}_i, \partial B)$, $\operatorname{dist}(B, \partial\Omega)$, *the solution u, and σ.*

Proof. The proof follows directly from (2.52) by superposition. Let the $u^i \in W^{1,p}(\Omega)$, $p \in (1, 3/2)$, be solutions of the weak formulation of the Poisson problem (1.14) with singular right-hand sides $\delta_{\mathbf{x}_i}$ and u_h^i the corresponding finite element solutions. For each u^i (2.52) holds true with constant C_i. Due to the linearity of (1.14) $\sum q_i u^i$ is a solution of the problem with the full source term $f = \sum q_i \delta_{\mathbf{x}_i}$ and as the uniqueness of the solution is preserved (cf. Theorem 2.1, Babuška, 1971; Köppl and Wohlmuth, 2014) we have $\sum q_i u^i = u$. The same is valid for the discrete solution, $\sum q_i u_h^i = u_h$.
From (2.52) one obtains

$$\begin{aligned}
\|u - u_h\|_{L^2(\Omega \setminus B)} &= \|\textstyle\sum q_i u^i - \sum q_i u_h^i\|_{L^2(\Omega \setminus B)} \\
&= \|\textstyle\sum q_i (u^i - u_h^i)\|_{L^2(\Omega \setminus B)} \\
&\leq \textstyle\sum |q_i| \|(u^i - u_h^i)\|_{L^2(\Omega \setminus B)} \\
&\leq \textstyle\sum C_i h^2 |\ln h| |q_i| \\
&\leq C h^2 |\ln h| \textstyle\sum |q_i|
\end{aligned}$$

for a constant $C > \max C_i > 0$. □

Remark 10. *Corollary 2 provides a heuristic, why it is not reasonable to actually use the current dipole as introduced in Section 1.4 as a source term in FEM. This would correspond to*

$$f = \lim_{\substack{\|\mathbf{d}\|_2 \to 0 \\ q \to \infty}} (q \delta_{\mathbf{x}_0 + \mathbf{d}/2} - q \delta_{\mathbf{x}_0 - \mathbf{d}/2}).$$

Assuming a scenario where the requirements of Corollary 2 are fulfilled, with $q \to \infty$ also the right-hand side of (2.53) *approaches infinity.*

Given the estimates for jumping conductivities derived by Li et al. (2010) and Corollary 2.53, which are both derived for solutions u of the weak problem, it seems desirable to join these

estimates to gain a result akin to Corollary 1 also for Venant and partial integration approach. However, amongst other things, the assumed requirements on the regularity of the solution u differ for the two estimates, so that this is expected to be a non-trivial task.

A point that was not discussed so far is the behaviour of the constants $C = C(\mathbf{x}_0)$ in the error estimates when the source position $\mathbf{x}_0$ approaches the domain boundary $\partial\Omega$ or a conductivity jump. Wolters et al. (2007c) and Scott (1973) showed for the constants in (2.47) and an estimate akin to (2.50), respectively, $C(\mathbf{x}_0) \to \infty$ when $\mathbf{x}_0$ approaches the domain boundary. A similar behaviour can be expected for the other estimates. Since the source position $\mathbf{x}_0$ is always close to the gray matter/CSF interface in realistic head models, the actual benefit of the error estimates for the EEG forward problem is thus questionable.

However, besides poviding upper bounds for the approximation error, the error estimates also allow conclusions about possibilities to improve the accuracy of the numerical solution. One apparent possibility is to increase the polynomial degree of the space of test and trial functions $V_h = M_0^k$. While a polynomial degree $k = 1$ was assumed throughout this section, for higher degrees in many estimates the exponent of h grows linearly with increasing k. For singular right-hand sides, also a local refinement of the mesh around the singularity can be applied to improve the convergence, this can also be combined with the use of weighted Sobolev spaces (Agnelli et al., 2014; Apel et al., 2011; D'Angelo, 2012; D'Angelo and Quarteroni, 2008). Finally, optimal convergence rates can also be recovered by applying a mesh dependent smoothing kernel (Rüde, 1988).

2.8. Solving the MEG Forward Problem

To calculate a solution for the MEG forward problem, it is necessary to evaluate the integral (1.31) for each coil. For circular shaped coils this can be done analytically, otherwise first order rod elements are used to generate a representation of the coil shape and a numerical line integration is performed subsequently. Details regarding the implementation in SimBio are described by Lanfer (2007). The primary flux Φ_p can now directly be evaluated. To calculate the secondary flux it is necessary to access the gradient of the electric potential, ∇u. For the direct approaches, one can make use of the representation of u in S_h, $u_h(\mathbf{x}) = \sum_j u_j h_j(\mathbf{x})$, and easily compute ∇u_h to be

$$\nabla u_h(\mathbf{x}) = \sum_j u_j \nabla h_j(\mathbf{x}). \tag{2.54}$$

For the subtraction approach, only an approximation of $u^c \in V_h$ was derived so far. The simplest way to compute Φ_s using the subtraction approach is to project the potential u^∞ to the space V_h by evaluating it at the vertex positions $\mathbf{x}_i$, $u_h^\infty(\mathbf{x}) = \sum_j u^\infty(\mathbf{x}_j) h_j(\mathbf{x})$, so that we have

$$u_h^{sub} = u_h^\infty + u_h^c = \sum_j (u_j^c + u^\infty(\mathbf{x}_j)) h_j. \tag{2.55}$$

This expression allows for an easy implementation, but a similar loss of accuracy for very eccentric sources as for the projected subtraction approach has to be expected (Wolters et al., 2007c).
The calculation of the secondary magnetic flux Φ_s through the i-th coil/sensor now simplifies to

$$(\Phi_s)_i = -\frac{\mu_0}{4\pi}\int_\Omega \sigma(\mathbf{x}')\sum_i u_i\langle\nabla h_i(\mathbf{x}'),\mathbf{C}_j(\mathbf{x}')\rangle\,\mathrm{d}x' = -\frac{\mu_0}{4\pi}\sum_i u_i\int_\Omega \sigma(\mathbf{x}')\langle\nabla h_i(\mathbf{x}'),\mathbf{C}_j(\mathbf{x}')\rangle\,\mathrm{d}x' \tag{2.56}$$

and with the definition $S_{ij} \coloneqq -\frac{\mu_0}{4\pi}\int_\Omega \sigma(\mathbf{x}')\langle\nabla h_i(\mathbf{x}'),\mathbf{C}_j(\mathbf{x}')\rangle\,\mathrm{d}x'$ it can be written in matrix form:

$$\Phi_s = Su. \tag{2.57}$$

∇h_i is piecewise constant and supp h_i only consists of few mesh elements, so that the calculation of the matrix S_{ij} is relatively simple.

2.9. Transfer Matrices

All of the presented FEM-approaches result in a linear equation system with the same matrix A and the unknown being the potential u/u^c (in the following only the notation u is used throughout):

$$Au = b. \tag{2.58}$$

As previously mentioned, the dimension of this equation system is usually very large; for realistic head models the number of unkowns n can be about 3 millions (for a hexahedral head model with a resolution of $h = 1$ mm). For most of the commonly used inverse approaches it is necessary to define a *source space*, i.e., a discrete set of dipole positions and directions inside the brain compartments, which are considered as possible sources of neural activity; it is thus common to precompute a so-called leadfield matrix L. In each column the forward solution for one pair of source position $\mathbf{x}_i$ and dipole direction $\mathbf{p}_i$ is stored. For s EEG/MEG-sensors and m source positions the size of L is thus $s \times (d \cdot m)$. d indicates the number of dipole directions per source position and is usually either $d = 3$, i.e., at each source position the cartesian directions are chosen as dipole directions, or $d = 1$ when a normal constraint is assumed, i.e., the sources are distributed on a surface approximating the shape of the gray matter and their dipole moment is oriented perpendicular to this surface as it is physiologically plausible (Brette and Destexhe, 2012). To set up L it is thus necessary to solve the equation system (2.58) $d \cdot m$ times. Since the value of m can be in the range of some thousands, this would be very time consuming and thus not feasible. However, the number of sensors s is usually clearly smaller (at most a few hundred) than m. This fact is exploited by introducing *transfer matrices* (Gencer and Acar, 2004; Weinstein et al., 2000; Wolters et al., 2004). This approach makes

use of the fact that the operator a and thereby also the matrix A is self-adjoint/symmetric, i.e., $A^T = A$. Since one is only interested in the potential at the sensor positions, it is not necessary to compute the potential u for every mesh vertex/degree of freedom. Therefore, a restriction/mapping matrix R is introduced that maps the solution vector u to the EEG/MEG forward solution at the electrodes/sensors u^{eeg}/Φ^{meg}. This restriction matrix R has size $s \times n$ with n being the number of degrees of freedom.

The EEG case is first discussed here, the MEG case is essentially identical and derived subsequently. For the EEG, commonly each electrode is assigned with the potential of the mesh vertex that is next to its position when using CG-FEM, so that R has only one non-zero entry per line; $R_{ij} = \delta_{i,sens(i)}$ with $sens(i)$ indicating the vertex corresponding to electrode i and thus

$$u^{eeg} = Ru. \tag{2.59}$$

The transfer matrix T^{eeg} is now defined via the equation

$$T^{eeg} = RA^{-1}. \tag{2.60}$$

Thus, to calculate the forward solution u^{eeg} a simple matrix-vector multiplication of transfer matrix T and right-hand side vector b has to be performed

$$Tb = (RA^{-1})b = R(A^{-1}b) = Ru = u^{eeg}. \tag{2.61}$$

However, even though the inverse of the stiffness matrix A^{-1} exists, its direct computation is not feasible due to the size of A and the loss of sparseness for A^{-1}. Instead, the transfer matrix T can be expressed by a linear equation system so that the computation of T reduces to numerically solving $(s-1)$ equation systems (since the potential at one reference electrode is fixed). Multiplying (2.60) with matrix A from the right and transposing the equation gives

$$AT^T = R^T, \tag{2.62}$$

where symmetry of A is exploited. T can now be computed line by line solving (2.62) with the column vectors of R^T as right-hand side vectors. This can be done in the same manner as solving the equation system (2.58). The resulting matrix T is densely populated. The calculation of the electrode potential u^{eeg} is thus reduced to a matrix-vector multiplication with a sparse (direct approaches) or dense (subtraction approach) vector. For the subtraction approach, the homogeneous medium solution u^{∞} still needs to be calculated and added. As the computation of the right-hand side vector is more time-consuming, the speed-up factor is lower for the subtraction approach compared to the direct approaches.

The use of transfer matrices is advisable as soon as the number of sources is larger than the number of sensors. Due to its size of $(s-1) \times$ #vertices and the dense structure, the necessary amount of memory to store T can become an issue for fine meshes. In this case, it is possible to store T on the hard disk and load it to the working memory line by line and

directly multiply each line with the matrix of right-hand side vectors b, so that L is computed row by row.
For the MEG, the secondary flux matrix S as introduced in (2.57) in Section 2.8 has to be used instead of the restriction matrix R to compute the magnetic transfer matrix T^{meg}. The secondary flux Φ_s is then given by $\Phi_s = T^{meg}b$ and the overall flux is $\Phi = \Phi_p + \Phi_s$.

2.10. Numerical Evaluation I: Sphere Studies

In this section, a variety of studies comparing the previously derived FEM approaches in multi-layer sphere models for both EEG and MEG is presented. Comparison studies in sphere models have the huge advantage that the analytical solutions given in Section 1.6 can be used as (exact) references. These studies are therefore commonly the first step in comparing the accuracies of different numerical approaches to solve the EEG/MEG forward problem. The analytical solution allows for an unbiased comparison that is not distorted by inaccuracies in the reference solution, as it might occur when numerically calculated reference solutions are used. A possible pitfall that should be considered when conducting such comparisons is the high symmetry of the scenario, which might influence the observed accuracy. Furthermore, the highly regular shape of the domain Ω might influence the convergence of the numerical approaches (cf. Section 2.7). Thus, it is especially important to consider different source positions and not to distribute the test sources regularly, e.g., on a single line, in the used model. Complementary evaluations including more realistic head models are presented in Section 2.11 and Chapter 3. The results shown in this section mainly rely on the previously published studies by Bauer et al. (2015); Vorwerk (2011); Vorwerk et al. (2012).

2.10.1. Methods

For the following comparisons four-compartment sphere models, representing the head tissues brain, cerebrospinal fluid (CSF), skull, and skin, were used. Compartment boundaries are set to radii of 78 mm, 80 mm, and 86 mm and the outer head radius was chosen to be 92 mm; conductivities were chosen as indicated in Table 2.2.

Table 2.2.: 4-layer sphere models (compartments from in- to outside)

Comp.	Out. Radius	Cond.	Reference
Brain	78 mm	0.33 S/m	(Ramon et al., 2004)
CSF	80 mm	1.79 S/m	(Baumann et al., 1997)
Skull	86 mm	0.01 S/m	(Dannhauer et al., 2011)
Skin	92 mm	0.43 S/m	(Dannhauer et al., 2011; Ramon et al., 2004)

Following the study of Lew et al. (2009b), two different tetrahedral head models for the different FEM approaches were used. Model *4layer-802k* has a homogeneous mesh resolution and is used for the direct approaches Venant, partial integration, and Whitney. Model *4layer-519k* has a coarse resolution inside the brain compartment but a high resolution at the

compartment boundaries and is used for the subtraction approach following the results of Lew et al. (2009b). The meshes were created applying a *constrained Delaunay tetrahedralization* (CDT) as implemented in *TetGen* (Si, 2004, http://tetgen.berlios.de/). More information on the parameters used in the mesh generation are given in Table A.1 and Vorwerk (2011); visualizations of the meshes are shown in Figure A.1. Furthermore, a regular hexahedral model with an edge length of 1 mm was used, *4layer-hex-1mm*. The parameters of this model are indicated in Table A.2 and Section 2.10.3.

Synthetic electrode configurations were created by distributing the electrode positions regularly on the outer mesh surface. Numerical and analytical solutions were then evaluated at these measurement points. The actual number of evaluation points may differ from study to study. Due to the high number of electrodes and the statistical evaluation of the accuracies, as it is explained later, this should not have any measurable effect on the shown results.

Two error measures are used to evaluate the accuracy of the numerical approaches, the *relative difference measure* (RDM) and the *logarithmic magnitude error* (lnMAG) (Güllmar et al., 2010; Meijs et al., 1989).

$$\begin{aligned} RDM(u^{num}, u^{ref}) &= \left\| \frac{u^{num}}{\|u^{num}\|_2} - \frac{u^{ref}}{\|u^{ref}\|_2} \right\|_2 \\ lnMAG(u^{num}, u^{ref}) &= \ln\left(\frac{\|u^{num}\|_2}{\|u^{ref}\|_2} \right) \end{aligned} \tag{2.63}$$

with $u^{num}, u^{ref} \in \mathbb{R}^s$, s being the number of sensor nodes, and $\|u\|_2 \coloneqq \sqrt{\sum_{i=1}^{s} u_i^2}$ being the Euclidian norm. The RDM can thus be interpreted as a normalized ℓ^2-error; it is not influenced by errors in the calculation of the overall magnitude $\|u^{num}\|_2$ of the solution but only measures differences in the topography; it is bounded between 0 (= no error) and 2 ($u^{num} = -u^{ref}$). In the studies by Cho et al. (2015); Dannhauer et al. (2011) it was shown that a higher topography error – and thus a higher RDM – is related to a worse source localization and connectivity estimation (cf. Section 3.1.5). The lnMAG measures the difference in overall magnitude compared to the reference solution and has an optimal value of 0. Compared to the frequently used MAG error it has the advantage of being symmetric around 0, simplifying the comparison of over- and underestimations of the magnitude. Due to the relation $\ln(1+x) \approx x$ for small $|x|$, we have $lnMAG \approx \|u^{num}\|_2 / \|u^{ref}\|_2 - 1$ for small deviations and $100 \cdot lnMAG$ is about the change of the magnitude in percent.

As the achieved accuracy of the forward solution is known to be influenced by the local mesh geometry and the position of the source inside a mesh element, the errors are evaluated statistically. This is especially important for the direct approaches, where the actual approximation of the current dipole depends on the local mesh geometry, while the subtraction approach was found to be less influenced by these factors (Vorwerk, 2011). Instead of only placing sources on a single ray from the center to the outside of the sphere, several sources were randomly distributed at each considered eccentricity, i.e., the quotient of source radius and radius of the innermost conductivity jump. Subsequently, at each eccentricity either the arithmetic mean

of the errors was calculated and depicted in a common line chart or a so-called boxplot (also known as box-and-whisker plot) was created. This displays median, upper and lower quartile, and minimum and maximum of the errors. The advantage of the presentation using boxplots is that median and quartiles are robust against outliers, furthermore the representation as boxplots contains more information about the possible range of the errors. In many cases both ways of visualization are presented side by side.

2.10.2. Study 1: Direct approaches - EEG

In this study, published by Bauer et al. (2015), the accuracies of Venant, partial integration, and Whitney approach were compared. In contrast to previous studies that only included Venant, partial integration, and possibly the subtraction approach, this was the first study that compared the newly presented Whitney source model (Pursiainen et al., 2011) to the previously evaluated methods. For reasons of clarity, the subtraction approach was excluded in this comparison, as it is conceptually and with regard to computation times clearly different from these approaches.

Methods

The tetrahedral model *4layer-802k* was used for all computations in this study. $s = 200$ measurement electrodes were distributed on the outer surface of the model. Eccentricities of 0.20, 0.40, 0.60, 0.80, and 0.99 were considered, i.e., the outermost sources were placed at a distance of 0.78 mm to the next conductivity jump. For each eccentricity 200 source positions were generated. In the first part of the study the positions and directions of the sources were optimized for each approach, i.e., shifted to the element center for the partial integration approach (Vorwerk, 2011), to the next mesh vertex for the Venant approach (Vorwerk, 2011), and to the next face for the Whitney approach (Pursiainen et al., 2011). Since the Whitney approach is also restricted with regard to the source orientation, the source orientation for all approaches was chosen fitting to the Whitney approach, i.e., $\mathbf{p} = (\mathbf{v}_4 - \mathbf{v}_1)/\|\mathbf{v}_4 - \mathbf{v}_1\|_2$ with $\mathbf{v}_4$, $\mathbf{v}_1$ defined according to Figure 2.2. For the second part, the source position and orientation were randomly chosen, thus an interpolation using the PBO scheme had to be applied for the Whitney approach (cf. Section 2.4).

Results

Figure 2.8 illustrates the results gained for optimized source locations and orientations. Mean and maximal RDM errors are below 0.016 and 0.03, respectively, and with regard to the lnMAG mean and maximum are below 0.001 and 0.01 in absolute values, respectively. Corresponding to maximal errors of 1.5% and 1.0% for RDM and lnMAG, respectively, these results indicate that all approaches achieve high numerical accuracies in this scenario. For all three methods, both errors and the spread, i.e., the distance between minimal and maximal value, increase with the eccentricity. Here, the Whitney model shows the overall best results. The maximal errors with regard to the RDM (Figure 2.8, top right) at an eccentricity of 0.99 for the Whitney

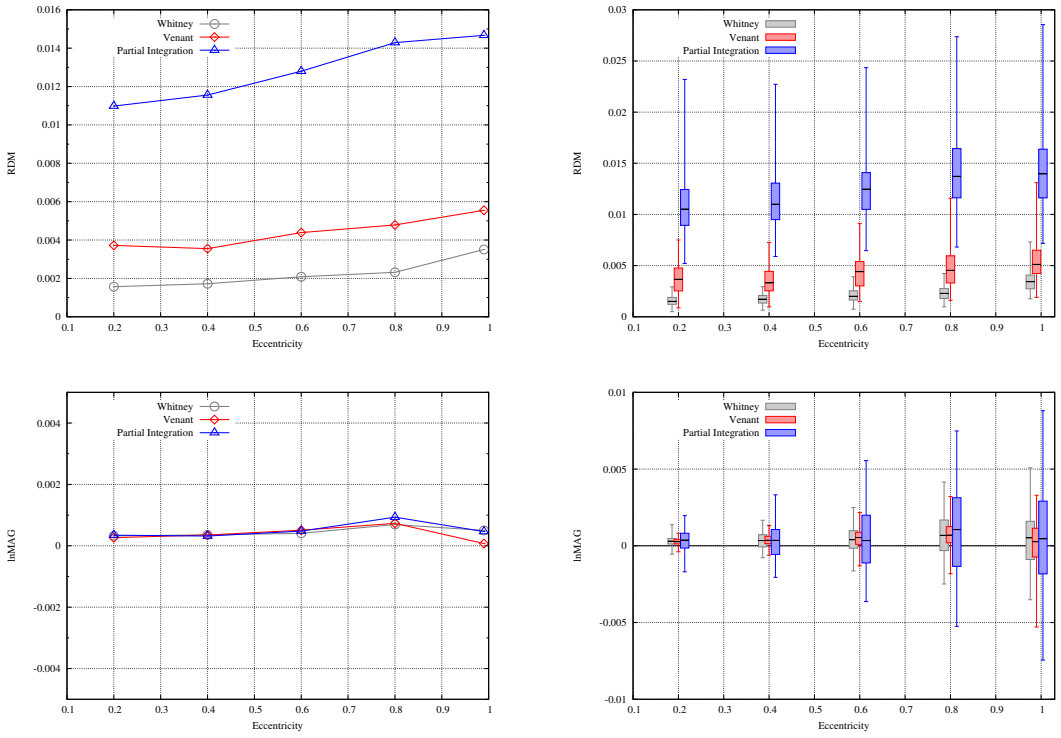

Figure 2.8.: Mean errors (left) and boxplots (right) of RDM (top row) and lnMAG (bottom row) versus eccentricity for optimized source positions and directions.

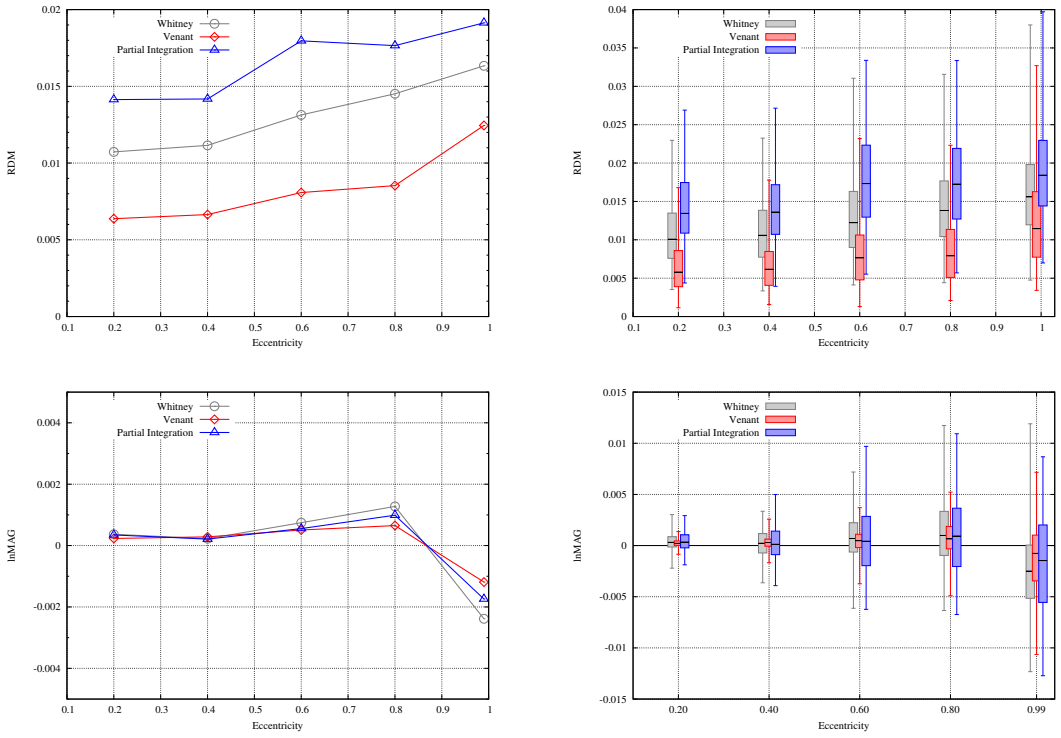

Figure 2.9.: Mean errors (left) and boxplots (right) of RDM (top row) and lnMAG (bottom row) versus eccentricity for random source positions and directions.

model are below 0.008 (Venant ≤ 0.014, PI ≤ 0.028) and the median value is at 0.004 (Venant 0.006, PI 0.014). The Whitney model also yields the smallest interquartile range (IQR), i.e., difference between upper and lower quartile, with only 58% and 28% of that of Venant and partial integration approach, respectively. With regard to the lnMAG (Figure 2.8, bottom row) the maximal errors for the Whitney model at an eccentricity of 0.99 are nearly below 0.005, corresponding to just 0.5% (Venant $\leq 0.005/0.5\%$, PI $\leq 0.009/0.9\%$) and the median value is almost at zero, i.e., without any error, for all three methods. The Venant approach has the smallest IQR at 76% and 39% of that of Whitney and partial integration approach, respectively.

Considering random source positions and orientations all three approaches again yield low errors, with maxima of RDM and lnMAG below 0.04/2.0% and 0.013/1.3%, respectively. In this kind of comparison, the Venant approach overall shows the best results. Comparing Figures 2.8 and 2.9, one notes that the accuracy of the Whitney model decreases significantly in the case of random orientations, when multiple basis functions are utilized to represent a single dipole via the PBO interpolation strategy. This is particularly disadvantageous for sources with high eccentricity. Again, the mean and median of the RDM (Figure 2.9, top right) increase with the eccentricity for all three approaches. At the highest eccentricity, the maximal error of the Venant approach is below 0.033/1.7% (Whitney $\leq 0.038/1.9\%$, PI $\leq 0.04/2.0\%$) and the median value is at 0.012/0.6% (Whitney 0.016/0.8%, PI 0.018/0.9%). Venant and Whitney approach yield an IQR of 0.08/0.4%, while the IQR for the partial integration approach is 0.1/0.5%. With regard to the lnMAG (Figure 2.9, bottom), the maximal and median errors for the Venant approach are at a absolute values of 0.011/1.1% (Whitney and PI 0.013/1.3%) and 0.001/0.1% (Whitney 0.003/0.3%, PI 0.002/0.2%), respectively. Again, the Venant approach yields the smallest IQR, i.e., only 85% and 59% of that of Whitney and partial integration approach, respectively.

2.10.3. Study 2: Venant, PI, Subtraction - EEG

In this study, also the subtraction approach was included, therefore the Whitney approach was not considered to break down the results, however, one can conclude from the previous comparison that its accuracy should be in between that of Venant and partial integration approach. In Vorwerk (2011) a variety of comparisons between these three approaches was performed, a selection of these results is recalled here.

Methods

As previously, the model *4layer-802k* was used for Venant and partial integration approach, for the subtraction approach model *4layer-519k* was used. Furthermore, a hexahedral model, *4layer-hex-1mm*, with an edge length of 1 mm – resulting in 3,342,701 vertices and 3,262,312 elements – was used (cf. Table A.2). $s = 522$ measurement positions were regularly distributed on the outer surface of the model. 125 random positions on the unit sphere were generated and subsequently scaled to radii between 2 mm and 77 mm in 1 mm steps to generate the set

of dipole positions. For each of the dipole positions a radial and tangential dipole direction was computed.

Results

Only the results for radial dipole directions are presented here for reasons of conciseness and since the results for tangential dipoles do not add much new information. The complete results can be found in Vorwerk (2011).

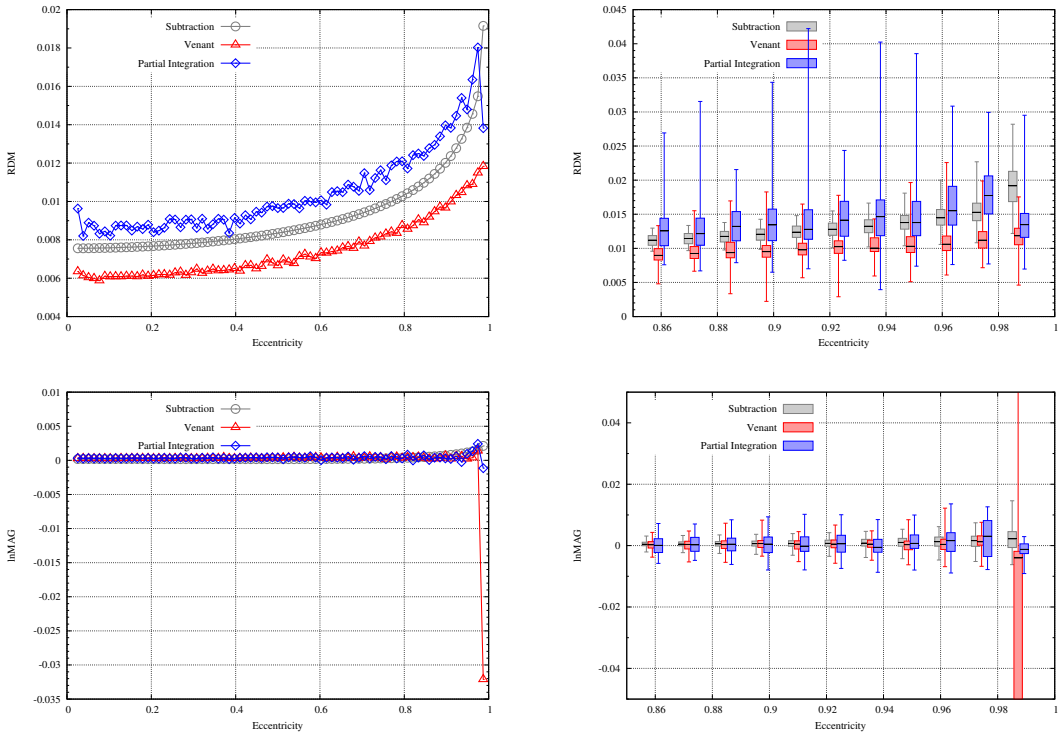

Figure 2.10.: Mean errors (left) and boxplots (right) of RDM (top row) and lnMAG (bottom row) versus eccentricity for random source positions and radial directions. *Source: Vorwerk (2011)*

With regard to the RDM, Figure 2.10 (top left) shows an increase of the mean errors with increasing eccentricity for all approaches. Overall, a maximal error of only about 0.04/2% is found (Figure 2.10, top right), underlining the findings of the previous study of a high accuracy for all considered approaches. Both with regard to the mean errors (maximally 0.012/0.6%) and the boxplots, i.e., the error statistic (maximum $\leq$0.023/1.2%), the Venant approach shows the lowest errors at all eccentricities. Except for the highest eccentricity, where it has a higher median, upper, and lower quartile, the subtraction approach performs better than the partial integration approach. Figure 2.10 shows that the subtraction approach leads to a decreased dependency of the solution accuracy on the local mesh structure, so that the errors of the subtraction approach grow gradually with increasing eccentricity and the IQR is lower than for the direct approaches except for the highest eccentricity. Here, maximal errors below 0.03/1.5% for subtraction and partial integration approach can be observed, while the Venant approach performs best with errors constantly below 0.022/1.1%. The decrease

of errors at higher eccentricities for the partial integration approach shows the effect of the already discussed mesh dependency.

Also with regard to the lnMAG (Figure 2.10, bottom row) all approaches achieve high accuracies aside from the Venant approach at the highest eccentricity. This excluded, the maximal lnMAG errors are below 0.015/1.5% at all eccentricities and the medians are below 0.005/0.5%. Except for the highest eccentricity, the subtraction approach yields the lowest errors with maximal errors below 0.01/1% and error medians below 0.002/0.2%. The Venant approach performs slightly worse, mainly due to higher maximal errors than the subtraction approach, while error medians and IQRs are very similar. The partial integration leads to the worst results except for the highest eccentricity. At this eccentricity the partial integration approach performs best, while it particularly leads to higher maximal lnMAG errors and IQRs otherwise.

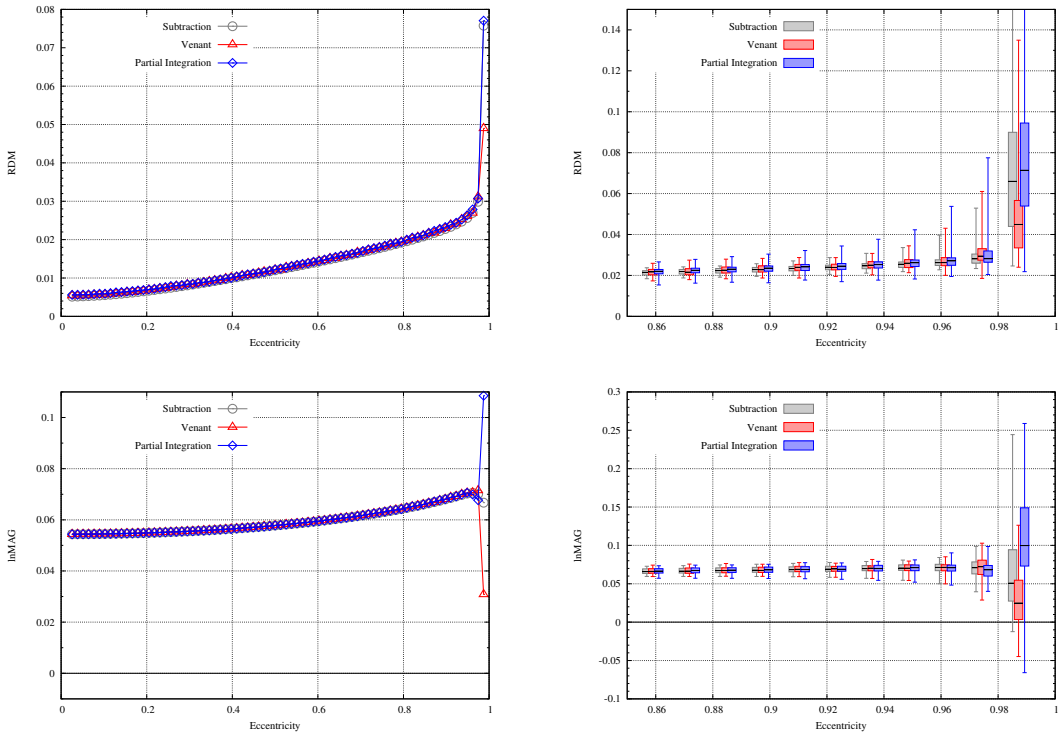

Figure 2.11.: Mean errors (left) and boxplots (right) of RDM (top row) and lnMAG (bottom row) versus eccentricity for random source positions and radial directions. *Source: Vorwerk (2011)*

Since the current implementation of the subtraction approach is unable to deal with geometry-adapted meshes, this comparison study was carried out using a four-layer regular hexahedral model (Figure 2.11). For deep sources all approaches lead to similar RDM errors (top row). The maximal RDM is below 0.03/1.5% and the median below 0.025/1.3% up to an eccentricity of over 0.92 (top right). For more superficial sources especially the maximal errors strongly increase, while the upper quartile is below 0.03/1.5% for all approaches up to an eccentricity of nearly 0.98. Median and IQR are very similar for all approaches, the partial integration approach performs slightly worse than the other two approaches with regard to the maximal

errors at values of up to 0.08/4%. At the most eccentric set of sources, higher errors are found for all approaches with the partial integration and subtraction approach performing worst and the Venant approach performing clearly better, however still with maximal errors above 0.13/6.5%.
In the regular hexahedral model all approaches show a tendency towards overestimating the magnitude with mean errors mainly in the range of 0.055 and 0.07, i.e., between 5.6% and 7.3% (Figure 2.11, bottom left). The boxplot does not show any remarkable differences between the approaches except for the highest eccentricity. Here, all approaches show a higher IQR, a high difference between minimal and maximal values and a median error that clearly differs from that at the lower eccentricities. Due to its higher stability with regard to mean and median error, the performance of the subtraction approach can be judged as best.

2.10.4. Study 3: Venant, PI, Subtraction - MEG

Even though the forward problems of EEG and MEG are closely linked via the law of Biot-Savart as shown in Sections 1.5 and 2.8, it is nevertheless valuable and necessary to also study the MEG forward problem due to the special characteristics of the MEG. Radial dipoles do not cause an outside measurable magnetic field in sphere models (cf. Section 1.6; Sarvas, 1987), therefore only tangential dipoles are evaluated here. Furthermore, since all dipoles become nearly radial when their position approaches the center of the sphere, the strength of the measured signal becomes very low. This causes that small deviations in the numerical solutions lead to high errors in relative measures, such as RDM and lnMAG, due to the small numerator. The signal measured with circular, radially oriented sensors is dominated by the primary magnetic flux, and therefore only weakly influenced by the accuracy of the numerically computed secondary flux. When tangentially oriented sensors are simulated instead, this leads to higher errors than to be expected in realistic scenarios, however, this is a tough test case.

Methods

The same models (both tetrahedral and hexahedral) and source positions as in Section 2.10.3 were used, just with randomly chosen tangential instead of radial source orientations. 258 artificial MEG sensor coils with a radius of 9 mm were regularly distributed at a radius of 110 mm with tangential orientation (precisely, parallel to the e_φ unit vector).

Results

For both models the results for secondary and total magnetic flux are displayed separately. Mainly the results for the secondary magnetic flux are discussed, since the total magnetic flux is simply the result of the summation with the analytically computed primary magnetic flux. For the tetrahedral models, the results for the secondary magnetic flux differ strongly between the highest eccentricity and the lower ones. With regard to the RDM (Figure 2.12, top row), the subtraction approach performs exceptionally well, except for the highest eccentricity. The mean error and upper quartile are below 0.005/0.25%, for the second highest eccentricity the

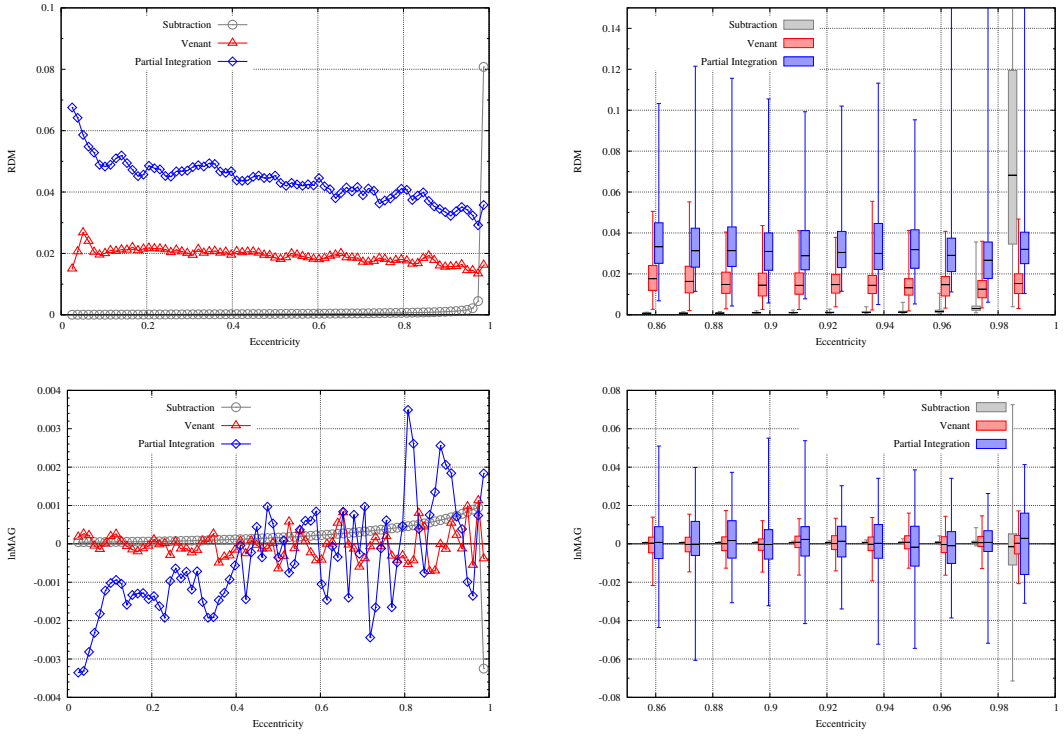

Figure 2.12.: Tetrahedral model: Mean errors (left) and boxplots (right) of RDM (top row) and lnMAG (bottom row) versus eccentricity for secondary flux, random source positions and radial directions for MEG.

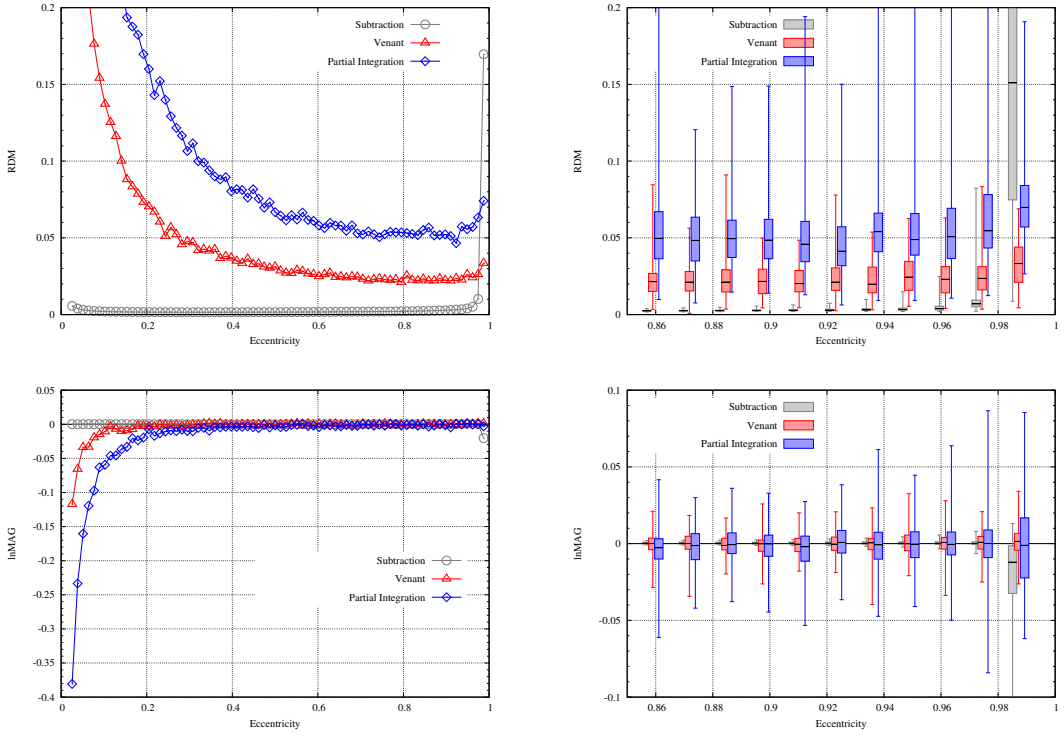

Figure 2.13.: Tetrahedral model: Mean errors (left) and boxplots (right) of RDM (top row) and lnMAG (bottom row) versus eccentricity for total flux, random source positions and radial directions for MEG.

maximal error is still below 0.04/2%. However, for the highest eccentricity a median error of 0.07/3.5% and maximal errors above 0.15/7.5% are found. In contrast, except for the maximal errors of the partial integration approach, for the other two approaches the accuracies are very similar across all eccentricities. The median of the errors for the Venant approach fluctuates around 0.015/0.75% with maximal errors constantly below 0.06/3% and an IQR of about 0.015/0.75%. The errors for the partial integration approach are also quite constant, but at a higher level. The median varies around 0.03/1.5% and the IQR is at about 0.02/1%. For lower eccentricities, the maximal errors of the partial integration approach are below 0.12/6%, but above 0.15/7.5% for the highest eccentricities.

The subtraction approach also achieves very high accuracies with regard to the lnMAG (Figure 2.12, bottom row), again apart from the highest eccentricity. For the lower eccentricities, the lnMAG is nearly negligible, only a slight increase of the maximal lnMAG to 0.01/1% is noticeable, while the median remains at about 0 with a very low IQR. At the highest eccentricity the median is again nearly at 0 but the IQR is about 0.02/2% and maximal errors reach up to 0.08/8.3%. The direct approaches again show a stronger variance, however the median is also around 0. The IQR for the Venant approach is up to 0.015/1.5% and maximal errors are below 0.02/2%, while the IQR for the partial integration approach is up to nearly 0.04/4% at the highest eccentricities and maximal errors of up to 0.04/4% are found.

The results for the total magnetic flux are in line with the results for the secondary magnetic flux (Figure 2.13). Again, especially the high accuracy achieved by the subtraction approach even at very low eccentricities, i.e., for nearly radial sources, is notable.

The results obtained using the hexahedral sphere model are basically in line with the findings using the tetrahedral model, again all approaches show a high numerical accuracy – at least apart from the highest eccentricity. This set of sources excluded, the mean RDM for the secondary magnetic flux is below 0.01/0.5% for all approaches, for the subtraction approach even below 0.005/0.25% (Figure 2.14 top row, left). The upper quartile of errors is below 0.01/0.5% for all approaches for eccentricities between 0.86 and 0.98 (top row, right). For the partial integration approach the upper quartile of errors in this eccentricity range is constantly below 0.01/0.5% even for the highest eccentricity, the maximal error increases from 0.015/0.75% to slightly less than 0.03/1.5%. The subtraction approach shows clearly lower errors for lower eccentricities starting with maximal errors of about 0.005/0.25% at an eccentricity of 0.86, however, at the second highest eccentricity it performs nearly identical to the partial integration approach and for the highest eccentricity the median of the errors is at 0.075/3.8% and upper quartile and maximum error are above 0.1/5%. Also the Venant approach performs better than the partial integration approach for lower eccentricities, having a maximal error below 0.01/0.5% up to an eccentricity of 0.92. Again, the errors are nearly identical to that of the partial integration approach at the second highest eccentricity and clearly higher for the highest eccentricity with a median of 0.015/0.75% and a maximal error of 0.09/4.5%.

Both mean and median for the lnMAG are negligibly small for all approaches when excluding the highest eccentricity. For lower eccentricities (below 0.95) the subtraction approach shows

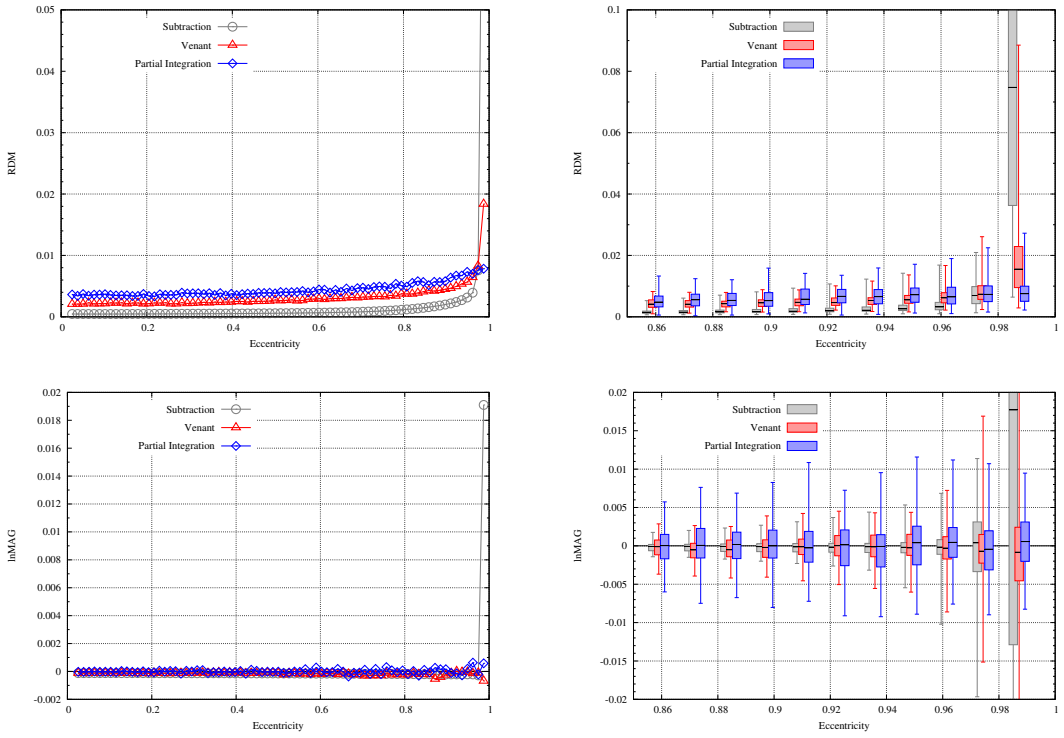

Figure 2.14.: Hexahedral model: Mean errors (left) and boxplots (right) of RDM (top row) and lnMAG (bottom row) versus eccentricity for random source positions and tangential directions for MEG.

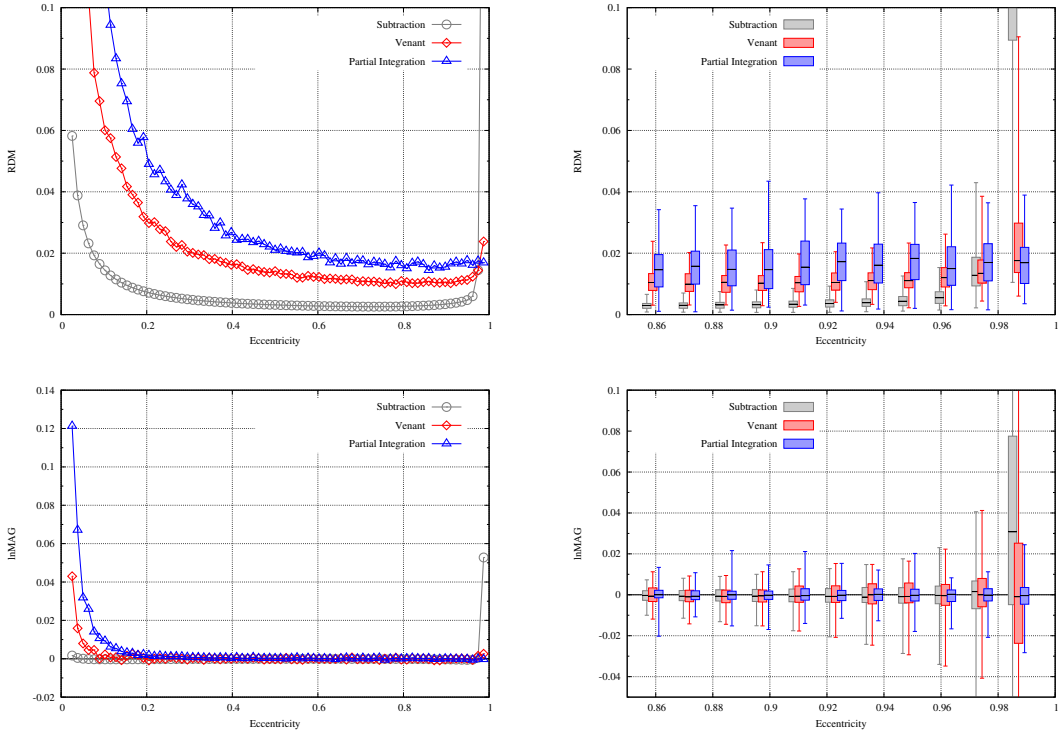

Figure 2.15.: Hexahedral model: Mean errors (left) and boxplots (right) of RDM (top row) and lnMAG (bottom row) versus eccentricity for random source positions and tangential directions for MEG.

the smallest IQR ($\leq 0.002/0.2\%$) and the smallest spread between minimal and maximal lnMAG ($\leq 0.01/1\%$). The Venant approach performs slightly worse with a similar difference between minimal and maximal lnMAG, but a higher IQR ($\leq 0.004/0.4\%$). The partial integration approach performs worst (with a still high accuracy) for the lower eccentricities. The IQR is below 0.005/0.5% and the spread between minimum and maximum is 0.022/2.2%. However, these bounds also hold for the highest eccentricity. At this eccentricity, the subtraction approach performs worst with a median of 0.018/1.8% and an IQR of over 0.04/4%. The Venant approach performs only slightly worse than the partial integration approach with regard to the IQR at this eccentricity ($\leq 0.008/0.8\%$), but minimal and maximal error are below/above -0.02/-2% and 0.02/2%.
The results for the total magnetic flux are, again, in line with these results (Figure 2.15). The results for the subtraction approach at lowest eccentricities are not as good as for the tetrahedral model, however, this should not have any practical implications. The highest eccentricity excluded, the maximal absolute values of the RDM are below 0.04/2% (top row, right) and below 0.04/4% in lnMAG (bottom row, right) for all approaches. For the highest eccentricity the partial integration approach performs best, again.

2.10.5. Computational effort

In this section, the computational effort of the used FEM approaches shall be discussed, i.e., timing and hardware requirements that are necessary for solving the EEG/MEG forward problem using CG-FEM. The results were obtained using the sphere models also applied for the accuracy evaluations. Despite being obtained in sphere models, these results are similar to those in realistic head models with a comparable number of vertices, since the efficiency of the used solvers is only weakly dependent on the geometrical structure of the meshes as long as these are not degenerated. Thus, the crucial parameters influencing computation times and hardware requirements (particularly necessary RAM) are the number of mesh vertices and the number of sources. When using the transfer matrix approach, the number of sensors becomes a third, very important, parameter. In this case, except for the subtraction approach, the setup of the transfer matrix becomes the most costly step in the computation. It is obvious that the computation time for the transfer matrix is linearly related to the number of sensors. A critical point is the storage of the transfer matrix in the RAM as it is a dense matrix of size $\#sensors \times \#nodes$. However, this problem can be solved by precomputing the (except for the subtraction approach) sparse right-hand-side vectors and subsequently computing the transfer matrix line-by-line and directly executing the matrix-vector product.
Lew et al. (2009b); Wolters et al. (2002) evaluated the performance of different solvers for Equation (2.14); an AMG-CG solver was found to perform best. Vorwerk (2011) compared the computation times for Venant, partial integration, and subtraction approach in the models *4layer-802k*, *4layer-519k*, and *4layer-hex-1mm* using this solver, the drawn conclusions are recited here and abutted by computation times for the Whitney approach. For Venant and partial integration approach the computation times in the hexahedral model were gained in a node-shifted model; this has no measurable influence on the computation times. The

measurements in the tetrahedral models were carried out on a PC with an Intel Core2 Quad Processor at 2.83 GHz with 8 Gb of RAM and Ubuntu 9.10 installed, for the hexahedral models a PC with an Intel Core i7 Processor at 2.80 GHz with 16 Gb of RAM and Ubuntu 9.10 was used. The results of this study, complemented by the computation times for the Whitney approach in model *4layer-802k*, are indicated in Table A.4.
The influence of the conceptual differences between the approaches on the computational effort is obvious. While the setup time for the transfer matrix is of course about the same for all considered approaches, the computation time for a single right-hand side vector strongly differs by more than two magnitudes. For the direct approaches these are in the range of some tens of ms, while multiple seconds are needed for the subtraction approach. The differences between the direct approaches are irrelevant in praxis and therefore not further discussed here, as the computation of the right-hand side and the sparse matrix-vector multiplication of transfer matrix and right-hand side hardly contribute to the overall computation time, e.g., lasting only 20 min 37 s for 19,000 sources using the partial integration approach, which is thereby already the slowest of the direct approaches (cf. Table A.4). The setup time, which is dominated by the computation of the transfer matrix, amounts to 98 min 59 s. The overall computation time for 19,000 sources using the partial integration approach is therefore less than 2 hours. In contrast, with a duration of more than 50 h for the computation of the 19,000 sources, the time effort of the subtraction approach is in a range where the application in praxis is nowadays not reasonable, unless it would be mandatory due to undisputable advantages compared to the other approaches, e.g., regarding numerical accuracy.

2.11. Numerical Evaluation II: Realistic Head Model Studies

In the so far presented studies it was shown that CG-FEM approaches achieve high numerical accuracies in sphere models for both EEG and MEG. As already mentioned, these studies can only be seen as a first step of a comprehensive evaluation and need to be accompanied by studies using more realistic head models. In this section, two studies evaluating the different CG-FEM source modeling approaches and also boundary element methods (BEM) in more realistic scenarios are presented. In Section 2.11.1, the results of Vorwerk et al. (2012) are presented, where the accuracies of Venant, partial integration, and subtraction approach were compared to that of two BEM approaches – the frequently applied double-layer BEM (Barnard et al., 1967; Geselowitz, 1967; Zanow, 1997; Zanow and Knösche, 2004) and the symmetric BEM (Adde et al., 2003; Gramfort et al., 2011; Kybic et al., 2005) – in a three-compartment realistically shaped head model. This study was limited to the EEG forward problem. The errors of the different approaches were evaluated by using the solution in a high-resolution model as reference. Furthermore, a first approach to set these errors in relation to the effect of model simplifications was made by additionally evaluating the effect of neglecting the highly-conductive CSF compartment. This study is accomplished by a comparison study of the four CG-FEM approaches introduced in this chapter in a six-compartment realistic head model. In this second study, the accuracies for both EEG and MEG forward problem were

evaluated; again a high-resolution model was used as reference.

2.11.1. Study 4: BEM-FEM comparison in realistically shaped three-compartment model

An introduction into boundary element methods is skipped here, an extensive description and a first comparison study between BE and FE methods in sphere models can be found in Vorwerk (2011). At this point it shall suffice to know that boundary element methods rely on a discretization of the interfaces between compartments with different conductivity instead of a volume discretization as it is the case for FE methods. This leads to certain theoretical and practical limitations for example related to the treatment of non-nested compartments or of holes in surfaces, e.g., due to the spinal cord or the eye nerve penetrating the skull. A major goal of this study was to show that FE methods are able to match BE methods in both accuracy and computation time already in a three-compartment head model. The allegedly higher computational effort was frequently used as an argument against the application of FEM in praxis. As the computational effort to directly invert the matrices that occur for BEM grows asymptotically cubic with the number of surface vertices (Kybic et al., 2005), BE head models are usually restricted to three layers that can be represented by smooth surfaces (skin, skull, and brain). The separation between brain and the CSF is omitted since a representation of the strongly folded brain surface with an amount of vertices that still allows a reasonable computation time is usually not possible. Therefore, this study also aimed at showing that the errors introduced by neglecting certain conductive compartments, e.g., in this case the CSF, clearly surpass the numerical differences between the numerical methods, motivating an increase of the efforts to make the usage of four or more compartment head models practically feasible.

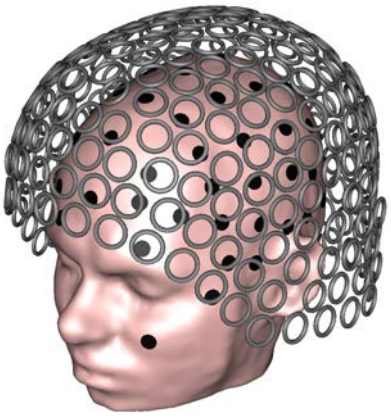

Figure 2.16.: EEG and MEG sensor distribution in realistic head model.

Methods

Considering the previously explained limitations, a three-compartment realistically shaped head model was constructed. A T1-weighted (T1w-) MRI scan of a healthy 25-year-old male subject was acquired on a 3 T MR scanner (Magnetom Trio, Siemens, Munich, Germany) using a 32-channel head coil. An MP-RAGE pulse sequence (TR/TE/TI/FA = 2300 ms/3.03 ms/1100 ms/8°, FOV = 256 × 256 × 192 mm, voxel size = 1 × 1 × 1 mm) with fat suppression and GRAPPA parallel imaging (acceleration factor 2) was used. Surfaces with 2,219, 1,814, and 2,879 vertices were extracted representing skin, outer skull, and inner skull, respectively, using the proprietary toolbox Curry (http://www.neuroscan.com). While these surfaces could directly be used for the BEM approaches, a tetrahedralization based on these surfaces was performed using TetGen to create a tetrahedral model for the FEM approaches. This approach ensures that the geometry of the volume conductor is identical in all models. As for the sphere studies, different models for the direct approaches and the subtraction approach were created according to Lew et al. (2009b). The tetrahedralization resulted in a model with 933,038 vertices and 5,891,852 elements and a homogeneous mesh density for the direct approaches and a model with 653,664 vertices and 4,075,056 elements and a high mesh density at compartment boundaries and a low density inside the homogeneous source compartment for the subtraction approach. Since no analytical solution exists in this scenario, a high-resolution FE model was created to calculate a reference solution. This resulted in a mesh consisting of 2,242,186 vertices and 14,223,508 elements. Finally, a high-resolution FE model additionally considering the CSF compartment was generated to evaluate the influence of modeling/not modeling this conductive compartment (2,268,847 vertices, 14,353,897 elements). The parameters used to generate these meshes are indicated in Table A.3.
18,893 test sources were distributed regularly on an extracted gray/white matter interface. This assures a sufficient distance between source positions and brain surface in order to avoid numerical errors as a consequence of sources being too close to a conductivity jump, especially when taking into account the CSF compartment. The surface normals were chosen as source directions. The simulated potentials were evaluated at the sensor positions of a realistic 80 electrode cap (10-10 system with six additional electrodes). The reference solutions were computed for the high-resolution three and four compartment model using the Venant approach.

Results

The results of this study are shown in Figure 2.17. The graphs show cumulative relative frequencies, i.e., the ordinate of each point of a curve indicates the amount of sources that has an error below the respective abscissa value. Regarding the RDM, the symmetric BEM performs best having an error below 0.025 for over 95% of the dipole positions (Figure 2.17, left). However, it shows a tendency to underestimate magnitudes (Figure 2.17, right). In contrast, the subtraction approach shows only slightly higher RDM errors, while achieving a low and unbiased lnMAG (90% within the range from -0.01 to 0.01, i.e., a variation of ±1%).

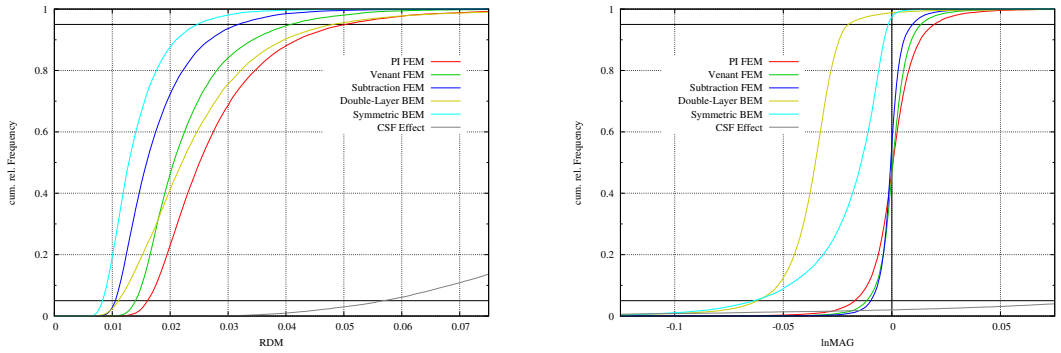

Figure 2.17.: Cumulative relative frequencies of RDM (left) and lnMAG (right) errors for EEG in realistically shaped three-layer head model with truncated x-axis. *Source: Vorwerk et al. (2012)*

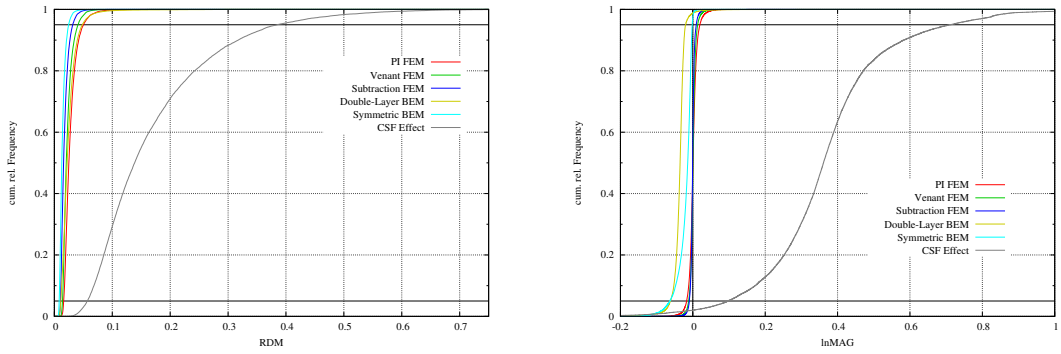

Figure 2.18.: Cumulative relative frequencies of RDM (left) and lnMAG (right) errors for EEG in realistically shaped three-layer head model. *Source: Vorwerk et al. (2012)*

The same holds true for the Venant approach with, again, slightly higher overall errors than the subtraction approach, but still 95% of the RDM errors being below 0.04. Finally, the partial integration approach shows the worst results of the FEM approaches. The double layer BEM performs good with regard to the RDM, being in the range of the FEM approaches, but it shows high deviations for the lnMAG that are asymetrically distorted. It is eye-catching that, while the results for all other approaches are well-ordered and none of the displayed curves intersect, the RDM of the double layer BEM is in the range of the subtraction approach for the best performing 5% of sources, but in the range of the partial integration approach for the worst performing 5% of sources. Possibly most important, a glance at the CSF effect shows that all numerical errors lie clearly below the model error (Figure 2.18). For 95% of the dipole positions the effect in the RDM introduced by neglecting the CSF compartment is larger than 0.05/2.5% and the caused lnMAG effect is larger than 0.1/10% and strongly varying (Figure 2.18).

2.11.2. Study 5: Direct approaches in realistic six-compartment head model

The results gained by Vorwerk et al. (2012) (Figures 2.17, 2.18) show that also a realistically shaped three-layer head model still suffers from distorted results due to simplifications in

the modeling process, particularly the omission of differing conductivities for some large compartments, e.g., CSF, gray matter, and white matter. As basis for further investigations of effects caused by these simplifications, the numerical accuracy achieved by the different FEM approaches in solving the EEG/MEG forward problem in a six-compartment realistic head model and using realistic sensor configurations is studied. The explicit effects of the particular omissions are then in-depth studied in the following chapter and set in relation to the numerical accuracies.

Methods

Two six-compartment (skin, skull compacta, skull spongiosa, CSF, gray matter, and white matter) head models with isotropic conductivities, again one with a normal and one with an especially high resolution, were used as test scenario. The details of the model generation and the chosen conductivity parameters are described in the following chapter (Section 3.1.1; Table 3.1, model *6CI*; Figure 3.1); this resulted in one model with 984,569 vertices and 6,107,561 tetrahedral elements and the high-resolution model with 2,159,337 vertices and 13,636,249 elements. As in the previous study, 18,893 sources were distributed on the gray/white matter interface. Since the white matter was considered as an additional conductive compartment in this study, the source positions were shifted to the centroid of the next tetrahedron that was fully contained in the gray matter, i.e., all of its vertices exclusively belonged to gray matter elements. As source directions again the surface normal at the respective position was chosen. The EEG was evaluated using a realistic 74 electrode cap (10-10 system), for the MEG a realistic 275 channel whole head sensor configuration (CTF Omega 2005 MEG by MISL, http://www.vsmmedtech.com/hardware.html) was simulated (Figure 2.16). Reference solutions for EEG and MEG were computed using the high-resolution model and the Venant approach.

Results

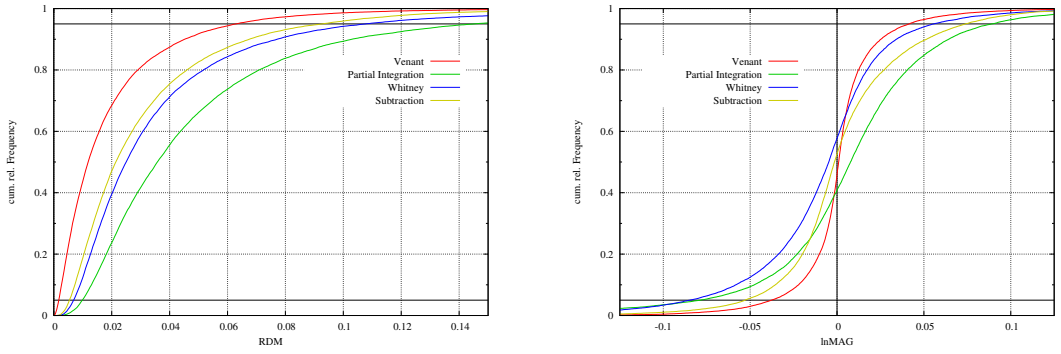

Figure 2.19.: Cumulative relative errors of RDM (left) and lnMAG (right) for EEG in realistic six-layer head model

The results gained using the realistic six-compartment head model underline the findings made in the sphere studies (Figure 2.19). For the EEG, the Venant approach has the highest

accuracy both regarding RDM with 95% of the errors below 0.06/3% and lnMAG with 90% of the errors between -0.04 and 0.04 (i.e., a variation of ±4%). Subtraction and Whitney approach show a similar accuracy regarding the RDM with 95% of the errors below 0.09/4.5% and 0.11/5.5%. For the partial integration approach the mark of 95% of the errors is just reached before the end of the displayed x-range at 0.15/7.5%. With regard to the lnMAG the results might be slightly biased due to the choice of the reference method, as Whitney and partial integration approach have a too low/high magnitude for 60% of the sources, respectively, while this is more symmetric for Venant and subtraction approach. Regarding the extent of the intervall containing 90% of the lnMAG values, the Venant approach performs best with a value of 0.08. Whitney and subtraction approach also perform similar regarding this measure with a value of about 0.13 with the already mentioned tendency to underestimate the magnitude compared to the reference for the Whitney approach. For the partial integration approach the extent of the interval containing 90% of the sources is about 0.16.

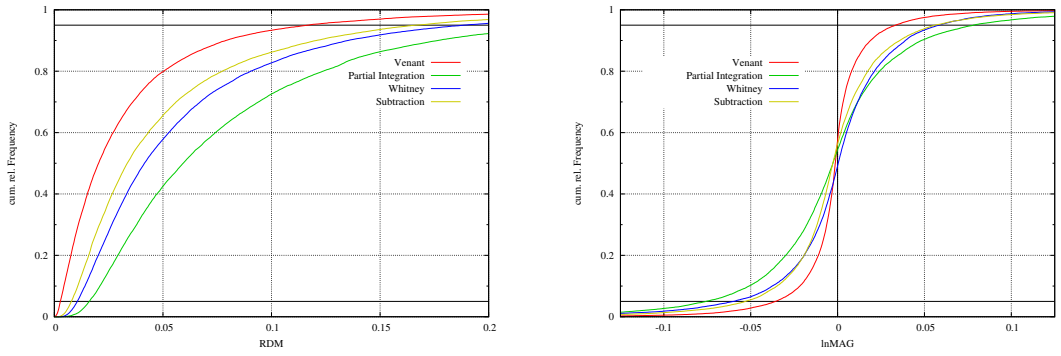

Figure 2.20.: Cumulative relative errors of RDM (left) and lnMAG (right) for secondary magnetic flux in realistic six-layer head model

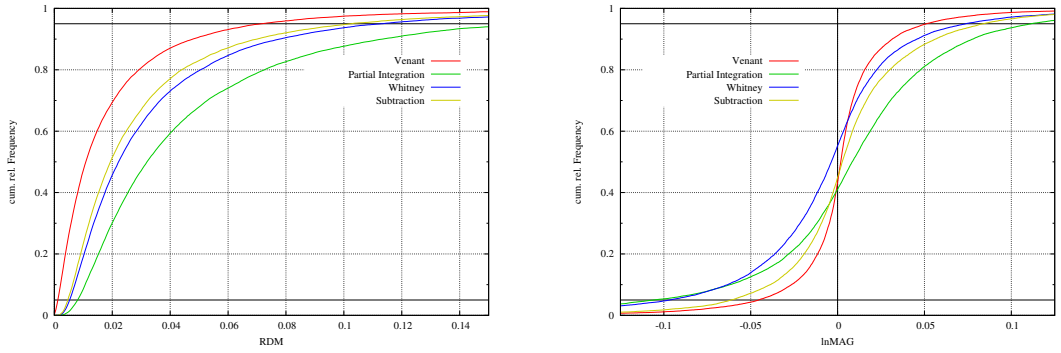

Figure 2.21.: Cumulative relative errors of RDM (left) and lnMAG (right) for MEG in realistic six-layer head model

The results for the MEG (Figures 2.20 and 2.21) are very similar to those for the EEG. When considering only the secondary magnetic flux (Figure 2.20) the Venant approach performs best with 80% of the RDM errors below 0.05/2.5% and 95% below 0.12/6% and 90% of the lnMAG errors in a range of 0.08 and a variation of ±4% compared to the reference. As for the

three-layer scenario, the partial integration approach performs worst and the mark of 95% of the errors is out of the displayed graph range of up to 0.2 for the RDM and the range for 90% of the lnMAG errors is 0.16, corresponding to a variation of ±8%. Subtraction and Whitney approach perform similarly with the subtraction approach being slightly better with regard to the RDM and 95% of the errors below 0.17/8.5%, while for both approaches 90% of the lnMAG errors lie in the range between -0.06 and 0.06.
When adding the analytically calculated primary magnetic flux and thus evaluating the overall MEG signal, the results with regard to the RDM are more accurate than for the secondary magnetic flux alone, while the lnMAG results become slightly less accurate (Figure 2.21). The general tendency remains the same as for evaluating the secondary magnetic flux separately. Again, the Venant approach performs best, with 95% of the RDM errors below 0.07/3.5% and 90% of the lnMAG results between -0.05 and 0.05 (i.e., a variation of ±5%). Subtraction and Whitney approach still perform very similar with regard to the topography error, each with 95% of the RDM errors below 0.11/5.5%, while the subtraction approach performs clearly better when considering the lnMAG (90% between -0.06 and 0.08, Whitney 90% between -0.10 and 0.07). The partial integration aproach achieves the worst results both with respect to topography and magnitude.

2.12. Discussion

In this chapter, several approaches to solve the EEG/MEG forward problem were introduced based on a conforming finite element formulation, the continuous Galerkin FEM (CG-FEM). Basic theory regarding existence and uniqueness of a solution was presented and suitable error measures were introduced. The theoretical considerations were followed by a comprehensive evaluation of the numerical performance of the presented approaches in both sphere and realistic head models for both the EEG and MEG forward problem.
The results gained in the sphere studies for the EEG forward problem underline and augment previous findings. Especially the statistical evaluation allows for a better assessment of the reliability of the numerial approaches than in the previously presented studies, where often only a single dipole per eccentricity was evaluated.
For the first time the study presented in Bauer et al. (2015) (Section 2.10.2) compared the accuracy of the newly introduced Whitney approach to that of previously proposed FEM forward approaches, namely Venant and partial integration approach. The results for optimized source positions and orientations (Figure 2.8) confirmed the assumptions of Section 2.5, showing the highest accuracy for the Whitney approach in this scenario. Thus, when the source space in a tetrahedral model is generated out of a surface representation of the gray matter and a normal constraint is implied, i.e., sources are oriented perpendicular to this surface (cf. Figure 2.3), the use of the Whitney approach should be considered. The non-interpolated Whitney type sources have been applied to EEG inversion by Calvetti et al. (2009). For random locations and source orientations the Venant approach showed a higher accuracy than the Whitney approach (Figure 2.9). However, the accuracy for all

three approaches in the sphere model was very high so that at this point of evaluation also the focality of the monopole representation might be considered. A higher focality simplifies fulfilling the constraints that have to be respected in the construction of a source space, as no monopoles should be placed on vertices outside the source compartment. In this aspect, the partial integration approach is the best approach (4 nodes, cf. Table 2.1), followed by Whitney (8 nodes) and Venant (≈16 nodes) approach.

When also considering the subtraction approach in the evaluation, the Venant approach remains overall most accurate with regard to mean and median errors in a tetrahedral model (Section 2.10.3, Figure 2.10). However, it shows very high magnitude errors for the highest eccentricity and the maximal error is higher than for the subtraction approach at some eccentricities. These findings are in line with the findings by Lew et al. (2009b), where likewise a high magnitude error at highest eccentricities was found for the Venant approach and radial source directions. In the regular hexahedral sphere model all three approaches achieved nearly identical accuracies except for the highest eccentricity, where the Venant approach performed best (Figure 2.11). These results generalize the study of Wolters et al. (2007b). A dependency of the numerical accuracy of Venant and partial integration approach on the position of the source inside the mesh was observed in this study. This finding was in detail investigated by Vorwerk (2011), showing that optimal accuracies for the direct approaches can be achieved when sources are placed appropriately inside the mesh, i.e., no monopoles are placed on vertices outside the source compartment (usually the gray matter). This is not necessary for the subtraction approach, for which it is sufficient when the source remains inside the brain compartment and respects a sufficient distance to the conductivity jump. However, due to the higher computational effort (Section 2.10.5) the direct approaches are to be preferred in practical applications.

In the MEG sphere study, the general performance of Venant and partial integration approach in both tetrahedral (Figures 2.12 and 2.13) and hexahedral models (Figures 2.14 and 2.15) was in line with the findings of Lanfer (2007); Lanfer et al. (2007), showing high relative errors for deep sources due to the weak signal and good numerical accuracies for more superficial sources. The finding of the Venant approach performing best confirms the assumption that the results for the EEG can mostly be transferred to the MEG due to the law of Biot-Savart. In this context, the clearly better performance of the subtraction approach, especially in tetrahedral models, might be a bit surprising. Recalling that the potential in the source compartment, where the strongest volume currents occur, is mainly calculated analytically here, this result gets plausible.

The study deduced by Vorwerk et al. (2012) (Section 2.11.1) was a first step to proof that the results gained in sphere studies can be transferred to more realistic scenarios. This study shows that the approaches based on the FEM can match the accuracy and speed of the until now widely applied BE methods also in a three-layer realistically shaped head model. Though the symmetric BEM was discriminated by choosing the solution of a FEM approach as reference, it outperformed the other approaches regarding RDM (Figure 2.17, left). With regard to the lnMAG both BEM approaches show a bias compared to the reference solution,

a result that was previously also found in sphere studies for the double-layer approach but not that distinct for the symmetric BEM (Gramfort et al., 2011; Vorwerk, 2011; Vorwerk et al., 2012). In this scenario with a large homogeneous source compartment and a relatively high distance between sources and conductivity jumps, the subtraction approach was the best performing FEM approach. However, Figure 2.18 shows that it is highly advisable to extend realistic head models by further conductive compartments as done in the following study (Section 2.11.2) and investigated in more detail in Chapter 3.

When comparing the different FEM approaches in a six-compartment realistic head model without using a specifically adjusted head model for the subtraction approach, the results are slightly different than in the three-layer scenario. Though the number of vertices and elements was nearly identical in both scenarios, the achieved accuracies are decreased when using the six-compartment model. The main reason for this is probably found in the smaller distance of the source positions to the conductivity jumps, as the sources are now placed in the relatively thin gray matter compartment which is enclosed by the CSF and the white matter compartment. This behaviour corresponds to the increase of errors at higher source eccentricities in the sphere models. Especially the subtraction approach suffers under this change in geometry, as it performs best for large compartment of homogeneous conductivity. The Venant approach performs best in this scenario for both EEG and MEG in contrast to the three-layer scenario (Figure 2.17). This result is not fully in line with the sphere results, where subtraction and/or partial integration approach outperformed the Venant approach in certain scenarios (Figure 2.10, bottom row for most eccentric sources, Figures 2.13 and 2.12 for all except most eccentric sources), however, the general trend showed that the Venant is the most stable approach and is thereby confirmed in the more realistic scenario. It has to be kept in mind that the reference results were computed using the Venant approach, so that a certain bias towards this approach cannot be excluded for these results. However, the source positions were optimized for the partial integration and Whitney approach so that especially the bad performance of the partial integration approach is rather surprising (cf. Pursiainen et al., 2011; Vorwerk, 2011).

Some general possibilities to improve the accuracy of the FEM were already indicated in Section 2.7. The use of higher order test and trial functions, i.e., increasing the polynomial degree of the discrete space V_h, is suggested by the error bounds in Section 2.7 and was evaluated for the subtraction approach by Grüne (2014). A reduction of the error for higher polynomial degrees was found in sphere models. However, this comes at the cost of an increase in computation time, as the number of degrees of freedom and thereby the dimension of the equation system (2.14) that has to be solved grows strongly. If the computation time was kept constant, no improvements for high source eccentricities could be found. Thus, it seems arguable that the use of finer meshes should be preferred over an increase of the polynomial degree as this allows a better approximation of the geometry. Besides the better approximation of the potential, also a better representation of the dipole source when increasing the polynomial degree would be expected for the direct appoaches (Section 2.7) and should be evaluated. Especially for the partial integration approach using tetrahedral elements, the problem of the right-hand side

being constant inside a mesh element could thereby be overcome.
For the subtraction approach, also the use of adaptive mesh refinement techniques with an residual-based error estimator was tested (Meyer, 2013), but did not lead to satisfying results so far. At least for the EEG forward problem, where one is only interested in the solution at the electrode positions, it seems reasonable to consider the use of dual-weighted error estimators. Thereby, it would be possible to define the regions in which one is especially interested in an accurate solution, i.e., the electrode positions for the EEG forward problem (Bangerth and Rannacher, 2003; Johansson, 2010; Ramm et al., 2003). For problems with a singular right-hand side, also local mesh refinements around the position of the singularity have been proposed (Agnelli et al., 2014; Apel et al., 2011; D'Angelo, 2012; D'Angelo and Quarteroni, 2008). However, this is not feasible as usually a large number of sources at different positions has to be computed to set up the leadfield L, so that one should instead rather consider a global refinement of the source compartment. The influence of the mesh width – and thereby of mesh refinements in the source compartments – for the Venant direct approach is studied by Hanrath et al. (in prep.), where optimal convergence rates were found. Thus, a global refinement of the source compartment seems reasonable, but is only easily realizable for tetrahedral models. In hexahedral meshes, it unavoidably leads to *hanging nodes* (cf. Figure 2.1, middle), which complicate the numerical treatment using CG-FEM. Hanging nodes can easily be treated using the discontinuous Galerkin (DG) method that is introduced in Chapter 4.
The accuracy of the Venant approach can further be improved by replacing the here defined moments by those of the multipole expansion (Hanrath et al., in prep.), by increasing the number of electrical monopoles considered for the approximation of the source (Medani et al., in prep.), and by preventing that monopoles are placed outside the source compartment (Medani et al., in prep.). Pursiainen et al. (submitted) propose the use of further basis functions, namely face-intersecting and edgewise ones, to improve the approximation of the dipole source in the Whitney approach. Thereby, an increase in numerical accuracy could be achieved without including further monopoles.
However, in some – possibly even many – scenarios the numerical accuracy is less important for an accurate solution of the forward problem than an accurate representation of the underlying geometry. Here, tetrahedral meshes are usually advantageous as they allow the modeling of smooth surfaces, while for (regular) hexahedral meshes staircase effects occur. The accuracy in hexahedral models can be easily improved by the use of geometry-adapted meshes that allow for a better representation of the underlying geometry and weaken the influence of staircase effects (Camacho et al., 1997; Vorwerk, 2011; Wolters et al., 2007a). To further improve the representation of the geometry, Vallaghé and Papadopoulo (2010) proposed a trilinear immersed FEM. This method is based on structured hexahedral grids that are independent of the geometry; the compartment interfaces are represented using levelsets and included by a modification of the basis functions. A similar approach can also be applied for the discontinuous Galerkin method as introduced in Chapter 4, leading to the unfitted discontinuous Galerkin (UDG) method (Bastian and Engwer, 2009; Nüßing et al., 2015).

3 Effects of Realistic Volume Conductor Modeling in EEG/MEG Source Analysis

The results obtained in the previous chapter (cf. Section 2.11.1; Figures 2.17 and 2.18) gave a clear hint that in order to solve the EEG/MEG forward problem accurately, it is necessary to model the head volume conductor as realistic as possible. Furthermore, it is evident that this particularly includes the distinction of more than the three conductive compartments skin, skull, and brain. In this chapter, which is in large parts based on and recites the study published by Vorwerk et al. (2014), the influence of additionally distinguishing the conductive compartments skull spongiosa, skull compacta, cerebrospinal fluid (CSF), gray matter, and white matter and of the inclusion of white matter anisotropy on the EEG/MEG forward solution is investigated. To be able to include these complicatedly shaped head compartments, the Venant approach was used to compute forward solutions. The Venant approach was derived in the previous chapter (cf. Section 2.3) and showed a high numerical accuracy in solving the forward problem in all of the performed evaluations. A highly realistic six-compartment tetrahedral head model with white matter anisotropy was created; the mesh generation is described in Section 3.1.1. Furthermore, a high-resolution reference model was created. Realistic sensor configurations were used for EEG and MEG. Sources were distributed with a high, regular density in the gray matter compartment and their orientations chosen perpendicular to the gray/white matter interface, i.e., the physiologically plausible normal constraint was applied. On this basis, the effects of the respective model refinements are studied.

Starting from a three-compartment scenario (skin, skull, and brain), the head model was

refined step-by-step by distinguishing one further of the above-mentioned compartments. For each of the thereby generated five head models, both the effect on the signal topography and signal magnitude in relation to a reference model and to the model that was generated in the previous refinement step was measured. The differentiation between topography and magnitude effects is of high importance as these effects strongly differ in their impact on inverse solutions. The results of the simulations are evaluated using a variety of visualization methods, allowing to gain a general overview of effect strengths, of the most important source parameters triggering these effects, and of the most affected brain regions. The results are visualized on an inflated brain surface to depict the spatial distribution of the changes for both EEG and MEG. Additionally, these effects are presented in special diagrams – known as heat maps – where their strength is related to parameters characteristic for the respective source location. These analyses allow to estimate the influence of the simplifications applied in the head model creation on the investigation of activity originating in certain brain regions. Thereby, it is possible to show the high importance of detailed volume conductor modeling in order to achieve accurate EEG and, to a lesser degree, for accurate MEG forward solutions. The results of the forward study are underlined by reflecting the most important results of a study considering the inverse problem of EEG/MEG that was conducted by Cho et al. (2015). Here, it is shown that the results of the forward study are directly related to the accuracy in computing inverse solutions and source connectivity. Based on these results, a guideline for volume conductor modeling in EEG and MEG source analysis is worked out. The consideration of the highly conductive CSF and the distinction of gray/white matter conductivity differences are found to be the most important modeling steps.
Finally, a MATLAB-based pipeline that allows for an easy generation and application of realistic five-compartment hexahedral head models is presented. It is shown that the usage of the head models generated with this pipeline can clearly improve the accuracy of the forward solutions compared to a simpler three- or four-compartment head model. Furthermore, the results of this pipeline in localizing somatosensory evoked data measured from a healthy subject are shown.

3.1. A Guideline for EEG/MEG Head Volume Conductor Modeling

3.1.1. Segmentation and Mesh Generation

To construct a realistic, high-resolution volume conductor with anisotropic white matter, T1-weighted (T1w-), T2-weighted (T2w-), and diffusion-tensor (DT-) MRI scans of a healthy 25-year-old male subject were acquired with a 3 T MR scanner (Magnetom Trio, Siemens, Munich, Germany) using a 32-channel head coil. For the T1w-MRI, an MP-RAGE pulse sequence (TR/TE/TI/FA = 2300 ms/3.03 ms/1100 ms/8°, FOV = 256 × 256 × 192 mm, voxel size = 1 × 1 × 1 mm) with fat suppression and GRAPPA parallel imaging (acceleration factor 2) was used. For the T2w image, an SPC pulse sequence (TR/TE = 2000 ms/307 ms, FOV = 255 × 255 × 176 mm, voxel size = 0.99 × 1.0 × 1.0 mm interpolated to 0.498 × 0.498 × 1.00 mm) was used. The MR images were resampled to an isotropic resolution of

1 mm. DT-MRIs (DTI) were acquired with the standard Siemens pulse sequence ep2d_diff (TR/TE = 7700 ms/89 ms). Geometry parameters were: FOV 220 × 220 × 141 mm, voxel size = 2.2 × 2.2 × 2.2 mm. Seven volumes were acquired with diffusion sensitivity b = 0 s/mm^2 (i.e., flat diffusion gradient) and 61 volumes with b = 1000 s/mm^2 for diffusion weighting gradients in 61 directions, equally distributed on a sphere. Seven additional data sets with flat diffusion gradients and reversed spatial encoding gradients were acquired for distortion correction according to Ruthotto et al. (2012). The T2w-MRI was registered onto the T1w-MRI using a rigid registration approach and mutual information as cost-function as implemented in the FSL-toolbox (http://fsl.fmrib.ox.ac.uk/fsl/fslwiki/FSL). The skin, skull compacta, and skull spongiosa were segmented by applying a gray-value based active contour approach (Vese and Chan, 2002). Subsequently, the segmentation was manually corrected and, because of the importance of modeling skull holes for source analysis (Oostenveld and Oostendorp, 2002; van den Broek et al., 1998), the foramen magnum and the two optic canals were physiologically correct modeled as skull openings. Following the advice of Lanfer et al. (2012b), the model was not cut off directly below the skull but realistically extended at the neck. Curry was used to extract highly resolved surfaces of skin, skull compacta, and skull spongiosa. A Taubin smoothing was applied to remove staircase-like effects (Taubin, 1995). The FreeSurfer-toolbox (https://surfer.nmr.mgh.harvard.edu) was then used to segment and extract the cortex surface and the gray/white matter interface.

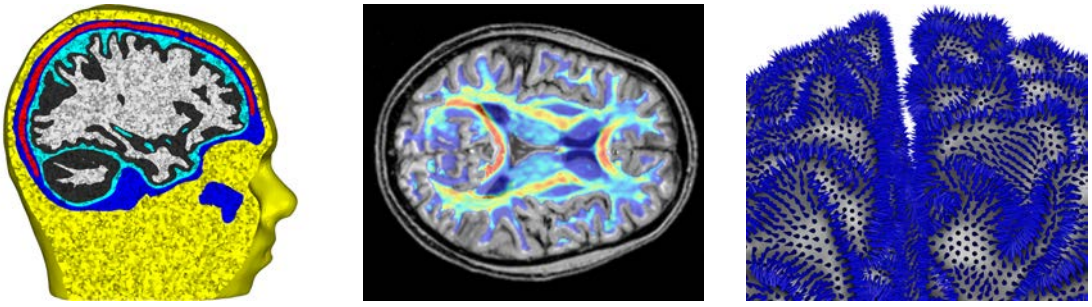

Figure 3.1.: Sagittal cut through the volume conductor model (white matter shown in light gray, gray matter in dark gray, CSF in light blue, skull compacta in dark blue, skull spongiosa in red, and skin in yellow) (left), fractional anisotropy (color-coded) visualized on an axial slice of the T1-MRI (middle), source space visualized on the brain surface (right).

In order to apply a constrained Delaunay tetrahedralization (CDT), all obtained surfaces were checked for intersections and those found were corrected by flattening the inner surface, ensuring a minimal distance between all surfaces. The CDT was executed using TetGen; the resulting mesh consists of 984,569 vertices and 6,107,561 tetrahedral elements (Figure 3.1). Additionally, a mesh with a higher resolution of 2,159,337 vertices and 13,636,249 elements was constructed using the same surfaces in order to compare numerical errors and modeling errors. The conductivities used in this study were chosen according to Table 3.1 (Akhtari et al., 2002; Baumann et al., 1997; Dannhauer et al., 2011; Ramon et al., 2004).

To construct anisotropic white matter conductivity tensors, after an affine registration for eddy current correction, the DW-MRIs were corrected for susceptibility artifacts using a novel

Table 3.1.: Overview of the compartment conductivities, the conductive features of the different head models (| is considered, – is disregarded,: is further divided, and A is anisotropic), and their resolution.

Compartment	σ (S/m)	*3CI*	*4CI*	*5CI*	*6CI*	*6CA*	*6CA_hr*
Brain	0.33	|	|	:	:	:	:
Brain GM	0.33	–	–	|	|	|	|
Brain WM	0.14	–	–	|	|	A	A
CSF	1.79	–	|	|	|	|	|
Skin	0.43	|	|	|	|	|	|
Skull	0.01	|	|	|	:	:	:
Skull comp.	0.008	–	–	–	|	|	|
Skull spong.	0.025	–	–	–	|	|	|
Resolution	# vertices	984,569	984,569	984,569	984,569	984,569	2,159,337

reversed gradient approach based on the images acquired with flat diffusion gradient that leads to a diffeomorphic, smooth, and thus physically reasonable transformation (Ruthotto et al., 2012). Finally, the corrected DW-MRIs were registered to the T2-MRI using a rigid transformation. Following the effective medium approach proposed by Tuch et al. (2001) that has been positively validated in a variety of studies (Butson et al., 2007; Chaturvedi et al., 2010; Oh et al., 2006; Tuch et al., 2001), conductivity tensors σ were deduced from the diffusion tensors D using the linear relationship $\sigma = sD$. Instead of using the theoretically derived scaling factor s as proposed by Tuch et al. (2001), s was computed empirically adapting the approach used in Rullmann et al. (2009). The modeling of gray matter anisotropy was dispensed due to the severe influence of partial volume effects at the resolutions achieved with 3 T MR scanners and previous studies showing only weak radial cortical anisotropy (cf. Figure 4 in Heidemann et al., 2010; Figure 3.1, middle). Thus, the computation of s reduced to

$$s = \sigma_{wm}^{iso} \left(\frac{d_{wm}}{N_{wm}} \right)^{-1}. \tag{3.1}$$

d_{wm} denotes the sum over the product of the diffusion tensor eigenvalues for all voxels classified as white matter and N_{wm} is the number of these tensors. This approach ensures that the mean conductivity of the anisotropic white matter fits that of isotropic white matter, while local variations in conductivity are preserved. Finally, to each element the conductivity tensor corresponding to its centroid was assigned.

To investigate the influence of considering/not considering conductivity differences between the different compartments on the accuracy of the forward simulation, head models with a differently detailed discrimination of these compartments were generated. Except for the highly resolved model *6CA_hr*, the finite element mesh was not changed, so that the geometrical structure of the head model remained the same for all models, i.e., the influence of geometrical errors is not examined here.

Five differently detailed head models were constructed based on the finite element mesh

with the lower resolution (i.e., 984,569 vertices). To simulate the same steps that one would usually follow to achieve a more realistic head model, the starting point is the commonly used three-compartment head model with homogenized isotropic skull and brain compartments, which in this study was extended by the realistic modeling of skull holes that were already included as a necessity of the approach not to change the geometrical representation of the volume conductor (model *3CI* in Table 3.1). This model was extended by the distinction of further compartments, namely the CSF (model *4CI*), gray and white matter separation (model *5CI*), skull compacta and spongiosa separation (model *6CI*), and finally by the inclusion of white matter anisotropy (model *6CA*). Head model *6CA_hr* was based on the highly resolved mesh (2,159,337 vertices) and served as a reference to estimate the numerical error. Due to the fact that the anisotropic conductivity tensors were assigned according to each element's centroid, this error contained not only the numerical error caused by the different model resolutions, but also the effect of the possibly slightly different subsampling of tensors between the two models. Since the numerical error is expected to dominate, it is nevertheless denoted as numerical error.

3.1.2. Sensor Setup

Realistic sensor configurations were used for both EEG and MEG. The positions of 74 electrodes (10–10 system) were digitized using a Polhemus device and projected onto the skin surface. A 275-channel whole head MEG gradiometer sensor configuration (CTF Omega 2005 MEG by MISL, http://www.vsmmedtech.com/hardware.html) was modeled and a rigid transformation to the head model was calculated using the positions of head localization coils inside the MEG and the positions of fiducials placed at the corresponding positions during the MRI recordings. The positioning of EEG/MEG sensors in relation to the model surface is shown in Figure 2.16.

3.1.3. Methods

To achieve the goal of systematically describing the effects of using differently detailed head models to solve the EEG/MEG forward problem, it is – besides a suitable head discretization and accurate numerical methods, which were already introduced – necessary to have the right tools (especially for visualization) available to describe the underlying relations between the observed effects and certain parameters. In the following section, the used visualization methods as well as the used effect measures and the parameters used to distinguish the affected sources are described.

Source space construction

As shown in Chapter 2, despite its generally high accuracy, the Venant approach requires special care in the construction of volume conductor and source space mesh. In this study, sources with a normal constraint are placed in the gray matter as it is physiologically plausible (Brette and Destexhe, 2012). Therefore, it had to be ensured that the vertex closest to the

source position is exclusively part of elements belonging to the gray matter. Otherwise, the examined effects of conductivity changes especially in the neighboring compartments, i.e., white matter and CSF, might have been corrupted by numerical inaccuracies (Vorwerk, 2011). Starting from 129,640 regularly distributed source positions on the gray/white matter surface, the surface normal at each position was calculated and fixed as the source orientation (Figure 3.1, right). Then, all vertices in the gray matter compartment fulfilling the Venant condition were computed and the source positions were moved into the direction of the next valid node, until this node was the node closest to the source position. Thereby, it is ensured as good as possible that the results are not disturbed by numerical inaccuracies.

Error measures

As error measures the RDM and lnMAG as introduced in Section 2.10 were used. It has to be noted that in some applications the absolute values of the lnMAG are of less interest, e.g., if one wants to compare the magnitude of the reconstructed sources at different locations. In such scenarios, a large variance of the lnMAG, i.e., the ratios of signal magnitudes of sources at different positions are strongly distorted, might easily lead to misinterpretations. Thus, also the width of the distribution of the lnMAG differences is taken into account when analyzing the results.

Effect evaluation/visualization

Different kinds of diagrams are used to display the overall distribution of the quantities that were analyzed (RDM, lnMAG, signal magnitude, etc.). To visualize the effect of both single steps of head model refinement and the difference in relation to the reference model, cumulative relative frequencies are shown (cf. Figure 3.4). This representation has the advantage that the shape of the plotted curve is less dependent on the choice of the interval length than in common histograms. Furthermore, 2d-histograms are used to show the dependency of the magnitude of the effect measures on a certain model parameter and previous to this to analyze the interdependency between the model parameters used here. To create these plots, a matrix was calculated where each entry determined the frequency of values that are both inside a specific interval on ordinate and abscissa. This distribution is visualized using heat maps, where, for the sake of better recognizability, each column was scaled by the inverse of its maximum (i.e., normalized to a maximum of 1; cf. Figure 3.7). The heat maps provide more information than the frequently used boxplots or floating mean plots, since they allow a more detailed overview of the effect distribution and it is also possible to recognize weak dependencies that might be overlooked in other modalities. Common graphs were created using gnuplot (http://www.gnuplot.info), heat maps were created using MATLAB.
For visualization purposes, an inflation of the gray/white matter surface was created using BrainVISA (http://www.brainvisa.info). On the resulting surface the values of effect measures or parameters are depicted (cf. Figure 3.3). In Figure 3.2, the inflation process is presented. This visualization allowed to easily identify and classify the brain regions that were most affected or not affected by the refinement steps. In addition to the color-coded visualization

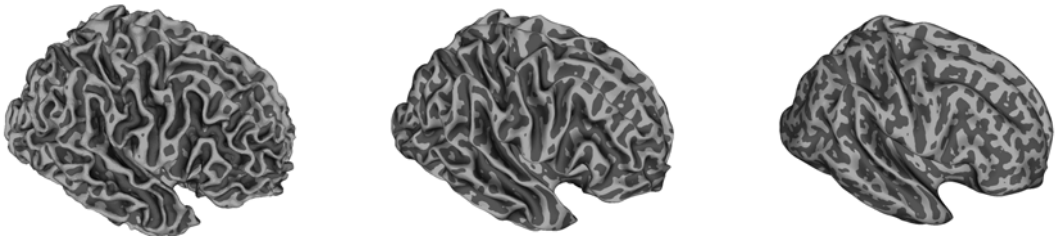

Figure 3.2.: Inflation of the gray/white matter surface: Segmented gray/white matter surface (left), after half of the inflation steps (middle), and final result on which effect surface plots are presented (right).

of effects, the curvature of the original surface was calculated and displayed underneath the effect results to allow for a better identification of brain regions. A positive curvature, which roughly corresponds to gyri, is shown in light gray, a negative curvature is shown in dark gray (cf. Figure 3.2). The most tangential source orientations were thus roughly achieved around the intersection between light and dark gray and the most radial source orientations in the middle of the light and dark gray regions. An increasing transparency for smaller values was used so that the underlying curvature is still visible in the plots (cf. Figure 3.8, right column). All visualizations were carried out using SCIRun (http://www.sci.utah.edu/cibc-software/scirun.html).

3.1.4. Results

Forward solutions for the models presented in Table 3.1 and the respective source space as introduced in Section 3.1.3 were calculated. RDM and lnMAG differences were computed for each source position, both relative to the reference model and to the model with one refinement step in between. Furthermore, the signal magnitude was calculated for each source position in all models. On this basis, a series of different evaluations was performed to achieve a decent overview of effect magnitudes.

EEG and MEG signal magnitude

Figure 3.3 shows the distribution of the signal magnitude (relative to the maximum for the respective model) plotted on the brain surface for EEG (top row) and MEG (bottom row) computed in models *3CI* (left column) and *6CA* (right column). These plots underline the different sensitivities of EEG and MEG, an important parameter by which to interpret effect results in the later investigations. The EEG signal magnitudes (top row) have their local peaks for superficial sources close to or on the gyral crowns, where sources are very close to the electrodes, and decrease continuously when going to deeper source positions. The EEG signal magnitudes are weakest for sources in sulcal valleys. The *3CI* distribution (top left) showed large areas of above 90% relative signal strength and hardly any areas below 22%, while the *6CA* distribution (top right) was less smooth and had a broad range with only a few small areas of above 90% relative signal magnitude and large areas of below 22%. In contrast,

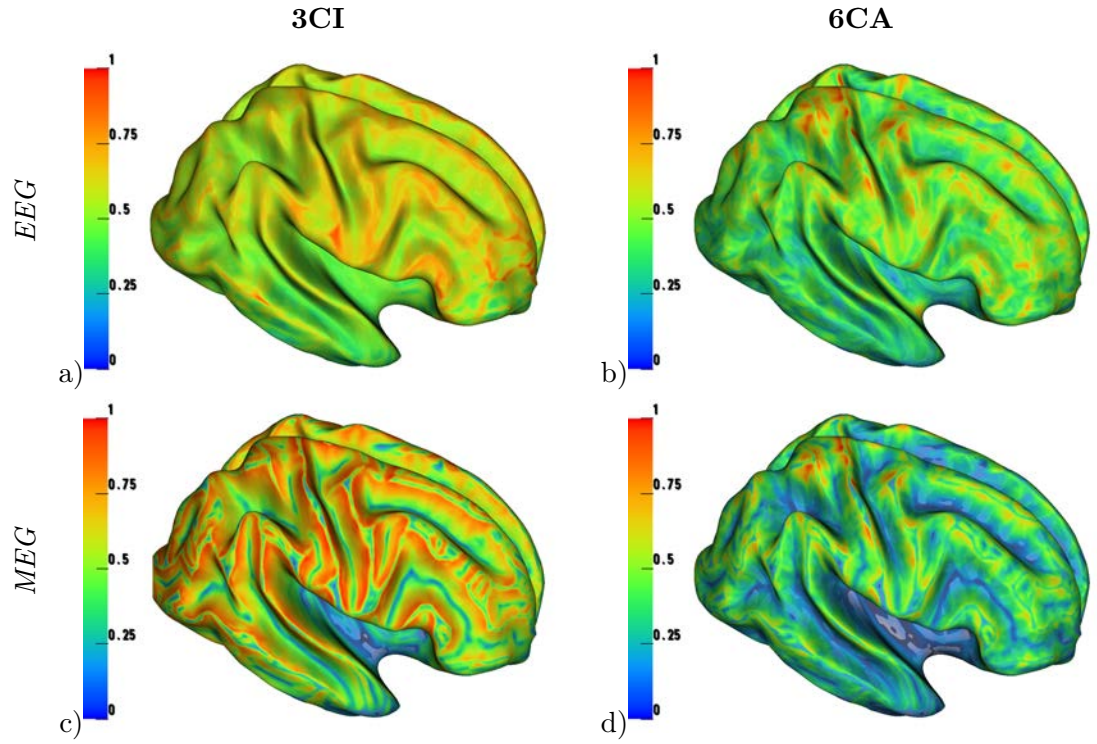

Figure 3.3.: Signal magnitude relative to its maximum for the respective model for EEG (upper row) and MEG (lower row) computed in models *3CI* (left column) and *6CA* (right column).

for the MEG (bottom row) the signal decay into the depth was stronger than for the EEG and the signal magnitude was very weak on a thin line on gyral crowns and a broader line in sulcal valleys, where sources are quasi-radial. A small displacement of the source from the thin line at the gyral crown caused the orientation to change strongly towards a more tangential direction and the signal rapidly increased to its local peak value. As for the EEG, the full *6CA* head model (compare right column top and bottom) led to a more scattered sensitivity profile. Even though the overall properties described for the *3CI* model were still visible, the influence of the more detailed conductivity distinction on the local distribution of the signal magnitude can be clearly observed, which is no longer nearly exclusively dominated by source depth and orientation.

Topography and magnitude differences

As a first evaluation of topography and magnitude changes, the cumulative relative frequencies of RDM (upper rows) and lnMAG (lower rows) for EEG (Figure 3.4) and MEG (Figure 3.5) are depicted, showing the effects between single refinement steps (left columns) and the overall effects of the various models compared to the reference model *6CA_hr* (right columns). This presentation allows for a first, very general, interpretation of the influence of the distinction of certain conductive compartments on the forward solution. Second, the inter-dependencies of the different properties that were used to classify the effects of the model refinements were investigated (Figures 3.6 and 3.7). Finally, heat maps of RDM and lnMAG as a function of these properties as well as surface plots of the effect measures were used to identify and

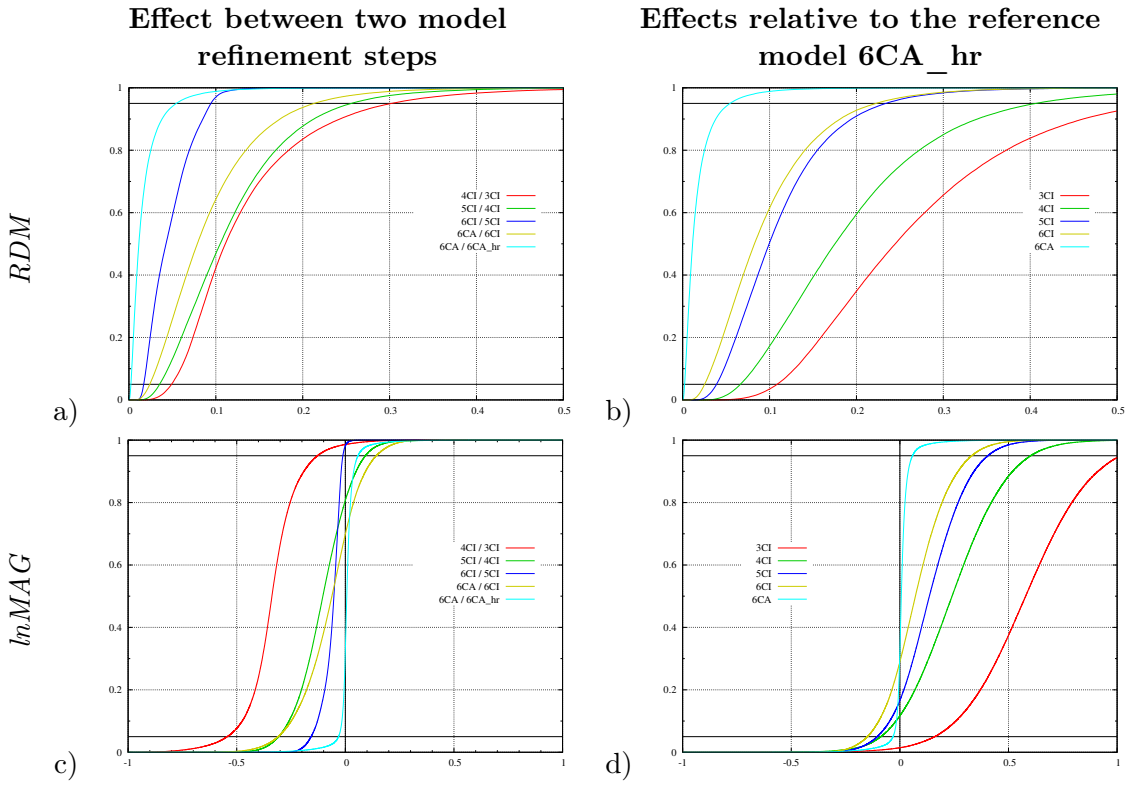

Figure 3.4.: Cumulative relative frequencies for effects induced in EEG. RDM (upper row) and lnMAG (lower row) between two refinement steps (left column) and relative to the reference model *6CA_hr* (right column). The horizontal lines indicate frequencies of 0.05 and 0.95.

classify the brain regions most affected by the model refinements (Figures 3.8 - 3.16).

The introduction of the CSF had the biggest influence on the EEG forward simulation, both regarding RDM and lnMAG (dark blue lines in Figure 3.4, left column). While for the RDM the plot shows that the influence of gray/white matter distinction (red line in Figure 3.4a) and white matter anisotropy (light blue line in Figure 3.4a) was only slightly smaller, the consideration of the CSF led to by far the biggest effect regarding the lnMAG in absolute values (dark blue line in Figure 3.4c). Looking at the variance of the lnMAG effects for each of these three steps (dark blue, red, and light blue lines) about 90% of the sources lay in an interval with a width of about 0.4 in lnMAG (e.g., the red line in Figure 3.4c reaches a cumulative relative frequency of 0.05 at about -0.3 and of 0.95 at about 0.1). This would correspond to a misestimation by a factor of up to 1.5 when comparing the magnitudes of reconstructed sources. In both modalities, the influence of modeling the different skull compartments showed a minor effect (orange lines in Figure 3.4, left column). Nevertheless, the caused effects were still higher than the numerical error, i.e., the difference between model *6CA* and *6CA_hr* (green lines in Figure 3.4). As the Figures 3.4b and d show, the effects of the different refinement steps mainly added up and did not cancel each other out.

The RDM results of the MEG simulations were very similar to those of the EEG simulations. Again, distinction of CSF (dark blue line in Figure 3.5a) and gray/white matter (red line in Figure 3.5a) showed the biggest influence. The magnitudes of these effects were nearly

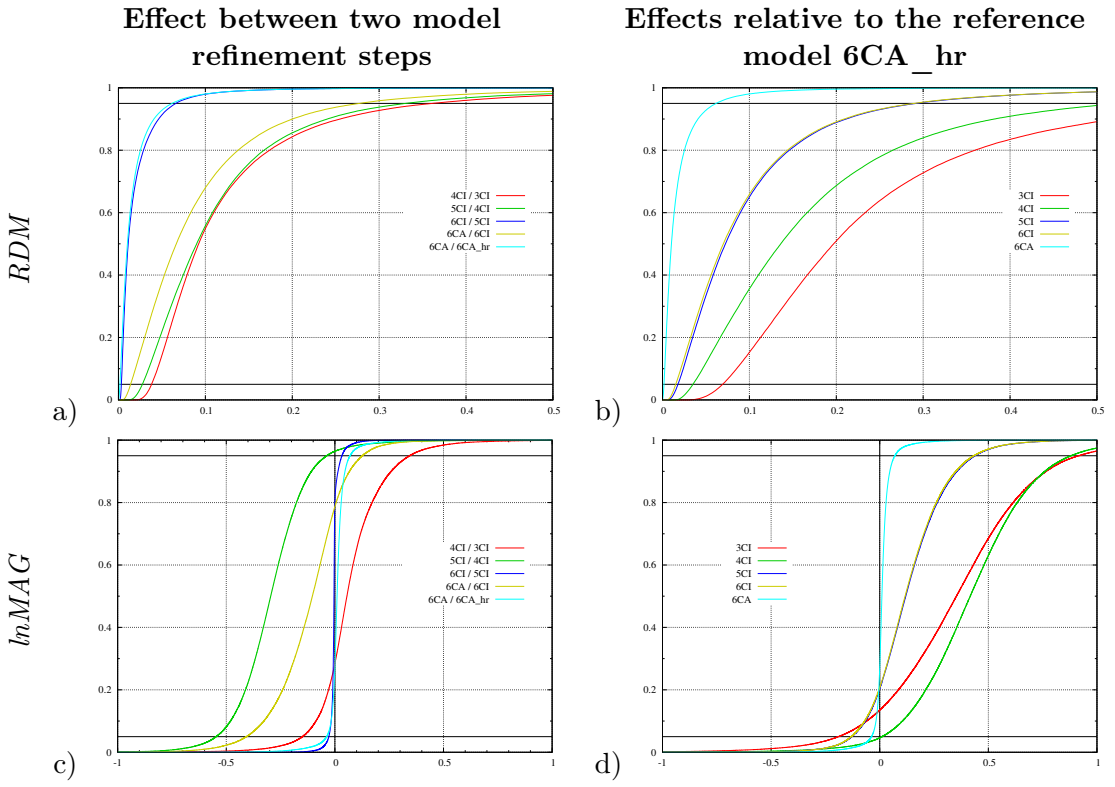

Figure 3.5.: Cumulative relative frequencies for effects induced in MEG. RDM (upper row) and lnMAG (lower row) between two refinement steps (left column) and relative to the reference model 6CA_hr (right column). The horizontal lines indicate frequencies of 0.05 and 0.95.

identical in this case. The influence of white matter anisotropy was clearly smaller (light blue line in Figure 3.5a), while skull modeling (orange line in Figure 3.5a) and numerical error (green line in Figure 3.5a) were at the same, small, level. Regarding the lnMAG, the effect of gray/white matter distinction (red line in Figure 3.5c) was even bigger than that of CSF modeling in absolute values (blue line in Figure 3.5c). These effects had opposite signs – a result in line with the increase (CSF added) and decrease (WM added) of the conductivity in large parts of the head. As in the EEG case, the width of the distribution of the lnMAG for the distinction of CSF and gray/white matter, as well as for the inclusion of anisotropy, was in the same range. For all three of these effects, 90% of the sources fell within a range of about 0.5 in lnMAG (e.g., the light blue line in Figure 3.5c reaches a cumulative relative frequency of 0.05 at about -0.4 and of 0.95 at about 0.1), which would correspond to a misestimation by a factor of over 1.6 when comparing source magnitudes. In comparison, the numerical error would only lead to a maximal factor of 1.1.

Comparing the size of the effects for EEG and MEG, both are at a similar level. This might be counterintuitive at first glance, since one would expect the MEG to be less influenced by conductivity changes, but actually this is a consequence of the approach to choose sources perpendicular to the brain surface so that also quasi-radial and very deep sources were included in the analysis. These sources generate a weak MEG sensor signal, and, thus, small absolute effects could directly lead to large relative effects. This effect can possibly be avoided by

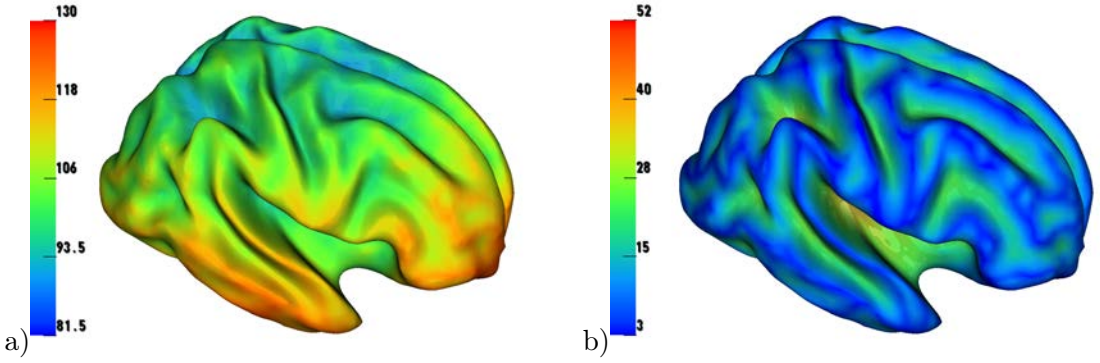

Figure 3.6.: Median of the distances between a source position and the electrodes (in mm, left) and distance between a source position and the inner skull surface (in mm, right).

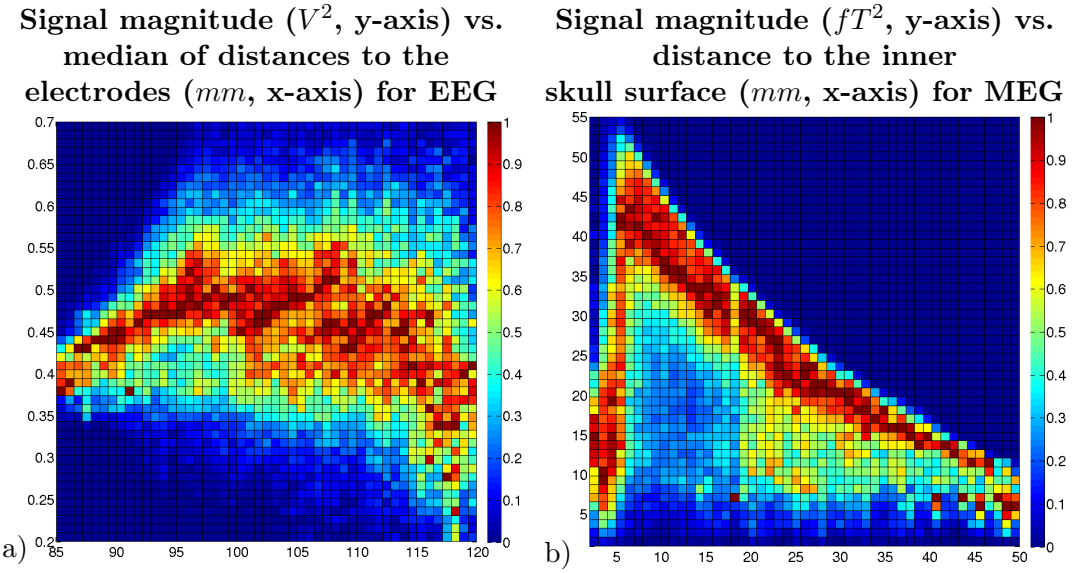

Figure 3.7.: Signal magnitude (in V^2/fT^2) computed in model *3CI* as a function of median of distances between the source position and the electrodes for EEG (left) and distance to the inner skull surface for MEG (right).

excluding sources with low signal magnitude or a pre-selection of sources with regard to positions and directions, but this would have increased the possibility of a biased evaluation result. Instead, all sources were included in the analysis and it was tried to create visualizations where one can particularly identify the effects due to quasi-radial and deep sources.

Finally, one observes that the numerical error, i.e., the error of model *6CA* in reference to the highly resolved model *6CA_hr*, was smaller than all observed modeling effects in both modalities, underlining the high accuracy of the used FEM approach and of the head model.

Evaluation of spatial measures

The plots of the cumulative relative frequency of RDM and lnMAG already gave a valuable overview of the importance of the different head tissue properties for the EEG and MEG forward problem. However, the goal of this study was to pursue a deeper insight into the relationship

of source properties and volume conduction effects. As the following investigations show, this relationship can be further enlightened using the additional measures and visualization means introduced in Section 3.1.3.

The important characteristics of the spatial distribution of the signal magnitude for EEG and MEG are shown in Figure 3.3 and have already been discussed in Section 3.1.4.

In Figure 3.6, the median of the distances between a source position and the electrodes (left) and the distance between a source position and the inner skull surface (right) are visualized on the brain surface. In Figure 3.6a it can be observed that a high median is mainly given for temporal and frontal regions. In comparison to Figure 3.6b, the different focus of this parameter becomes clear.

Figure 3.7 shows the dependency of the signal magnitude computed in model *3CI* for EEG (left) and MEG (right) on the parameters visualized in Figure 3.6. Interestingly, Figure 3.7a shows that sources with the smallest and with the largest median have the smallest signal magnitude for the EEG, while those with an intermediate median have the strongest signal. The surface representation in Figure 3.6a shows that the latter correspond to more central and superficial sources, which were expected to have the strongest signal. For the MEG, a set of superficial sources with a weak signal could be identified corresponding to quasi-radial sources on gyral crowns (Figure 3.7b, sources with lowest distance to the skull). For both EEG and MEG, Figures 3.3a-d and 3.7b clearly show the decay of the signal magnitude as a consequence of source depth/distance to the inner skull surface. One can not distinguish the quasi-radial sources at sulcal valleys as clearly as those at gyral crowns; they can only be suspected as outliers with low signal magnitude at distances between 18 and 30 mm (Figure 3.7b). This can be explained by the higher variety in the distance between the sources in the sulcal valleys and the inner skull surface due to the different sulci depths (causing a blurring in x-direction in Figure 3.7b). Furthermore, the difference between the signal magnitude of quasi-radial sources in the sulcal valleys and neighboring sources at similar depth is much smaller than at gyral crowns (causing a blurring in y-direction).

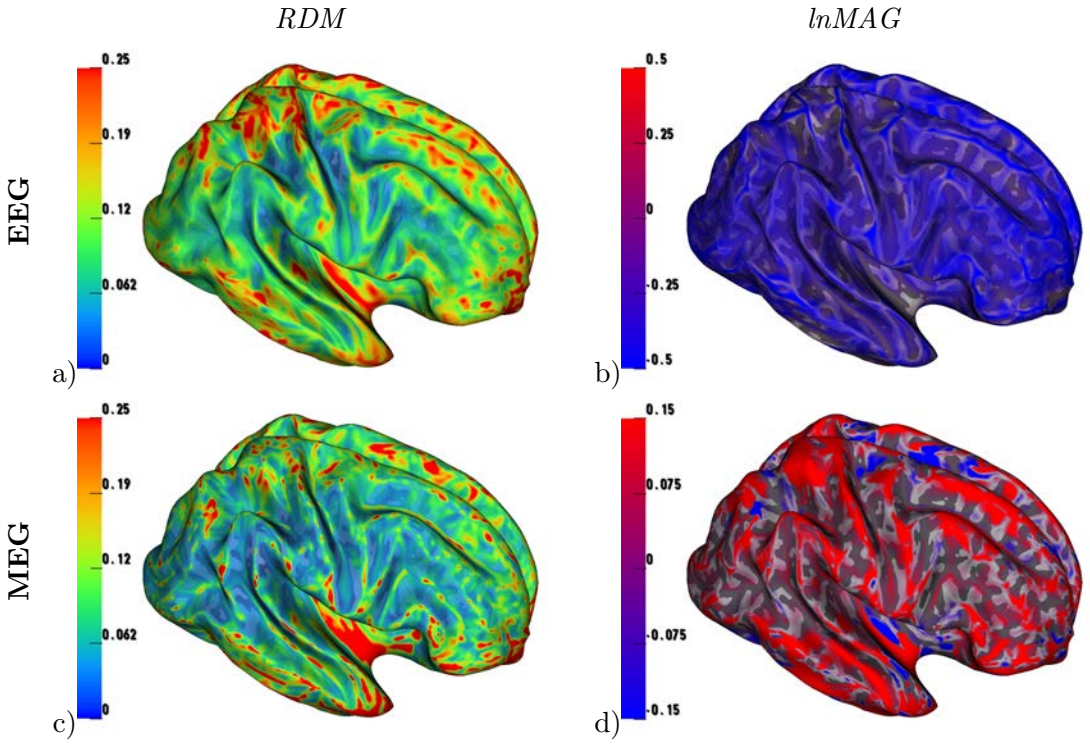

Figure 3.8.: Effect of CSF distinction - difference between models *4CI* and *3CI* plotted on brain surface.

Single tissue compartment sensitivity investigation

Finally, detailed single tissue sensitivity analyses complemented the investigations. For each refinement step a heat map was created using one of the above proposed parameters for both RDM and lnMAG in addition to the surface plots. In most cases the distance to the inner skull surface was found to be the most meaningful parameter.

Distinction of CSF: When evaluating the effect of including the CSF compartment on the EEG, the visual inspection of the surface plots (Figure 3.8a,b) is in line with the visualization in the heat maps (Figure 3.9a,b) for both difference measures. The lnMAG in Figure 3.8b shows a strong decrease of signal magnitude especially for superficial sources (on gyral crowns), which is evident in the diagram in Figure 3.9b. A negative lnMAG was especially observed for the most superficial sources, while it was constantly at a smaller but still clearly negative level for deeper sources. Such an effect might lead to significant misinterpretations when comparing source magnitudes of superficial and deep reconstructed sources. For the used model, a possible decrease/increase by a factor of up to 1.6 was found. The RDM distribution in Figure 3.8a is less clear; significant effects were identified at the very top of the brain in the vicinity of the interhemispheric fissure, in deep areas like the Sylvian fissure, and the frontal and temporal poles as well as the inferior temporal lobe were found to be affected, too. Figure 3.8a and especially Figure 3.9a show a trend towards lower RDM effects for deeper sources. Here, a lower limit was reached at a depth of about 15 mm below the inner skull surface; for even deeper sources the RDM stayed at a constant level. Even though the trend was clearly

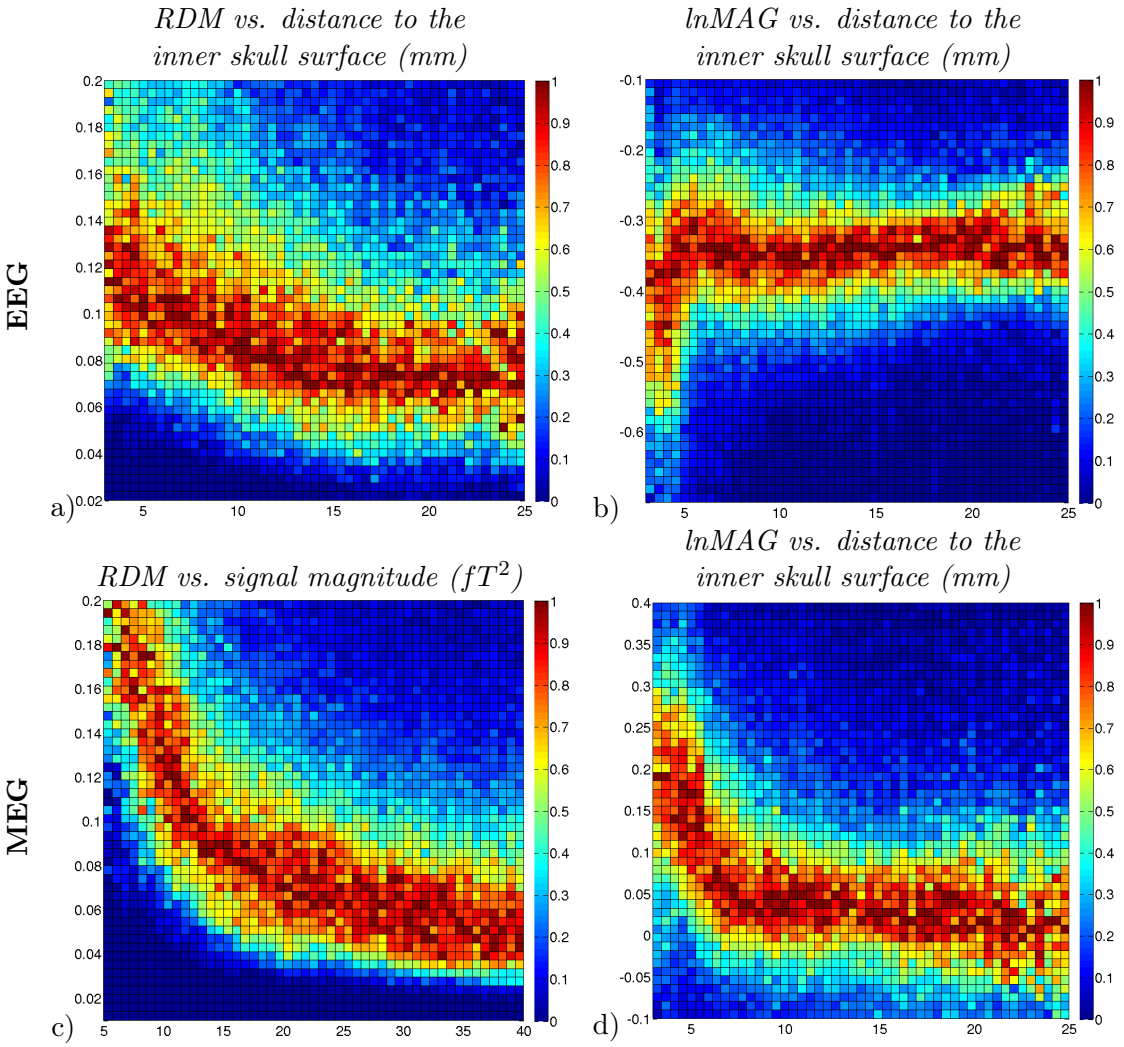

Figure 3.9.: Effect of CSF distinction - difference between models *4CI* and *3CI* in 2d-histogram.

recognizable, a considerable variance of effect sizes was observed at all source depths.
A clear effect of the CSF distinction on the MEG was found in the lnMAG, where the optical impression of increased signal magnitude for superficial sources in Figure 3.8d is visible in the heat map plot in Figure 3.9d. A lower limit was reached at a depth of 8 mm below the inner skull surface. As for the EEG, this is especially problematic when comparing the strength of superficial and deeper lying reconstructed sources. The topography of the RDM plot in Figure 3.8c is again less clear, but, similar to the EEG case, significant effects were found on some gyral crowns, at the top of the brain, in the Sylvian fissure, at the frontal and temporal poles, and at the inferior temporal lobe. Furthermore, a clear correlation of RDM and signal magnitude is visible in Figure 3.9c.

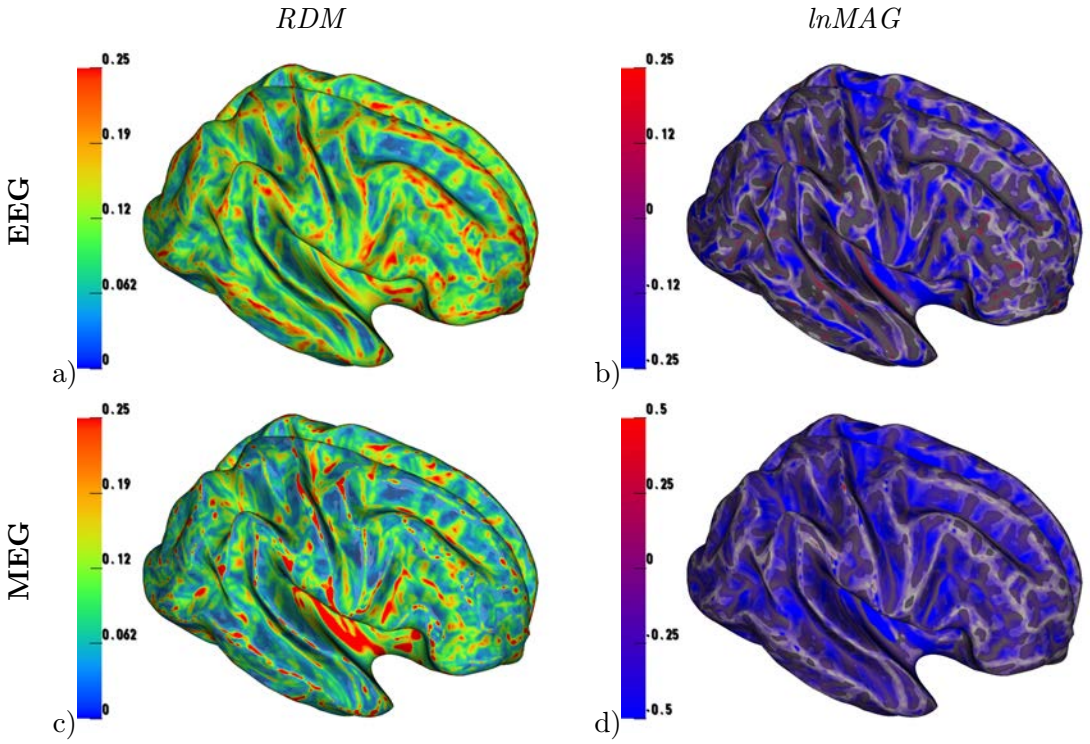

Figure 3.10.: Effect of gray/white matter distinction - difference between models *5CI* and *4CI* plotted on brain surface.

Distinction between gray and white matter: For the EEG, strong effects both regarding RDM and lnMAG were found for the most superficial sources in Figure 3.10a and b and 3.11a and b. The surface plot in Figure 3.10b shows a strongly decreased magnitude with the lnMAG being partially even below -0.25 – and thus exceeding the limit of the color bar – mainly on top of gyri; a finding that is also apparent in the heat map visualization in Figure 3.11b. For deeper sources, a weaker decrease of EEG signal magnitude (lnMAG between 0 and -0.2; cf. Figure 3.11b) was observed. For the few visible areas with an increased magnitude in Figure 3.10b, no representation in the heat map plot in Figure 3.11b could be found. As seen in Figure 3.4, the width of the distribution of the lnMAG effects is as large as for the CSF distinction. Again, especially the differences between very superficial and deeper sources are huge. The spatial distribution of the highest RDM effects is very similar to that of the lnMAG (Figures 3.10a,b). RDM effects above 0.2 were found for very superficial sources. Visually, these could be identified predominantly on the gyral crowns. For the remaining deeper source positions the RDM effects are still non-negligible with values mainly between 0.05 and 0.1.

The RDM surface plot for the MEG in Figure 3.10c shows high effects in areas where sources are suspected to be quasi-radial, again. Furthermore, a clear correlation of these RDM effects to the MEG signal magnitude is found (similar to Figure 3.9c and therefore not shown here). Figure 3.11c shows a slight decrease of the effects up to a depth of about 6 mm, followed by an increase for even deeper sources where both the lower bound of effects and the mean effects are higher. The visualization of the lnMAG in Figure 3.10d mainly shows a decrease of MEG signal magnitude, corroborated by the systematic plot in Figure 3.11d with nearly

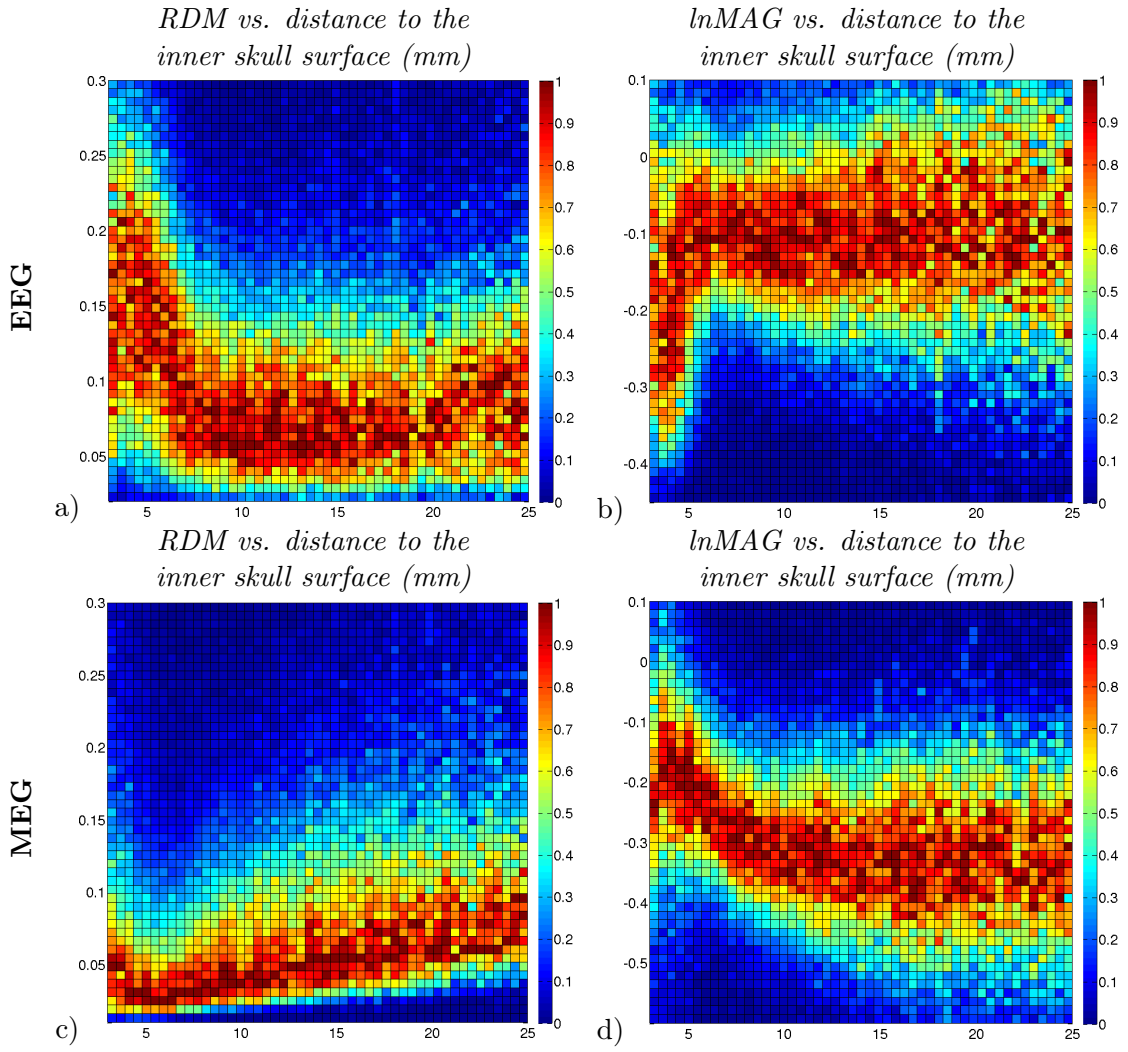

Figure 3.11.: Effect of gray/white matter distinction - difference between models *5CI* and *4CI* in 2d-histogram.

all magnitude effects being below 0. At values between -0.3 and -0.1, effects were lowest for superficial sources (as in Figure 3.11c the more superficial quasi-radially oriented sources show bigger effects), getting stronger towards a RDM of -0.4 at a distance of about 1 cm to the inner skull surface and remaining constant for even deeper sources.

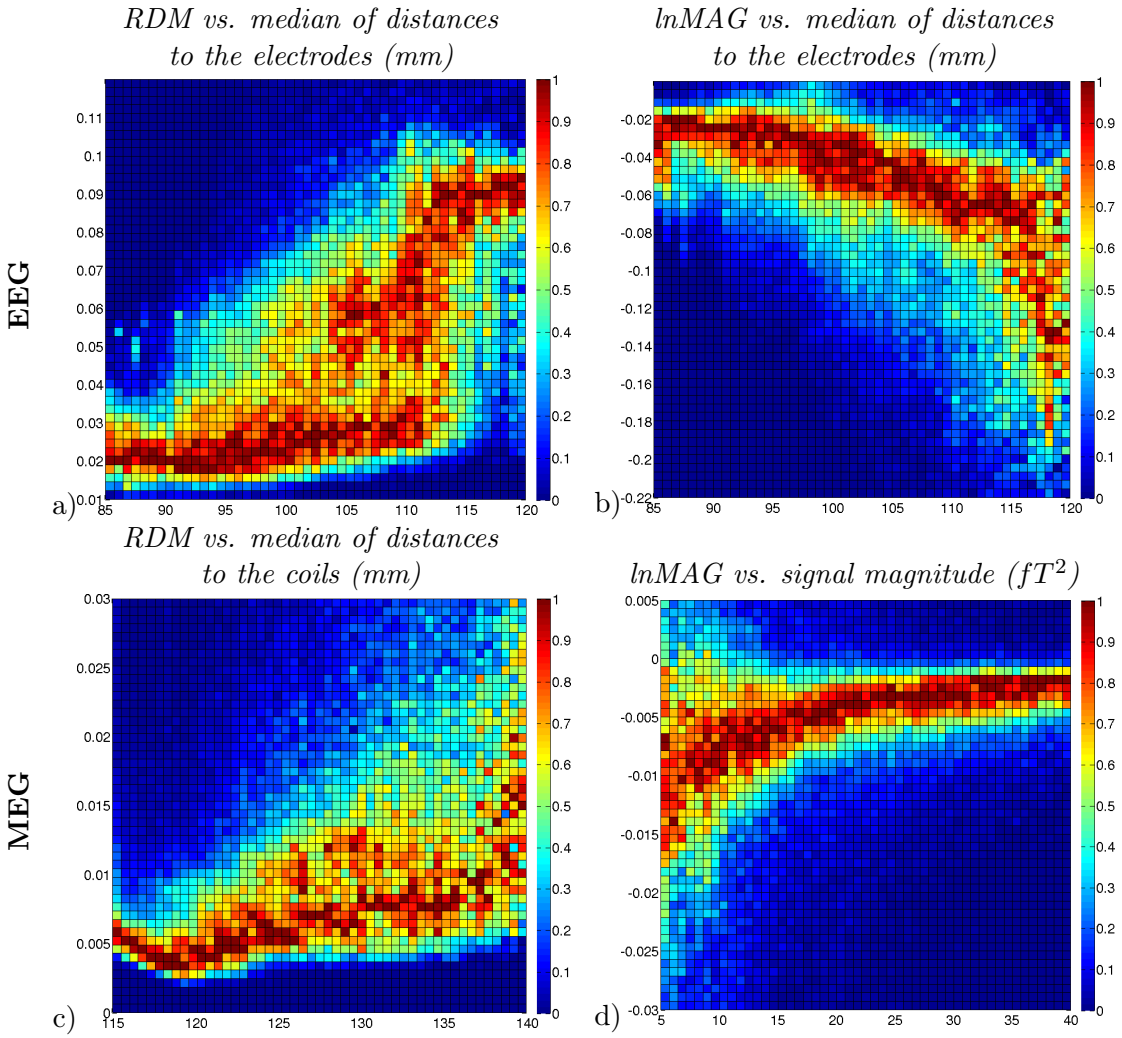

Figure 3.12.: Effect of spongiosa/compacta distinction - difference between models *6CI* and *5CI* in 2d-histogram.

Distinction between skull compacta and spongiosa: In Figure 3.13 and Figure 3.12, notable RDM effects for the EEG are mainly found at the temporal lobe and its surrounding region, i.e., in a relatively deep area with bad sensor coverage (Figure 3.13a). Furthermore, some notable topography changes are found at the very top of the brain. The same locations were affected when looking at the lnMAG, finding a moderate decrease of signal magnitude (Figure 3.13b). Since the areas with a larger median in Figure 3.6a strongly correlate to the affected areas in Figure 3.13a and b, these were used as a parameter for computing the heat maps. The magnitude of the RDM and lnMAG effects clearly increased with the median of the distances to the electrodes (Figures 3.12a,b), showing that the spatial measure used was able to resolve the effects in the visually identified areas as desired. lnMAG effects of up to -0.15 were found in temporal areas (Figure 3.13b), this corresponds to an underestimation of the source strength by a factor of up to 1.17 when comparing reconstructed sources in temporal areas to those in brain areas with negligible lnMAG effects using a head model that does not include the distinction between skull spongiosa and compacta.

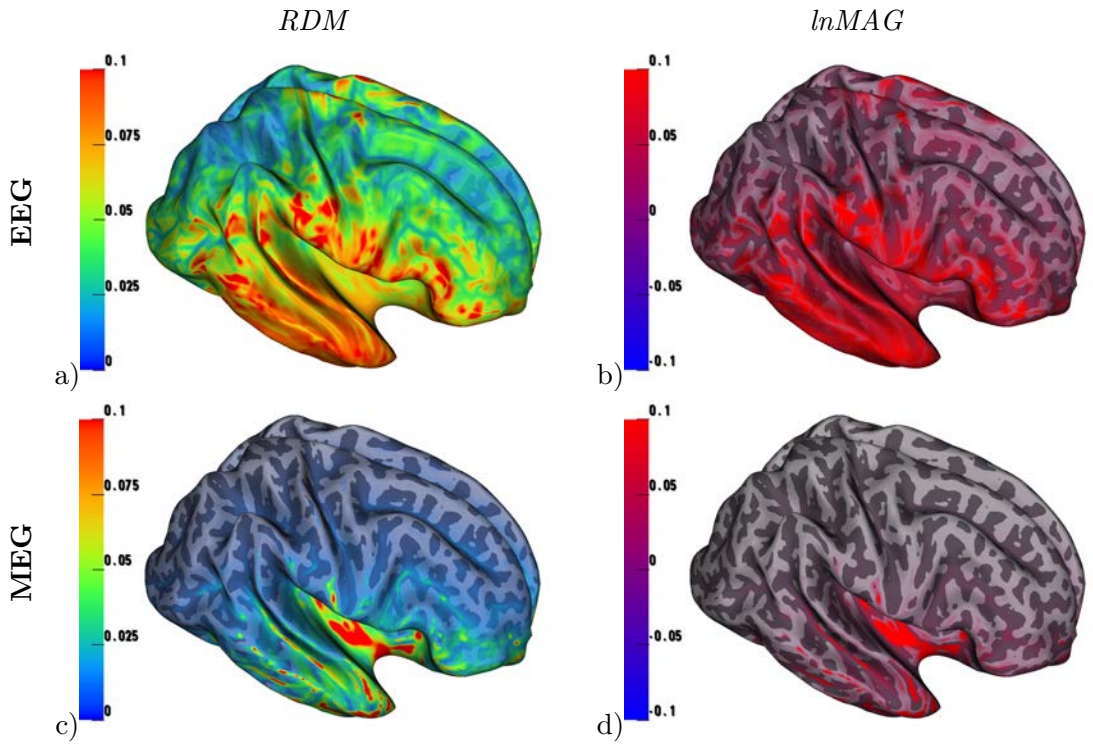

Figure 3.13.: Effect of spongiosa/compacta distinction - difference between models *6CI* and *5CI* plotted on brain surface.

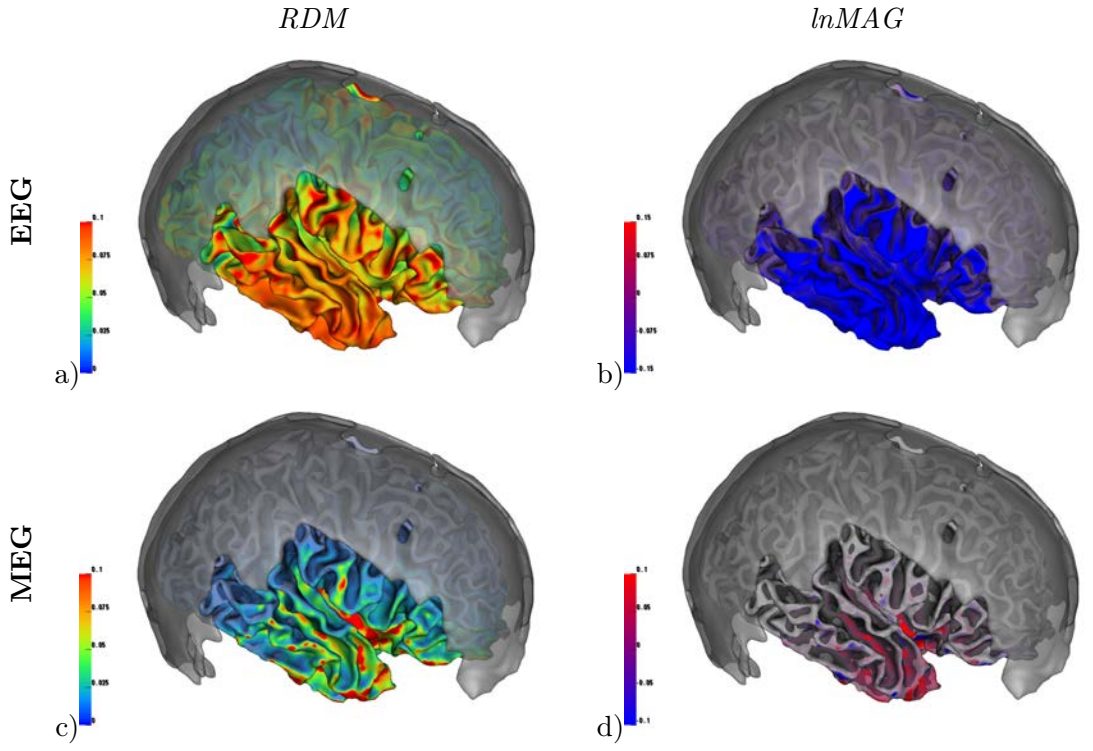

Figure 3.14.: Effect of spongiosa/compacta distinction - difference between models *6CI* and *5CI* plotted on brain surface together with spongiosa compartment.

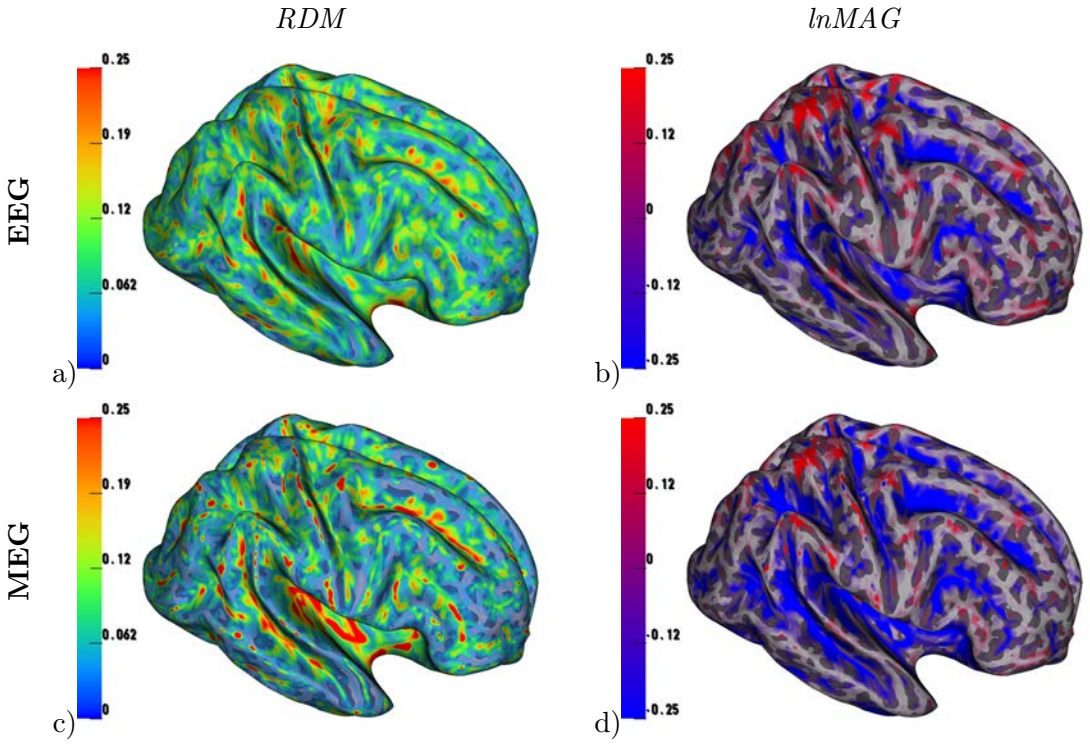

Figure 3.15.: Effect of anisotropic white matter conductivity - difference between models *6CA* and *6CI* plotted on brain surface.

Figures 3.13c and d and 3.12c and d clearly show that the impact of skull spongiosa/compacta distinction is by far weaker for the MEG. A weak influence on the topography was found for deep sulcal sources (Figure 3.13c) in combination with a positive lnMAG (Figure 3.13d). This was more pronounced in sulci at the pole of the temporal lobe, in the Sylvian fissure, and in some areas at the base of the frontal lobe. The only considered parameters that correlated with these small effects were the median of the distances between the source position and the MEG sensors (RDM increases with median in Figure 3.12c) and the MEG signal magnitude (Figure 3.12d showing a tendency towards a slightly negative lnMAG for weak sources).
However, the probably best visualization of the effects of the distinction between skull compacta and spongiosa is shown in Figure 3.14. Here, the correlation between existence of spongiosa in the overlying skull and the effect on RDM and lnMAG especially for the EEG is nicely visible, showing that high effects mainly occur in areas where no spongiosa is modeled.

White matter anisotropy: Figures 3.15a and c and 3.16a and c show the RDM changes due to white matter anisotropy. For both EEG (Figures 3.15a and 3.16a) and MEG (Figures 3.15c and 3.16c), the most significant topography changes occurred for sources in sulcal valleys and on gyral crowns. The heat map for the EEG results in Figure 3.16a shows RDM effects with values mainly between 0.02 and 0.10 at all source depths. A slight trend towards higher effects for deeper sources could be observed, but this was not as distinct as for the other refinement steps. The RDM heat map for the MEG in Figure 3.16c shows a clear correlation between signal magnitude and topography effect, underlining the visual finding of strongest effects for

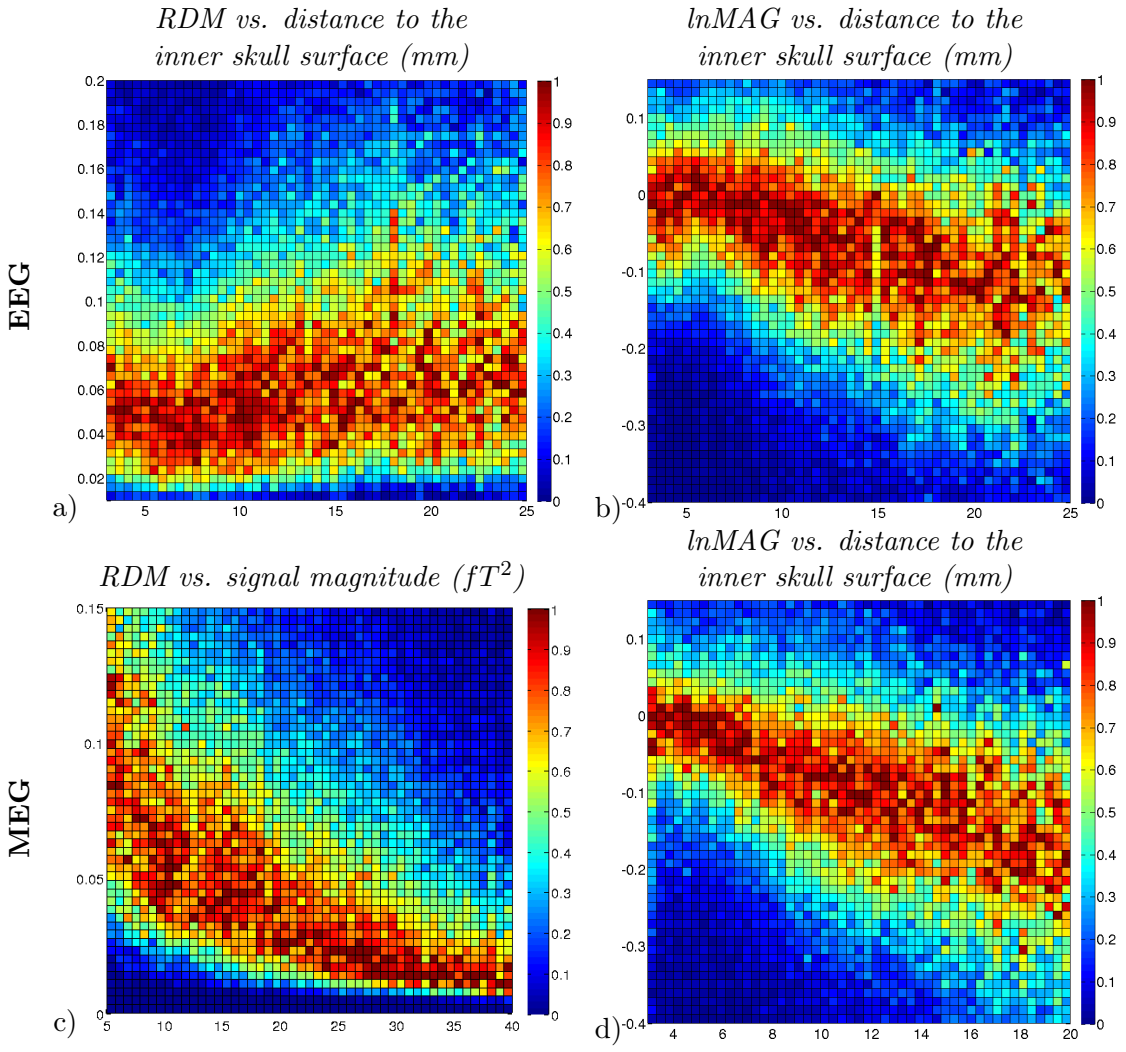

Figure 3.16.: Effect of anisotropic white matter conductivity - difference between models *6CA* and *6CI* in 2d-histogram.

quasi-radial sources.

For both EEG and MEG the effects with regard to the lnMAG were very similar and the visual impression obtained from Figures 3.15b and d was in line with the heat maps in Figures 3.16b and d. Minor effects could be reported for the most superficial sources with an lnMAG between -0.1 and 0.1 in both modalities. For deeper sources, the signal magnitude continuously decreased in comparison to the isotropic model *6CI*, an effect which was weaker for the EEG than for the MEG (Figures 3.16b, d).

3.1.5. Relevance of the Forward Results to Inverse Solutions and Connectivity Estimations

A question that naturally poses for studies only considering the accuracy of the solution of the EEG/MEG forward problem is the influence of these results in the context of source and/or connectivity analysis. A first idea of this interdependency was given by Dannhauer et al. (2011), who visualized the influence of the forward topography error, i.e., the RDM, on the accuracy of the inverse solution. In the present case, the forward study published by Vorwerk et al. (2014) was accompanied by a follow-up study (Cho et al., 2015), where the effect of the simplifications in the forward model on the subsequent analysis, e.g., source reconstruction or connectivity analysis, was investigated. In a first step, the consequences of simplifications of the forward model on source reconstruction were investigated. Therefore, artificial source time courses were generated in the fully detailed model and subsequently the accuracy of a source reconstruction in the simplified model was evaluated. As inverse approach a *linear constrained minimum variance* (LCMV)-beamformer was applied (Van Veen et al., 1997). Second, the influence of model simplifications on the reconstruction of connectivity using the measures *ICoh* (imaginary coherence; Nolte et al., 2004) and *generalized partial directed coherence* (GPDC; Baccald and de Medicina, 2007) was investigated. The results of the source analysis study and of that only the results of one of the evaluated measures, namely the output SNR, are recited in the following to provide basic evidence that the results of the accuracy investigations for the forward problem are also of high relevance when estimating the accuracy in subsequent steps of analysis. For further results it is referred to Cho et al. (2015).

Methods

To preserve a high comparability of the results, the used head model remained essentially unchanged. However, instead of extending the head model *3CI* step-by-step by adding one further compartment at a time, in this study the starting point was the model *6CI*. As all of the considered models only included isotropic conductivities, it is simply denoted as model *6C* here. For this model then single refinements, e.g., the distinction between gray and white matter, were neglected. The thereby generated five compartment models are *5C-w/g* (no gray/white matter distinction – white matter set to gray matter conductivity), *5C-c/s* (no compacta/spongiosa distinction – skull conductivity set to isotropic skull conductivity; cf. Table 3.1, Dannhauer et al., 2011), and *5C-CSF* (no CSF distiction – CSF compartment set to gray matter conductivity). Furthermore, the size of the source space was reduced to decrease the computational effort; this resulted in a source space consisting of 16,000 nodes.

To investigate the source analysis accuracy, an artificial source network was generated using neural mass modeling (David et al., 2005; Jansen and Rit, 1995). Here, the position for one source was kept fixed (Figure 3.17, blue dot), which was chosen so that it has a small RDM for all of the considered model simplifications and both for EEG and MEG, and the position of the second source was varied over all remaining source space positions. More details on the generation of the artificial source time courses are given in Cho et al. (2015).

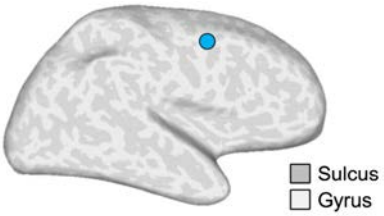

Figure 3.17.: Location of source 1 (blue dot). *Source: Cho et al. (2015), CC BY-NC-ND (http://creativecommons.org/licenses/by-nc-nd/4.0/)*

Subsequently, the LCMV beamformer was used to reconstruct the source time courses in the simplified head models. The LCMV beamformer is an adaptive spatial filtering technique that is widely used for source analysis because of its high spatial resolution (Sekihara et al., 2005). Assuming that the measured signal m is generated by few, focal neural sources at locations q_r each with activity $x(q_r)$, i.e., x is a 3×1 vector containing the source activity for each cartesian direction, it can be represented by

$$m = \sum_r L(q_r)x(q_r). \tag{3.2}$$

$L(q_r)$ is the leadfield for source position q_r, i.e., the $\#sensors \times 3$-matrix containing the forward simulation results for dipoles oriented in the three cartesian directions. The idea of the LCMV beamformer is to construct a spatial filter $w(q_i)$ whose output $\hat{x}(q_i)$, i.e., the reconstructed source activity at a particular location q_i in the source space, is given by

$$\hat{x}(q_i) = w^t(q_i)m. \tag{3.3}$$

The weights of the spatial filter $w(q_i)$ are selected to minimize the variance of the filter output under the constraint that signals from the pointing location are passed with a unit gain:

$$\min_{w(q_i)} \operatorname{tr}\left(w^t(q_i)C_m^{-1}w(q_i)\right) \qquad \text{with } w^t(q_i)L(q_i) = \mathbf{I}. \tag{3.4}$$

C_m denotes the spatial covariance matrix of the measurement data. This optimization problem can be solved using Lagrangian multipliers (Van Uitert et al., 2004):

$$w(q_i) = C_m^{-1}L(q_i)\left(L^t(q_i)C_m^{-1}L(q_i)\right)^{-1}. \tag{3.5}$$

For the two source scenario with sources r_1 and r_2 the covariance matrix can be expressed as

$$C_m = \sigma_0^2\mathbf{I} + \sigma_{r_1}^2 L(q_{r_1})L^t(q_{r_1}) + \sigma_{r_2}^2 L(q_{r_2})L^t(q_{r_2}). \tag{3.6}$$

σ_0^2 is the noise variance, $\sigma_{r_1}^2$ and $\sigma_{r_2}^2$ are the power of the sources q_{r_1} and q_{r_2}, respectively. Accordingly, one can define the signal-to-noise ratio (SNR)

$$\mathrm{SNR}(r_1, r_2) = \frac{\sigma_{r_1}^2 \|L(q_{r_1}\| + \sigma_{r_2}^2 \|L(q_{r_2})\|}{\sigma_0^2}. \tag{3.7}$$

As a measure of the quality of the spatial filter – and thereby also of the source reconstruction – the output SNR (or Z^2) can be defined, a ratio between reconstructed source power and projected noise power, to compare the properties of the spatial filters obtained from the reference head model and test head models:

$$Z^2(q_i) = \frac{w^t(q_i)C_m w(q_i)}{w^t(q_i)(\sigma_0 \mathbf{I})w(q_i)} \tag{3.8}$$

The Z^2 value can be interpreted as 1 plus original source power divided by projected noise ratio, i.e., the higher the value the better. Similar to the previous study, the influence of RDM and input SNR on the output SNR was visualized using heat maps. Therefore, the sources were sorted in ascending order regarding their RDM (for source 1 the RDM of source 2 was chosen for sorting) and for each input SNR the respective output SNR was computed and color coded (Figure 3.18). Furthermore, the values of $\ln(Z^2)$ for an input SNR of 300 were visualized on an inflated brain surface to be able to estimate the areas where the accuracy of the inverse analysis is most affected by the model simplifications (Figure 3.19). The values for source 1 are plotted at the position of source 2, as the position of source 1 was kept constant.

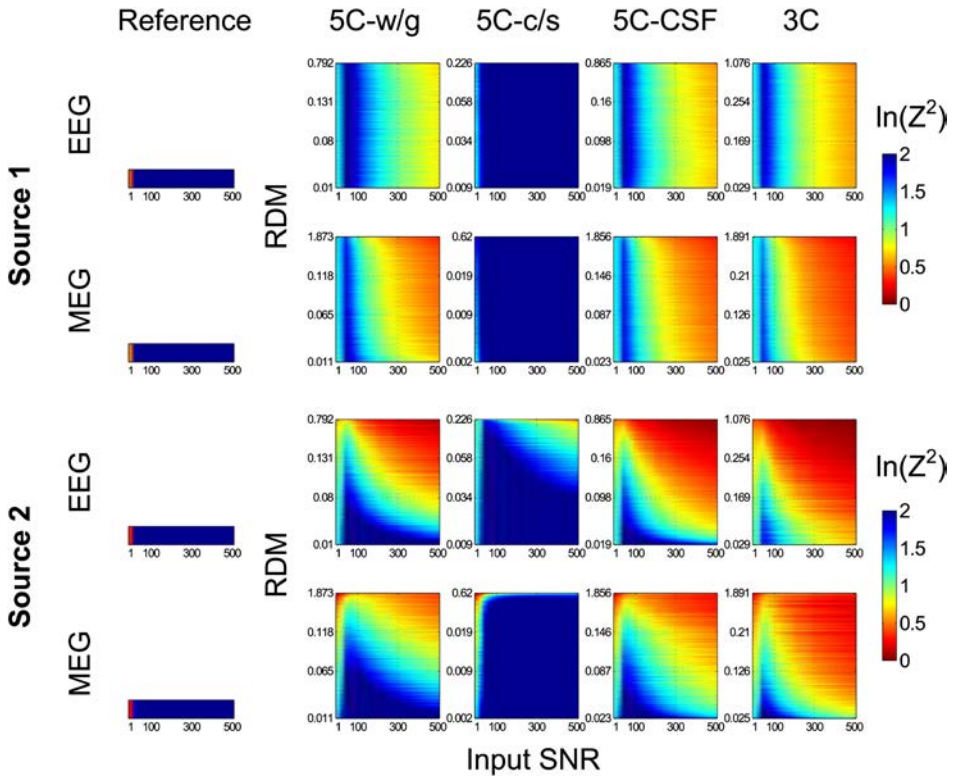

Figure 3.18.: Heat maps of $\ln(Z^2)$ for sources 1 and 2, as a function of input SNR and RDM in EEG and MEG. Note the different RDM ranges of the y-axis. The output SNR was calculated with different input SNRs. Then, the output SNR was sorted in ascending order of the RDM value for each head model. The heat maps for the reference head model represent the mean output SNR value at each input SNR. *Source: Cho et al. (2015), CC BY-NC-ND (http://creativecommons.org/licenses/by-nc-nd/4.0/)*

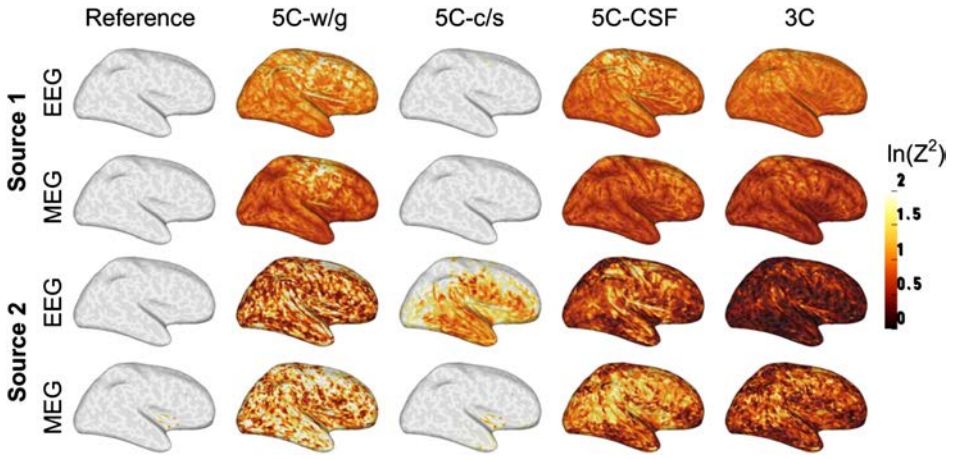

Figure 3.19.: $\ln(Z^2)$ for sources 1 and 2 in EEG and MEG for an input SNR of 300, plotted on the inflated white/gray matter interface. Note that in the maps for source 1, the $\ln(Z^2)$ value for source 1 is mapped onto the corresponding location of source 2 for visualization purposes because the location of source 1 is fixed in one location and only the location of source 2 varies. *Source: Cho et al. (2015), CC BY-NC-ND (http://creativecommons.org/licenses/by-nc-nd/4.0/)*

Results

In general, Figure 3.18 shows that for a minimal SNR (input SNR = 1) $\ln(Z^2)$ is also very small, as one would naively expect. When only slightly increasing the input SNR (1 < input SNR < 100 in Figure 3.18), $\ln(Z^2)$ rises sharply; a further increase of the input SNR (100 < input SNR in Figure 3.18) often causes $\ln(Z^2)$ to decrease again. For source 1, the slope of this decay does not depend on the RDM for the EEG (Figure 3.18, top row) and only slightly so for the MEG (Figure 3.18, second row), but becomes steeper for a larger RDM. For the reference and the *5C-c/s* model, no decrease of $\ln(Z^2)$ with increasing input SNR was visible at all, while it is strongest for model *3C*. Models *5C-w/g* and *5C-CSF* show very similar results. The relative insensitivity to the RDM is probably due to the choice of source 1 to have a small RDM for all tested models. For source 2 a higher RDM causes the maximum of $\ln(Z^2)$ to decrease and the decay of $\ln(Z^2)$ with increasing input SNR becomes steeper for both EEG and MEG (Figure 3.18, bottom two rows). Furthermore, for any considered input SNR $\ln(Z^2)$ decreases with increasing RDM. Again, the strongest effects are observable for model *3C* and the effect of neglecting the CSF is slightly stronger than that of neglecting the distinction between gray and white matter.

The spatial distributions (Figure 3.19) reveal that for source 1 (top two rows) deeper areas show smaller $\ln(Z^2)$ in EEG, while the crests of gyri and troughs of sulci show smaller $\ln(Z^2)$ in MEG. The values of $\ln(Z^2)$ are large (> 2) when both sources are very close to each other, i.e., the position of source 2 is close to the position of source 1 (cf. Figure 3.17), but these patterns differ between EEG and MEG. This could be due to the varying crosstalk effects of the test head models. No obvious dependency between the spatial distribution of the RDM as shown in Section 3.1 and the $\ln(Z^2)$ for source 1 can be seen. This is clearly different for source 2 (Figure 3.19, bottom two rows), where the values computed for $\ln(Z^2)$ very much resemble the spatial maps of the RDM, also with regard to the intensity of these effects. Here,

a quantitative relation between the accuracy of the forward solution and the inverse analysis is found. The values of $\ln(Z^2)$ are nearly unchanged high for the *5C-c/s* model, while the strongest effects, i.e., the smallest values of $\ln(Z^2)$ are, again, found for model *3C*.

3.1.6. Discussion

In this section, the influence of modeling or omitting different conductive compartments in realistic head models on the finite element forward solution was evaluated for both EEG and MEG. The practical relevance of these results was underlined by illustrating the strong correlation between inacuraccies in the forward simulation and the results of inverse analysis. It was shown that the CSF is one of the most important compartments to be modeled. Especially for superficial sources, modeling the CSF compartment had a large influence on the signal topography for both the EEG (Figures 3.4a, 3.8a, 3.9a) and the MEG (Figures 3.5a, 3.8c, 3.9c), while it had a much larger influence on the signal magnitude in EEG (Figures 3.4c, 3.8b, 3.9b) than in MEG (Figures 3.5c, 3.8d, 3.9d). In both modalities the influence on the signal magnitude, measured by the lnMAG, strongly varied depending on source position and orientation. The huge effect for the EEG can be explained by the strong increase of conductivity between sources and sensors that causes a shunting effect, while the effect for the MEG is probably due to the strong volume currents in the now highly conductive CSF compartment. In Wolters et al. (2006) these volume currents were visualized, underlining the need for an accurate modeling of this conductive compartment.

While this is a pure computer simulation sensitivity study and the effects were not validated in real experiments, some experimental studies allowing indirect conclusions on the effects of CSF modeling can be found in the literature and are in line with the results. Rice et al. (2013) showed in EEG experiments that brain shift and the resulting small changes in CSF layer thickness, induced by changing the subject's position from prone to supine, have a significant effect on the EEG in several standard visual paradigms. They describe a local increase of signal magnitude when decreasing the thickness of the CSF by changing the subject's position. This effect is consistent with the finding of a decreased signal magnitude due to the distinction of the CSF. Bijsterbosch et al. (2013) investigated the effect of head orientation on subarachnoid CSF distribution and concluded that minor differences in local CSF thickness are likely to significantly affect the accuracy of EEG source localization. In a further experimental validation study, Bangera et al. (2010) found that the inclusion of both CSF and brain anisotropy in the forward model is necessary for an accurate description of the electric field inside the skull.

Besides the strong effect on signal topography and magnitude, a further argument for the inclusion of the CSF in realistic head models is that the conductivity of human CSF at body temperature is well known; it was measured to be 1.79 S/m with a low inter-individual variance (Baumann et al., 1997; average over 7 subjects ranging in age from 4.5 months to 70 years with a standard deviation of less than 2.4% between subjects and for frequencies between 10 and 10,000 Hz). Thus, the CSF conductivity is one of the best-known parameters in the modeling process. The influence of modeling the CSF on forward solutions was also

investigated in other computer simulation studies, though the used models as well as the evaluation methods differ strongly (Ramon et al., 2004; Vallaghé and Clerc, 2009; Wendel et al., 2008). In this section, both the influence on EEG and MEG for realistically chosen sensor arrangements was investigated and thereby a more systematic evaluation of the CSF effect was added. The examination of the CSF effects in this study confirms and elaborates upon the previous studies, which also observed the decrease of signal amplitudes for the EEG.

Furthermore, it was shown that the effect of the distinction between gray and white matter is nearly as strong as that of the CSF inclusion in both modalities (Figures 3.4a,c, 3.5a,c), especially with regard to signal magnitude (Figures 3.4c, 3.5c). This stresses the strong effect of conductivity changes in the vicinity of the source as it was previously shown by Haueisen et al. (2000). While the EEG was affected the most for superficial sources both with regard to topography and magnitude (Figures 3.10a, b, 3.11a,b), a stronger decrease of signal amplitude was found for deep sources than for superficial ones for the MEG (Figures 3.10d, 3.11d). Here, strongest topography effects were found for the most superficial sources and for relatively deep sources (Figures 3.10c, 3.11c). For the MEG, Figures 3.8d and 3.10d show that the areas most affected by the magnitude effects of the two refinement steps from model *3CI* to model *5CI* do not overlap, but are mainly disjoint. This is underlined by the distribution of the magnitude effects in relation to the distance to the inner skull (Figures 3.9d, 3.11d), showing the clearly different effect of adding the CSF and of distinguishing between gray and white matter on sources at different depths. As for including the CSF compartment, the gray/white matter distinction induced a conductivity change for a large volume, explaining the strong effect on the signal magnitude.

To the best of the author's knowledge, only relatively few publications have investigated the effect of the (isotropic) distinction between gray and white matter so far, even though Haueisen et al. (2000) demonstrated the significant effect of local conductivity changes around the source position. The results of Haueisen et al. (1997) suggest a strong change of the signal topography and magnitude for both EEG and MEG when the white matter conductivity is chosen in the range of the gray matter conductivity. From the results presented, it can be concluded that the strength of this effect is slightly lower than the effect of the CSF modeling in *4CI* vs. *3CI* comparisons, which is supported by the findings presented here. The systematic evaluation adds important information about the locations of the most affected sources compared to the single source scenario evaluated by Haueisen et al. (1997), as described previously. Ramon et al. (2004) also found a decrease of the scalp potentials, i.e., the EEG signal, due to the introduction of gray and white matter compartments of differing conductivities, even though the magnitude of the decrease was not further classified. Van Uitert et al. (2004) found the conductivity of white and gray matter to appear especially influential in determining the magnetic field and showed that using a too high white matter conductivity, as it is of course the case when not distinguishing between gray and white matter, leads to high forward and inverse errors.

Compared to the previous two steps, the distinction of skull compartments of different conductivity only showed comparatively weak effects on the EEG (Figures 3.4a,c) and nearly

no effect on the MEG (Figures 3.5a,c). Mainly the temporal lobe and its surrounding area were affected in the EEG both with respect to topography and magnitude (Figures 3.13a,b). The effect on the MEG was even weaker; it could almost exclusively be seen for deep sources in sulcal valleys (Figures 3.13c,d). The relatively small impact of skull spongiosa and compacta distinction was probably at least partly caused by the use of an already optimized conductivity value for the homogenized skull compartment that represents the best fit to the realistic spongiosa/compacta scenario (Dannhauer et al., 2011; Stenroos et al., 2014). This is underlined by the findings in Figure 3.14. It is apparent that the highest RDM errors occur where no compacta is modeled and the optimized conductivity value is thus no longer a good approximation.

Surely, these results do not imply that an accurate modeling of the geometry and conductivity of the skull plays a minor role in forward modeling as it is also subsequently shown in Section 3.2. Much research was conducted with regard to skull modeling. Hence, it is now well known that the EEG is very sensitive to it, while the MEG is assumed to be mainly not affected as long as the inner skull surface is represented appropriately (Fuchs et al., 1998; Hämäläinen et al., 1993; Lew et al., 2013; Marin et al., 1998; van den Broek et al., 1998; Vanrumste et al., 1998). However, Stenroos et al. (2014) have recently shown that assuming the skull to be fully insulating leads to errors that are larger than the geometrical errors in a three-shell model and especially larger than those that are induced by assuming a homogeneous skull compartment. Skull conductivity parameters might vary across individuals and within the same individual due to variations in age, disease state, and environmental factors (Akhtari et al., 2002). The huge sensitivity of the EEG signal to these changes was shown (Vallaghé and Clerc, 2009). The use of suboptimal values for the skull conductivity and uncertainties about the actual value strongly influence the EEG as shown in various studies (Dannhauer et al., 2011; Fuchs et al., 1998; Huang et al., 2007; Lew et al., 2013; Montes-Restrepo et al., 2014). Recent studies proposed ways to individually estimate parameters such as the skull conductivity (Aydin et al., 2014; Gonçalves et al., 2001, 2003; Huang et al., 2007; Wolters et al., 2010) that are important not only in EEG but also in combined EEG and MEG source analysis. It was furthermore shown that skull holes, included in all of our models, play an important role for EEG, but are less important for MEG (Lanfer et al., 2012b; Lew et al., 2013; van den Broek et al., 1998). Akhtari et al. (2002); Dannhauer et al. (2011); Ollikainen et al. (1999); Sadleir and Argibay (2007) studied the importance of skull inhomogeneity and of distinguishing skull compacta and spongiosa. However, Dannhauer et al. (2011); Stenroos et al. (2014) have shown that differences between EEG and MEG forward solutions computed in models with skull spongiosa and compacta and those with homogenized isotropic skull can be kept at a rather small level compared to other effects by using an optimized isotropic skull conductivity, as it was done in this study. The results of this study are in line with the results of the MEG study by Stenroos et al. (2014), who found only small effects of neglecting the fine structure of the skull when using an optimized isotropic conductivity. The EEG study of Dannhauer et al. (2011) reported the strongest changes in motor areas, occipital and frontal lobe, while notable effects of skull spongiosa/compacta distinction for the EEG were mainly

found at the temporal lobe, at the base of the frontal lobe, and in some spots at the very top of the brain in present study. Possible reasons for these differences might be found in the differing model setup. The head model used by Dannhauer et al. (2011) neglected the CSF compartment and thereby the here observed strong smearing of the potentials was not present. This might have changed the influence of variations in the skull compartment on the forward simulation. Furthermore, Dannhauer et al. (2011) used a conductivity of 0.0042 S/m for the isotropic skull compartment, while here already their proposed optimized value of 0.01 S/m was used, which minimizes the differences between isotropic and multi compartment skull models.

The influence of modeling white matter anisotropy was also found to be strong, but less influential than that of CSF or brain compartment distinction (3.4a,c, 3.5a,c), and the spatial pattern of the induced changes was difficult to interpret (Figures 3.15 and 3.16). The signal magnitude decreased with increasing source depth in both modalities (Figures 3.16b,d), while the distribution of the topography effects was scattered with a trend towards higher effects for deeper sources (Figures 3.15a,b, 3.16a,b).

Bangera et al. (2010) have experimentally shown that an anisotropic model leads to an improved performance compared to isotropic models for the calculation of intracranial EEG forward solutions. Butson et al. (2007) and Chaturvedi et al. (2010) demonstrated in patient studies that the tissue activated by deep brain stimulation (DBS) can be reliably predicted by finite element simulations using realistic head models incorporating tissue anisotropy calculated following the approach of Tuch et al. (2001). These studies can be seen as an experimental validation of this approach also for EEG/MEG simulations, since the underlying mechanisms of volume conduction are identical. As further experimental evidence for the importance of modeling white matter anisotropy, Liehr and Haueisen (2008) presented phantom studies and demonstrated that anisotropic compartments influence directions, amplitudes, and shapes of potentials and fields at different degrees. They conclude that anisotropic structures should be considered in volume conductor modeling when source orientation, strength, and extent are of interest.

Additionally, several simulation studies investigated the influence of white matter anisotropy on EEG and MEG source analysis. Güllmar et al. (2010); Haueisen et al. (2002) investigated effects of white matter anisotropy on topography and magnitude measures. While these studies provide a comprehensive evaluation of white matter anisotropy effects, this study adds a more detailed investigation of the spatial distribution of these effects and the comparison of effect strengths in relation to other important modeling effects. Even though Güllmar et al. (2010) visualized the effects for a fixed anisotropy of 1:10, the depicted effect distribution appears very similar to the one presented here. Their so-called *directv approach* showed the same tendency towards a negative lnMAG for both EEG and MEG when the cumulative relative frequency was plotted as it is observable in our Figures 3.15 and 3.16. Of all their approaches it is the one that is most similar to the one used here, since it is also based on the model of Tuch et al. (2001). A more detailed comparison of the RDM effects is hardly possible, since the results were depicted as histograms by Güllmar et al. (2010) in contrast to the cumulative

relative frequencies plotted here. For most sources they reported an RDM below 0.1, while slightly higher overall effects were found here. This might be explained by the different approaches used to scale the conductivity tensors. In the directv approach the tensors for each element are scaled so that they fit best to the isotropic conductivity. This results in a better approximation of the isotropic model than the approach used here and thus leads to smaller relative effects. However, this does not allow for a conclusion which approach is more realistic, but only which is closer to the isotropic model. Haueisen et al. (2002) used the theoretically derived scaling factor from Tuch et al. (2001) to compute anisotropic conductivity tensors for both gray and white matter and also found a decrease of signal magnitude for deeper, dipolar sources in both EEG and MEG due to the introduction of anisotropic conductivity. The change in correlation between the topography in the isotropic and anisotropic model was less clear. While the correlation in the MEG was still high and a – even though weak – depth dependency could be found, the EEG was more strongly affected, but the behavior was rather unsteady. Hallez et al. (2008) showed that particularly the omission of conductivity anisotropy leads to a large displacement of reconstructed sources that are oriented parallel to the fiber structure in the main direction of anisotropy, while it was considerably smaller for sources oriented perpendicular to the local fiber structure. The observed localization errors reached up to 10 mm.

Wolters et al. (2006) showed that white matter anisotropy causes volume currents to flow in directions more parallel to the white matter fiber tracts, with a clearly increased influence of white matter anisotropy on a deep source compared to superficial sources. However, they only investigated the effect of prolate anisotropy at fixed ratios on the forward solution for three sources; one deep in the thalamus and both a radial and a tangential source in the somatosensory cortex.

As previously mentioned, Dannhauer et al. (2011) presented a first approach to estimate the influence of changes in the forward solution on the inverse solution. They investigated the relationship between RDM and localization error for the EEG using scatter plots and correlation analysis. A clear correlation between these measures was observed. Upper and lower limits for the localization error were found to exist as linear functions of the RDM; an RDM of 0.025 predicted, for example, maximal localization errors between 8 and 10 mm and an RDM of 0.25 predicted minimal localization errors of about 2 mm. These results allow the conclusion that, even though the present study focused on the forward problem, the conclusions derived for volume conductor modeling are directly related to the accuracy in the EEG and MEG inverse problem. This conclusion is further underlined by the more detailed results gained by Cho et al. (2015) that were partly recited in Section 3.1.5. The results show that source analysis using the LCMV beamformer is for both EEG and MEG clearly affected by the considered head model simplifications, leading to decreased output SNR and increased crosstalk (crosstalk results not depicted here). The output SNR as a measure of the soure reconstruction accuracy is inversely correlated with both the topography changes of the forward solution (RDM; Figure 3.18) and the input SNR (Figure 3.19). Figure 3.19 shows that the values of the input SNR even replicate the patterns of the topography

effects in the study of the forward solution (cf. Figures 3.8, 3.10, and 3.13). Furthermore, the results of Cho et al. (2015) show that the effects of the model simplifications also propagate to further analysis based upon the results of the source reconstruction, i.e., the output of the LCMV beamformer, e.g., when conducting connectivity analysis using GPDC (Baccald and de Medicina, 2007). This is due to crosstalk and a higher correlation of the weights of the LCMV beamformer caused by the introduced head model simplifications. Furthermore, the crosstalk induced by model simplifications might even lead to spurious connectivity for the GPDC. When using imaginary coherence (ICoh) (Nolte et al., 2004) instead of GPDC as a connectivity measure, the effects of the model simplifications were clearly decreased. However, in some regions still large relative errors for ICoh are visible and the patterns found are very similar to those of RDM and output SNR. It can thus be inferred that the results obtained by ICoh are also affected by imperfect head modeling, albeit less severely.

For the MEG on its own, the importance of the changing volume currents seems to be lower than for the EEG, since the main results were changes in signal magnitude, while the topography was strongly affected only for sources with a weak sensor signal. Indirectly, the results of Ahlfors et al. (2010) were confirmed and expanded, who showed that – similar to spherical head models – also in the classic three-compartment isotropic head model a source orientation to which the MEG is nearly insensitive exists. In the more realistic six-compartment anisotropic head model used here, the measured sensor signal in the MEG is still strongly influenced by source orientation and depth; namely being weak for quasi-radial and deep sources, while the dependency of the EEG on these parameters is much weaker. This shows the benefits of EEG for source analysis in a variety of scenarios despite the stronger interference of volume conduction effects.

Nevertheless, all of the discussed results, including those from this study, were gained under the assumption of point-like dipole sources. Since sources in practice might most often have an extent of at least some mm, not many purely quasi-radial sources at gyral crowns might exist in realistic scenarios. Hillebrand and Barnes (2002) for example concluded that source depth and not orientation is the main factor that compromises the sensitivity of MEG to activity in the adult human cortex. They argue that even if there are thin (approximately 2 mm wide) strips of poor MEG resolvability at the crests of gyri, these strips account for only a relatively small proportion of the cortical area and are abutted by elements with nominal tangential component and thus high resolvability due to their proximity to the sensor array. This study clearly showed that also in a six-compartment anisotropic head model the strips of poor MEG resolvability are rather thin (cf. Figure 3.15). The presented effects for the weak quasi-radial sources at gyral crowns might therefore not be relevant in practice. But, when aiming to evaluate EEG and MEG data simultaneously, these effects become much more important when trying to explain the multimodal measurement.

This study elaborates upon the results of Vorwerk et al. (2012) presented in Section 2.11.1, which already suggested that the effect of model simplifications can be much larger than the accuracy differences between the examined numerical approaches exemplarily for the CSF compartment. It demonstrates that also the effect of gray/white matter distinction or of

modeling the white matter anisotropy is clearly bigger than possible accuracy differences. Even the least influential modeling effect investigated in this study, the distinction of skull spongiosa/compacta, was still in the range of the numerical error between models *6CA* and *6CA_hr*.

In order to achieve a high practical relevance of our results, the number of sensors was not adjusted between modalities. Instead, realistic sensor configurations were used as they are currently applied in our lab, e.g., in epilepsy diagnosis (Aydin et al., 2014, 2015), since it can be assumed that these provide a sufficient spatial sampling (Ahonen et al., 1993; Grieve et al., 2004; Lantz et al., 2003) so that the different number of sensors does not significantly influence the results. Additionally, the influence of sensor coverage on the observed effects was investigated. When evaluating the effect of the distinction between skull spongiosa and skull compacta a possible relation between weak sensor coverage and an increased topography error was found, especially for the EEG. In practice, this issue can be addressed by using sensor caps reaching further downwards, thereby better covering the temporal lobe and the base of the frontal lobe.

3.2. The FieldTrip-SimBio Pipeline for EEG Forward Solutions

In the previous sections of this chapter the great importance of detailed volume conductor models for an accurate inverse analysis was demonstrated and especially the huge influence of distinguishing the compartments gray matter, white matter, and CSF instead of modeling a homogeneous brain compartment was shown. Tetrahedral head models – commonly generated based on triangulations of the compartment boundaries – allow the accurate modeling of compartments of almost arbitrarily complicated shape, e.g., the strongly folded interface between cortex and CSF. However, a frequently raised argument against the usage of realistic head models that include more than the commonly used three compartments in praxis is the high effort that is necessary to construct these (tetrahedral) head models. This is in huge parts caused by the restrictions that have to be fulfilled by the surface triangulations representing the compartment boundaries. These are mainly a necessity of the used model generation techniques such as the here applied constrained Delaunay tetrahedralization. The surfaces should be non-intersecting/touching and optimally have a certain distance between each other. The additional consideration of skull holes – be it naturally existing ones such as the foramen magnum or as a consequence of brain surgery – as it is suggested by Lanfer et al. (2012b); Montes-Restrepo et al. (2014), further complicates the model generation due to the more complicated compartment topologies. A possibility to simplify the head model generation is the use of hexahedral head models. Thereby, finite element meshes can be directly generated out of segmented images of the human head such as MR or CT images. When using regular hexahedra, this is achieved at the cost of a less accurate representation of the compartment interfaces, where so-called staircase effects may occur. These effects can be weakened by the use of geometry-adapted hexahedral meshes (Camacho et al., 1997; Wolters et al., 2007a). Examples for the use of geometry-adapted hexahedral meshes can, e.g, be

found in the studies of Aydin et al. (2014, 2015); Rullmann et al. (2009); Wagner et al. (2014); evaluations of the numerical accuracy achieved using geometry-adapted hexahedral meshes in sphere models were, e.g., performed by Vorwerk (2011); Wolters et al. (2007a). In this section, a MATLAB-based – and therefore multi-platform – pipeline is presented that was integrated in the FieldTrip-toolbox (http://www.fieldtriptoolbox.org) and allows for the easy computation of accurate solutions to the EEG forward problem using FE methods with automatically generated hexahedral head models. Therefore, it was necessary to provide tools to generate hexahedral multi-compartment finite element head models and to implement the Venant approach (cf. Chapter 2) from the SimBio-toolbox in MATLAB. Thereby, this pipeline also directly makes a further analysis, e.g., source reconstructions, possible using the functionality of the FieldTrip-toolbox. It is important to note that unlike implementing the generation of hexahedral meshes and the fully MATLAB-based computation of FEM forward solutions on multiple platforms, improving the segmentation algorithm was not a main goal of the work presented here. In the following, the basic implementation and workflow of the pipeline is sketched, the accuracy of forward solutions computed in a realistic five-compartment head model generated using this pipeline is evaluated, and an exemplary source reconstruction of somatosensory evoked potentials (SEP) is performed.

3.2.1. Implementation

The segmentation algorithm – even though a very basic one – distinguishing the five compartments white matter, gray matter, CSF, skull, and skin out of individual MRIs was already existing in the FieldTrip-toolbox, the additional implementation of two necessary features remained to make the computation of EEG forward solutions using realistic multi-compartment head volume conductor models possible: The generation of hexahedral meshes out of the segmented images and the computation of FEM forward solutions using these meshes. To achieve this, a set of low-level functions was generated, which were afterwards integrated into the high-level functions of the common FieldTrip workflow.

Hexahedral mesh generation

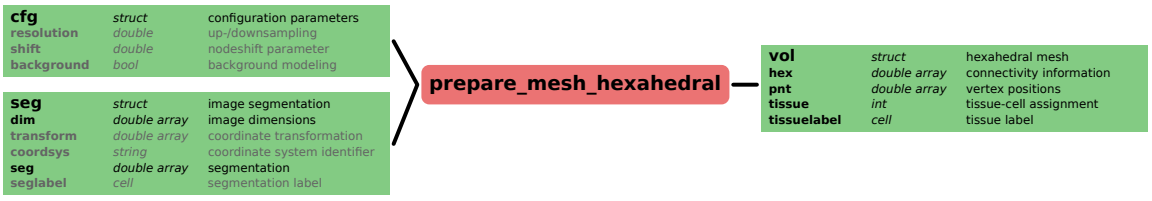

Figure 3.20.: Sketch of the function *prepare_mesh_hexahedral*. Not all possible input parameters are shown. Optional parameters are indicated by gray font. Green background indicates MATLAB structs, red background MATLAB functions.

For the generation of hexahedral meshes the function *prepare_mesh_hexahedral* was implemented; a sketch of the function call is shown in Figure 3.20. This function allows to generate hexahedral meshes directly out of segmented MR images. A basic segmentation can be

generated using the FieldTrip-toolbox, but also segmentations from other MATLAB-toolboxes such as SPM (http://www.fil.ion.ucl.ac.uk/spm/) or from commercial tools like BESA or Curry (after loading them to MATLAB) can be included. Further options for the mesh creation are the generation of geometry-adapted meshes following the approach proposed by Camacho et al. (1997); Wolters et al. (2007a), up-/downsampling of the image resolution, and modeling/not modeling the image background.

EEG forward solution computation

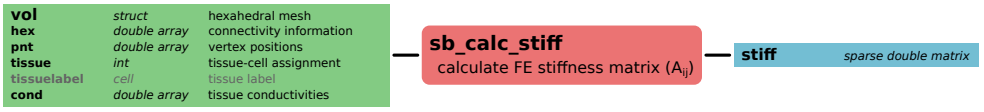

Figure 3.21.: Sketch of the function *sb_ calc_ stiff*. Not all possible input parameters are shown. Optional parameters are indicated by gray font. Green background indicates MATLAB structs, red background MATLAB functions, blue background matrices.

The next necessary step after the mesh generation was to enable the computation of FEM solutions to the EEG forward problem using a fully MATLAB-based multi-platform pipeline. Therefore, it is necessary to be able to calculate the stiffness matrix A (cf. Equation (2.12)). The goal was to easily enable the usage of the isoparametric FEM approach implemented in the SimBio-toolbox directly out of MATLAB. A *MATLAB Executable* (MEX-function) was implemented to enable a convenient execution of the core *Fortran*-functions of the SimBio-toolbox from within MATLAB. The MEX-function is written in Fortran and can be compiled on any platform for which a supported compiler is available (for supported compilers in MATLAB R2015b cf. http://de.mathworks.com/support/compilers/R2015b/index.html). The resulting function providing this functionality is *sb_ calc_ stiff*; a sketch of the function call is shown in Figure 3.21. Pre-compiled binaries of this function for, e.g, most Linux distributions, MAC OS X, and Windows XP/7/8 are available with the FieldTrip-toolbox.
The remaining necessary functions were directly implemented in the MATLAB script language, some of the implemented functions are (in alphabetic order)

sb_check_sources checks whether the source positions are valid, i.e., whether the mesh vertex next to the source position is fully inside the source compartment; takes the mesh geometry, the source positions, and the source compartment identifier as input, output is a boolean vector indicating whether the respective vertices are valid or not

sb_rhs_venant calculates the rhs-vector b^{ven} (cf. (2.24)); takes the mesh geometry and source position and direction as input, output is the rhs-vector b^{ven}

sb_set_bndcon sets the Dirichlet boundary conditions necessary to achieve a unique solution of (2.12); takes the stiffness matrix A, the rhs-vector b, the dirichlet nodes, and the dirichlet values as input, outputs are the corrected stiffness matrix $\tilde{A}$ and rhs-vector $\tilde{b}$

sb_solve solves the equation system (2.14) using an *IC(0)-CG*-solver; takes the output from *sb_set_bndcon*, i.e., the stiffness matrix $\tilde{A}$ and rhs-vector $\tilde{b}$, as input, output is the solution vector u

sb_transfer computes the EEG transfer matrix T^{eeg}; takes the stiffness matrix, the mesh geometry, and the sensor positions as input, output is the transfer matrix

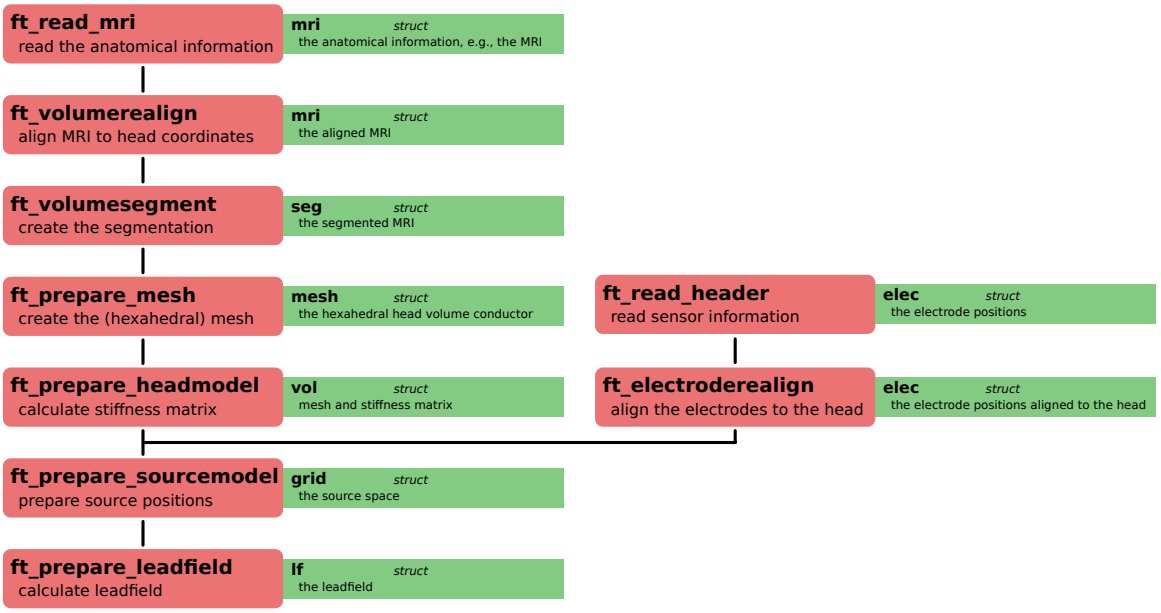

Figure 3.22.: Sketch of the FieldTrip-SimBio pipeline (workflow goes from top to bottom). Red background indicates MATLAB/FieldTrip-functions, green background the (main) output of the respective function.

These functions were integrated into the high-level functions of the FieldTrip-toolbox to create an easy-to-use pipeline for FEM-based EEG forward simulations. The resulting pipeline is sketched in Figure 3.22. Due to the FieldTrip workflow – which was originally designed for forward analysis using BEM or sphere models – the main computational effort, i.e., the setup of the transfer matrix, is not included in the function *ft_prepare_headmodel* as one might expect from Figure 3.22, instead only the stiffness matrix A is computed in this function. The transfer matrix T^{eeg} is subsequently computed in the function *ft_prepare_sourcemodel*, where the sensor information is available to the pipeline functions for the first time.

3.2.2. Evaluation

To evaluate the accuracy of the results gained with the FieldTrip-SimBio pipeline, the generation of a head model as performed in Section 3.1 was repeated with the same image data using this pipeline and afterwards the results of forward simulations were compared to those gained using the highly accurate tetrahedral head model generated in Section 3.1.

Methods

A five-compartment (white matter, gray matter, CSF, skull, and skin) hexahedral head model was generated based on the segmentation of a T1-MRI (cf. Subsection 3.1.1) using the FieldTrip-Simbio pipeline (Figure 3.22). This model is denoted *5CI_hex_ft* in the following. Instead of SPM8, which is the standard for brain segmentation in FieldTrip, SPM12 was used here, as it leads to a (at least visually) more accurate brain segmentation. Furthermore a *scalpthreshold* of 0.06 was chosen instead of the standard value 0.10 in the call to *ft_volumesegment*. The segmentations used to create model *5CI_hex_ft* along with the segmentation used to generate the models used in Section 3.1 are shown in Figure 3.23. For the generation of the hexahedral head model a node-shift of 0.3 was chosen.

Figure 3.23.: Original MRI (left), manually corrected segmentation (middle), and automatically generated segmentation using FieldTrip (right).

The electrode positions were aligned to the respective model surfaces and the source positions from Section 3.1 (cf. Figure 3.1, right) that are also valid source positions in the newly generated mesh (i.e., the mesh vertex next to the source position is fully inside the gray matter compartment) were selected; this led to 89,902 sources in the comparisons.
To classify the accuracy of the newly generated head model *5CI_hex_ft*, Figure 3.4 was expanded by displaying the deviation of this model from the reference solution additionally to the modeling effects, leading to Figure 3.24.

Results

Comparing the results of the segmentation visually (Figure 3.23), it is obvious that the main inaccuracies of the automatic segmentation are found for the skull mask, which is simply generated by a dilation of the inner skull surface in the FieldTrip-pipeline, and in the nose/mouth area, where the contrast of the original image is very bad. In contrast, the automatic segmentation of the brain compartments seems to be accurate, possibly even more accurate than the previously generated and manually corrected segmentation underlying the tetrahedral head model, where a minimal distance between outer brain and inner skull surface had to be assured to enable the tetrahedralization and the ventricles were modeled as white matter to achieve a closed topology of the surfaces.

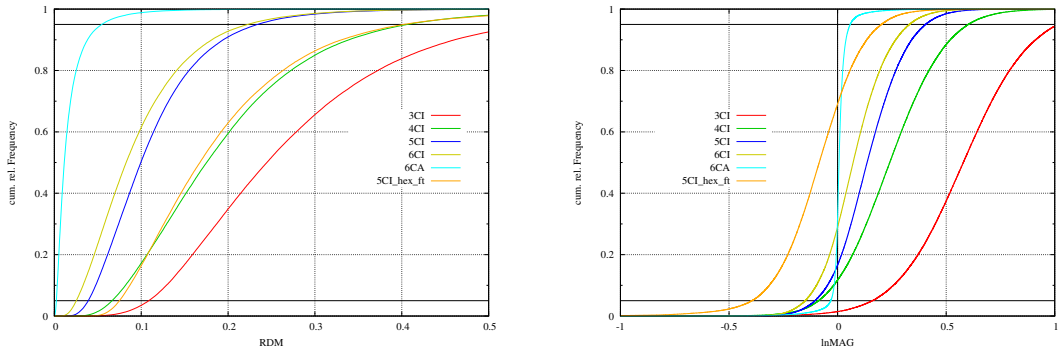

Figure 3.24.: Cumulative relative frequencies of RDM (left) and lnMAG (right) effects (cf. Figure 3.4) and error of model *5CI_hex_ft* for EEG with model *6CA_hr* as reference.

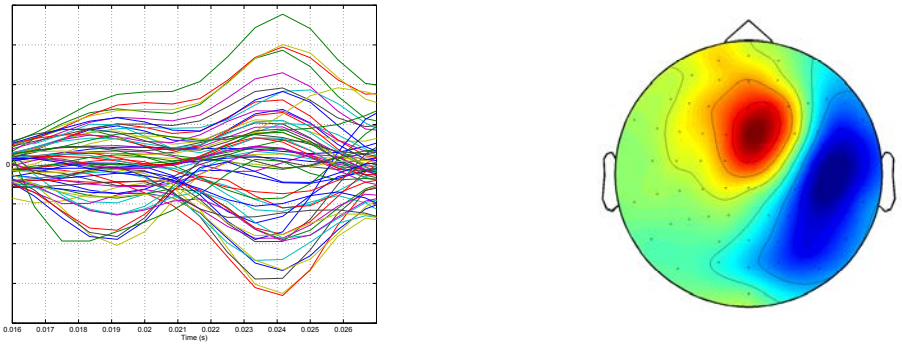

Figure 3.25.: Butterfly plot of preprocessed SEP data (+16 to +27 ms, left) and peak topography (24 ms, right).

In Figure 3.24, the deviation of the forward solutions computed with model *5CI_hex_ft* in comparison to the modeling effects is depicted, augmenting Figure 3.4. With regard to the RDM, the values are similar to those of model *4CI*, i.e., a four-compartment model distinguishing skin, skull, CSF, and brain. Looking at the lnMAG, the hexahedral model shows a tendency towards an underestimation of source magnitudes, about 70% of the sources have a negative lnMAG value and 90% of the lnMAG values are in the range from -0.4 to 0.2. The error range is similar to model *5CI*.

3.2.3. Source Localization of SEP Data

Finally, to perform an actual source reconstruction and test the FieldTrip-SimBio pipeline from start to finish, a subject dataset was measured including MRI data and somatosensory evoked potentials (SEP).

A T1-weighted (T1w-)MRI scan of a healthy 23-year-old male subject was acquired with a 3 T MR scanner (Magnetom Prisma, Siemens, Munich, Germany) using a 32-channel head coil. An MP-RAGE pulse sequence (TR/TE/TI/FA = 2300 ms/3.5 ms/1100 ms/8°, FOV = 256 × 256 × 192 mm, voxel size = 1 × 1 × 1 mm) with water selective excitation was used. 80

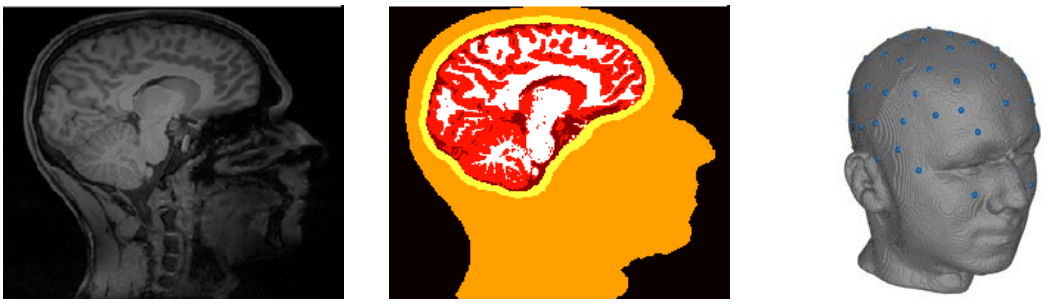

Figure 3.26.: Original MRI (left), segmentation (middle), and hexahedral mesh with aligned electrodes (right).

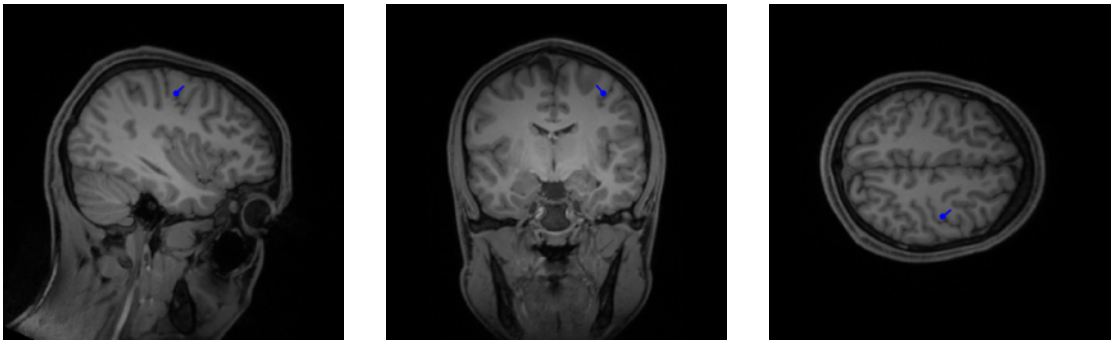

Figure 3.27.: Result of source analysis of SEP data.

channel EEG and electrocardiography (ECG) were measured simultaneously. The EEG cap had 74 Ag/AgCl sintered ring electrodes placed equidistantly according to the 10-10 system (EASYCAP GmbH, Herrsching, Germany). In addition to those 74 electrodes, 6 additional channels were available and used for both eye movement detection (with a bipolar software montage) and as additional EEG channels for source reconstruction. The electrode locations were digitized with a Polhemus Fastrak system (Polhemus Incorporated, Colchester, Vermont, U.S.A.) prior to the measurement. The patient was measured in lying position to avoid erroneous CSF effects due to brain shift when combining EEG and MRI following the results of Rice et al. (2013). To generate somatosensory evoked potentials (SEP), one measurement run with electrical stimulation of the left median nerve and varying inter-stimulus intervall (ISI) to avoid habituation (ISI: 350 ms to 450 ms, pulse duration 0.5 ms) was recorded at a frequency of 1200 Hz, resulting in 967 trials.

The EEG data were preprocessed using the FieldTrip-functions *ft_preprocessing*, *ft_rejectvisual*, and *ft_timelockanalysis*. Using *ft_preprocessing* a 20 Hz high pass filter, a 250 Hz low pass filter, and a discrete fourier transform (DFT) filter for line noise removal at frequencies of 50, 100, and 150 Hz were applied. A baseline correction was performed using the window from 150 ms to 50 ms before stimulus onset. *ft_rejectvisual* was used to reject bad channels and artifacts, e.g., due to eye-blinks. 10 channels (C4, Pz, FC2, CP2, F1, C2, P6, AF8, TP8, PO7) and 104 trials were rejected, thus resulting in 64 channels available for source reconstruction and 863 trials for signal averaging. Finally, a time-locked average of the

trials was computed with *ft_timelockanalysis*. A butterfly plot and the peak topography of the resulting data are shown in Figure 3.25.

Following the pipeline sketched in Figure 3.22, a hexahedral five-compartment head model was generated. Again, a *scalpthreshold* of 0.06 was chosen instead of the standard value 0.10 for *ft_volumesegment*. The resulting segmentation and the mesh with aligned electrodes are shown in Figure 3.26. In the call of *ft_prepare_sourcemodel* a grid resolution of 2 mm was chosen for the source space.

Finally, the *P20 component* was localized at the peak (i.e., at +24 ms, cf. Buchner et al., 1994) using the function *ft_dipolefitting*, which performs a goal function/dipole scan (when choosing the parameter *cfg.nonlinear = 'no'*). The result of the source reconstruction is shown in Figure 3.27, the *goodness of fit* (GoF)-value was 0.963 (optimal value is 1).

3.2.4. Further Applications in Brain Research

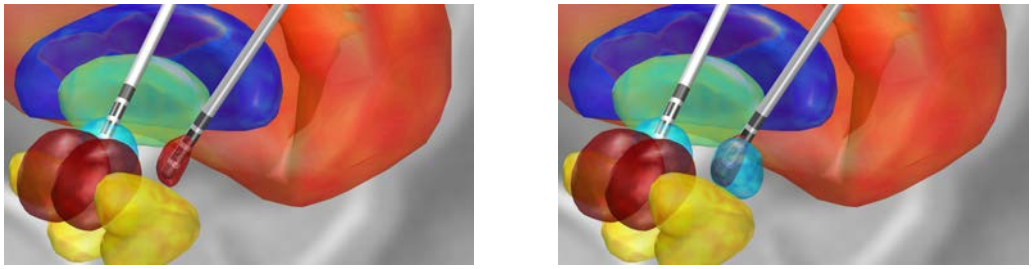

Figure 3.28.: Visualizations of volume of activated tissue (VAT, dark red, tip of right electrode) for deep brain stimulation of subthalamic nucleus (cyan, left image only). Bipolar stimulation of lowermost, i.e., first, contact (-3 V) and second contact (+3 V). Furthermore, nucleus ruber (dark red), striatum (orange), external globus pallidus (dark blue), internal globus pallidus (green), and subtantia nigra (yellow) are shown.

The integration of the FEM approach into the MATLAB-based FieldTrip-pipeline also allows for the easy application in other areas of bioelectric research, e.g., *deep brain stimulation* (DBS) or *transcranial direct/alternating current stimulation* (tDCS/tACS). To achieve this, it is only necessary to change the boundary conditions and right-hand side vectors applied in the derivation (Section 2.1, Equation (2.12)). The possibility to simulate the effects of DBS using highly realistic volume conductor models was integrated into the *LEAD-DBS*-toolbox (http://www.lead-dbs.org/). FEM was previously used to simulate the effects of deep brain stimulation, e.g., by Butson et al. (2007); Chaturvedi et al. (2010); Schmidt and van Rienen (2012). Simulations of DBS effects gained using LEAD-DBS are shown in Figure 3.28. Furthermore, also the MATLAB-based simulation of tDCS stimulation is possible, corresponding to the approach used in Wagner et al. (2014). Examples are shown in Figure 3.29. These results shall not be further discussed here as DBS and tDCS are not in the scope of this thesis.

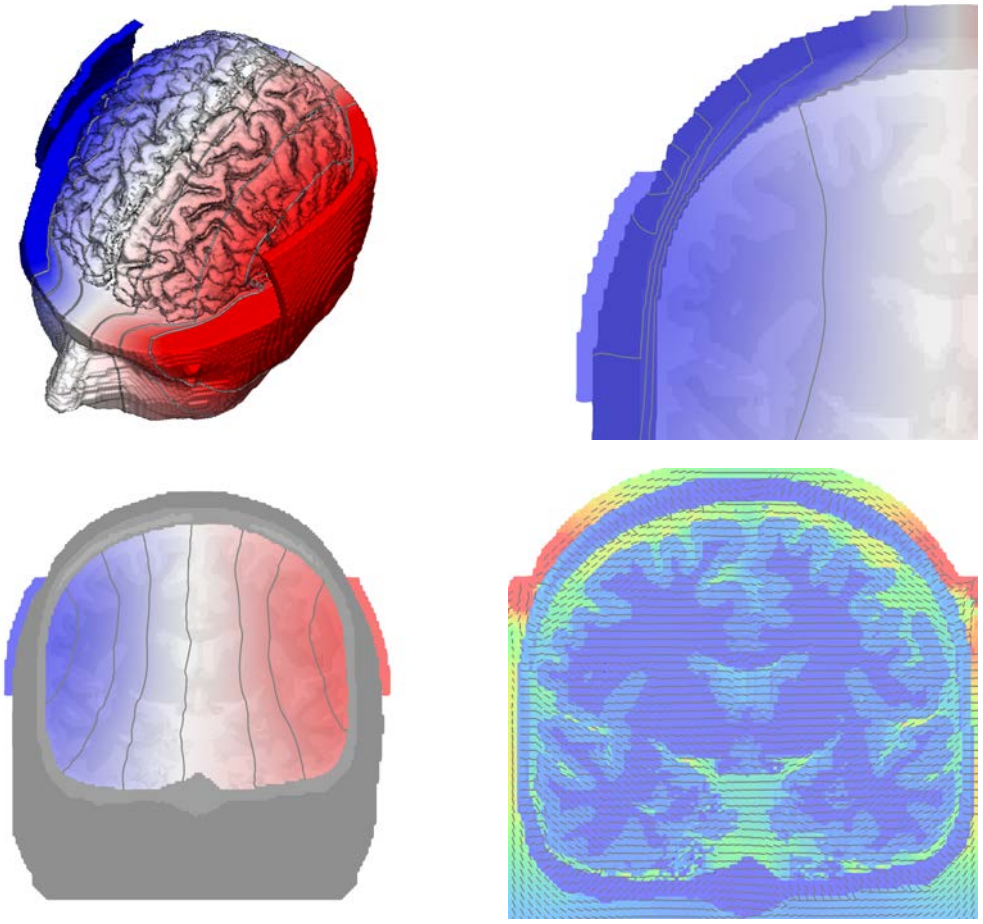

Figure 3.29.: Visualizations of auditory cortex tDCS. Visualization of surface potential with isovalue lines, skin and skull clipped at $z = 140$ plane (top left), detail of potential at cathode in $y = 128$ plane with isopotential lines (top right), potential in CSF, gray, and white matter in $y = 128$ plane with isopotential lines (bottom left), and visualization of injected currents in $y = 128$ plane, short gray lines indicate direction of the current and the color-coding the current strength (bottom right). In all potential visualizations blue coloring corresponds to negative values, red coloring to positive ones; for current visualization blue coloring corresponds to smaller current strength, red coloring to larger current strength.

3.2.5. Discussion

In this section, the FieldTrip-SimBio pipeline for finite element EEG forward computations in MATLAB was presented and evaluated. This pipeline was implemented to allow for the easy computation of EEG forward solutions using basic five-compartment (skin, skull, CSF, gray matter, and white matter) hexahedral head models. The accuracy that can be achieved with such a simplified head model in comparison to the highly accurate model used in Section 3.1 was evaluated and an exemplaric source reconstruction of SEP-data using this pipeline was shown.

As already mentioned in the introduction, only few work was invested so far to improve the accuracy of the MRI segmentation. Major differences are found for the segmentation of the skull and the segmentation of the brain compartments (compare Figures 3.23 and 3.26).

The skull segmentation is generated by a dilation of the inner skull/outer brain surface in the FieldTrip-SimBio pipeline, which is a very simple, but robust approach. This results in a constant skull thickness and thereby a missestimation of the original skull thickness in many areas, which is unfavorable due to the major influence of an accurate modeling of the skull on EEG forward solutions, as it was discussed in Section 3.1. However, the open structure of the pipeline also allows the user to include the possibly more accurate skull segmentations from other toolboxes such as SPM (http://www.fil.ion.ucl.ac.uk/spm/), FSL (http://fsl.fmrib.ox.ac.uk/fsl/fslwiki/), or BrainSuite (http://brainsuite.org). A comparison study including these toolboxes was conducted by Kazemi and Noorizadeh (2014). A main cause for the differences in the brain segmentation were the restrictions of the tetrahedral mesh generation, which requires a sufficient distance between inner skull and outer brain surface. As the huge effect of the varying CSF thickness due to the movement of the brain with changing body position of the subject was shown by Rice et al. (2013), hexahedral meshes possibly even allow for a more realistic modeling in this aspect as they allow realistically touching skull and brain compartments. The inaccurate segmentation of the nose/mouth area with FieldTrip should only have a minor influence as the model is nevertheless not cut off directly below the skull following the results of Lanfer et al. (2012b). Furthermore, this problem only occured for the specific dataset used in the comparison study, while the scalp surface could be nicely estimated using the FieldTrip-SimBio pipeline in Section 3.2.3 (cf. Figure 3.26). Thus, this might rather be a problem of the recorded MRI than of the segmentation algorithm.

When comparing the head model generated using this pipeline with the simplified head models generated in Section 3.1, the simple five-compartment model *5CI_hex_ft* performs about as good as the tetrahedral model *4CI* with regard to the RDM (Figure 3.24), i.e., the effect of using the simple five-compartment model is as big as that of neglecting the differentiation between gray and white matter (Figure 3.24). As no manual corrections were applied for the segmentation, this can be considered a button-press pipeline. Thus, given the negligible amount of time invested in the model generation and the big influence of the highly-conductive CSF compartment on the EEG forward solution that was already discussed in Section 3.1, this is a quite remarkable result.

Finally, in Section 3.2.3 it was demonstrated that this pipeline can actually be applied to evaluate real data. The results of the localization of SEP generated by medianus nerve stimulation are in line with the literature results (cf. Figure 3.27; Buchner et al., 1994).

3.3. Conclusion

In Section 3.1 it was shown that a realistic modeling of the volume conductor has strong effects on both EEG and MEG forward simulations that should be taken into account. Especially for superficial sources, which were often assumed to be less affected by volume conduction effects than deep sources, the strongest changes with regard to signal topography and magnitude were found. The following recommendations can be concluded for an accurate EEG/MEG forward simulation:

***a)* CSF** This study systematically showed the importance of including the highly conductive CSF as a separate compartment in the volume conductor for both EEG and MEG. This step only requires moderate additional effort in the segmentation procedure.

***b)* Gray/white matter distinction** The same conclusions as for the CSF hold true for the gray/white matter distinction. Strong effects were found for this modeling step, while the additional amount of work for including gray/white matter distinction into a volume conductor model is at a reasonable level.

***c)* White matter anisotropy** The inclusion of white matter anisotropy showed smaller (but still significant) effects than a) and b). However, the complexity of modeling anisotropy and the limitations of the underlying model have to be taken into account. Therefore, not modeling white matter anisotropy can be concluded to be admissible unless the last doubts in a realistic modeling of white matter anisotropy (sufficient DTI resolution, appropriate scaling between diffusion and conductivity tensors) have been eliminated.

***d)* Skull** The distinction between skull compacta and spongiosa showed weak effects especially for the MEG. Thus, it might in most cases be disregarded for the MEG. For the EEG, distinguishing different skull compartments is clearly less important than the previously mentioned modeling steps, especially when using an optimized conductivity value for the homogenized skull. However, the otherwise high importance of an accurate modeling of the skull was shown in a variety of studies and was therefore not in the focus of this study. The influence of the uncertainty in the skull conductivity values found in the literature should not be underestimated and a conductivity calibration should be considered (Aydin et al., 2014, 2015; Aydin, 2015; Lew et al., 2007, 2009a).

In summary, the study performed in Section 3.1 shows the most reasonable steps one should take to expand the commonly used three-layer head model by additional compartments. Furthermore, this study demonstrates that the numerical inaccuracies of the used finite element approach appear to be negligible compared to these modeling effects.
However, despite the advantages of highly-realistic multi-compartment volume conductor models, the issue of the often high workload to create these models remained, especially for tetrahedral models. To allow the practical use of FEM approaches for EEG source analysis on several platforms, the FEM originally implemented in SimBio was integrated in a FieldTrip-pipeline. It was shown that an automatically generated five-compartment head model achieved a reasonable accuracy that is clearly superior to the accuracy of the commonly used three compartment head models. Furthermore, the analysis of SEP-data using this pipeline was demonstrated in Section 3.2.3 and the obtained results are in line with the literature.
Finally, in Section 3.2.4 examples were shown that the used FEM approach – and thereby also the results gained in its analysis in the current and previous chapter – is not limited to the use in source analysis, but can also be easily applied in other fields of bioelectric research such as deep brain stimulation or transcranial current stimulation.

4

The Discontinuous Galerkin Finite Element Method

The conforming finite element approaches introduced in Chapter 2 achieve a high numerical accuracy using hexahedral and tetrahedral meshes in both sphere and realistic head model scenarios. In Chapter 3, tetrahedral meshes generated by constrained Delaunay tetrahedralizations (CDT) from given tissue surface representations were used (Lew et al., 2009b; Vorwerk et al., 2014). These have the advantage that smooth tissue surfaces are well represented by the model. Also the drawbacks of CDT modeling were mentioned. The generation of such models is difficult in practice and might cause unrealistic model features, e.g., holes in tissue compartments such as the foramen magnum and the optic canals in the skull are often artificially closed to allow CDT meshing. Furthermore, CDT modeling necessitates nested surfaces, while in reality surfaces might touch, like for example the inner skull and outer brain surface. Hexahedral models do not suffer from such limitations, can be easily generated from voxel-based magnetic resonance imaging (MRI) data as shown in Chapter 3, and are more and more frequently used in source analysis applications (Aydin et al., 2014; Rullmann et al., 2009). However, when aiming to apply hexahedral meshes in praxis, for certain geometries unwanted effects might occur. More specifically, when the segmented skull compartment is in some areas so thin that mesh elements corresponding to the originally separated compartments in- and outside the skull (usually CSF or gray matter and skin) touch in single vertices (cf. Figure 4.1), an unphysical *leakage of volume currents* through these vertices may occur (Sonntag et al., 2013). This leads to a distortion of the simulated surface potentials, since the skull in reality functions as a low-conducting barrier between the higher conducting compartments (except for the actually existing skull openings of course). This behaviour is a consequence of certain properties of the CG-FEM that was applied to simulate the potential u. While this method enforces the continuity of the potential u, it

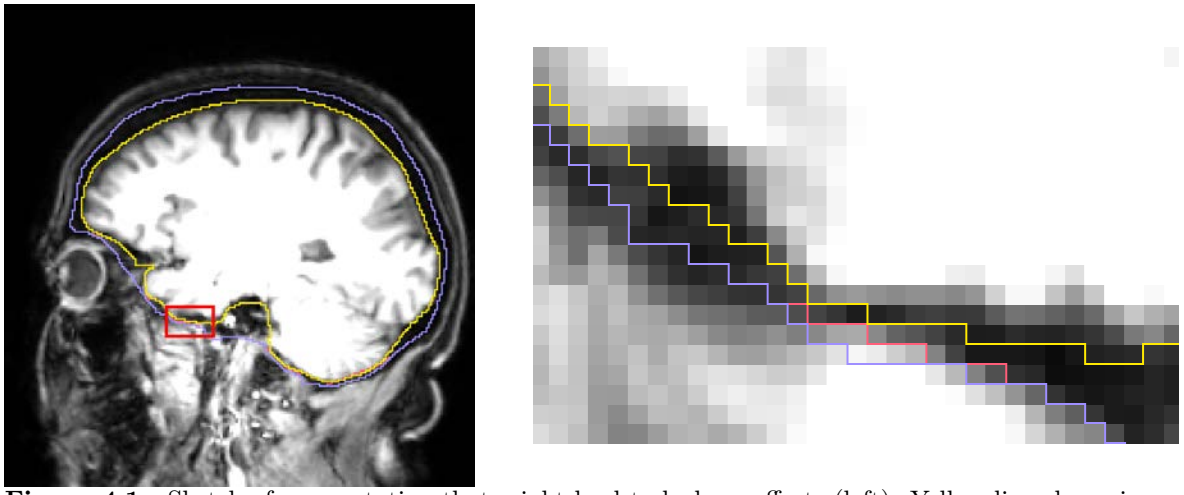

Figure 4.1.: Sketch of segmentation that might lead to leakage effects (left). Yellow line shows inner skull surface, red line original outer skull surface, blue line corrected outer skull surface. Where the red and the blue line overlap, only the blue line is visible. In the magnified detail scalp and CSF show two erroneous connections via single vertices or edges (right subfigure, where red and yellow lines touch each other). *Source: Engwer et al. (submitted)*

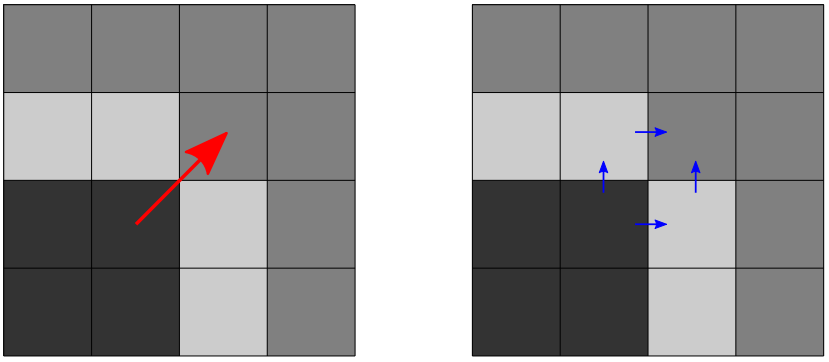

Figure 4.2.: Illustration of current flow/leakage effect for CG-FEM (left) and DG-FEM (right). While for the CG-FEM an "unphysical" current flow through a single vertex occurs, the DG-FEM only allows current flow over faces. *Source: Engwer et al. (submitted)*

does not control for a realistic flow of the volume currents $\mathbf{j}$, i.e., with a continuous normal component over element faces and fulfilling the important physical property of *conservation of charge*. This behaviour is directly connected to the choice of trial and test functions (cf. Section 2.1, Equation (2.7)). As these are supported on all elements containing a single vertex, this leads to a *mixing of conductivities* when the entries of the stiffness matrix are computed (cf. Equation (2.10)), thereby to inadequately high matrix entries for these functions, and finally to current leakage "through" single vertices (cf. illustration in Figure 4.2, left).

Two main options to prevent these leakages exist when using finite element methods that rely on a representation of the geometry through an unstructured volumetric mesh, as it is the case in this thesis. Either the volume conductor model has to be adapted to prevent this unwanted behaviour of the numerical method or the method has to be modified, so that a realistic simulation of the volume currents is enforced. Adapting the volume conductor model would usually mean to either artificially thicken the skull in the affected areas or to increase

the resolution of the segmentation locally or globally. Thickening the skull in the volume conductor model would cause a deviation of the model from the segmented geometry and thereby decrease the accuracy of the simulation. A global refinement of the segmentation would require a higher resolution of the underlying image data and is therefore usually not practically feasible. A locally refined segmentation could be achieved by involving data gained with zoomed MRI technology in the segmentation (Blasche et al., 2012). However, this opposes the goal of an as simple as possible pipeline for mesh generation and leads to meshes that either have a very fine resolution, and a thereby strongly increased computational effort, or are no longer admissible (cf. Definition 2) as they include hanging nodes, which again complicates the numerical treatment.

In the following, two numerical methods that fulfill the goal of a realistic modeling of the volume currents are introduced and evaluated, the *discontinuous Galerkin finite element method* (DG-FEM) and a method based on *mixed finite elements* (Mixed-FEM or M-FEM). In this chapter, the DG-FEM is introduced and evaluated. This method has the advantageous feature of being locally charge preserving and controlling for the current flow through element faces and thereby preventing possible leakage effects. An illustration of the conceptual difference in current simulation between CG- and DG-FEM is shown in Figure 4.2. To achieve this, the previously used vertex-based trial and test functions, which are supported on multiple elements of possibly varying conductivity, are replaced by functions that are only supported on a single element each. The coupling between the elements is then introduced by controlling the normal current over element faces. The chosen functions are not in the space $H^1(\Omega)$, where we expect the solution, so that this approach is not conforming. In general, this approach does not result in a continuous solution for the potential u. However, the discontinuities between elements can be controlled by including additional terms in the problem formulation that penalize jumps of the potential at the element boundaries. The previously derived subtraction and partial integration approach can be easily adapted to the DG-framework.

In the following, the theoretical basics of the DG-FEM are derived and the subtraction and partial integration approach are formulated in this framework. Subsequently, the implementation of these approaches in the *DUNE-toolbox* (http://www.dune-project.org) is shortly described and they are evaluated in comparison to the implementations based on the CG-FEM. Therefore, both common sphere models with a geometry as it was introduced in Chapter 2 (cf. Table 2.2) and sphere models with a reduced thickness of the skull compartment in order to provoke leakages are used. Furthermore, the current flow for both CG- and DG-FEM for a single source scenario is visualized in models with differing skull thicknesses to allow for a better understanding of the effect of skull leakages. Parts of this chapter are cited from Engwer et al. (submitted), which was submitted for publication.

4.1. Derivation

The historic idea that later led to the formulation of DG methods was proposed by Lions (1968) to solve elliptic problems with very rough Dirichlet boundary data. Instead of directly

enforcing the boundary conditions by the definition of the space of trial functions v, as it was usually done, it was proposed to weakly enforce the Dirichlet boundary conditions by means of adding a penalty term in the weak formulation of the underlying PDE (Arnold et al., 2002; Lions, 1968). For example, instead of solving the Dirichlet problem $-\Delta u = f$ in Ω with boundary condition $u = g$ on $\partial\Omega$, the boundary condition is replaced by the Robin boundary condition $u + \mu^{-1}\partial_{\mathbf{n}} u = g$ with a large penalty parameter $\mu > 0$. This boundary condition is then weakly enforced by an additional term in the weak formulation of the problem (cf. Equation (1.12)), penalizing deviations from the original boundary conditions:

$$\int_\Omega \langle \nabla u, \nabla v \rangle \,\mathrm{d}x + \int_{\partial\Omega} \mu(u-g)v \,\mathrm{d}x = \int_\Omega fv \,\mathrm{d}x \quad \text{for all } v \in H^1(\Omega). \tag{4.1}$$

The Dirichlet boundary condition is fulfilled for the limit case $\mu \to +\infty$, even though the trial functions v do not satisfy it. The DG approach founds on the observation that – just as the exterior boundary conditions – also the interior boundary conditions can be enforced in this way. These could, e.g., be the interelement continuity of the solution, in our case the continuity of the potential u or the continuity of the normal component of the current $\mathbf{j}$. These quantities are called *numerical fluxes*. In the following, it is shown that a DG formulation has advantageous properties such as consistency and conservation of the numerical fluxes. Therefore, one often aims to choose a numerical flux such that it can be linked to a conserved physical property, e.g., the electric charge. Depending on the actual definition of the numerical fluxes, different DG methods with specific properties with respect to stability and accuracy can be derived (Hartmann, 2008). For a more detailed discussion of the historical motivation and a general description of theory and applications of DG methods, it is referred to Arnold et al. (2002). Some general properties of DG-FEM in comparison to CG-FEM are discussed and illustrated in Ludewig (2013).

4.1.1. A Weak Formulation

Prior to the derivation, some basic notations are introduced in the following. For a triangulation $\mathcal{T}$ (cf. Definition 2), the *internal skeleton* is defined by

$$\Gamma_{\text{int}} = \{\gamma_{e,f} = \partial T_e \cap \partial T_f \mid T_e, T_f \in \mathcal{T},\, T_e \neq T_f,\, |\gamma_{e,f}| > 0\} \tag{4.2}$$

and correspondingly the *skeleton* is defined by $\Gamma = \Gamma_{\text{int}} \cup \partial\Omega$. Furthermore, the *broken Sobolev spaces* on a partition $\mathcal{T}$ of Ω are defined:

$$\begin{aligned} W^{k,p}(\mathcal{T}) &\coloneqq \left\{ v \in L^2(\Omega) : v|_T \in W^{k,p}(T) \text{ for all } T \in \mathcal{T} \right\}, \\ H^k(\mathcal{T}) &\coloneqq W^{k,2}(\mathcal{T}). \end{aligned} \tag{4.3}$$

Unlike the spaces $W^{k,p}(\Omega)$ and $H^k(\Omega)$, the elements of $W^{k,p}(\mathcal{T})$ and $H^k(\mathcal{T})$ may admit jumps at the boundary of the partition elements also for $k > 0$. The broken Sobolev spaces are indicated by the explicit reference to a triangulation $\mathcal{T}$, i.e., by writing $W^{k,p}(\mathcal{T})$ or $H^k(\mathcal{T})$. In

the following derivation, an admissible triangulation $\mathcal{T}_h(\Omega)$ and a for now not further specified general space of test and trial functions are assumed, possibly $V = H^k(\mathcal{T}_h(\Omega))$, $k > 0$.
Instead of following the original idea of a derivation by enforcing boundary conditions along element interfaces, a less formal but easier accessible approach via Gauss's theorem (integration by parts) is chosen here. In Section 1.3, it was mentioned that the weak formulation (1.12) of the classical forward problem (1.11) can be derived by testing with a test function v and subsequently applying integration by parts. Repeating this with the here chosen space of test functions V, the (possible) discontinuities across element boundaries of the elements of V lead to the additional occurence of (non-zero) terms on the internal skeleton Γ_{int}. Following, a general DG formulation of (1.11) exploiting the homogeneous Neumann boundary conditions is derived. The derivation of the partial integration approach is then straight-forward, for the subtraction approach this formulation has to be modified to also consider the non-zero terms on the outer boundary $\partial\Omega$.
Let u be a solution of (1.11), we test with $v \in V$

$$-\int_\Omega (\nabla \cdot \sigma \nabla u) v \,\mathrm{d}x = \int_\Omega f v \,\mathrm{d}x. \tag{4.4}$$

Since v might be discontinuous, integration by parts cannot be applied globally on Ω. Instead, it is applied on each element $E \in \mathcal{T}_h(\Omega)$, where v is by construction in $H^k(E)$, separately. On the left hand side we obtain

$$\begin{aligned}
\text{lhs} &= -\int_\Omega (\nabla \cdot \sigma \nabla u) v \,\mathrm{d}x \\
&= -\sum_{T_e \in \mathcal{T}_h} \int_{T_e} (\nabla \cdot \sigma \nabla u) v \,\mathrm{d}x \\
&= \int_\Omega \langle \sigma \nabla u, \nabla v \rangle \,\mathrm{d}x - \sum_{T_e \in \mathcal{T}_h} \int_{\partial T_e} \langle \sigma \nabla u, \mathbf{n} \rangle v \,\mathrm{d}s \\
&= \int_\Omega \langle \sigma \nabla u, \nabla v \rangle \,\mathrm{d}x - \int_{\partial\Omega} \underbrace{\langle \sigma \nabla u, \mathbf{n} \rangle}_{=0^{(*)}} v \,\mathrm{d}s \\
&\quad - \sum_{\gamma_{e,f} \in \Gamma_{\text{int}}} \left(\int_{\gamma_{e,f} \cap \partial T_e} \langle \sigma \nabla u, \mathbf{n}_{e,f} \rangle v \,\mathrm{d}s + \int_{\gamma_{e,f} \cap \partial T_f} \langle \sigma \nabla u, \mathbf{n}_{f,e} \rangle v \,\mathrm{d}s \right),
\end{aligned} \tag{4.5}$$

where $\mathbf{n}_{e,f}$ denotes the outwards pointing normal unit vector on the boundary of T_e to T_f, i.e., pointing from T_e to T_f.
The sum over all element boundaries is split into the domain boundary and all internal edges, each being visited twice, once from left and once from right. The electric current $(*)$ through the boundary is fixed by the homogeneous Neumann boundary conditions in (1.11).
To simplify the above expressions, additional notations following Arnold et al. (2002) are introduced, the *jump operators*

$$[x]_{e,f} \coloneqq x|_{\partial T_e} - x|_{\partial T_f} \qquad [\![x]\!]_{e,f} \coloneqq x|_{\partial T_e}\mathbf{n}_{e,f} + x|_{\partial T_f}\mathbf{n}_{f,e} \tag{4.6}$$

and on boundary edges $\partial T_e \cap \partial\Omega \neq \emptyset$

$$[x]_e \coloneqq x|_{\partial T_e} \qquad [\![x]\!]_e \coloneqq x|_{\partial T_e}\mathbf{n}_{\partial\Omega} \tag{4.7}$$

and the *average operator*

$$\{x\}_{e,f} \coloneqq \omega_{e,f}x|_{\partial T_e} + \omega_{f,e}x|_{\partial T_f} \qquad \{x\}_e \coloneqq x|_{\partial T_e} \tag{4.8}$$

of a piecewise continuous function x on the interface $\gamma_{e,f}$ between two adjacent elements T_e and T_f. We have the relation $\mathbf{n}_{e,f}[x] = [\![x]\!]$. Both jump and average operators can easily be generalized for arbitrary interfaces γ that allow the definition of a surface normal $\mathbf{n}$. The weights $\omega_{e,f}$ and $\omega_{f,e}$ could, e.g., be chosen to be the arithmetic mean. However, Ern et al. (2009) have shown that a conductivity-dependent choice is optimal in the case of heterogeneous, isotropic conductivities σ:

$$\omega_{e,f} \coloneqq \frac{\sigma_f}{\sigma_f + \sigma_e} \quad \text{and} \quad \omega_{f,e} \coloneqq \frac{\sigma_e}{\sigma_e + \sigma_f} \tag{4.9}$$

with $\sigma_e = \sigma(\mathbf{x})|_{\partial T_e}$, $\sigma_f = \sigma(\mathbf{x})|_{\partial T_f}$. Jump and average operator fulfill the following multiplicative property

$$[\![xy]\!]_{e,f} = [\![x]\!]_{e,f}\{y\}_{e,f} + \{x\}_{e,f}[\![y]\!]_{e,f}. \tag{4.10}$$

(4.5) can now be rewritten and we obtain

$$\text{lhs} = \int_\Omega \langle\sigma\nabla u, \nabla v\rangle \,\mathrm{d}x - \int_{\Gamma_{\text{int}}} [\![(\sigma\nabla u)v]\!] \,\mathrm{d}s.$$

With the multiplicative property (4.10) follows

$$\text{lhs} = \int_\Omega \langle\sigma\nabla u, \nabla v\rangle \,\mathrm{d}x - \int_{\Gamma_{\text{int}}} \underbrace{[\![\sigma\nabla u]\!]}_{=0}\{v\} + \{\sigma\nabla u\}[\![v]\!] \,\mathrm{d}s, \tag{4.11}$$

exploiting that the electrical current should be continuous over element boundaries by definition (and of course also by physics) and thus $[\![\sigma\nabla u]\!] = [\![\mathbf{j}]\!] = 0$. Defining

$$\tilde{a}(u,v) \coloneqq \int_{\Omega} \langle \sigma \nabla u, \nabla v \rangle \,\mathrm{d}x - \int_{\Gamma_{\mathrm{int}}} \{\sigma \nabla u\} \, [\![v]\!] \,\mathrm{d}s, \tag{4.12}$$

$$l(v) \coloneqq \int_{\Omega} f v \,\mathrm{d}x, \tag{4.13}$$

one has the weak formulation

$$\text{Find } u \in V, \text{ such that} \quad \tilde{a}(u,v) = l(v) \quad \text{ for all } v \in V. \tag{4.14}$$

A subscript DG for $\tilde{a}$ and l is dispensed in the following for the sake of simplicity, despite competing previous definitions in Chapter 2. The formulation (4.14) is by construction consistent with the strong problem (1.11), however, it does not show adjoint consistency, i.e., consistency of the adjoint problem, and is not stable since it lacks coercivity. As discussed by Arnold et al. (2002), consistency of the adjoint problem is important to ensure conservation properties, i.e., the conservation of charge in the present case, as it is directly linked to conservation properties of the discrete fluxes. The conservation of charge is equivalent to the continuity of the electric current $\mathbf{j}$ $(= \sigma \nabla u)$:

$$\int_{\partial K} \sigma \partial_{\mathbf{n}} u \,\mathrm{d}s = \int_{K} f \,\mathrm{d}x, \tag{4.15}$$

for any control volume $K \subseteq \Omega$. Furthermore, adjoint consistency is necessary to obtain optimal L^2-error estimates, where a duality argument has to be used (Arnold et al., 2002). A lack of adjoint consistency leads to non-smooth adjoint solutions and a sub-optimal convergence (Harriman et al., 2003; Hartmann, 2007). In the context of inverse problems, the adjoint approach can be used to reduce the computational effort (Vallaghé et al., 2009) and is closely linked to the transfer matrix approach. In both cases the discrete representation of the adjoint operator is needed and for the transfer matrix approach also a self-adjoint/symmetric operator (cf. Section 2.9). Coercivity is necessary to ensure existence and uniqueness of the solution.

To gain adjoint consistency, symmetry of the operator $\tilde{a}$ has to be achieved by adding the term

$$\tilde{a}^{sym}(u,v) \coloneqq - \int_{\Gamma_{\mathrm{int}}} \{\sigma \nabla v\} \, [\![u]\!] \,\mathrm{d}s, \tag{4.16}$$

and we define

$$\begin{aligned} a(u,v) &= \tilde{a}(u,v) + \tilde{a}^{sym}(u,v) \\ &= \int_{\Omega} \langle \sigma \nabla u, \nabla v \rangle \,\mathrm{d}x - \int_{\Gamma_{\mathrm{int}}} \{\sigma \nabla u\} \, [\![v]\!] + \{\sigma \nabla v\} \, [\![u]\!] \,\mathrm{d}s. \end{aligned} \tag{4.17}$$

To obtain coercivity, the left-hand side is supplemented with the additional penalty term

$$J(u,v) = \eta \int_{\Gamma_{\text{int}}} \frac{\hat{\sigma}_\gamma}{h_\gamma} [\![u]\!][\![v]\!] \,\mathrm{d}s, \tag{4.18}$$

where h_γ and $\hat{\sigma}_\gamma$ denote local definitions of the mesh width and the electrical conductivity on an edge γ, respectively. This penalty term represents the idea of weakly enforcing the interior boundary conditions. After addings these terms, the operator $a + J$ is still continuous as shown below after some general remarks.

Remark 11. *If the problem* (1.11) *is not posed with pure Neumann boundary conditions, the integral defining J in* (4.18) *has to be evaluated on $\Gamma_{int} \cup \Gamma_D$.*

h_γ is chosen following Giani and Houston (2012) and the isotropic conductivities $\hat{\sigma}_\gamma$ are defined as the harmonic average of the conductivities of the adjacent elements, following Di Pietro and Ern (2011, 2012):

$$h_{\gamma_{e,f}} \coloneqq \frac{\min(|T_e|, |T_f|)}{|\gamma_{e,f}|} \tag{4.19}$$

$$\hat{\sigma}_{\gamma_{e,f}} \coloneqq \frac{2\sigma_e \sigma_f}{\sigma_e + \sigma_f}. \tag{4.20}$$

For the proper choice of $\hat{\sigma}_{\gamma_{e,f}}$ in the case of anisotropic conductivities the reader is referred to Di Pietro and Ern (2011). To ensure coercivity, it is important that the penalty parameter $\eta > 0$ is chosen large enough.
This yields the *symmetric interior penalty Galerkin* (SIPG) formulation or in the case of weighted averages the *symmetric weighted interior penalty Galerkin* (SWIPG or SWIP) method. After showing continuity of the bilinearform $a + J$ on a properly defined subspace of V, V is restricted to a discrete space V_h and it is shown that the discrete formulation is coercive, consistent, and adjoint consistent. The SIPG formulation now reads

$$\text{Find } u \in V \text{ such that } a(u,v) + J(u,v) = l(v) \quad \text{for all } v \in V, \tag{4.21}$$

with a, J, and l as previously defined.
In the following, $k = 1$, i.e., $V = H^1(\Omega)$, is assumed. To show existence and uniqueness of (4.21), a subspace of $H^1(\mathcal{T}_h)$ has to be defined analog to Chapter 2

$$H^1_*(\mathcal{T}_h) \coloneqq \left\{ v \in H^1(\mathcal{T}_h) : \int_\Omega v \,\mathrm{d}x = 0 \right\} \tag{4.22}$$

and akin to Babuška et al. (1999) the norm

$$\begin{aligned} \|v\|_\eta^2 &\coloneqq \|\sigma^{1/2} \nabla_h v\|^2_{L^2(\Omega)} + \eta |v|_J^2, \\ |\!|\!| v |\!|\!|_\eta^2 &\coloneqq \|v\|_\eta^2 + \eta^{-1} \| \{v\} \|^2_{L^2(\Gamma)}, \end{aligned} \tag{4.23}$$

where $\nabla_h v$ denotes the piecewise gradient of v, i.e., $(\nabla_h \cdot)|_T = \nabla(\cdot|_T)$ for $T \in \mathcal{T}$, and $|\cdot|_J$ is the jump seminorm

$$|v|_J^2 \coloneqq \sum_{\gamma \in \Gamma} \frac{\hat{\sigma}_\gamma}{h_\gamma} \|[\![v]\!]\|_{L^2(\gamma)}^2.$$

The restriction of $H^1(\mathcal{T}_h)$ in (4.22) is necessary so that $\|\cdot\|_\eta$ is actually a norm.

Lemma 4 (Continuity)**.** *Let $a + J$ be the SIPG bilinearform as in* (4.17) *and* (4.18) *and η the constant in* (4.18)*. Then,*

$$\|a(v,w) + J(v,w)\| \leq C |\!|\!| v |\!|\!|_\eta |\!|\!| w |\!|\!|_\eta \quad \text{for all } v, w \in H_*^1(\mathcal{T}_h), \tag{4.24}$$

where C is a constant, $C \leq 2$.

Proof. cf. Hartmann (2008); Prudhomme et al. (2000) □

To show existence and uniqueness of a solution for (4.21), it is necessary to show the coercivity of $a + J$ in the space $H_*^1(\mathcal{T}_h)$. For the conforming approach in Chapter 2, coercivity was implicitly given as the bilinearform is elliptic. However, to the best of our knowledge, to date no such proof for the SIPG bilinearform $a + J$ exists (Hartmann, 2008; Prudhomme et al., 2000). Instead, coercivity can be shown for a finite dimensional subspace of V. Therefore, the broken polynomial spaces of degree k on a partition $\mathcal{T}_h(\Omega)$ are defined ,

$$V_h^k = \left\{ v \in L^2(\Omega) : v|_T \in P_k(T) \text{ for all } T \in \mathcal{T}_h(\Omega) \right\}, \tag{4.25}$$

where P_k denotes the space of polynomial functions of degree k (cf. Section 2.1). For hexahedral meshes, the definition follows accordingly when replacing P_k by Q_k. The elements of this space are functions that exhibit elementwise polynomial behaviour, but may be discontinuous across element interfaces (in contrast to the elements of the space M_0^k that was introduced in Chapter 2, which are by construction continuous on Ω). In the following, $k = 1$ is assumed and V_h^1 is denoted by V_h.

Lemma 5 (Discrete coercivity)**.** *Let $a + J$ be the SIPG bilinearform as in* (4.17) *and* (4.18) *and η the constant in* (4.18)*. For a sufficiently large $\eta > 0$, it exists a constant $\kappa > 0$, such that*

$$a(v_h, v_h) + J(v_h, v_h) \geq \kappa \|v_h\|_\eta^2 \text{ for all } v_h \in V_h.$$

Proof. cf. Hartmann (2008); Prudhomme et al. (2000) □

With Lemma 1 (Lax-Milgram), existence and uniqueness of a solution to (4.21) follow from continuity and coercivity.

Remark 12. *A relation between the upper bound for the constant κ and the parameter η in* (4.18)*, depending on the mesh width h and the polynomial degree k of V_h, is shown by Hartmann (2008).*

Remark 13. *The discrete coercivity as proven in Lemma 5 can also be proven with differently defined norms on the space $H^1_*(\mathcal{T}_h(\Omega))$ than the here used definition of $|||\cdot|||_\eta$. For example, Di Pietro and Ern (2012) use the energy norm*

$$\|v_h\|_{E(a+J)} \coloneqq \|v_h\|_{L^2(\Omega)} + \|\sigma^{1/2}\nabla_h v_h\|^d_{L^2(\Omega)} + |[\![v]\!]|_\gamma \tag{4.26}$$

with

$$|[\![v_h]\!]|^2_\gamma \coloneqq \sum_{\gamma\in\Gamma} \frac{\hat{\sigma}_\gamma}{h_\gamma} \|[\![v_h]\!]\|_{L^2(\gamma)}. \tag{4.27}$$

Again, it is necessary to define the restricted space $H^1_*(\mathcal{T}_h)$ so that $\|\cdot\|_{E(a+J)}$ is actually a norm. However, using this norm the proof of continuity of $a+J$ requires a special construction of the space V (Di Pietro and Ern, 2012).

Though the continuous formulation (4.14) is by construction consistent with the strong problem, it is not per se clear that this also holds true for the discrete problem (Di Pietro and Ern, 2011).

Lemma 6 (Discrete consistency)**.** *The SIPG discretization* (4.21) *is consistent with the strong problem* (1.11)*.*

Proof. For a solution u of (1.11), the jump $[\![u]\!]$ vanishes on Γ_{int} since u is continuous, so that $\tilde{a}^{sym}(u, v_h) = 0$ in (4.16) and $J(u, v_h) = 0$ in (4.18) for $v_h \in V_h$. Using partial integration and the homogeneous Neumann boundary condition (1.11b), (4.21) reduces to

$$\begin{aligned}
&a(u, v_h) - l(v_h) \\
&= \int_\Omega \langle \sigma\nabla u, \nabla v_h\rangle \,\mathrm{d}x - \int_{\Gamma_{\text{int}}} \{\sigma\nabla u\}\,[\![v_h]\!]\,\mathrm{d}s + \int_\Omega f v_h \,\mathrm{d}x \\
&= \int_\Omega \langle \sigma\nabla u, \nabla v_h\rangle \,\mathrm{d}x - \int_\Gamma \{\sigma\nabla u\}\,[\![v]\!]\,\mathrm{d}s + \int_\Omega f v_h \,\mathrm{d}x \\
&= \int_\Omega (\nabla\sigma\nabla u) v_h \,\mathrm{d}x + \int_\Omega f v_h \,\mathrm{d}x \\
&= 0
\end{aligned}$$

Thus, u is also a solution of the weak formulation. □

Furhtermore, adjoint consistency is obtained.

Definition 5 (Adjoint consistency; Hartmann, 2008)**.** *Given a function $g_\Omega \in L^2(\Omega)$ and $g_N \in L^2(\Gamma)$, let $z \in V$ be the exact solution of the dual or* adjoint problem

$$\begin{aligned}
\nabla\cdot(\sigma\nabla z) &= g_\Omega \ \textit{in}\ \Omega, \\
\mathbf{n}z &= g_N \ \textit{on}\ \Gamma.
\end{aligned}$$

Then, the discretization of (4.21) *is* adjoint consistent*, iff*

$$a(v,z) + J(v,z) = \int_\Omega g_\Omega \,\mathrm{d}x \quad \textit{for all } v \in V.$$

Lemma 7 (Adjoint consistency)**.** *The SIPG discretization* (4.21) *is adjoint consistent.*

Proof. cf. Arnold et al. (2002); Hartmann (2007) □

A goal of the introduction of the DG-FEM was to formulate an approach that fulfills fundamental physical properties, in our case the *conservation of charge* (cf. (4.15)). Due to the construction, it is easy to show that – in contrast to the conforming approach with test space P_1 as in Chapter 2 – the DG approach with the test space V_h fulfills this property in a discrete sense, i.e., for an arbitrary domain being a union of triangulation elements, $K = \bigcup T_e$, $T_e \in \mathcal{T}_h$. This is possible since the indicator function for each element is an element of the test space now. Therefore, the discrete current $\mathbf{j}_h = \{\sigma\nabla u\} - \eta\frac{\hat\sigma_\gamma}{\hat h_\gamma}[\![u]\!]$ is defined.

Lemma 8 (Discrete conservation property)**.** *For an arbitrary volume $K \subseteq \mathcal{T}_h(\Omega)$, the SIPG discretization* (4.21) *fulfills a discrete conservation property $\int_{\partial K}\langle\{\sigma\nabla u\} - \eta\frac{\hat\sigma_\gamma}{\hat h_\gamma}[\![u]\!], \mathbf{n}\rangle \,\mathrm{d}s = \int_K f \,\mathrm{d}x$, which converges to* (4.15) *for $h \to 0$.*

Proof. Testing with $v_h = \mathbb{1}_K \in V_h$ on a control volume $K \in \mathcal{T}(\Omega)$, we observe that $\nabla v_h = 0$ inside K and $[\![v_h]\!] = \mathbf{n}$ on ∂K. The boundary ∂K is partitioned into boundary facets $\partial K \cap \partial\Omega$ and internal facets $\partial K \setminus \partial\Omega$. Then, (4.21) simplifies to

$$\begin{aligned}
&a(u,v_h) + J(u,v_h) = l(v_h)\\
\Leftrightarrow\ &-\int_{\partial K\setminus\partial\Omega} \langle\{\sigma\nabla u\},\mathbf{n}\rangle \,\mathrm{d}s - \int_{\partial K} \eta\langle\frac{\hat\sigma_\gamma}{\hat h_\gamma}[\![u]\!],\mathbf{n}\rangle \,\mathrm{d}s = \int_K f\,\mathrm{d}x\\
\Leftrightarrow\ &-\int_{\partial K} \langle\{\sigma\nabla u\},\mathbf{n}\rangle \,\mathrm{d}s - \int_{\partial K} \eta\langle\frac{\hat\sigma_\gamma}{\hat h_\gamma}[\![u]\!],\mathbf{n}\rangle \,\mathrm{d}s = \int_K f\,\mathrm{d}x
\end{aligned}$$

and we obtain the discrete conservation property

$$\Leftrightarrow \int_{\partial K} \underbrace{\langle\{\sigma\nabla u\} - \eta\frac{\hat\sigma_\gamma}{\hat h_\gamma}[\![u]\!],\mathbf{n}\rangle}_{\mathbf{j}_h} \,\mathrm{d}s = \int_K f\,\mathrm{d}x.$$

Thus, the discrete problem (4.21) fulfills a conservation property with discrete flux $\mathbf{j}_h = \{\sigma\nabla u\} - \eta\frac{\hat\sigma_\gamma}{\hat h_\gamma}[\![u]\!]$. For $h \to 0$, $[\![u]\!]$ vanishes and the discrete flux $\mathbf{j}_h$ converges to the flux $\mathbf{j}$ as defined in (4.15). □

A basis of the space V_h could be generated by restricting the hat functions h_k introduced in Section 2.1 to single elements:

$$S_h^{DG} \coloneqq \{v \in L^2(\Omega) : v|_T = h_k \in S_h, v|_{\Omega\setminus\bar T} = 0, T \in \mathcal{T}_h\} \tag{4.28}$$

However, this is not reasonable, as the elements of S_h^{DG} do not inherit the advantages of S_h (e.g., the unique identification between basis function and mesh vertices) and lack other advantageous features, e.g., they are not $L^2(\Omega)$-orthonormal. Instead an $L^2(\Omega)$-orthonormal basis is used here, i.e., for each tetrahedral mesh element a basis is given by an orthonormalization of $\{1, x, y, z\} \in V_h(T)$ for all $T \in \mathcal{T}_h$. This can be achieved by a Gram-Schmidt process. For hexahedral elements, an orthonormalization of $\{1, x, y, z, xy, yz, zx, xyz\} \in V_h(T)$ has to be performed. It is obvious that the discrete space V_h is clearly larger than in the continuous case, as we have 4/8 basis functions per (tetrahedral/hexahedral) mesh element instead of one per mesh vertex now.
Just like for the CG-FEM (cf. Chapter 2), u can now be replaced by its approximation in the discrete space of test functions, $u_h(\mathbf{x}) = \sum_j u_j v_j(\mathbf{x})$ and we obtain a linear system $Au = b$, where A is the matrix representation of the bilinear operator $a + J$ and b the right hand side vector:

$$A_{ij} = a(v_j, v_i) + J(v_j, v_i), \tag{4.29}$$

$$b_i = l(v_i). \tag{4.30}$$

In the test setup (polynomial degree k = 1, hexahedral mesh), the number of unknowns per mesh cell is eight for the DG approach, so that the dimension of A is $m = n = 8 \times \#\text{cells}$ (compared to one degree of freedom per vertex for the CG approach, i.e., $m = n = \#\text{vertices}$). For a sufficiently large $\eta > 0$, the matrix A is symmetric positive definite after fixing a Dirichlet node (Rivière, 2008), where the lower bound for η depends on the shape regularity of the mesh and the polynomial degree k. Nevertheless, η should not be chosen too high, as the condition number of A increases rapidly with the penalty parameter (Castillo, 2002). After a proper (re-)arrangement, A has sparse block structure with small dense blocks; in the present setup with polynomial degree $k = 1$ and hexahedral meshes each block is a 8×8 matrix (Figure 4.3). The outer structure is similar to that of a finite volume discretization, i.e., rows corresponding to each grid cell and one off-diagonal entry for each cell neighbour. Principally, the resulting equation system can, e.g., be solved using BiCGStab- or MINRES-solvers. By now, a range of

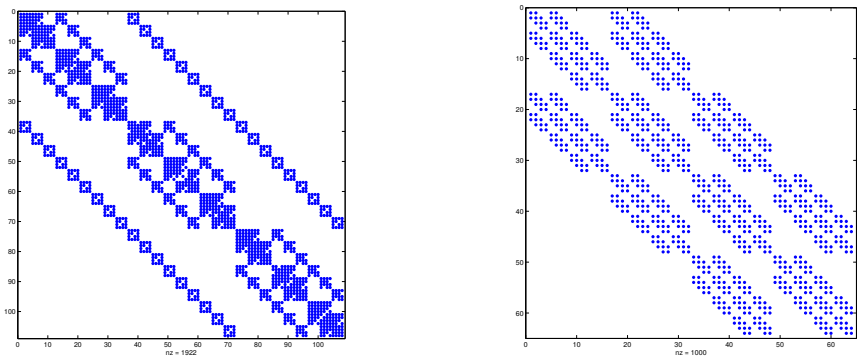

Figure 4.3.: Matrix Structure of a DG-FEM discretization (left) on a 3x3x3 cubic domain using a polynomial degree of $k = 1$ for the local basis functions compared to that of a conforming CG-FEM discretization using Lagrange basis functions (right). *Source: Ludewig (2013)*

efficient solvers for DG discretizations is available, using techniques like multigrid methods (Bastian et al., 2012) or domain decomposition methods (Antonietti and Houston, 2011).
As in the CG case in Chapter 2, the question how to deal with the irregular source term f, which can not be evaluated directly, was set aside until now. In the following, two of the approaches already used in the continuous case, namely the partial integration and the subtraction approach, are adapted to the DG-framework.

4.1.2. The Partial Integration (PI) Direct Approach

As in the continuous scenario in Section 2.2, also in the discontinuous case the derivation of the partial integration approach is fairly simple. Starting from the definition of the right-hand side vector b in (4.13) and (4.30) for a source term $f = \nabla \cdot \mathbf{j}^p$ and $\mathbf{j}^p = \mathbf{p}\delta_{\mathbf{x}_0}$, the distributional derivative is used to shift the derivative to the test function. The remaining integral can be easily evaluated and we obtain a sparse rhs-vector:

$$\begin{aligned} b_i^{pi} &= \int_\Omega f v_i \,\mathrm{d}x = \int_\Omega \nabla \cdot \mathbf{j}^p v_i \,\mathrm{d}x = \int_\Omega \langle \mathbf{j}^p, \nabla v_i \rangle \,\mathrm{d}x \\ &= \begin{cases} \langle \mathbf{p}, \nabla v_i(\mathbf{x}_0) \rangle \text{ if } \mathbf{x}_0 \in \operatorname{supp} v_i \in \mathcal{T}_h(\Omega), \\ 0 \text{ otherwise.} \end{cases} \end{aligned} \tag{4.31}$$

Considering the discussion conducted in Section 2.5 regarding the extent of the monopole distributions for the direct approaches, the partial integration DG approach has the advantage that all test functions corresponding to non-zero entries in b^{pi} are supported only on a single mesh element. The numerical accuracy of the partial integration DG approach is evaluated in Section 4.2.

4.1.3. The Subtraction Approach

Two ways to derive a DG formulation of the subtraction approach have been considered so far. The first idea is to exploit the derivation performed in Section 4.1 and replace the potential u in (4.14) by the correction potential u^c from (2.35) (Ludewig, 2013). This causes additional terms in the definition of $l(v)$ in (4.13) as a consequence of the inhomogeneous Neumann boundary condition (2.35b). A second approach is presented by Engwer et al. (submitted). Taking the strong formulation (2.35) as a starting point, the derivation performed in Section 4.1 is repeated for the correction potential u^c from (4.4) onwards. In both cases, basic properties like the coercivity of the bilinear form a – and thereby also existence and uniqueness of a solution – and the discrete conservation property for the current u^c are passed on. Here, it shall suffice to adapt the weak form (4.14) to the subtraction approach and provide the proofs of consistency and the charge preserving property of the correction potential u^c as derived by Engwer et al. (submitted).
First of all, it is noted that akin to (4.15) also the correction potential u^c fulfills a conservation property that can be derived by inserting the decomposition (2.34) to (4.15):

$$\int_{\partial K} \sigma \partial_{\mathbf{n}} u^c \, \mathrm{d}s = -\int_{\partial K} \sigma^c \partial_{\mathbf{n}} u^\infty \, \mathrm{d}x \underbrace{- \int_{\partial K} \sigma^\infty \partial_{\mathbf{n}} u^\infty \, \mathrm{d}s + \int_K f dx}_{\equiv 0}.$$

Applying Gauss' theorem to the right hand side, a conservation property for the correction potential is obtained,

$$\int_{\partial K} \langle \underbrace{\sigma \nabla u^c}_{\mathbf{j}^c}, \mathbf{n} \rangle \, \mathrm{d}s = \int_K \underbrace{\nabla \cdot \sigma^c \nabla u^\infty}_{f^c} \, \mathrm{d}x, \tag{4.32}$$

which basically states that u^c is a conserved property with flux $\mathbf{j}^c = \sigma \nabla u^c$ and a source term $f^c = \nabla \cdot \sigma^c \nabla u^\infty$.

Using the same assumptions and notations as in Section 2.6, the weak formulation of the subtraction approach in the DG formulation reads

$$a(u^c, v) + J(u^c, v) = l(v) \quad \text{for all } v \in V \tag{4.33}$$

with $a(u^c, v)$ and $J(u^c, v)$ defined as in (4.17) and (4.18), respectively, u^c and u^∞ defined as in (2.34a), σ^c and σ^∞ defined as in (2.34b), and

$$l(v) = -\int_\Omega \langle \sigma^c \nabla u^\infty, \nabla v \rangle \, \mathrm{d}x + \int_{\Gamma_{\text{int}}} \{\sigma^c \nabla u^\infty\} [\![v]\!] \, \mathrm{d}s - \int_{\partial\Omega} \sigma^\infty \partial_{\mathbf{n}} u^\infty v \, \mathrm{d}s. \tag{4.34}$$

Compared to (2.37) in Section 2.6, the second term in the defintion of $l(v)$ is an additional term accounting for the inter-element discontinuities of the test functions v.

The bilinearform a is unchanged compared to Lemma 5, thus existence and uniqueness of a solution follow directly. To show consistency of the DG subtraction approach, we note

Lemma 9. *Given a strong solution u of (1.11) with a continuous flux $\sigma \nabla u$ as a result of the subtraction approach, also $\sigma \nabla u^c + \sigma^c \nabla u^\infty$ is continuous.*

Proof. Considering an arbitrary interface γ, at each point $\mathbf{x}$ along γ the fluxes $\sigma \nabla u$ and $\sigma^\infty \nabla u^\infty$ are continuous. Thus, the jump terms vanish and we obtain

$$[\sigma \nabla u] = 0 = [\sigma^\infty \nabla u^\infty]. \tag{4.35}$$

Rewriting $[\sigma \nabla u]$ in terms of $\sigma^c, \sigma^\infty, u^c$, and u^∞, we have

$$\begin{aligned} &\Leftrightarrow [\sigma^\infty \nabla u^c] + [\sigma^c \nabla u^c] + [\sigma^c \nabla u^\infty] = 0 \\ &\Leftrightarrow [\sigma \nabla u^c] = -[\sigma^c \nabla u^\infty] \\ &\Leftrightarrow [\sigma \nabla u^c + \sigma^c \nabla u^\infty] = 0. \end{aligned} \tag{4.36}$$

As this property holds for any control volume and for any interface γ, the combined flux $\sigma \nabla u^c + \sigma^c \nabla u^\infty$ is also continuous. □

Note that this also implies the identity

$$[\sigma\nabla u^c] = -[\sigma^c\nabla u^\infty]. \tag{4.37}$$

Lemma 10 (Consistency)**.** *The SIPG discretization* (4.33) *for the subtraction approach is consistent with the strong problem* (2.35)*.*

Proof. For a solution u^c of the strong problem for the correction potential (2.35), the jump $[\![u^c]\!]$ vanishes since minimally $u^c \in H^1$, so that $\tilde{a}^{sym}(u^c, v_h) = 0$ in (4.16) and $J(u^c, v_h) = 0$ in (4.18). Using partial integration and both (2.35a) and (2.35b), (4.33) reduces to

$$\begin{aligned}
&a(u^c, v_h) - l(v_h)\\
&\quad= \int_\Omega \langle\sigma\nabla u^c, \nabla v_h\rangle \,\mathrm{d}x - \int_{\Gamma_{\text{int}}} \{\sigma\nabla u^c\}\,[\![v_h]\!]\,\mathrm{d}s\\
&\qquad+ \int_\Omega \langle\sigma^c\nabla u^\infty, \nabla v_h\rangle \,\mathrm{d}x - \int_{\Gamma_{\text{int}}} \{\sigma^c\nabla u^\infty\}\,[\![v_h]\!]\,\mathrm{d}s\\
&\qquad+ \int_{\partial\Omega} (\sigma^\infty\partial_{\mathbf{n}} u^\infty) v_h \,\mathrm{d}s\\
&\underset{(2.35b)}{=} \int_\Omega \langle\sigma\nabla u^c, \nabla v_h\rangle \,\mathrm{d}x - \int_\Gamma \{\sigma\nabla u^c\}\,[\![v_h]\!]\,\mathrm{d}s\\
&\qquad+ \int_\Omega \langle\sigma^c\nabla u^\infty, \nabla v_h\rangle \,\mathrm{d}x - \int_\Gamma \{\sigma^c\nabla u^\infty\}\,[\![v_h]\!]\,\mathrm{d}s.
\end{aligned}$$

We use (4.36) and add $0 = -\int_\Gamma [\![\sigma\nabla u^c]\!]\,\{v_h\}\,\mathrm{d}s - \int_\Gamma [\![\sigma^c\nabla u^\infty]\!]\,\{v_h\}\,\mathrm{d}s$ to obtain

$$\begin{aligned}
&= \int_\Omega \langle\sigma\nabla u^c, \nabla v_h\rangle \,\mathrm{d}x - \int_\Gamma \{\sigma\nabla u^c\}\,[\![v_h]\!] + [\![\sigma\nabla u^c]\!]\,\{v_h\}\,\mathrm{d}s\\
&\quad+ \int_\Omega \langle\sigma^c\nabla u^\infty, \nabla v_h\rangle \,\mathrm{d}x - \int_\Gamma \{\sigma^c\nabla u^\infty\}\,[\![v_h]\!] + [\![\sigma^c\nabla u^\infty]\!]\,\{v_h\}\,\mathrm{d}s\\
&\underset{(4.10)}{=} \int_\Omega \langle\sigma\nabla u^c, \nabla v_h\rangle \,\mathrm{d}x - \int_\Gamma [\![\sigma\nabla u^c v_h]\!]\,\mathrm{d}s\\
&\quad+ \int_\Omega \langle\sigma^c\nabla u^\infty, \nabla v_h\rangle \,\mathrm{d}x - \int_\Gamma [\![\sigma^c\nabla u^\infty v_h]\!]\,\mathrm{d}s\\
&= -\int_\Omega (\nabla\cdot\sigma\nabla u^c) v_h \,\mathrm{d}x - \int_\Omega (\nabla\cdot\sigma^c\nabla u^\infty) v_h \,\mathrm{d}x\\
&\underset{(2.35a)}{=} 0.
\end{aligned}$$

Thus, u^c is also a solution of the weak formulation. □

Furthermore, the conservation of charge in the discrete problem as shown in Lemma 8 also holds true for the discrete correction potential u_h^c and the discrete flux $\mathbf{j}_h^c = \{\sigma\nabla u^c\} - \eta\frac{\hat{\sigma}_\gamma}{h_\gamma}[\![u^c]\!]$,

which converges to $\mathbf{j}^c = \sigma \nabla u^c$ for $h \to 0$:

Lemma 11 (Discrete conservation property)**.** *For a control volume $K \in \mathcal{T}_h(\Omega)$, a solution u_h of the SIPG discretization* (4.21) *fulfills the discrete conservation property $\int_{\partial K} \langle \mathbf{j}_h^c, \mathbf{n} \rangle ds = \int_K f^c \,\mathrm{d}x$ with f^c according to* (2.35a)*. The numerical flux $\mathbf{j}_h^c$ converges to* (4.32) *for $h \to 0$.*

Proof. Testing with $v_h = \mathbb{1}_K \in V_h$ on a control volume $K \in \mathcal{T}_h(\Omega)$ and 0 everywhere else, we observe that $\nabla v_h = 0$ inside K and $[\![v_h]\!] = \mathbf{n}$ on ∂K. The boundary ∂K is partitioned into boundary facets $\partial K \cap \partial\Omega$ and internal facets $\partial K \setminus \partial\Omega$. (4.33) simplifies to

$$
\begin{aligned}
& a(u_h^c, v_h) + J(u_h^c, v_h) = l(v_h) \\
\Leftrightarrow \qquad & -\int_{\partial K \setminus \partial\Omega} \langle \{\sigma \nabla u_h^c\}, \mathbf{n} \rangle \,\mathrm{d}s + \int_{\partial K} \eta \langle \frac{\hat{\sigma}_\gamma}{\hat{h}_\gamma} [\![u_h^c]\!], \mathbf{n} \rangle \,\mathrm{d}s = \\
& \qquad + \int_{\partial K \setminus \partial\Omega} \langle \{\sigma^c \nabla u^\infty\}, \mathbf{n} \rangle \,\mathrm{d}s - \int_{\partial K \cap \partial\Omega} \sigma^\infty \partial_{\mathbf{n}} u^\infty \,\mathrm{d}s
\end{aligned}
$$

We exploit $\int_{\partial_K \setminus \partial\Omega} = \int_{\partial\Omega} - \int_{\partial K \cup \partial\Omega}$, $\{\sigma^c \nabla u^\infty\} + \sigma^\infty \nabla u^\infty = \{\sigma \nabla u^\infty\}$, rearrange terms, and obtain

$$
\begin{aligned}
\Leftrightarrow \qquad & -\int_{\partial K \setminus \partial\Omega} \langle \{\sigma \nabla u_h^c\}, \mathbf{n} \rangle \,\mathrm{d}s + \int_{\partial K \cap \partial\Omega} \langle \{\sigma \nabla u^\infty\}, \mathbf{n} \rangle \,\mathrm{d}s \\
& \qquad + \int_{\partial K} \eta \langle \frac{\hat{\sigma}_\gamma}{\hat{h}_\gamma} [\![u_h^c]\!], \mathbf{n} \rangle \,\mathrm{d}s = \int_{\partial K} \langle \{\sigma^c \nabla u^\infty\}, \mathbf{n} \rangle \,\mathrm{d}s.
\end{aligned}
$$

As σ^c is continuous on K, we obtain the discrete conservation property

$$
\Leftrightarrow \qquad \int_{\partial K} \underbrace{\langle \{\sigma \nabla u_h^c\} - \eta \frac{\hat{\sigma}_\gamma}{\hat{h}_\gamma} [\![u_h^c]\!], \mathbf{n} \rangle}_{\mathbf{j}_h^c} \,\mathrm{d}s = \int_K \underbrace{-\nabla \cdot \sigma^c \nabla u^\infty}_{f^c} \,\mathrm{d}s
$$

Thus, the discrete problem (4.33) fulfills a conservation property with numerical flux $\mathbf{j}_h^c = \{\sigma \nabla u^c\} - \eta \frac{\hat{\sigma}_\gamma}{\hat{h}_\gamma} [\![u^c]\!]$, which converges to $\mathbf{j}^c = \sigma \nabla u^c$ for $h \to 0$, and source term $f^c = -\nabla \cdot \sigma^c \nabla u^\infty$ for each control volume $K \in \mathcal{T}_h(\Omega)$. □

4.1.4. Error Estimates for the Discrete Solution

When deducing error estimates for the CG-FEM in Section 2.7, two main pitfalls occured: The discontinuity of the conductivity distribution σ and the singular source term $f \notin L^2(\Omega)$ for partial integration and Venant approach. Also for the DG-FEM, most error estimates rely on the assumption of a source term $f \in L^2(\Omega)$, which is apparently still only fulfilled for the subtraction approach and not for the partial integration approach. While in the CG-case, as presented in Section 2.7, also error estimates for singular source terms f exist, such estimates are to the best of the author's knowledge only derived in the two-dimensional case for DG methods so far, e.g., by Houston and Wihler (2012). Thus, the estimates presented in this

section can only strictly be applied to the subtraction approach.
Unlike for the CG-case in Section 2.7, the assumption of $\sigma \in H^1(\Omega)$ is usually dropped for the DG error estimates as a consequence of the discontinuous formulation and replaced by the weaker condition $\sigma \in L^\infty(\Omega)$. As a further consequence of the discontinuous formulation, only piecewise regularity of the solution u is assumed instead of demanding global regularity. A common assumption is that the exact solutions u lives in the previously introduced broken Sobolev spaces, $W^{k,p}(\mathcal{T}_h)$ or $H^k(\mathcal{T}_h)$. Other assumptions such as homogeneous Dirichlet boundary conditions and Ω being a convex polyhedral domain are already known from the CG-case.

Theorem 4 (Arnold et al., 2002)**.** *Let Ω be a convex polyhedral domain. Let $u \in H^2(\mathcal{T}_h)$ be a solution of the Poisson problem* (1.11a) *with homogeneous Dirichlet boundary conditions and coefficients $\sigma \in L^\infty(\Omega)$. One obtains the L^2-estimate*

$$\|u - u_h\|_{L^2(\Omega)} \leq C h^{k+1} |u|_{H^{k+1}(\Omega)}$$

for a constant $C > 0$ and k being the polynomial degree of the space V_h.

Proof. Arnold et al. (2002) □

This error estimate can be seen as an equivalent to the estimate (2.44) that was derived for the CG-FEM. This or similar error estimates still hold under the slightly weaker assumption of $u \in H^{3/2+\epsilon}(\mathcal{T}_h)$, $\epsilon > 0$ (Cai et al., 2011; Ern et al., 2009).

Corollary 3 (Quantitative error estimate for the DG subtraction approach)**.** *Let $u^c \in H^2(\mathcal{T}_h)$ be a solution of 2.35a and let Ω and σ fulfill the assumptions of Theorem 4. Then, for polynomial degree $k = 1$ the estimate*

$$\|u^c - u_h^c\|_{L^2(\Omega)} \leq C h^2 |u^c|_{H^2(\Omega)}$$

holds for a constant $C > 0$ independent of h.

Though no error estimates for singular data, as occuring for the partial integration approach, have been derived up to now, at least error estimates for solutions with lower regularity than assumed in Theorem 4 exist and one example shall be given. Di Pietro and Ern (2012) derived a priori error estimates for $u \in W^{2,p}(\mathcal{T}_h)$, $p \geq 2d/(d+2)$, and weights chosen as in (4.9) and (4.20). At least in the 2d-case it has been shown that such a solution exists for a conductivity distribution σ that is constant on each element $T \in \mathcal{T}_h$ (Kellogg, 1974; Nicaise and Sändig, 1994). Following the Sobolev embedding theorem, this yields $u \in H^{1+\alpha}(\mathcal{T}_h)$ with $\alpha \coloneqq 1 + d(1/2 - 1/p) > 0$. Based on the already introduced norm $\|\cdot\|_{E(a+J)}$, the estimate

$$\|u - u_h\|_{E(a+J)} \lesssim \bar{\lambda}_\sigma^{1/2} h^\alpha \|u\|_{W^{2,p}(\mathcal{T}_h)} \tag{4.38}$$

can be derived, where $\bar{\lambda}_\sigma$ indicates the maximal eigenvalue of σ.

The recitation of further a priori or a posteriori error estimates is omitted at this point. For an overview on error estimates for a variety of different DG formulations, it is referred to Arnold et al. (2002); Hartmann (2008).

4.2. Numerical Evaluation

After describing the methods used for the numerical evaluation, i.e., the used implementations, models, sensor setups, and methods for visualization, the results of various evaluations of the two source modelling approaches in the DG-formulation are presented in this section. Furthermore, these results are compared to the corresponding approaches in the CG formulation.

4.2.1. Methods

Implementation and parameter settings

The DG-FEM subtraction and partial integration approach were implemented in the DUNE framework (Bastian et al., 2008a,b) using the DUNE PDELab-toolbox (Bastian et al., 2010). For comparison, also the CG-FEM subtraction and partial integration approach were re-implemented in the same framework. Linear Ansatz-functions were used for both DG (i.e., $k = 1$ in (4.25)) and CG approaches throughout this study. For the DG approaches, the penalty parameter was chosen to $\eta = 0.390625$ according to Engwer et al. (submitted); Ludewig (2013) and for both CG and DG approaches an AMG-CG solver was used.

Volume conductor models

To validate and compare the accuracy of these numerical schemes, four layer sphere models were again chosen as test scenario making use of the analytical solution as reference (cf. Section 1.6). The parameters of the models are the same as indicated in Table 2.2. As motivated in the introduction to this chapter, hexahedral meshes were used in this study. To distinguish between numerical and geometrical errors, a variety of head models was constructed with different geometry/segmentation accuracies (1 mm, 2 mm, and 4 mm) and for each of these geometries different mesh resolutions (1 mm, 2 mm, and 4 mm) were used. The details of these head models are listed in Table 4.1 and Figure 4.4 visualizes a some of the used models.
To further evaluate the sensitivity of the different numerical methods to leakage effects, spherical models with intentional skull leakages were generated. Therefore, the model *seg_2_res_2* was chosen as basis and the radius of the outer skull boundary was reduced from the original 86 mm to 82 mm, 83 mm, and 84 mm, resulting in skull thicknesses of 2 mm, 3 mm, and 4 mm, respectively. Thereby, a leakage scenario similar to the one presented in Figure 4.1 was generated, while preserving the advantage of a spherical solution that can be used for error evaluations. Table 4.2 indicates the number of leaks for each model, i.e., the number of vertices belonging to both an element labeled as skin and an element labeled as CSF or brain.

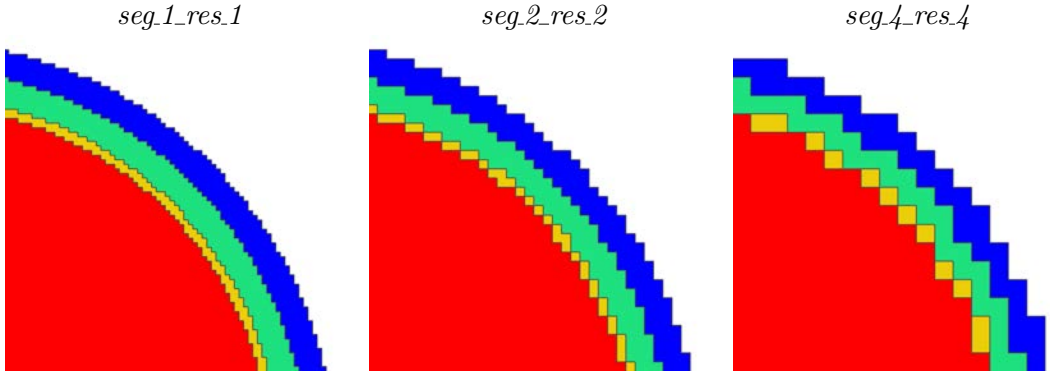

Figure 4.4.: Visualization of models *seg_1_res_1*, *seg_2_res_2*, and *seg_4_res_4* (from left to right), cut in $x = 0$ plane and detail taken for positive y- and z-axis; coloring is brain - red, CSF - yellow, skull - green, skin - blue.

Table 4.1.: Model parameters

	Segmentation res.	Mesh res. (h)	#vertices	#elements
seg_1_res_1	1 mm	1 mm	3,342,701	3,262,312
seg_2_res_1	2 mm	1 mm	3,343,801	3,263,232
seg_2_res_2	2 mm	2 mm	428,185	407,907
seg_4_res_1	4 mm	1 mm	3,351,081	3,270,656
seg_4_res_2	4 mm	2 mm	429,077	408,832
seg_4_res_4	4 mm	4 mm	56,235	51,104

Sources

10 different source eccentricities were used and for each eccentricity 10 sources were randomly distributed to gain a statistical overview of the numerical accuracy, which is expected to depend on the local mesh structure especially for the partial integration approach (cf. Section 2.1). The accuracy for both radial and tangential dipole directions was evaluated. For reasons of clarity and since they are more interesting with regard to the assumption of realistic sources being oriented perpendicular to the cortex surface, only the results for radial directions are presented here.

To make the effect of skull leakage better accessible, visualizations of the volume currents were generated for a dipole at position $(1, 47, 47)$, which corresponds to an element center, and direction $(0, 1, 1)$ for both CG- and DG-FEM and for all three models with reduced skull thickness that are listed in Table 4.2. A cut through the x-plane at the dipole position is visualized and both the direction and strength of the electric current is depicted for each

Table 4.2.: Model leaks

Model	Outer Skull Radius	#leaks
seg_2_res_2_r82	82 mm	10,080
seg_2_res_2_r83	83 mm	1,344
seg_2_res_2_r84	84 mm	0

numerical method and model (Figure 4.15). To visualize the differences between the CG and DG methods, the relative change in current strength and the difference between the simulated current vectors between the two numerical methods is depicted for each model using the error metrics $lnMAG_{\mathbf{j},loc}$ and $totDIFF_{\mathbf{j},loc}$ as defined in the following section (cf. Figure 4.16).

Error metrics

To achieve a result that purely represents the numerical and geometrical accuracy and that is independent of the chosen sensor configuration, the solutions were evaluated on the whole outer layer instead of choosing single points as "sensor nodes". Again, the difference measures RDM and lnMAG were used and besides presenting the mean RDM and lnMAG errors for all sources at a certain eccentricity (cf. Figure 4.5, left), the results are also presented using boxplots (cf. Figure 4.5, right).
To evaluate the local changes of the electric current, for each mesh element E furthermore the logarithm of the local change in current magnitude,

$$lnMAG_{\mathbf{j},loc}(E) = \ln\left(\|\mathbf{j}_{h,\mathrm{CG}}(\mathbf{x}_E)\|_2 / \|\mathbf{j}_{h,\mathrm{DG}}(\mathbf{x}_E)\|_2\right), \tag{4.39}$$

and the difference between the simulated current for the two methods,

$$totDIFF_{\mathbf{j},loc}(E) = \mathbf{j}_{h,\mathrm{CG}}(\mathbf{x}_E) - \mathbf{j}_{h,\mathrm{DG}}(\mathbf{x}_E), \tag{4.40}$$

are visualized, where $\mathbf{x}_E$ denotes the centroid of mesh element E and $\mathbf{j}_{h,\mathrm{CG}}(\mathbf{x}_E)$ and $\mathbf{j}_{h,\mathrm{DG}}(\mathbf{x}_E)$ the electric current at position $\mathbf{x}_E$ computed using the CG- and DG-FEM, respectively (cf. Figure 4.16). These metrics are denoted as $lnMAG_{\mathbf{j},loc}$ and $totDIFF_{\mathbf{j},loc}$. As for the common lnMAG, also for the $lnMAG_{\mathbf{j},loc}$ the change in percent can be estimated to be $100 \cdot lnMAG_{\mathbf{j},loc}$ for small deviations (cf. Section 2.10.1).

4.2.2. Results

To gain a deep understanding of the differences between the two derived DG approaches and the approaches based on the CG-FEM, a variety of comparisons was conducted. First, the results in the sphere models with common geometry but different resolutions of the geometry and different mesh widths are presented for each DG approach. This helps to obtain a general overview of the influence of the mesh resolution on the accuracy of the DG approaches. Second, the results of the DG approaches are compared to those of the corresponding CG-FEM approaches in the models *seg_1_res_1*, *seg_2_res_2*, and *seg_4_res_4*. Thereby, the differences in performance for the DG and CG approaches in regular geometries can be analyzed. Finally, the accuracy of DG and corresponding CG approach is again compared, this time in the sphere models with a thin skull compartment, i.e., *seg_2_res_2_r82*, *seg_2_res_2_r83*, and *seg_2_res_2_r84*, to investigate the behaviour in leaky scenarios. To further illustrate the differences, this chapter is concluded with the visualizations of the volume currents for DG and CG approaches in a single source scenario.

Convergence of the DG approaches

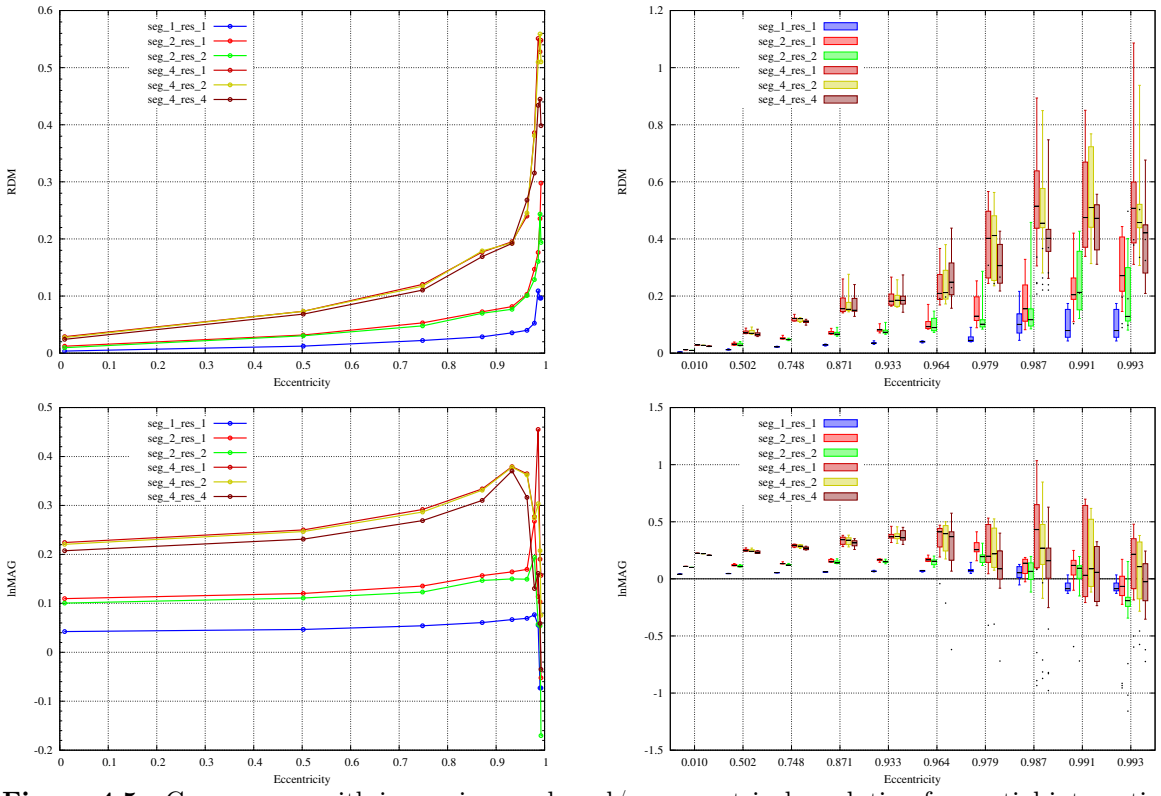

Figure 4.5.: Convergence with increasing mesh and/or geometrical resolution for partial integration DG approach. Results of radial dipole computations. Visualized are the mean error (left column) and boxplots (right column) of RDM (top row) and lnMAG (bottom row). Dipole positions that are outside the brain compartment in the discretized models are marked as dots. Note the different scaling of the x-axes.

Figure 4.5 shows the convergence of RDM and lnMAG errors for the partial integration DG approach when increasing the geometrical accuracy. Comparing the results for meshes *seg_1_res_1*, *seg_2_res_2*, and *seg_4_res_4* shows the clear reduction of both RDM and lnMAG when increasing the mesh resolution and improving the representation of the geometry at the same time. The finest mesh *seg_1_res_1* achieves maximal errors below 0.05 with regard to the RDM for eccentricities up to 0.964, i.e., a distance of 2.8 mm to the brain/CSF boundary. For an eccentricity of 0.979, i.e., a distance of 1.6 mm to the brain/CSF boundary, the maximal error increases to about 0.1. For even higher eccentricities, the maximal errors remain at about 0.2. However, the median error remains below 0.1 for all eccentricities and the minimal errors are below 0.05. The behaviour for the same mesh with regard to the lnMAG is very similar, having a nearly constant median up to an eccentricity of 0.979 with a slight increase of the maximal error. For higher eccentricities, the spread and IQR increase and the median drops from about 0.05 to below 0. The errors for meshes *seg_2_res_2* and *seg_4_res_4* are clearly higher than for mesh *seg_1_res_1*. However, additionally displaying the results for the refined meshes *seg_2_res_1*, *seg_4_res_1*, and *seg_4_res_2*, where the geometry error is kept constant, allows to estimate whether the increased errors are due to insufficient numerical accuracy or the inaccurate resolution of the geometry. For both a geometry resolution of 2 mm and 4 mm, the

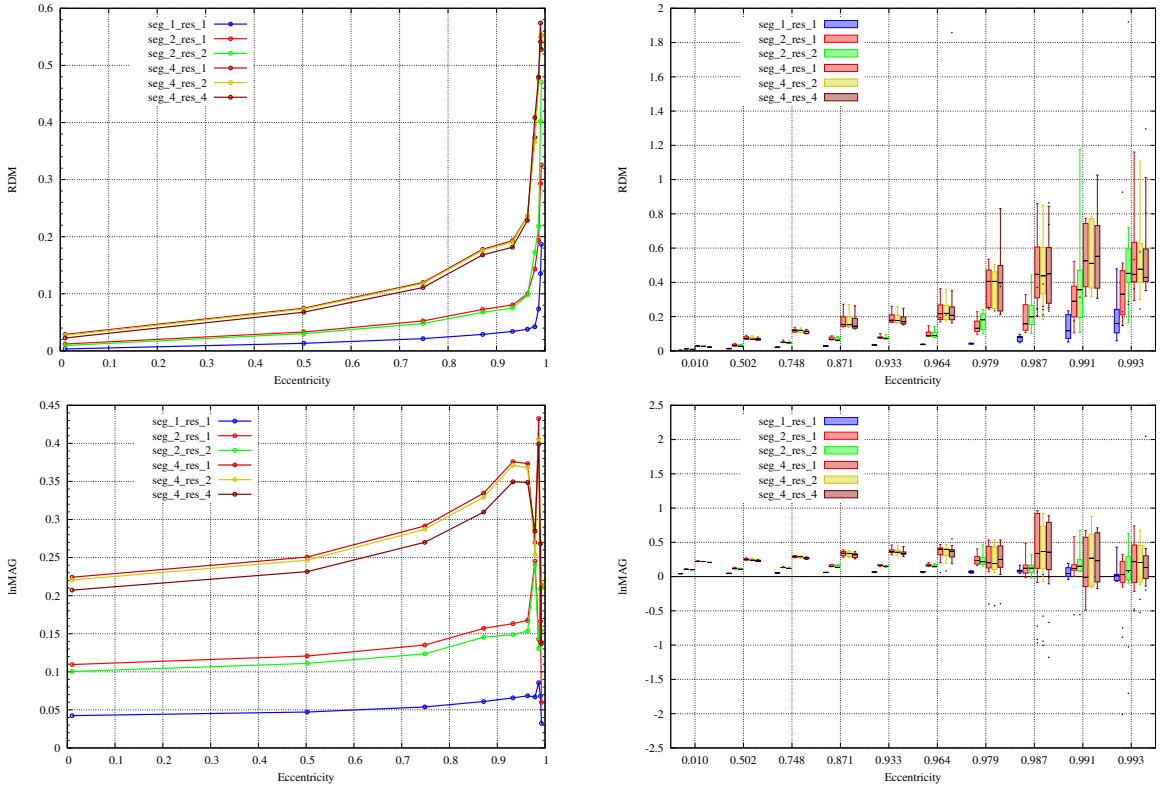

Figure 4.6.: Convergence with increasing mesh and/or geometrical resolution for subtraction DG approach. Results of radial dipole computations. Visualized are the mean error (left column) and boxplots (right column) of RDM (top row) and lnMAG (bottom row). Dipole positions that are outside the brain compartment in the discretized models are marked as dots. Note the different scaling of the x-axes.

errors are dominated by the geometry error; this is especially visible for the lower eccentricities. The observed errors for models with the same geometry are very similar. Comparing the models with a geometry resolution of 2 mm, the errors are at a similar level with regard to the RDM up to an eccentricity of 0.964 and the median of the errors is below 0.1 (Figure 4.5, top right). For higher eccentricities, where sources are already placed in the outermost layer of elements that still belong to the brain compartment, the errors increase clearly and almost double for the two highest eccentricities. Furthermore, the higher mesh resolution does not positively influence the accuracy here. Also with regard to the lnMAG, the effect of the higher mesh resolution is only weak, notable differences can only be seen at the highest eccentricities. For the meshes with a geometry resolution of 4 mm, only negligible differences can be seen at low eccentricities; the medians of the errors are very similar. For high eccentricities, the errors are even higher for the finer mesh resolutions. However, the errors are anyway already clearly increased compared to the models with a better approximation of the geometry: Already at an eccentricity of about 0.5 the median RDM is only slightly below 0.1, increasing to values above 0.4 for the highest eccentricities. The same behaviour is observed for the lnMAG, again finding significantly increased errors compared to the models with a more accurate representation of the geometry.

The results for the subtraction DG approach are overall very similar to those for the partial

integration DG approach (Figure 4.6). Here, it should be kept in mind that the scaling of the y-axis differs when comparing Figure 4.6 to Figure 4.5. This is due to the high errors for sources that are already outside the brain compartment (indicated by black dots in the graph). To avoid repetitions, a detailed general discussion is skipped here and only the main differences between the results for partial integration and subtraction DG approach are stressed. With regard to the RDM, the errors for both approaches are very similar for low eccentricities. For high eccentricities, the subtraction DG approach overall shows a slightly worse accuracy than the partial integration DG approach. However, the subtraction DG approach shows very similar errors for the differently resolved meshes with the same geometry; this is especially visible for the coarsest geometry with a mesh width of 4 mm. The same holds true for the lnMAG, where again the errors for different mesh resolutions and the same geometry differ less than for the partial integration DG approach.

Comparison of DG and CG approaches in common sphere models

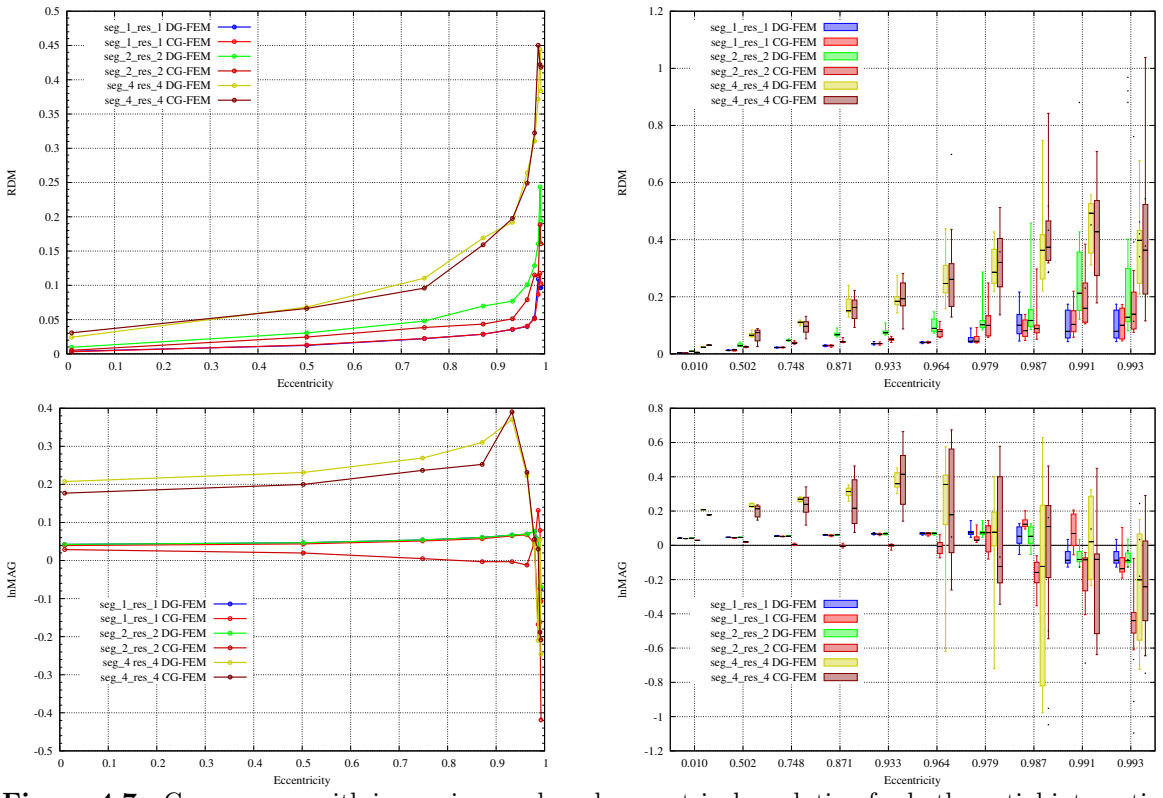

Figure 4.7.: Convergence with increasing mesh and geometrical resolution for both partial integration CG-FEM and DG-FEM. Results of radial dipole computations. Visualized are the mean error (left column) and boxplots (right column) of RDM (top row) and lnMAG (bottom row). Dipole positions that are outside the brain compartment in the discretized models are marked as dots. Note the different scaling of the x-axes.

In Figure 4.7 the results for the newly proposed partial integration DG-FEM are presented side by side with those of the CG-FEM for the meshes *seg_1_res_1*, *seg_2_res_2*, and *seg_4_res_4*. For the model *seg_1_res_1* the only notable differences with regard to the RDM can be observed for the three highest eccentricities. Here, the DG-FEM achieves slightly higher accuracies for

the two highest eccentricities. Similarly, also the evaluation of the lnMAG shows differences for the highest eccentricities. Also for model *seg_2_res_2* the two approaches achieve a very similar numerical accuracy for the lower eccentricities with RDM errors clearly below 0.1; for eccentricities higher than 0.871 the CG-FEM performs slightly better and at the highest eccentricity this difference becomes more distinct. However, as analyzed before, also in this scenario the main error source is the inaccurate representation of the geometry. With regard to the lnMAG, the DG-FEM achieves a similar level of accuracy as in model *seg_1_res_1*, while the CG-FEM leads to huge deviations for the highest eccentricities. In the coarsest model, *seg_4_res_4*, the DG-FEM performs better than the CG-FEM already for low eccentricities, leading to lower spread and IQR. Regardless of the high geometry errors observed in Figure 4.5, the differences in numerical accuracy between DG- and CG-FEM are large for both RDM and lnMAG up to an eccentricity of 0.964. For higher eccentricities, possible differences can be less clearly distinguished due to the dominance of the geometry error and the as a result of that generally increased error level.

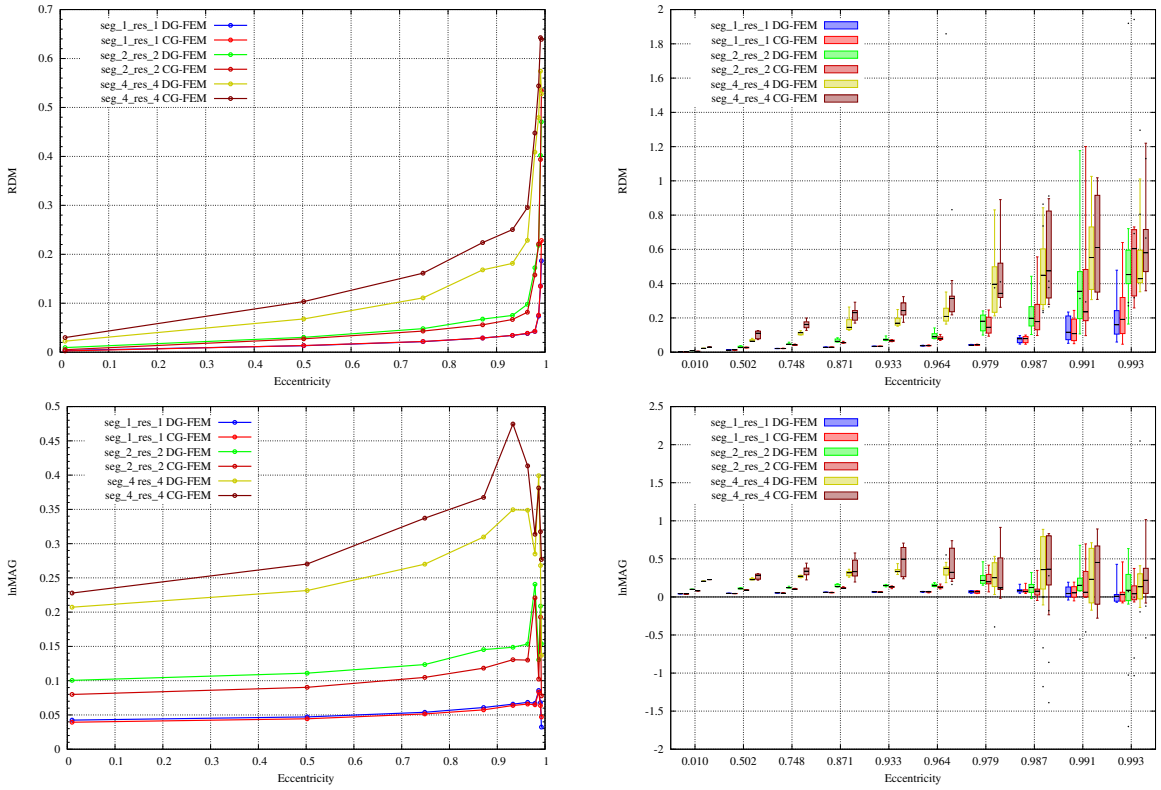

Figure 4.8.: Convergence with increasing mesh and geometrical resolution for both subtraction CG-FEM and DG-FEM. Results of radial dipole computations. Visualized are the mean error (left column) and boxplots (right column) of RDM (top row) and lnMAG (bottom row). Dipole positions that are outside the brain compartment in the discretized models are marked as dots. Note the different scaling of the x-axes.

Again, the results gained for the subtraction approach are similar to those of the partial integration approach (Figure 4.8). For the finest model *seg_1_res_1*, CG- and DG-FEM perform nearly identical, only for the highest eccentricity the DG-FEM is slightly favored with regard to the RDM. Also for model *seg_2_res_2*, though the errors for both approaches vary more

strongly, no tendency which approach performs better can be determined. For the coarsest model *seg_4_res_4*, the DG-FEM leads to lower errors both with regard to RDM and lnMAG.

Comparison of DG and CG approaches in leaky sphere models

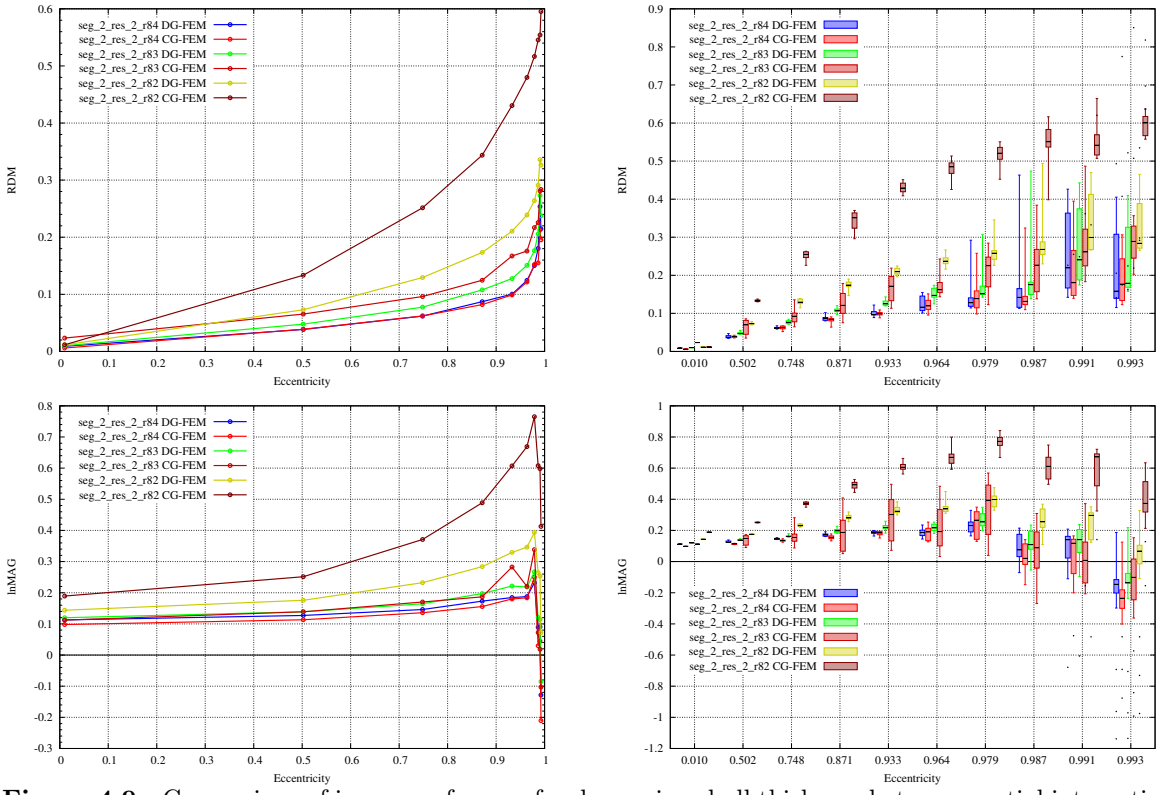

Figure 4.9.: Comparison of increase of errors for decreasing skull thickness between partial integration CG-FEM and DG-FEM. Results of radial dipole computations. Visualized are the mean error (left column) and boxplots (right column) of RDM (top row) and lnMAG (bottom row). Dipole positions that are outside the brain compartment in the discretized models are marked as dots. Note the different scaling of the x-axes.

The most significant accuracy differences between DG- and CG-FEM can be seen in Figures 4.9 and 4.10, where the increase of errors for decreasing skull thickness and a consequent increase of the number of skull leakages is studied (cf. Table 4.2). Again, Figure 4.9, i.e., the partial integration approaches, is discussed first. While the CG-FEM achieves higher accuracies than the DG-FEM in the leakage-free model *seg_2_res_2_r84* (4 mm skull thickness), the DG-FEM performs clearly better in the leaky models *seg_2_res_2_r82* (2 mm skull thickness) and *seg_2_res_2_r83* (3 mm skull thickness). Already for low eccentricities the sensitivity of the CG-FEM to leakages is distinct. The accuracy of the DG-FEM only slightly decreases when reducing the skull thickness, as can be seen when comparing the results for the three different models, showing that this approach shows only little, if any, sensitivity to leakages. In contrast, the errors of the CG-FEM grow strongly with decreasing skull thickness. Especially model *seg_2_res_2_r82* leads to high errors already at low eccentricities, but also the errors for model *seg_2_res_2_r83* are clearly higher for the CG- than for the DG-FEM. Overall, the DG-FEM achieves a significantly higher numerical accuracy than the CG-FEM already for low

eccentricities in the leaky models, both with regard to RDM and lnMAG, while the differences in the non-leaky model *seg_2_res_2_r84* are rather small.

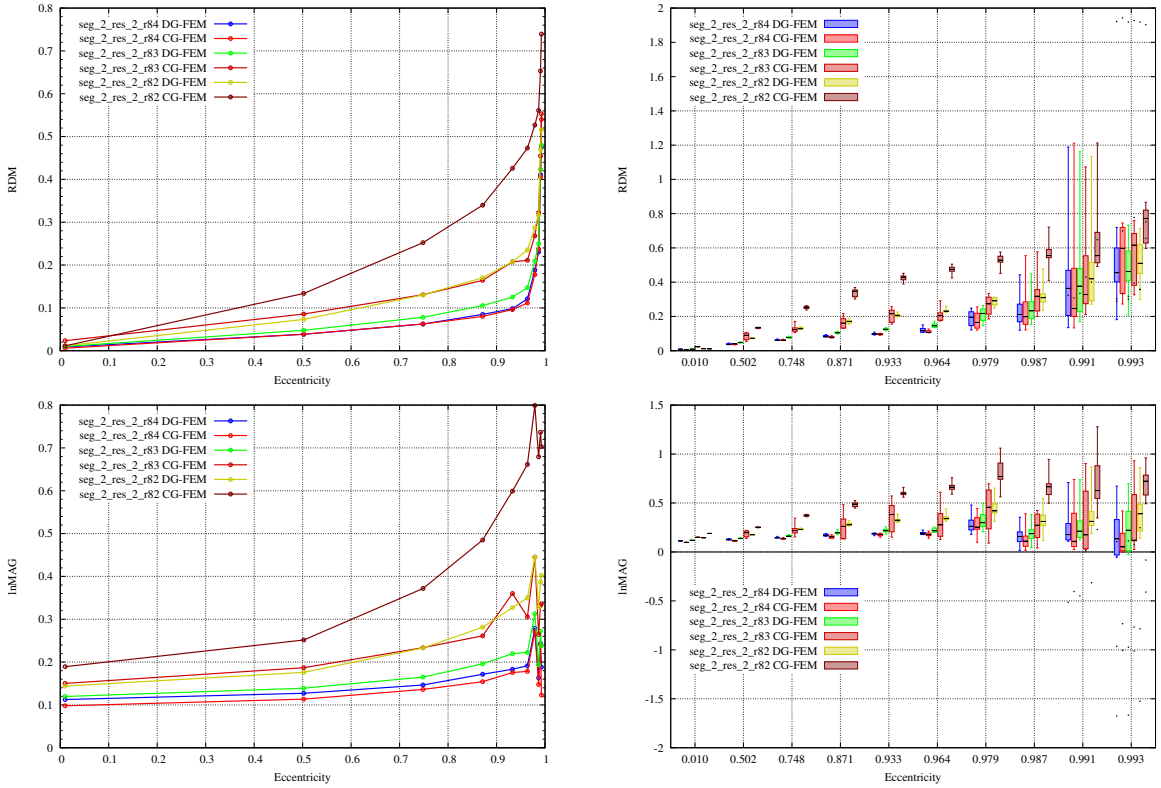

Figure 4.10.: Comparison of increase of errors for decreasing skull thickness between subtraction CG-FEM and DG-FEM. Results of radial dipole computations. Visualized are the mean error (left column) and boxplots (right column) of RDM (top row) and lnMAG (bottom row). Dipole positions that are outside the brain compartment in the discretized models are marked as dots. Note the different scaling of the x-axes.

The main tendency for the leaky models *seg_2_res_2_r82* and *seg_2_res_2_r83*, i.e., clearly higher errors for the CG- than for the DG-FEM, also holds true when appyling the subtraction approach (Figure 4.10). As in Figure 4.9, the differences in the leakage-free model *seg_2_res_2_r84* are clearly diminished, so that CG- and DG-FEM perform very similar both with regard to RDM and lnMAG.

Comparison of partial integration and subtraction DG approach

Until now, the evaluation concentrated on comparing the differences between the CG- and DG-FEM implementations of the same source model. Various comparisons between subtraction and partial integration approach using the CG-FEM implementation were already conducted in Chapter 2. Here, the differences between partial integration and subtraction approach in the DG-FEM implementation are discussed.

Using the common sphere models the results already shown in Figures 4.7 and 4.8 are combined to Figure 4.11 to allow for an easier comparison. For all models very similar accuracies are found for low eccentricities (up to 0.933) both with regard to RDM and lnMAG. For model *seg_1_res_1*, the subtraction approach performs better at eccentricities of 0.964 (maximal RDM

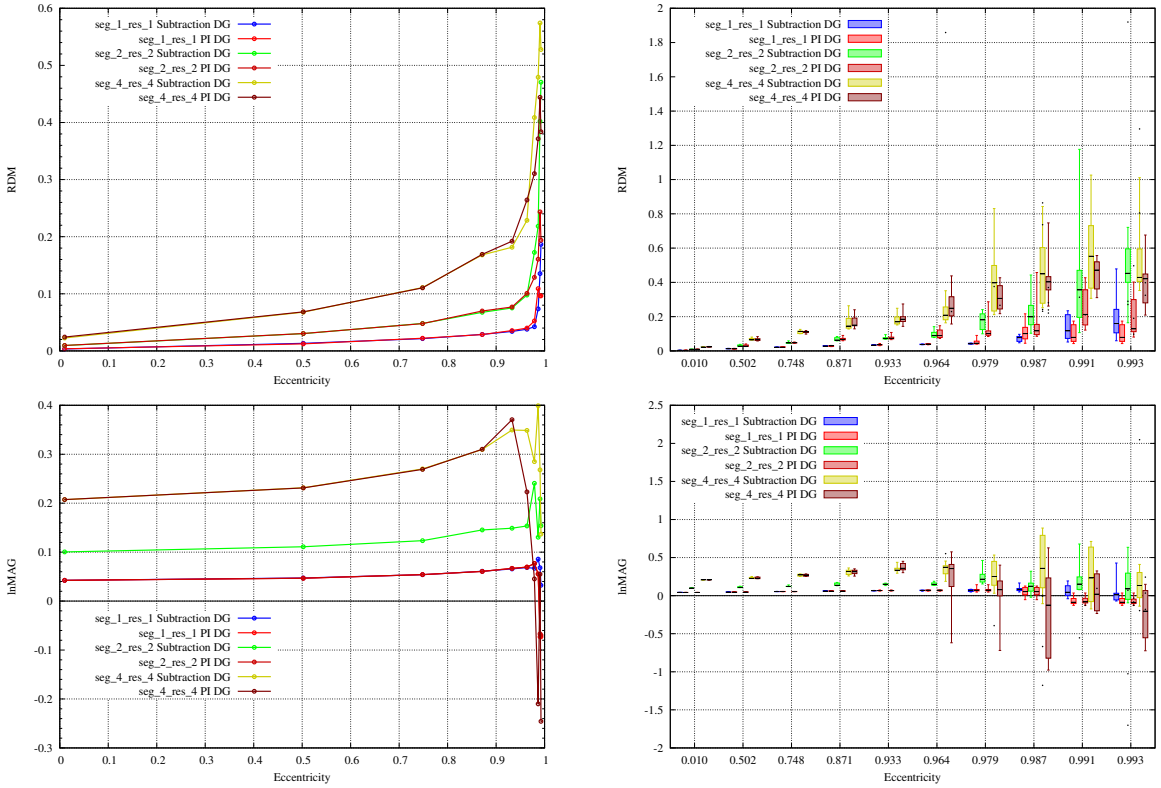

Figure 4.11.: Convergence for both partial integration (PI) and subtraction DG-FEM with increasing mesh and geometrical resolution. Results of radial dipole computations. Visualized are the mean error (left column) and boxplots (right column) of RDM (top row) and lnMAG (bottom row). Dipole positions that are outside the brain compartment in the discretized models are marked as dots. Note the different scaling of the x-axes.

partial integration ≈ 0.1, subtraction ≈ 0.05) and 0.979 (maximal RDM partial integration ≈ 0.2, subtraction ≈ 0.1), while for the even higher eccentricities the partial integration approach performs better (maximal RDM partial integration < 0.2, subtraction > 0.2). In the coarser model *seg_2_res_2*, the partial integration approach even outperforms the subtraction approach for the three highest eccentricities with regard to the RDM. Also in model *seg_4_res_4* advantages for the partial integration approach at high eccentricities can be observed. Also with regard to the lnMAG, major differences are only found for eccentricities of 0.964 and higher. In model *seg_1_res_1*, except for some outliers at highest eccentricities, no advantages of one approach are recognizable. Using model *seg_2_res_2*, the subtraction approach leads to a higher spread and IQR than the partial integration approach, while for model *seg_4_res_4* both approaches lead to a high spread at the highest eccentricities but with a better accuracy for the subtraction approach.

Looking at the results for the leaky models (Figure 4.12), both approaches again perform very similar for both RDM and lnMAG for eccentricities up to 0.964. With regard to the RDM, the partial integration approach outperforms the subtraction approach for the higher eccentricities, when considering median and upper quartile, in all tested models (e.g., median partial integration < 0.3, subtraction > 0.4 for all models at highest eccentricity). For the maximal error, this is only as clear for the two highest eccentricities. With regard to the

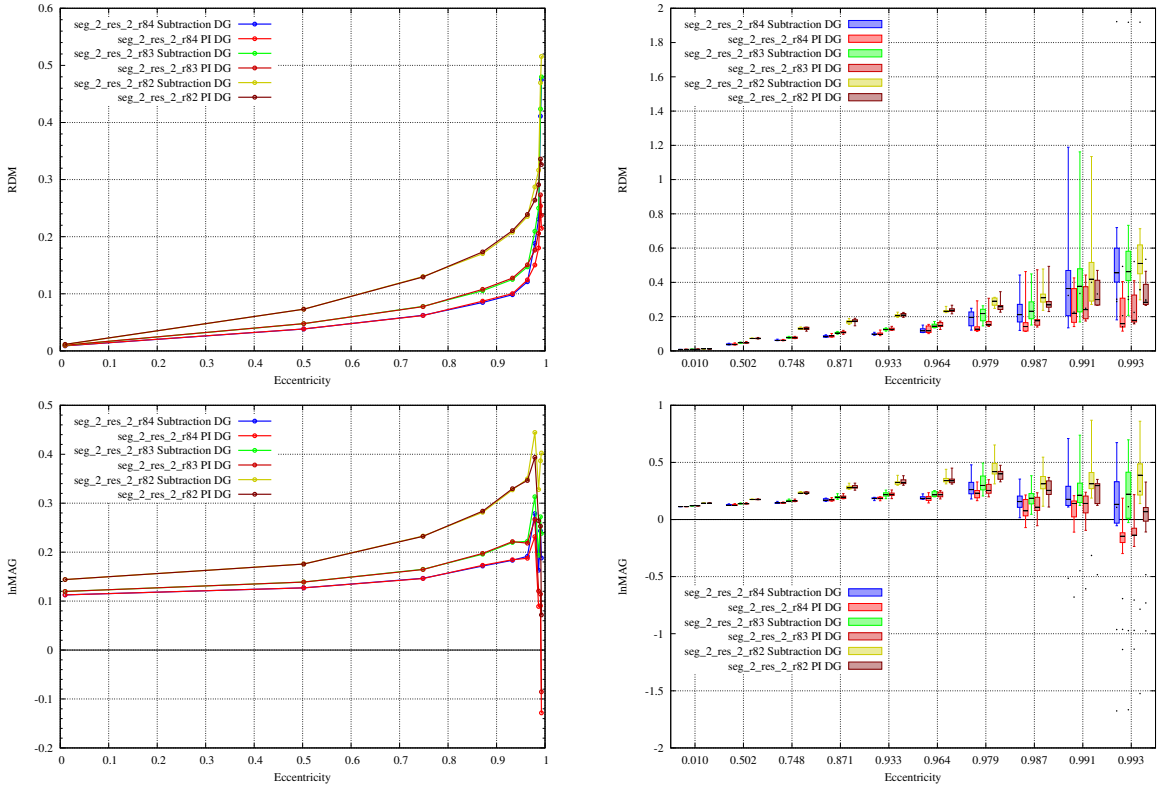

Figure 4.12.: Comparison of increase of errors for decreasing skull thickness between partial integration (PI) and subtraction DG-FEM. Results of radial dipole computations. Visualized are the mean error (left column) and boxplots (right column) of RDM (top row) and lnMAG (bottom row). Dipole positions that are outside the brain compartment in the discretized models are marked as dots. Note the different scaling of the x-axes.

lnMAG, a decrease of the median for the partial integration approach is recognizable at the highest eccentricities, while this change is smaller for the subtraction approach. However, spread and IQR are higher for the subtraction approach at high eccentricities.

Visualization of volume currents in leaky head models

To illustrate the effect of skull leakage, the visualizations shown in Figures 4.13 - 4.16 were generated. In Figures 4.13 and 4.15, the electric current direction and strength for a radial dipole with fixed position and orientation (turquoise cone in middle and right column) in the models *seg_2_res_2_r82* (top row), *seg_2_res_2_r83* (middle row), and *seg_2_res_2_r84* (bottom row) and with the two numerical approaches CG-FEM (middle column) and DG-FEM (right column) are visualized for partial integration (Figure 4.13) and subtraction approach (Figure 4.15), respectively. In Figures 4.14 and 4.16 $lnMAG_{\mathbf{j},loc}$ and $totDIFF_{\mathbf{j},loc}$ between DG- and corresponding CG-FEM approach are visualized. As previously, the results for the partial integration approach are discussed first (Figures 4.13, 4.14). When using CG-FEM in the model with the thinnest skull compartment (2 mm), *seg_2_res_2_r82*, very strong currents are found in the innermost layer of skin elements, i.e., at the interface to the skull. This is especially distinct for those elements the dipole is nearly directly pointing at. In comparison, the current strengths found in the skull compartment are negligible, which is a clear sign for a

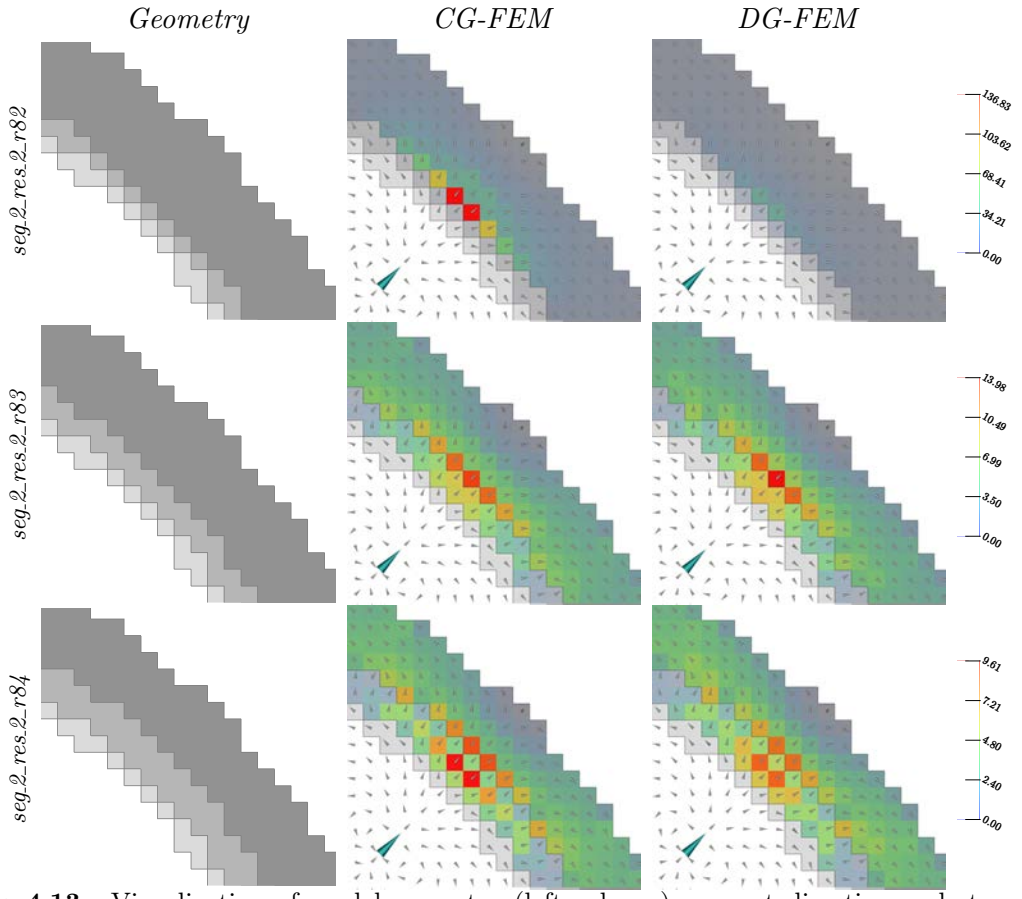

Figure 4.13.: Visualization of model geometry (left column), current direction and strength for partial integration approach and CG-FEM (middle column) and DG-FEM (right column) for models *seg_2_res_2_r82* (top row), *seg_2_res_2_r83* (middle row), and *seg_2_res_2_r84* (bottom row). The left column shows the model geometry, interior to exterior from bottom left to top right, brain in white, CSF, skull and skin in increasingly dark gray, and air in white. Dark gray lines mark compartment boundaries. In the middle and right columns, the large turquoise cone represents the dipole source. The small and normalized grey cones show the directions of the current flow and, for elements belonging to skull and skin compartments, the coloring indicates the current strength. For each model the color scale is kept constant for both approaches.

current leakage through the vertices shared between CSF and skin compartment, bypassing the thin and leaky skull compartment. For the DG approach, these extreme peaks are not found and the maximal current strength amounts to only about 30% of that of the CG approach. In the other two models (note the much lower scaling in the middle and bottom row in Figure 4.15), a clear decrease of the current strength compared to the *seg_2_res_2_r82* model is found, especially in the skin compartment. In these two models and with the given source scenario, none of the approaches seems to be obviously affected by skull leakage. While in model *seg_2_res_2_r83* (middle row), the DG approach shows about 4% higher peak currents in the innermost layer of skin elements compared to the CG-FEM, the maximal current strength for the CG-FEM is about 9% higher than for the DG-FEM and found in the skull compartment in model *seg_2_res_2_r84* (bottom row). These deviations seem reasonable considering the relatively coarse representation of the geometry and the thereby limited numerical accuracy. The visualizations show that the interplay between source position and direction and the local

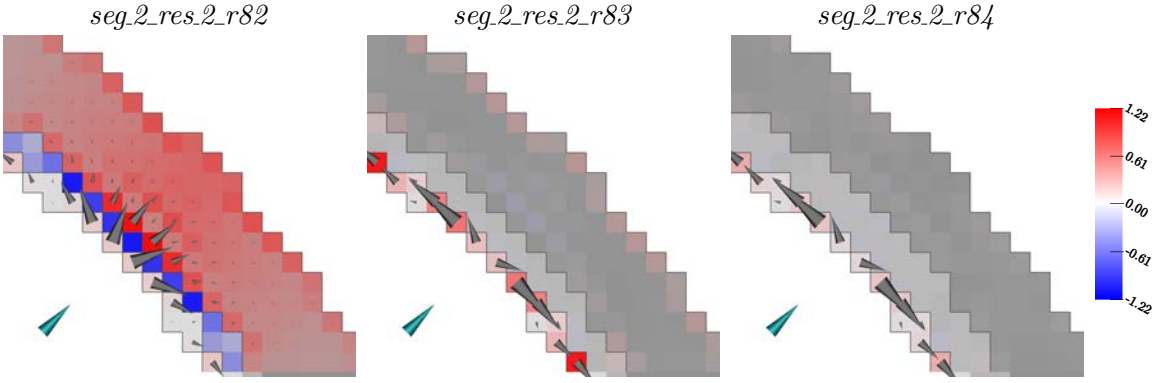

Figure 4.14.: Visualization of current flow differences for partial integration approach between CG- and DG-FEM in models *seg_2_res_2_r82* (left), *seg_2_res_2_r83* (middle), and *seg_2_res_2_r84* (right). The turquoise cone represents the dipole source. The coloring shows the $lnMAG_{\mathbf{j},loc}$ (increase/decrease of the current strength simulated with the CG- compared to the DG-FEM solution). For all models the maximum of the color scale is chosen as the maximal value in the skin and skull compartment. Grey cones, having the same linear scaling for all models, show the $totDIFF_{\mathbf{j},loc}$ (difference in current flow). In models *seg_2_res_2_r83* and *seg_2_res_2_r84* the arrows in skin and skull are not visible due to the relatively small values. Dark gray lines mark compartment boundaries.

geometry strongly influence the local current flow in these models, leading to current peaks in some elements while neighbouring elements show relatively low currents, as it is clearly visible in model *seg_2_res_2_r84*. In this model strong currents are found in the two skull elements the dipole is pointing at. These are providing a "shortcut" between CSF and skin compartment and thereby the lowest resistance.

In Figure 4.14 the two measures $lnMAG_{\mathbf{j},loc}$ and $totDIFF_{\mathbf{j},loc}$ are visualized to show the differences between the two methods more clearly. As Figure 4.13 already suggests, the current strength for model *seg_2_res_2_r82* is clearly higher for the CG-FEM compared to the DG-FEM in those elements of the innermost layer of the skin compartment that share a vertex with the CSF compartment; this is indicated by the high $lnMAG_{\mathbf{j},loc}$ (red coloring). The visualization of the $totDIFF_{\mathbf{j},loc}$ (gray arrows) clearly shows that the leakage generates a strong current from the CSF compartment directly into the skin compartment that is not existing for the DG-FEM. At the same time, the current in the skull compartment is decreased in the CG-FEM compared to the DG-FEM, as the visualization of the $totDIFF_{\mathbf{j},loc}$ shows (inwards pointing arrows visible when zooming into Figure 4.14, left). High values for the $totDIFF_{\mathbf{j},loc}$ are also visible in the CSF compartment, which are most probably caused by effects similar to the "leakage" effects, i.e., a mixing of conductivities in boundary elements/vertices. However, in model *seg_2_res_2_r82*, the color-coding for the $lnMAG_{\mathbf{j},loc}$ shows that this is not related to significant relative differences in current strength. The strongest values for the $lnMAG_{\mathbf{j},loc}$ can be found in the skin and skull compartment, here. In turn, for the other two models the largest deviations are found in the CSF compartment, both with regard to $totDIFF_{\mathbf{j},loc}$ and $lnMAG_{\mathbf{j},loc}$. However, these values are at a clearly lower level than in model *seg_2_res_2_r82*. For model *seg_2_res_2_r83* further strong values in $lnMAG_{\mathbf{j},loc}$, i.e., relative differences of current strength, are found for the innermost layer of skin elements. In these elements also the highest absolute current strength among skin and skull compartment is found (cf. Figure

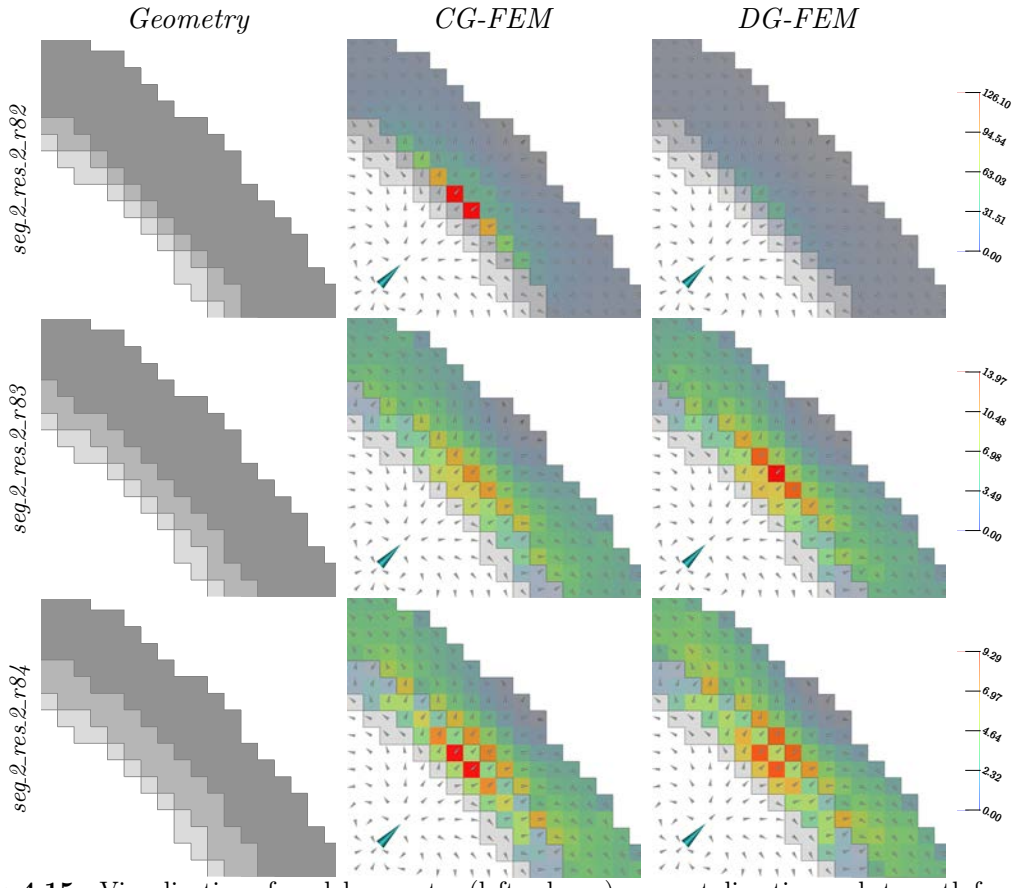

Figure 4.15.: Visualization of model geometry (left column), current direction and strength for subtraction approach and CG-FEM (middle column) and DG-FEM (right column) for models *seg_2_res_2_r82* (top row), *seg_2_res_2_r83* (middle row), and *seg_2_res_2_r84* (bottom row). The left column shows the model geometry, interior to exterior from bottom left to top right, brain in white, CSF, skull and skin in increasingly dark gray, and air in white. Dark gray lines mark compartment boundaries. In the middle and right columns, the large turquoise cone represents the dipole source. The small and normalized grey cones show the directions of the current flow and, for elements belonging to skull and skin compartments, the coloring indicates the current strength. For each model the color scale is kept constant for both approaches.

4.13). Also in the outermost layer of skin elements the values for the $lnMAG_{\mathbf{j},loc}$ are high. These might be artifacts due to the "staircase"-like geometry of the outer surface in the regular hexahedral model. In contrast to this, the $totDIFF_{\mathbf{j},loc}$ in skin and skull is negligible compared to the values in the CSF compartment. The same holds true for model *seg_2_res_2_r84*, where a high $lnMAG_{\mathbf{j},loc}$ in the skin compartment mainly occurs for elements with a small absolute current strength as a comparison to Figure 4.13 shows. Still, high differences in $lnMAG_{\mathbf{j},loc}$ and $totDIFF_{\mathbf{j},loc}$ are visible in the CSF compartment. These results indicate that model *seg_2_res_2_r83* and *seg_2_res_2_r84* are less affected by skull-leakage, the differences are rather due to the different computational approaches and do not show obvious errors resulting from the model geometry.

No major differences between the visualization of the volume currents for partial integration and subtraction approach can be identified when comparing Figures 4.13 and 4.15. The color bar indicates that the maximal current strength in model *seg_2_res_2_r82* is reduced by about

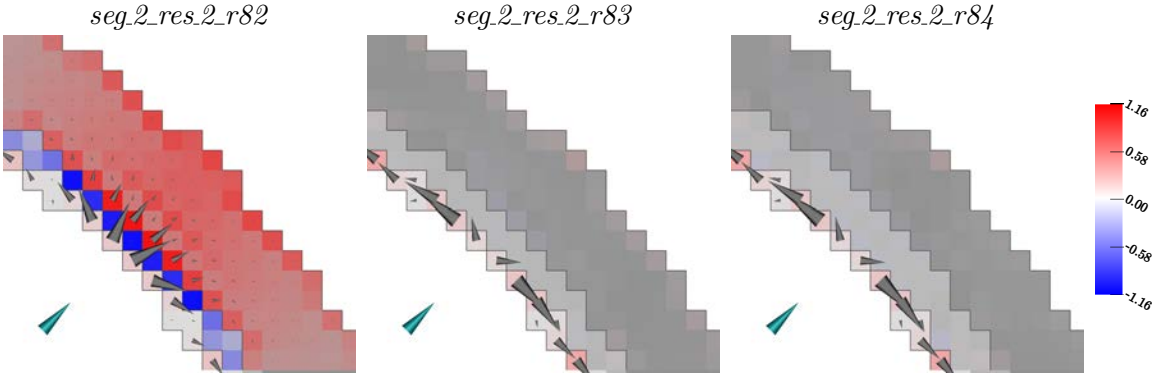

Figure 4.16.: Visualization of current flow differences for subtraction approach between CG- and DG-FEM in models *seg_2_res_2_r82* (left), *seg_2_res_2_r83* (middle), and *seg_2_res_2_r84* (right). The turquoise cone represents the dipole source. The coloring shows the $lnMAG_{\mathbf{j},loc}$ (increase/decrease of the current strength simulated with the CG- compared to the DG-FEM solution). For all models the maximum of the color scale is chosen as the maximal value in the skin and skull compartment. Grey cones, having the same linear scaling for all models, show the $totDIFF_{\mathbf{j},loc}$ (difference in current flow). In models *seg_2_res_2_r83* and *seg_2_res_2_r84* the arrows in skin and skull are not visible due to the relatively small values. Dark gray lines mark compartment boundaries.

7% when using the subtraction approach, while the general current distribution is very similar. The same holds true for models *seg_2_res_2_r83* and *seg_2_res_2_r84*, where also the maximal current strengths are about the same. This also reflects in the distribution of $lnMAG_{\mathbf{j},loc}$ and $totDIFF_{\mathbf{j},loc}$ as a comparison of the visualizations in Figures 4.14 and 4.16 shows. Again, a slightly lower difference between CG- and DG-FEM is found for the subtraction approach, while the general tendencies remain the same.

4.3. Discussion

In this chapter, the theoretical derivation of the Discontinuous Galerkin method for EEG forward simulations was presented and the partial integration and subtraction approach were introduced in this framework. It was shown that this scheme is consistent and fulfills a discrete conservation property. Existence and uniqueness follow from the coercivity of the bilinear form.

The numerical experiments showed the convergence of the DG solutions towards the analytical solution with increasing mesh resolution and better approximation of the spherical geometry. It was furthermore shown that the numerical accuracy of the DG approaches is dominated by the geometry error, while the actual mesh resolution in a model that badly approximates the geometry only had a minor influence on the numerical results (Figures 4.5, 4.6). The inaccurate representation of the geometry, especially in the coarser meshes, is visible by the "staircase-like" boundaries in Figure 4.4.

In the comparisons of DG- and the commonly used CG-FEM approaches, no remarkable differences were found for meshes with higher resolutions (1 mm, 2 mm), as the results in Figures 4.7 and 4.8 are in the same range for both the DG- and CG-based approaches for the models *seg_1_res_1* and *seg_2_res_2*. In this set of experiments, three main sources of errors can

be identified; namely geometry errors, numerical inaccuracies, and leakage effects:

First, we have the error due to the inaccurate representation of the geometry, which is especially strong in the models with low resolution as Figures 4.5 and 4.6 show. It is thus strongly recommendable to use geometry resolutions, and thereby necessarily MRI resolutions, as high as practically feasible; possibly even locally-refined when zoomed MRI technology can be used, as it is available for practical use as of late. This is based on a combination of parallel transmission of excitation pulses and localized excitation (Blasche et al., 2012). A first usage of this zoom technique can be found in Aydin (2015, Chapter 5). Moreover, Bastian and Engwer (2009) presented a cut-cell approach that allows for an accurate representation of the geometry while only introducing a negligible amount of additional degrees of freedom. Thereby, the achieved accuracy can be increased while the computational effort is hardly affected. First results for EEG forward simulations were shown by Nüßing et al. (2015).

A second point, as already discussed in Chapter 2, is the numerical inaccuracy due to the discretization of Equation (1.11) in combination with the strong singularity introduced by the assumption of a point dipole. This singularity is the main cause for the numerical inaccuracies at highest eccentricities, where the source positions are very close to the next conductivity jump (cf. Figures 4.7, 4.8).

The third source of errors, the "leakage effects", explains the large differences in numerical accuracy between CG- and DG-FEM that can be observed in model *seg_4_res_4*. Due to the coarse resolution in comparison to the thickness of the skull compartment (4 mm resolution, 6 mm thickness), this model can already be considered as (at least partly) leaky.

This observation motivated the evaluation of the two methods in a scenario where the assumed advantages of the DG-FEM have a bigger effect. Therefore, spherical models with an especially thin skull layer were constructed, finally ending up with the model *seg_2_res_2_r82* that has a skull layer as thin as the edge length of the hexahedra (cf. Figure 4.13, left column). Though a mesh resolution of 1 mm is highly recommendable for practical application of FEM in source analysis (Aydin et al., 2014; Rullmann et al., 2009), mesh resolutions of 2 mm are still used even in clinical evaluations (Birot et al., 2014) and indeed there are areas of the skull such as the temporal bone, where the thickness is actually only 2 mm or even less (Kwon et al., 2006, Table 2). Thus, the synthetic scenario used here actually has practical relevance. The DG-FEM achieved a higher numerical accuracy in the two models with the thinnest skull layers, *seg_2_res_2_r82* and *seg_2_res_2_r83*, while the results for model *seg_2_res_2_r84* are comparable for DG- and CG-FEM (Figures 4.9, 4.10). In the latter model, the ratio of resolution (2 mm) and skull thickness (4 mm) guarantees that the skull compartment can be appropriately resolved and thus avoids leakages.

To make the difference between CG- and DG-FEM in the presence of skull leakages better accessible, Figures 4.13 - 4.16 were generated. The skull leakage is clearly visible in all figures for model *seg_2_res_2_r82* and the CG-FEM as described in the results section. There are also slight differences visible in the CSF in all three models, which might be explained by the relatively thin CSF layer. At this resolution (2 mm thickness, 2 mm segmentation/mesh resolution) the elements of the CSF compartment are no longer completely connected via

faces, but often only via shared vertices (cf. Figure 4.13, left column). Using such a coarse model, the current is "blocked" in some regions although in the real geometry it is not. In this case, the CG-FEM shows slightly better results, as it allows the current to also flow through a single vertex, even though this is not strictly correct from a physical point of view. In contrast, the DG-FEM solution exactly fulfills the intuitive expactation in this particular geometry; the main current is channeled through the CSF, but due to the wrong representation of the CSF it yields slightly wrong currents (compared to the real geometry) and thereby reduces the usually very strong current in the highly-conductive CSF compartment. This might explain the slight advantages of the CG-FEM with regard to numerical accuracy for model *seg_2_res_2_r84* (cf. especially lnMAG in Figures 4.9, 4.10), which are in agreement with the strong lnMAG effect of the CSF as shown in Chapter 3. Still, it has to be pointed out that these geometry errors in the CSF only have a minor effect, as they do not block the current completely but only divert it slighty.

Overall, these results show benefits of the newly derived DG-FEM approach and motivate the introduction of this new numerical approach for solving the EEG forward problem. Furthermore, the DG-FEM approach allows for an intuitive interpretation of the results in the presence of geometry artifacts.

As shown in the presented studies, inaccuracies in the approximation of the geometry and resulting current leakages might become significant sources of error when using regular hexahedral meshes with coarse resolutions. However, possibilities to avoid such errors have been proposed. Vallaghé and Papadopoulo (2010) introduced a trilinear immersed finite element method to solve the EEG forward problem, which allows the use of structured hexahedral meshes, i.e., the mesh structure is independent of the physical boundaries. The interfaces are then represented by level-sets and finally considered using special basis functions. This method is still based on a CG-FEM formulation, so that the behaviour when the thickness of single compartments is in the range of the resolution of the underlying mesh is unclear, especially when both the compartment boundaries between CSF and skull (inner skull surface) and skull and skin (outer skull surface) are contained in one element; it is probable that it suffers from the same problems as the common CG-FEM in such situations. Unfortunately, no further in-depth analysis of this approach has been performed until now to the best of the author's knowledge. The cut-cell DG approach presented by Nüßing et al. (2015) has the same advantageous features with regard to the representation of the geometry as the approach presented by Vallaghé and Papadopoulo (2010), but additionally fulfills the charge preserving property of the DG-FEM as demonstrated here.

The charge preserving property could also be achieved by certain implementations of finite volume methods (FVM). Cook and Koles (2006) presented a vertex-centered finite volume approach to solve the EEG forward problem, which shares the advantage that anisotropic conductivities can be treated quite naturally with the here presented FEM approaches. However, due to its construction, the vertex-centered approach can also be affected by unphysical current flow between high-conducting compartments that touch in single vertices as seen for the CG-FEM. This problem could be avoided using a cell-centered finite volume

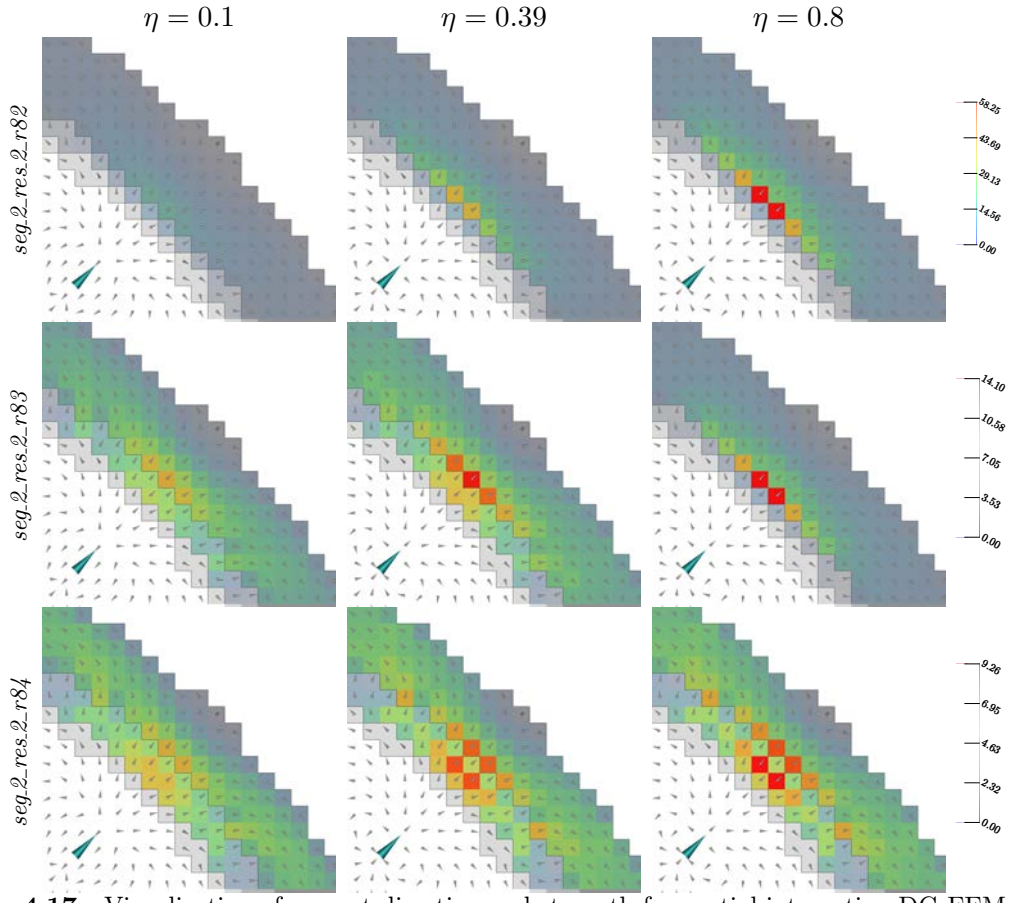

Figure 4.17.: Visualization of current direction and strength for partial integration DG-FEM and different choices of η for models *seg_2_res_2_r82* (top row), *seg_2_res_2_r83* (middle row), and *seg_2_res_2_r84* (bottom row). Dark gray lines mark compartment boundaries, the large turquoise cone represents the dipole source. The small and normalized grey cones show the directions of the current flow and, for elements belonging to skull and skin compartments, the coloring indicates the current strength. For each model the color scale is chosen according to the maximal current strength over all choices of η.

approach.

Two aspects concerning the DG approaches were not explicitly evaluated in this chapter. One is the computational effort. Due to the more complex structure (cf. Equation (4.33)), the setup of the stiffness matrix and the iterative solving is more time-consuming for DG- than for CG-FEM when using the same mesh for both approaches. Also the setup of the right-hand side for the subtraction approach is even more time consuming for DG- than for CG-FEM. However, the setup time for a single right-hand side can be kept in the range of tens of milliseconds for the less computationally demanding partial integration DG approach. Since moreover, as for CG-based approaches, the number of equation systems that have to be solved can be limited to the number of sensors by the implementation of transfer matrices (cf. Section 2.9), the additional time effort can be reduced to an increase of the unique setup time. For a detailed analysis of computation times and memory demands for the subtraction DG approach reference is made to Ludewig (2013).

The second aspect that could not be evaluated in the scope of this thesis is the choice of the penalty parameter η. This is interesting both with regard to numerical accuracy and

computational performance. That the numerical solution is actually influenced by the choice of η, can directly be seen in the derivation of the conservation property of the discrete solution, as $\mathbf{j}_h = \{\sigma\nabla u\} - \eta\frac{\hat{\sigma}_\gamma}{\tilde{h}_\gamma}[\![u]\!]$ depends on η. Figuratively speaking, a higher value of η penalizes jumps of the solution and could possibly diminish the advantages of the DG approaches as the solution is forced towards the solution of the conforming formulation (Arnold et al., 2002). In contrast, a low value of η to a certain degree allows jumps of the numerical solution for the originally continuous potential u. Castillo (2002) compared numerical accuracy and speed of different DG formulations, namely SIPG, *local discontinuous Galerkin* (LDG), and *non-symmetric interior Penalty Galerkin* (NIPG) method, for different choices of η and concluded that for large values of η all methods achieve the same accuracy, while the symmetric methods SIPG and LDG perform better than non-symmetric methods for lower values.

Some of the computational issues that have to be considered in the choice of η were already mentioned at the end of Section 4.1.1. To ensure coercivity of the bilinear form the value of η has to be chosen high enough (cf. Lemma 5), but at the same time high values of η may cause an increase of the condition number of the system matrix A and as a consequence a decrease of the solver performance (Castillo, 2002). From this point of view, it seems desirable to choose η as low as possible. To avoid a loss of stability, lower bounds for η in the SIPG or SWIPG formulation were derived in different scenarios (Ainsworth and Rankin, 2012; Di Pietro and Ern, 2012; Epshteyn and Rivière, 2007; Shahbazi, 2005). However, these bounds have practical limitations, such as being mesh dependent, costly to compute, or limited to the 2d-case. Thus, η is often chosen user-dependent as it was also done here (Di Pietro and Ern, 2012). In the numerical evaluations, $\eta = 0.390625$ was chosen according to Engwer et al. (submitted); Ludewig (2013), so that coercivity of the bilinearform was guaranteed for all considered models.

Figure 4.17 illustrates the effect of varying η on the simulated volume currents for the partial integration DG approach. These are visualized for the models *seg_2_res_2_r82*, *seg_2_res_2_r83*, and *seg_2_res_2_r84* and $\eta = 0.1$, which just guarantees convergence in these head models, $\eta = 0.390625$, and $\eta = 0.8$. The results underline the interpretation that choosing a high value for η forces the solution towards the CG-FEM solution, leading to higher peak currents, while choosing a very low η results in a smoother current distribution. This is especially visible for model *seg_2_res_2_r82*. The influence on the numerical accuracy of the EEG forward solution should therefore be investigated in further studies.

In conclusion, optimizing the value of η could possibly help to further increase accuracy and speed of the DG approaches on the one hand. On the other hand, empirically estimating an optimal value of η for each considered mesh would clearly complicate the application in praxis and is a complicated task if no reference solution is known. These aspects have to be balanced and should be kept in mind in the comparisons with the Mixed-FEM in the following chapter, where the choice $\eta = 0.390625$ is retained.

5

A Mixed-FEM Approach to Solve the EEG Forward Problem

In Section 2.4, an approach to model the source dipole by lowest-order Raviart-Thomas (RT_0) basis functions as it was proposed by Pursiainen et al. (2011) was evaluated. RT_0 elements are particularly interesting as a source model as they provide a simple means to model a divergence-conforming primary current vector field that is square integrable.

However, the presented approach still relies on the same CG-FEM formulation as introduced in Chapter 2. As shown in Chapter 4, this formulation can lead to numerical inaccuracies in some scenarios, e.g., when the volume conductor contains very thin, low-conducting layers such as the skull compartment. A first approach to tackle these problems was presented in Chapter 4, where formulations of subtraction and partial integration approach in the DG-framework were derived and it was shown that the effect of unwanted leakages through the skull compartment can thereby be prevented.

This chapter is devoted to the derivation of an approach to solve the EEG forward problem using a mixed finite element method (M-FEM). This method shares the property of conservation of charge with the DG-FEM by construction (Barrenechea et al., 2007; Ewing et al., 1999) and should thereby also prevent unwanted current leakages. Furthermore, it provides a natural way to implement RT_0 elements as primary current $\mathbf{j}^p$, since these elements are used as test and trial functions in this approach.

To derive the M-FEM formulation of the EEG forward problem, the equation system (1.10) instead of the previously used Poisson-type equation (1.11) is used as starting point. Thereby, the current flow $\mathbf{j}$, which was eliminated in the original derivation to achieve the second order PDE (1.11), becomes an additional unknown besides the potential u.

Before deriving the discretization, we recall the function spaces and basis functions that are used. While lowest-order Raviart-Thomas functions are used to discretize the electric current $\mathbf{j}$

in this chapter, also the use of higher order functions is possible. The potential u is discretized using P_0 functions, i.e., the indicator function on each element.

5.1. Variational Formulation

As mentioned, the basic function space in which we search for a solution for the potential u is the space of square integrable functions, $L^2(\Omega)$. To model the current, the vector-valued function space $H(\mathrm{div};\Omega)$ is used, which is a natural solution space for the current in the mixed formulation of the forward problem. We recall its definition,

$$H(\mathrm{div};\Omega) \coloneqq \left\{\mathbf{q} \in L^2(\Omega)^3 : \nabla\cdot\mathbf{q} \in L^2(\Omega)\right\},$$

and note that akin to the scalar-valued Sobolev spaces H^k this space becomes a Hilbert space with the norm

$$\|\mathbf{q}\|_{H(\mathrm{div};\Omega)} \coloneqq \left(\|\mathbf{q}\|^2_{L^2(\Omega)^3} + \|\nabla\cdot\mathbf{q}\|^2_{L^2(\Omega)}\right)^{\frac{1}{2}}. \tag{5.1}$$

The choice of $H(\mathrm{div};\Omega)$ can be motivated by the fact that with $\mathbf{E}$ also $\mathbf{j}-\mathbf{j}^p$ is a gradient field in the case of piecewise constant conductivities, as it is clear from the definition of the potential u in (1.8), and thereby curl-free. We introduce a subspace $H_*(\mathrm{div},\Omega)$ of $H(\mathrm{div};\Omega)$, such that the boundary condition $\langle\mathbf{j},\mathbf{n}\rangle = 0$ on $\partial\Omega = \Gamma$ is fulfilled by definition:

$$H_*(\mathrm{div},\Omega) \coloneqq \{\mathbf{q} \in H(\mathrm{div};\Omega) : \langle\mathbf{q}|_{\partial\Omega},\mathbf{n}\rangle = 0\} \tag{5.2}$$

Using these spaces, we introduce the weak formulation of (1.10):

$$\int_\Omega \langle\sigma^{-1}\mathbf{j},\mathbf{q}\rangle\,\mathrm{d}x - \int_\Omega \nabla\cdot\mathbf{q}u\,\mathrm{d}x = \int_\Omega \langle\sigma^{-1}\mathbf{j}^p,\mathbf{q}\rangle\,\mathrm{d}x \quad \text{for all } \mathbf{q}\in H_*(\mathrm{div},\Omega), \tag{5.3a}$$

$$\int_\Omega \nabla\cdot\mathbf{j}v\,\mathrm{d}x = 0 \quad \text{for all } v\in L^2(\Omega). \tag{5.3b}$$

The derivatives are shifted to the vector-valued functions here; this is the so-called *dual mixed formulation* of the Poisson problem (Arnold, 1990). For the following proof of existence and uniqueness of a solution of (5.3) it is reasonable to define the bilinearforms

$$a(\mathbf{p},\mathbf{q}) \coloneqq (\sigma^{-1}\mathbf{p},\mathbf{q})_{L^2(\Omega)^3}, \tag{5.4a}$$

$$b(\mathbf{p},v) \coloneqq (\nabla\cdot\mathbf{p},v)_{L^2(\Omega)} \tag{5.4b}$$

and the functional

$$l(\mathbf{q}) \coloneqq (\sigma^{-1}\mathbf{j}^p,\mathbf{q})_{L^2(\Omega)^3} \tag{5.5}$$

for $\mathbf{p},\mathbf{q}\in H_*(\mathrm{div},\Omega)$, $v\in L^2(\Omega)$, $l\in H(\mathrm{div};\Omega)'$, $\sigma\in L^\infty(\Omega)$, $\sigma>0$. As in the previous derivations, we leave the subspace of $L^2(\Omega)$ in which v lives, the actual definiton of $\mathbf{j}^p$, and

possible further restrictions on σ open for now and specify them when it is necessary.
Thereby, (5.3) reads

Find $(u, \mathbf{j}) \in L^2(\Omega) \times H_*(\mathrm{div}, \Omega)$, such that

$$a(\mathbf{j}, \mathbf{q}) + b(\mathbf{q}, u) = l(\mathbf{q}) \text{ for all } \mathbf{q} \in H_*(\mathrm{div}, \Omega), \tag{5.6a}$$

$$b(\mathbf{j}, v) = 0 \text{ for all } v \in L^2(\Omega). \tag{5.6b}$$

In this formulation the saddle point structure of problem (5.6) and thus also (5.3) is recognizable. As a consequence, the so far developed theory for proving existence and uniqueness of a solution, which mainly relied on the Lemma of Lax-Milgram (Lemma 1), is not applicable. Indeed, while the boundedness is satisfied for operator a as defined in (5.4a), ellipticity is not given. Thus, our theoretical framework needs to be expanded.

5.2. Existence and Uniqueness of a Weak Solution

As mentioned, the so far derived theory for systems of PDEs does not apply for problem (5.3)/(5.6). To prove existence and uniqueness of a solution, it is necessary that the operator b fulfills an *inf-sup condition*, which is in this case also called *LBB condition*, named after the mathematicians *Ladyzhenskaya*, *Babuska*, and *Brezzi*.
First, necessary conditions to show existence and uniqueness of a solution for general problems of saddle point structure are derived and it is then shown that problem (5.6) fulfills these conditions.
Let Q and V be Hilbert spaces and $X \coloneqq Q \times V$. We consider a general saddle point problem of structure

Find $(p, u) \in X$, such that

$$a(u, v) + b(v, p) = \langle l, v \rangle \quad \text{for all } v \in V \tag{5.7a}$$

$$b(u, q) = \langle g, q \rangle \quad \text{for all } q \in Q. \tag{5.7b}$$

with continuous bilinear forms

$$a : V \times V \to \mathbb{R},\ b : V \times Q \to \mathbb{R}, \text{ and } l \in V',\ g \in Q'.$$

Theorem 5. *Problem* (5.7) *admits a unique solution* $(p, u) \in X$*, iff*

(i) The bilinear form a *is* V_0*-elliptic, i.e., it exists* $\alpha > 0$ *such that*

$$a(v, v) > \alpha \|v\|_V^2 \text{ for all } v \in V_0 \tag{5.8}$$

with V_0 *being the kernel of* b*,* $V_0 \coloneqq \{v \in V : b(v, q)_{L^2(\Omega)} = 0 \text{ for all } q \in Q\}$.

(ii) *The bilinear form b fulfills an inf-sup condition (LBB condition), i.e., it exists $\beta > 0$ such that*

$$\inf_{q \in Q \setminus \{0\}} \sup_{v \in V \setminus \{0\}} \frac{b(v,q)}{\|v\|_V \|q\|_Q} \geq \beta. \tag{5.9}$$

Proof. Braess (2007, p. 124ff); Braack (2012, 9.1) □

A useful tool to proove the inf-sup condition for discrete subspaces, $V_h \subset V$, $Q_h \subset Q$, when it is already known to hold in the continuous formulation, is *Fortin's criterion.*

Theorem 6 (Fortin's criterion; Braess, 2007; Brezzi and Fortin, 1991)**.** *Let the bilinearform $b : V \times Q \to \mathbb{R}$ fulfill the inf-sup condition. Further assume that for the subspaces V_h and Q_h there exists a bounded, linear projection $\Pi_h : V \to V_h$, such that*

$$b(v - \Pi_h v, q_h) = 0 \quad \text{for all } q_h \in Q_h. \tag{5.10}$$

If $\|\Pi_h\| < C$ for some constant C independent of h, also V_h and Q_h fulfill the inf-sup condition.

Proof. For $q_h \in Q_h$, we have

$$\beta \|q_h\|_Q \leq \sup_{v \in V \setminus \{0\}} \frac{b(v,q_h)}{\|v\|_V} = \sup_{v \in V \setminus \{0\}} \frac{b(\Pi_h v, q_h)}{\|v\|_V} \leq c \sup_{v \in V \setminus \{0\}} \frac{b(\Pi_h v, q_h)}{\|\Pi_h v\|_V} = c \sup_{v_h \in V_h \setminus \{0\}} \frac{b(v_h, q_h)}{\|v_h\|_V}.$$

□

Corollary 4. *For every $l \in H^1(\Omega)'$, the problem* (5.6) *admits a unique solution $(u, \mathbf{j}) \in L^2(\Omega) \times H(\mathrm{div}; \Omega)$. Furthermore, $u \in H^1(\Omega)$.*

Proof. This proof mainly follows the ideas of the proof given by Braack (2012, 9.5). We have $V = H_*(\mathrm{div}, \Omega)$ and $Q = L^2(\Omega)$. Following Theorem 5 it has to be shown that the bilinear form a from (5.4a) is V_0-elliptic and b from (5.4b) fulfills the inf-sup condition.

(i) a is V_0-bounded and thus continuous. The kernel of b is

$$V_0 = \{v \in V : (\nabla \cdot v, q) = 0 \text{ for all } q \in L^2(\Omega)\}. \tag{5.11}$$

Since with $v \in V_0 \subset H(\mathrm{div}; \Omega)$ we have $\nabla \cdot v \in L^2(\Omega)$, it follows that $\|\nabla \cdot v\|_{L^2(\Omega)} = 0$ and thus

$$\begin{aligned} a(v,v) &\geq \underbrace{\min_{\mathbf{x} \in \Omega} \sigma^{-1}(\mathbf{x})}_{=\alpha} \|v\|^2_{L^2(\Omega)^3} = \alpha \|v\|^2_{L^2(\Omega)^3} \\ &= \alpha(\|v\|^2_{L^2(\Omega)^3} + \|\nabla \cdot v\|^2_{L^2(\Omega)}) = \alpha \|v\|^2_{H(\mathrm{div};\Omega)}. \end{aligned} \tag{5.12}$$

(ii) Let $q \in L^2(\Omega) \setminus \{0\}$. Since $C_0^\infty(\Omega)$ is dense in $L^2(\Omega)$, it exists a $\tilde{q} \in C_0^\infty(\Omega)$, such that

$$\|q - \tilde{q}\|^2_{L^2(\Omega)} \leq \frac{1}{2} \|q\|^2_{L^2(\Omega)} \tag{5.13}$$

We now define a $v \in L^2(\Omega)^3$ by setting its first component

$$v_1(\mathbf{x}) = v_1(x_1, x_2, x_3) \coloneqq \int_{-\infty}^{x_1} \tilde{q}(t, x_2, x_3)\mathrm{d}t. \tag{5.14}$$

The integral is well-defined, since Ω is by assumption bounded. The other components of v are set to zero, $v_2 = v_3 \equiv 0$. We now have

$$\nabla \cdot v = \frac{\partial v_1}{\partial x_1} = \tilde{q}. \tag{5.15}$$

Using the properties of the scalar product and the parallelogram equality *(1)*, (5.13), and Young's inequality *(2)*, we have

$$\begin{aligned} b(v,q) &= (\nabla \cdot v, q)_{L^2(\Omega)} = (\tilde{q}, q)_{L^2(\Omega)} \\ &\overset{(1)}{=} \frac{1}{2}\left(\|\tilde{q}\|^2_{L^2(\Omega)} + \|q\|^2_{L^2(\Omega)} - \|\tilde{q} - q\|^2_{L^2(\Omega)}\right) \\ &\overset{(5.13)}{\geq} \frac{1}{2}\left(\|\tilde{q}\|^2_{L^2(\Omega)} + \frac{1}{2}\|q\|^2_{L^2(\Omega)}\right) \\ &\geq \frac{1}{4}\left(\|\tilde{q}\|^2_{L^2(\Omega)} + \|q\|^2_{L^2(\Omega)}\right) \\ &\overset{(2)}{\geq} \frac{1}{2}\|\tilde{q}\|_{L^2(\Omega)}\|q\|_{L^2(\Omega)}. \end{aligned}$$

With Friedrichs' inequality and a constant $c = c(\Omega)$, we have

$$\begin{aligned} \|v\|_{L^2(\Omega)^3} &\leq c|v|_{H^1(\Omega)} = c\|\nabla \cdot v\|_{L^2(\Omega)}, \\ \|v\|^2_{H(\mathrm{div};\Omega)} &= \|v\|^2_{L^2(\Omega)^3} + \|\nabla \cdot v\|^2_{L^2(\Omega)} \\ &\leq (1 + c^2)\|\nabla \cdot v\|^2_{L^2(\Omega)} \\ &\leq (1 + c^2)\|\tilde{q}\|^2_{L^2(\Omega)}. \end{aligned}$$

With $c' = (1 + c^2)^{-1/2} > 0$ it follows that

$$\frac{b(v,q)}{\|v\|_{H(\mathrm{div};\Omega)}\|q\|_{L^2(\Omega)}} \geq \frac{1}{2}\frac{\|\tilde{q}\|_{L^2(\Omega)}\|q\|_{L^2(\Omega)}}{\|v\|_{H(\mathrm{div};\Omega)}\|q\|_{L^2(\Omega)}} \geq \frac{c'}{2}\frac{\|\tilde{q}\|_{L^2(\Omega)}\|q\|_{L^2(\Omega)}}{\|\tilde{q}\|_{L^2(\Omega)}\|q\|_{L^2(\Omega)}} \geq \frac{c'}{2}. \tag{5.16}$$

Thus, the LBB condition is fulfilled and we have a unique solution $(u, \mathbf{j}) \in L^2(\Omega) \times H(\mathrm{div};\Omega)$.

Since $C_0^\infty(\Omega)^3 \subset H_*(\mathrm{div}, \Omega)$, we have for any $\varphi \in C_0^\infty(\Omega)^3$ and the solution u

$$\begin{aligned} (\nabla \cdot \varphi, u)_{L^2(\Omega)} = b(\varphi, u) &= -a(\mathbf{j}, \varphi) + l(\varphi) \\ &= -(\sigma^{-1}\mathbf{j}, \varphi)_{L^2(\Omega)^3} + (\sigma^{-1}\mathbf{j}^p, \varphi)_{L^2(\Omega)^3} \\ &= (\sigma^{-1}(\mathbf{j}^p - \mathbf{j}), \varphi)_{L^2(\Omega)^3} \text{ for all } \varphi \in (C_0^\infty\Omega)^3. \end{aligned} \tag{5.17}$$

For $i \in \{1, 2, 3\}$ we now explicitly set $\varphi_i = \tilde{\varphi}$, $\tilde{\varphi} \in C_0^\infty(\Omega)$, and $\varphi_j \equiv 0$ for $j \neq i$. We

have $(u, \partial\tilde{\varphi}/\partial x_i)_{L^2(\Omega)} = ((\sigma^{-1}(\mathbf{j}^p - \mathbf{j}))_i, \tilde{\varphi})_{L^2(\Omega)}$ for any $\tilde{\varphi} \in C_0^\infty(\Omega)$ and $i \in \{1,2,3\}$ and thus the weak derivative $\partial u/\partial x_i = (\sigma^{-1}(\mathbf{j}^p - \mathbf{j}))_i$. It follows that $u \in H^1(\Omega)$ with weak derivative $\nabla u = \sigma^{-1}(\mathbf{j}^p - \mathbf{j})$.

□

5.3. Discretization

Next, the finite dimensional subspaces of $L^2(\Omega)$ and $H(\mathrm{div};\Omega)$ to which we restrict the numerical solution are fixed. As mentioned, $H(\mathrm{div};\Omega)$ is approximated using the space RT_0 of lowest-order Raviart-Thomas elements that was already introduced in Section 2.4. Here, the continuity of the normal component $\langle \mathbf{q}, \mathbf{n} \rangle$ becomes especially important, as it is a necessary requirement to ensure that the integration by parts formula holds, which was used in the construction of the dual mixed formulation. Some further properties of these elements are recited here, for a more detailed presentation it is referred to Brezzi and Fortin (1991); Nédélec (1980).

Proposition 7. *For any tetrahedral/hexahedral element T we have for $\mathbf{q} \in RT_k(T)$*

$$\begin{aligned} \nabla \cdot \mathbf{q} &\in P_k(T)/Q_k(T), \\ \langle \mathbf{q}, \mathbf{n}_{\partial T} \rangle &\in R_k(\partial T) \end{aligned}$$

with

$$R_k(\partial T) = \{p \in L^2(\partial T) : p|_{f_i} \in P_k/Q_k(f_i) \text{ for all } f_i \in \mathcal{F}(T)\}$$

Proof. $\mathbf{q} \in RT_k(T)$ can be written as $\mathbf{q} = \mathbf{q}_0 + \mathbf{x}p_k$ with $\mathbf{q}_0 \in (P_k/Q_k)^d$, $p_k \in P_k/Q_k$. Thus, it is clear that also $\nabla \cdot \mathbf{q} \in P_k/Q_k$.
We multiply $\mathbf{q}$ by the face normal vector $\mathbf{n}_{\partial T}$, $\langle \mathbf{q}, \mathbf{n}_{\partial T} \rangle = \langle \mathbf{q}_0, \mathbf{n}_{\partial T} \rangle + \langle \mathbf{x}, \mathbf{n}_{\partial T} \rangle p_k$. Since $\langle \mathbf{x}, \mathbf{n}_{\partial T} \rangle$ is constant on a face f_i, $\langle \mathbf{q}, \mathbf{n}_{\partial T} \rangle \in P_k/Q_k$. □

While the introduction of the RT_0 elements in Section 2.4 was rather informal, these would commonly be defined by fixing the degrees of freedom on each element $T \in \mathcal{T}_h$. For reasons of completeness, we indicate the definition of the degrees of freedom here. To ensure continuity of $\langle \mathbf{q}, \mathbf{n} \rangle$ over element interfaces, the degrees of freedom Σ_k for $\mathbf{q} \in RT_k(T)$ are in the tetrahedral case chosen to be (Brezzi and Fortin, 1991)

$$\begin{aligned} \int_{\partial T} \langle \mathbf{q}, \mathbf{n}p \rangle \, \mathrm{d}s, \quad & p \in P_k(\partial T), \\ \int_T \langle \mathbf{q}, \mathbf{p} \rangle \, \mathrm{d}x, \quad & \mathbf{p} \in (P_{\max(k-1,0)}(T))^3, \end{aligned} \tag{5.18}$$

and accordingly with properly defined subspaces of Q_k in the hexahedral case. We have $\mathbf{q} \equiv 0$ if the degrees of freedom are 0 for all $p \in P_k(\partial T)$ and $\mathbf{p} \in (P_{\max(k-1,0)}(T))^3$. From

this definition, it can be deduced that the dimensions of the RT_k space for each element are (Brezzi and Fortin, 1991)

$$\dim RT_k(T) = \frac{1}{2}(k+1)(k+2)(k+4) \quad \text{for a tetrahedron T,}$$
$$\dim RT_k(H) = 3(k+1)^2(k+2) \quad \text{for a hexahedron H.}$$

In the following, $k = 0$ is chosen and it suffices to recognize that $\dim RT_0(T)$ is just the number of faces per element, corresponding to the previous interpretation of face-bound degrees of freedom. We furthermore note that the set of RT_0 elements is unisolvent in $H(\mathrm{div};\Omega)$ (Nédélec, 1980).
To approximate $L^2(\Omega)$, the space of piecewise constant functions $P_0 = M^0$ is chosen (cf. (2.4))

$$P_0(\mathcal{T}_h) \coloneqq \left\{ v \in L^2(\Omega) : v|_T \in P_0(T) \text{ for all } T \in \mathcal{T}_h \right\}. \tag{5.19}$$

In the following, this space is simply denoted as P_0. It is obvious that P_0 is not a subspace of $H^1(\Omega)$, however, we have $\mathrm{div}\, RT_0 \subset P_0$. For the 2d-case the resulting degrees of freedom on each element are illustrated in Figure 5.1 (right).

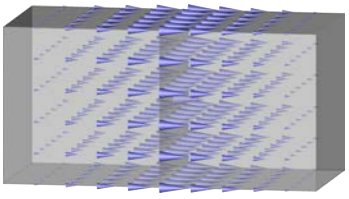

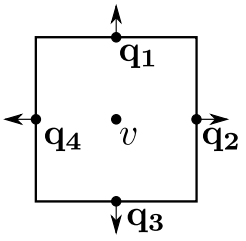

Figure 5.1.: RT_0 basis function on hexahedral mesh elements (left), degrees of freedom for rectangular mesh, $\mathbf{q_i}$ indicating vector-valued, v indicating scalar ones, respectively (right)

Corollary 5. *The choice $V_h = RT_0$ and $Q_h = P_0$ fulfills the conditions of Theorem 5.*

Proof. The V_0-ellipticity follows directly, since $RT_0(\mathcal{T}_h(\Omega)) \subset H(\mathrm{div};\Omega)$. To prove the inf-sup condition, Fortin's criterion (Theorem 6) can be used, i.e., it has to be shown that for the operator b and the subspaces V_h and Q_h a bounded, linear projection $\Pi_h : V \to V_h$ exists, such that

$$b(v - \Pi_h v, q_h) = 0 \quad \text{for all } q_h \in Q_h.$$

This can be fulfilled by defining Π_h via a PDE of type (5.6) (Braess, 2007, p. 143f; Brezzi and Fortin, 1991, p. 137f; Arnold et al., 2006). □

As next step to discretize the equation system (5.3), the basis functions for the discrete spaces are defined. For the space P_0, this can simply be done by choosing the indicator function on each element $T_i \in \mathcal{T}_h$

$$v_i(\mathbf{x}) \coloneqq \mathbb{1}_{T_i}(\mathbf{x}) = \begin{cases} 1 \text{ if } \mathbf{x} \in T_i \\ 0 \text{ otherwise} \end{cases} \text{ for } T_i \in \mathcal{T}_h. \tag{5.20}$$

Due to the face-bound degrees of freedom, the basis functions for the Raviart-Thomas space can be defined by the normal component of the flux over the face $f_j \in F(\mathcal{T}_h)$ between two elements of the triangulation. The actual definitions were given in Section 2.4. We denote by $S_h^{P_0}$ the set of $P_0(\mathcal{T}_h)$ basis functions and by $S_h^{RT_0}$ the set of $RT_0(\mathcal{T}_h)$ basis functions.
Writing the discrete solutions u_h and $\mathbf{j}_h$ in the basis of the respective function space, i.e., $u_h = \sum_i u_i v_i$, $v_i \in S_h^{P_0}$, $\mathbf{j}_h = \sum_k j_k \mathbf{w}_k$, $\mathbf{w}_k \in S_h^{RT_0}$, and defining $b_i \coloneqq \int_\Omega \langle \sigma^{-1}\mathbf{j}^p, \mathbf{w}_i\rangle \,\mathrm{d}x$, we have the matrix equation

$$\underbrace{\begin{pmatrix} A & B^T \\ B & 0 \end{pmatrix}}_{\coloneqq K} \begin{pmatrix} j \\ u \end{pmatrix} = \begin{pmatrix} b \\ 0 \end{pmatrix} \tag{5.21}$$

with

$$A_{i,j} = \int_\Omega \langle \sigma^{-1}\mathbf{w}_i, \mathbf{w}_j\rangle \,\mathrm{d}x \qquad B_{k,j} = \int_\Omega v_k(\nabla \cdot \mathbf{w}_j)\,\mathrm{d}x \tag{5.22}$$

$$\text{for } v_k \in S_h^{P_0},\ \mathbf{w}_i, \mathbf{w}_j \in S_h^{RT_0}.$$

For the submatrices A and B we have $m_A = n_A = \#\text{faces}$ and $m_B = \#\text{elements}$, $n_B = \#\text{faces}$, respectively, and thus the dimension of K is $m_K = n_K = \#\text{faces} + \#\text{elements}$.
In the following, we assume a partition $\mathcal{T}_h(\Omega)$ into hexahedra throughout.
Similarly to the Whitney approach presented in Section 2.4, the definition of b easily allows to solve the EEG forward problem for a primary current distribution $\mathbf{j}^p \in L^2(\Omega)$. However, in contrast to the so far presented approaches, also for the choice of a current dipole, $\mathbf{j}^p = \mathbf{m}\delta_{\mathbf{x}_0} \notin L^2(\Omega)$, the integral $\int_\Omega \langle \sigma^{-1}\mathbf{j}^p, \mathbf{w}_i\rangle \,\mathrm{d}x$ can be directly evaluated now. We can define b as

$$b_i = \int_\Omega \langle \sigma^{-1}\mathbf{m}\delta_{\mathbf{x}_0}, \mathbf{w}_i\rangle \,\mathrm{d}x = \begin{cases} \langle \sigma^{-1}\mathbf{m}, \mathbf{w}_k(\mathbf{x}_0)\rangle \text{ if } \mathbf{x}_0 \in \operatorname{supp}\mathbf{w}_i \\ 0 \text{ otherwise.} \end{cases} \tag{5.23}$$

In the following, directly applying b as a right-hand side is called the *direct approach*. It can be interpreted as a smoothing/blurring of the singular primary current $\mathbf{j}^p$. In contrast to the Whitney CG approach, the basis functions used to approximate the current distribution are this time naturally occuring in the finite element space.
Besides this intuitive way to calculate the right-hand side vector it is also possible to proceed similar as in Section 2.4, i.e., to calculate a projection of the current source from the vector-valued current space to the potential space. A projection matrix is already given by the matrix

B, which is similar to the matrix G in Section 2.4, just that the potential is approximated in P_0 instead of P_1 here. The projected right-hand side is then given by

$$h^{proj} = Bb \tag{5.24}$$

and (5.21) becomes

$$\begin{pmatrix} A & B^T \\ B & 0 \end{pmatrix} \begin{pmatrix} j \\ u \end{pmatrix} = \begin{pmatrix} 0 \\ h^{proj} \end{pmatrix}. \tag{5.25}$$

Both approaches are evaluated in Section 5.7.

5.4. Error Estimates for the Discrete Solution

As for the CG- and DG-FEM in Section 2.7 and 4.1.4, this section is devoted to error bounds for the previously derived discretization. These are mainly given without proof, for details, unless indicated differently, it is referred to the book of Brezzi and Fortin (1991).
While the discontinuous conductivity distribution σ remains a problem and general error estimates for solutions of (5.7) can again only be derived under the simplifying assumption of a single-layer model, the regularity of the source term is unproblematic when adapting the interpretation also used for the Whitney approach in Section 2.7. The definition (5.23) of b_i allows to interpret the right-hand side as a superposition of RT_0 basis functions, $\mathbf{j}^p_{rt} = \sum \langle \mathbf{j}^p, \mathbf{w}_i \rangle \mathbf{w}_i \in H(\mathrm{div}; \Omega)$, instead of the singular source term $\mathbf{j}^p$. A drawback of this interpretation is that only the convergence towards the mollified source $\mathbf{j}^p_{rt}$ is evaluated, while it remains unclear how well $\mathbf{j}^p_{rt}$ approximates the dipole source $\mathbf{j}^p$.
We start with a general derivation of error estimates, again assuming σ constant and $\partial\Omega$ (piecewise) C^2. For general finite dimensional subspaces $Q_h \hookrightarrow Q$ and $V_h \hookrightarrow V$ existence and uniqueness of a solution $p_h \in Q_h$ and $u_h \in V_h$ are given after a straight-forward definition of the operators a_h and b_h (Brezzi and Fortin, 1991). We define

$$\mathrm{Ker}\, B_h = \{v_h \in V_h : b(v_h, q_h) = 0 \text{ for all } q_h \in Q_h\}, \tag{5.26a}$$

$$\mathrm{Ker}\, B_h^t = \{q_h \in Q_h : b(v_h, q_h) = 0 \text{ for all } v_h \in V_h\} \tag{5.26b}$$

and have the general approximation properties

Theorem 8. *Let* (1.13) *admit a unique solution. Let* a_h *fulfill the condition*

$$\inf_{u_h \in \mathrm{Ker}\, B_h} \sup_{v \in \mathrm{Ker}\, V_h} \frac{a_h(u_h, v_h)}{\|u_h\|_V \|v_h\|_V} \geq \alpha \tag{5.27}$$

and $\mathrm{Ker}\, B_h \neq \emptyset$. *Let* $(p_h, u_h) \in X_h$ *be a solution of the redefined problem* (5.7). *Then, there exist constants* c_1 *and* c_2 *independent of* h *such that*

$$\|u - u_h\|_V \leq c_1 \inf_{v_h \in V_h} \|u - v_h\|_V + c_2 \inf_{q_h \in Q_h} \|p - q_h\|_Q. \tag{5.28}$$

If moreover $\operatorname{Ker} B_h \subset \operatorname{Ker} B$*, we have*

$$\|u - u_h\|_V \leq c_1 \inf_{v_h \in V_h} \|u - v_h\|_V. \tag{5.29}$$

With k_0 *being a constant depending on* b *and* b_h *and* $k_h \geq k_0$ *depending on* h*, we have*

$$\|p - p_h\|_{Q/\operatorname{Ker} B_h^t} \leq \left(1 + \frac{\|b\|}{k_h}\right) \inf_{q_h \in Q_h} \|p - q_h\|_Q + \frac{\|a\|}{k_h} \|u - u_h\|_V. \tag{5.30}$$

Proof. Brezzi and Fortin (1991, p. 56) □

Theorem 9. *Let* $(p, u) \in Q \times V$ *and* $(p_h, u_h) \in Q_h \times V_h$ *be solutions of* (5.7)*. Assume that the inf-sup condition*

$$\inf_{q_h \in Q_h} \sup_{v_h \in V_h} \frac{b(v_h, q_h)}{\|v_h\|_{V_h} \|q_h\|_{Q_h/\operatorname{Ker} B^t}} \geq \kappa_0 > 0 \tag{5.31}$$

is satisfied and let a *be uniformly coercive on* $\operatorname{Ker} B_h$*, i.e., there exists* $\alpha_0 > 0$ *such that*

$$a(v_{0h}, v_{0h}) \geq \alpha_0 \|v_{0h}\|_{V_h}^2 \text{ for all } v_{0h} \in \operatorname{Ker} B_h. \tag{5.32}$$

Then, one has the following estimate with a constant c *depending on* $\|a\|$*,* $\|b\|$*,* κ_0*, and* α_0 *but independent of* h*:*

$$\|u - u_h\|_{V_h} + \|p - p_h\|_{Q_h/\operatorname{Ker} B^t} \leq c \left(\inf_{v_h \in V_h} \|u - v_h\|_V + \inf_{q_h \in Q_h} \|p - q_h\|_Q \right). \tag{5.33}$$

Proof. Brezzi and Fortin (1991, p. 60) □

With the choices $V = H(\operatorname{div}; \Omega)$, $V_h = RT_0(\mathcal{T}_h)$, $Q = L^2(\Omega)$, and $Q_h = P_0(\mathcal{T}_h)$ the conditions of Theorems 8 and 9 are fulfilled (Brezzi and Fortin, 1991, p. 139) and one can conclude the approximation properties

$$\|u - u_h\|_{L^2(\Omega)} \leq C_1 \inf_{v_h \in P_0} \|u - v_h\|_{L^2(\Omega)}, \tag{5.34}$$

$$\|\mathbf{j} - \mathbf{j}_h\|_{H(\operatorname{div};\Omega)} \leq C_2 \left(\inf_{\mathbf{q}_h \in RT_0} \|\mathbf{j} - \mathbf{q}_h\|_{H(\operatorname{div};\Omega)} + \inf_{v_h \in P_0} \|u - v_h\|_{L^2(\Omega)} \right). \tag{5.35}$$

Using mesh dependent approximation properties of the spaces $RT_0(\mathcal{T}_h)$ and $P_0(\mathcal{T}_h)$, an upper bound for the approximation accuracy depending on $\|u\|_{H^s(\Omega)}$, $\|\mathbf{j}\|_{H^s(\Omega)}$, and h can be derived (Brezzi and Fortin, 1991, p. 139)

$$\|u - u_h\|_{L^2(\Omega)} \leq C_1 h^s \|u\|_{H^s(\Omega)}, \tag{5.36}$$

$$\|\mathbf{j} - \mathbf{j}_h\|_{L^2(\Omega)} \leq C_2 h^s (\|\mathbf{j}\|_{H^s(\Omega)^3} + \|u\|_{H^s(\Omega)}) \tag{5.37}$$

for $s \leq k + 1$ and k being the degree of the discrete spaces RT_k and P_k as before, i.e., in our case $k = 0$.

Corollary 6 (Quantitative error estimate for the Mixed-FEM direct approach in a one-layer model)**.** *Let* $(u, \mathbf{j})$ *be a solution of* (5.7)*,* $V = H(\mathrm{div}; \Omega)$ *and* $Q = L^2(\Omega)$*, with* $\langle l, v\rangle = \mathbf{j}^p_{rt} = \sum \langle \mathbf{j}^p, \mathbf{w}_i\rangle \mathbf{w}_i \in H(\mathrm{div}; \Omega)$ *and constant conductivity* σ*. Let* $(u_h, \mathbf{j}_h)$ *be a solution of the discrete problem,* $V_h = RT_0$ *and* $Q_h = P_0$*. Then, we have*

$$\|u - u_h\|_{L^2(\Omega)} \leq C_1 h \|u\|_{H^1(\Omega)}, \tag{5.38}$$

$$\|\mathbf{j} - \mathbf{j}_h\|_{L^2(\Omega)} \leq C_2 h (\|\mathbf{j}\|_{H^1(\Omega)^3} + \|u\|_{H^1(\Omega)}) \tag{5.39}$$

for constants $C_1, C_2 > 0$ *independent of* h*.*

We note that by modifying the space RT_0 (dropping the requirement of a continuous normal component and imposing it via a Lagrangian multiplier instead) the rate of convergence in h can be improved by one degree (Arnold and Brezzi, 1985; Brezzi and Fortin, 1991). Furthermore, under certain assumptions superconvergence of u_h and $\mathbf{j}_h$ can be proven (Brezzi and Fortin, 1991; Durán, 1990).
Especially in the present case, where the source term may admit large values but is only supported in a small neighborhood, error estimates in other norms, here particularly the L^∞-norm, are interesting. As an example, the inequality

$$\|u - u_h\|_{L^\infty(\Omega)} + \|\mathbf{j} - \mathbf{j}_h\|_{L^\infty(\Omega)^3} \leq c h^{k+1}. \tag{5.40}$$

holds (Brezzi and Fortin, 1991, p. 192).
As in Corollary 6, this estimate can be directly applied to the EEG forward problem in a one-layer model. Further error estimates in different norms were, e.g., derived by Douglas and Roberts (1985); Gastaldi and Nochetto (1987, 1989). As previously, most of these error estimates are derived under the assumption of Dirichlet boundary conditions.

5.5. Solving the Saddle-Point Problem

The matrix K is indefinite as no ground potential was fixed until now and has a large 0-block. Thus, directly solving 5.21 is not recommendable (Bergamaschi et al., 1994). Krylov subspace algorithms, such as variants of the CG or GMRES method, are not as efficient as for many other problems, since the commonly used methods for preconditioning fail. Nevertheless, much research has been performed trying to find preconditioning techniques that make a solution using CG-solvers possible (Axelsson, 1994; Golub and Van Loan, 1989). A different solution strategy that makes use of the fact that – unlike K – A is positive definite and non-singular is presented in this chapter following Braack (2012); Braess (2007). If we write (5.21) as a system of two equations and for now assume the direct approach, i.e.,

$$Aj + B^T u = b \tag{5.41a}$$

$$Bj = 0, \tag{5.41b}$$

we can left-multiply A^{-1} to (5.41a) and solve for j, i.e., $j = A^{-1}(b - B^t u)$. Inserting this into (5.41b) leads to

$$\begin{aligned} Bj = BA^{-1}(b - B^T u) = 0 \\ \Leftrightarrow BA^{-1}B^T u = BA^{-1}b. \end{aligned} \tag{5.42}$$

$S \coloneqq BA^{-1}B^T$ is the so-called *Schur complement*.

Lemma 12. *S is positive definite. If A is symmetric, also S is symmetric.*

Proof. Braess (2007, p. 216) □

Thus, with $h = h^{direct} \coloneqq BA^{-1}b$ (direct approach) or $h = h^{proj}$ (projected approach), solving (5.21) is reduced to solving

$$Su = h. \tag{5.43}$$

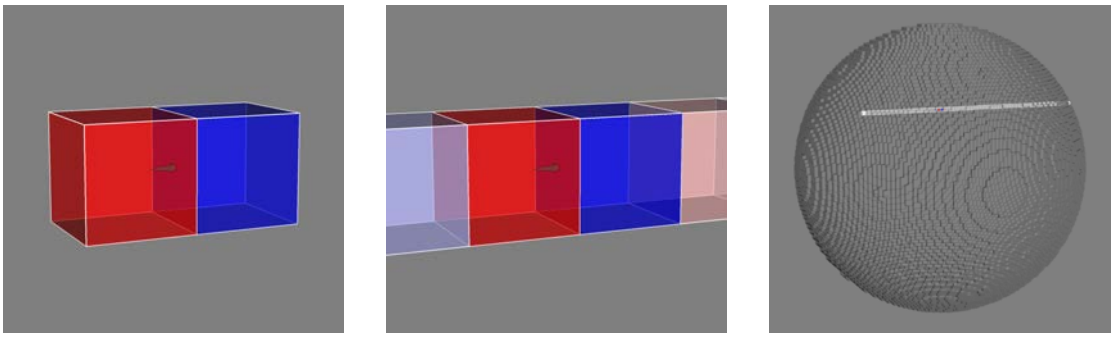

Figure 5.2.: Visualization of $h = h^{proj}$ (left), $h^{direct} = BA^{-1}b^{direct}$ (middle), and full view of the support of $h^{direct} = BA^{-1}b^{direct}$ (right) for a source positioned in the center of face f_i and direction $\mathbf{n}_{f_i}$. The coloring indicates the values for the P_0 basis function corresponding to the respective element; red is positive, blue is negative.

Remark 14. *The projection $h^{direct} = BA^{-1}b$ to the potential space causes a blurring of the current source. If a single RT_0 function is chosen as source, i.e., the source is positioned on the face f_i and the direction is $\mathbf{n}_{f_i}$, for a hexahedral mesh this leads to non-zero entries for all elements that lie "in the source direction" in the potential space (cf. Figure 5.2, middle and right; the white line indicates all elements with non-zero entries). However, most of these values are relatively small, as the truncated visualization for arbitrary dipole position and direction indicates (Figure 5.3, middle). In contrast, when applying the projection only using B as proposed in* (5.24)*, the right-hand side vector is given by $h = h^{proj}$, which only has two non-zero entries (Figure 5.2, left). This transforms accordingly to the case of arbitrarily positioned and oriented sources (Figure 5.3). The accuracies of the different representations are evaluated in Section 5.7.*

Due to the size of A, it is usually not efficient to calculate A^{-1} – and thereby also S – explicitly. Instead, A^{-1} is accessed implicitly by solving a linear equation system, i.e., instead

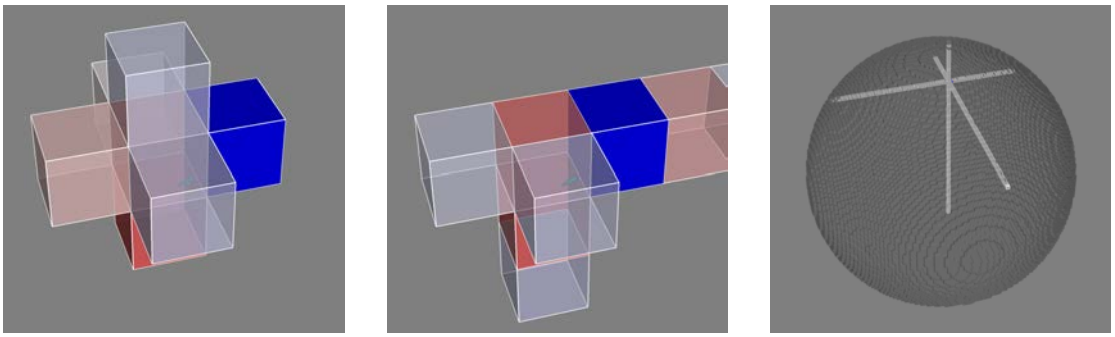

Figure 5.3.: Visualization of $h = h^{proj}$ (left), $h^{direct} = BA^{-1}b^{direct}$ truncated at 5% of maximum (middle), and full visualization of $h^{direct} = BA^{-1}b^{direct}$ (right) for dipole with random position and orientation. The coloring indicates the values for the P_0 basis function corresponding to the respective element; red is positive, blue is negative.

of calculating $x = A^{-1}y$ we solve $Ax = y$. This can usually be done very fast, e.g., using preconditioned CG-solvers. The influence of the accuracy with which this step is performed on the convergence of the solution algorithm for the full problem is evaluated in Section 5.6.1. The more challenging task is to solve Equation (5.43). A frequently described algorithm to solve (5.43) with an implicit representation of A^{-1} is the *UZAWA-algorithm* (Algorithm 1).

Algorithm 1 UZAWA algorithm with fixed step width.

Let $\alpha \in \mathbb{R}^+$, $u_0 \in \mathbb{R}^m$ and $Aj_1 = b - B^T u_0$.
For $k = 1, 2, \ldots$ calculate

$$\begin{aligned} q_k &= -Bj_k, \\ p_k &= B^T q_k, \\ h_k &= A^{-1} p_k, \\ u_k &= u_{k-1} - \alpha q_k, \\ j_{k+1} &= j_k + \alpha h_k. \end{aligned}$$

The convergence of the UZAWA-algorithm with fixed step width depends on the parameter α. Thus, the choice of α is critical. It can be shown that

Lemma 13. *For*

$$\alpha < 2\|S\|_2^{-1}$$

Algorithm 1 converges (Braess, 2007).
Let λ_{min}, λ_{max} be the minimal and maximal eigenvalue of S, respectively. Then, the optimal choice for α is

$$\alpha = \frac{2}{\lambda_{\min} + \lambda_{\max}}.$$

Proof. The UZAWA-algorithm with fixed step width corresponds to a Richardson-iteration, so that the optimal step width follows accordingly (Braack, 2012, p. 178). □

Since S is not explicitly computed, neither λ_{min} nor λ_{max} are easily accessible (this would

surely also be the case if S was explicitly computed due to the dimension of S). To resolve this problem and, even more important, to achieve a better convergence, it is useful to use an optimized step width (Braess, 2007, p. 217).

Algorithm 2 UZAWA algorithm with optimal step width.

Let $u_0 \in \mathbb{R}^m$ and $Aj_1 = b - B^T u_0$.
For $k = 1, 2, \ldots$ calculate

$$\begin{aligned} q_k &= -Bj_k, \\ p_k &= B^T q_k, \\ h_k &= A^{-1} p_k, \\ u_k &= u_{k-1} - \alpha_k q_k, \quad \alpha_k = \frac{q_k' q_k}{p_k' h_k}, \\ j_{k+1} &= j_k + \alpha_k h_k. \end{aligned}$$

It can be shown that the UZAWA-algorithm with optimal step width (Algorithm 2) is equivalent to the gradient descent method. This motivates the idea that the convergence can be further improved when switching to conjugated search directions (Algorithm 3). This algorithm is essentially equivalent to a CG algorithm for the equation system $Su = h$, where S is only implicitly given and an inner equation system has to be solved to invert A.

Algorithm 3 Conjugate UZAWA algorithm with optimal step width.

Let $u_0 \in \mathbb{R}^m$ and $Aj_1 = b - B^T u_0$. Set $d_1 = -q_1 = Bj_k$.
For $k = 1, 2, \ldots$ calculate

$$\begin{aligned} p_k &= B^T d_k, \\ h_k &= A^{-1} p_k, \\ u_k &= u_{k-1} + \alpha_k q_k, \quad \alpha_k = \frac{q_k' q_k}{p_k' h_k}, \\ j_{k+1} &= j_k - \alpha_k h_k, \\ q_{k+1} &= -Bj_{k+1}, \\ d_{k+1} &= -q_{k+1} + \beta_k d_k, \quad \beta_k = \frac{q_{k+1}' q_{k+1}}{q_k' q_k}. \end{aligned}$$

Several approaches to accelerate the UZAWA-algorithm are found in the literature, mainly concentrating on accelerating the inner iteration $Ah_k = p_k$ and improving the bad condition number of S. A frequent proposal is to replace the inner iteration $Ah_k = p_k$ by an approximate solution. Therefore, A is replaced by an approximation M that can be easily inverted (Elman and Golub, 1994; Golub and Overton, 1988). It can be shown that this leads to an improved performance at the cost of a slightly worse convergence. However, instead of this approach, we keep the original matrix A here and use a preconditioned CG-solver to solve the inner iteration. Thereby, a reasonable speed can be achieved in the present scenario. Furthermore,

one can vary the accuracy with which the inner iteration is solved. The effect on speed and convergence is investigated in Section 5.6.1. Decreasing the accuracy of the inner iteration can also be considered as an inexact UZAWA-algorithm. An optimal performance, i.e., an optimal combination of convergence and speed, was found when imposing a defect reduction in the inner iteration by a factor between 1e-3 and 1e-2 as stopping criterion.

The problem that S has a bad condition number is not resolved so far, so that it is suggested to use preconditioning also for the outer iteration. Since Algorithm 3 is equivalent to a CG algorithm for the equation system $Su = h$, the application of preconditioners in combination with Algorithm 3 can be simplified by implementing the algorithm using a CG-solver template with an implicit matrix operator to calculate Su, instead of explicitly implementing the algorithm. In the literature, several preconditioners were proposed for solving saddle point problems originating from mixed finite element formulations with the UZAWA-algorithm. It is frequently proposed to use the mass matrix of the potential space (also called pressure space due to the application in flow dynamics), i.e., $M_{i,j} = \int_\Omega \sigma v_i v_j \,\mathrm{d}x,\ v_i, v_j \in P_0(\mathcal{T}_h)$, as preconditioner (Elman and Golub, 1994). However, due to the choice of P_0 as scalar test-space this matrix is diagonal here and not expected to be an efficient preconditioner as it does not approximate S well. Also the use of BB^T as proposed by Ng et al. (1993) is only efficient in the case of constant conductivities as shown by Bergamaschi et al. (1994). Though BB^T approximates the pattern of S well enough, it does not provide a reasonable approximation of the matrix entries of S. Bergamaschi et al. (1994) instead suggest to choose a diagonal matrix D that in some sense approximates A and use $BD^{-1}B^T$ input to the preconditioner. They propose to choose $D_{i,i} = (\sum_j A_{i,j}^2)^{1/2}$ (denoted $\|A_{i\cdot}\|_2$ in the following). Besides this, also $D_{i,i} = A_{i,i}$ (denoted $\mathrm{diag}(A)$), $D_{i,i} = \sum_j A_{i,j}$ (denoted $\sum A_{i\cdot}$), and $D_{i,i} = \sum_j |A_{i,j}|$ (denoted $|A_{i\cdot}|$) are tested as preconditioners in Section 5.6.1.

The structure of the matrix $P = BD^{-1}B^T$ is identical to the structure of BB^T, since all considered choices for D are diagonal. Hence, it cannot be directly inverted. Also, due to the band structure of P, commonly chosen preconditioners such as the incomplete LU-factorization (ILU(0)) cannot be expected to be efficient (Chen, 2005, p. 330). In Section 5.6.1, the efficiency of the conjugated UZAWA-algorithm using no preconditioner, a Jacobi-preconditioner, successive over-relaxation (SOR), ILU(0)-factorization, an algebraic multigrid (AMG) method, and approximating P^{-1} by an iterative solution using an ILU(0)-CG solver is compared. All approaches were tested with different choices of D. Besides this, the performance was also compared to that of directly solving (5.21) with iterative solvers in Section 5.6.1. For this, a CG- and a BiCGStab-solver each in combination with an ILU(0)-preconditioner were used.

5.6. Implementation

Both the direct (i.e., $h = h^{direct} = BA^{-1}b$) and the projected ($h = h^{proj}$) M-FEM approach were implemented in the DUNE framework (Bastian et al., 2008a,b) using the DUNE PDELab toolbox (Bastian et al., 2010). In addition, a solver based on the UZAWA-algorithm was

implemented using the CG-solver template from the DUNE module *iterative solvers template library* (DUNE-ISTL) in combination with AMG, ILU(0), iterative, and further preconditioners.

5.6.1. Solvers

This section mainly focuses on the conjugate UZAWA-algorithm (Algorithm 3) for solving (5.21). For comparison, the performance when solving the full system (5.21) using a CG- and BiCG-solver with ILU(0) preconditioning was evaluated as well. For the UZAWA-algorithm, the interplay between accuracy of the inner solver and solving speed/convergence of the outer solver for different choices of the preconditioner was investigated. As a test scenario the single dipole scenario also used for the visualizations in Section 4.2 and the models *seg_1_res_1* and *seg_2_res_2* were chosen. In all tests the stopping criterion for the outer iteration was a relative reduction of the residual to 1e-8.

To evaluate the performance of the different solvers, besides evaluating solving times and necessary iterations, also convergence rate and defect reduction are visualized. The convergence rate indicates the ratio between the defect in the current and the previous iteration; the lower the convergence rate, the better. The defect reduction indicates the overall reduction relative to the initial defect up to the respective iteration, the steeper the decay of the curve, the better. The timing results were obtained on a PC with an Intel Core-i7 Processor at 3.40 GHz with 16 Gb of RAM running Ubuntu 14.04.

Table 5.1.: Timing of different solvers for different choices of preconditioner, matrix D, and accuracy of inner iteration for model *seg_2_res_2*.

Solver	Prec.	D	Accuracy	Iterations	Solving time
BiCG-Stab	ILU(0)	-	-	601.5	134.32 s
CG	ILU(0)	-	-	1072	121.14 s
UZAWA	AMG	$\lvert A_{i\cdot}\rvert$	1e-1	33	5.79 s
UZAWA	ILU(0)	$\lvert A_{i\cdot}\rvert$	1e-1	250	30.35 s
UZAWA	Iter	$\lVert A_{i\cdot}\rVert_2$	1e-2	16	10.78 s
UZAWA	Jac	diag(A)	1e-2	398	106.26 s
UZAWA	ILU(0) / M	-	1e-1	746	219.23 s
UZAWA	none	-	1e-1	1274	270.12 s
UZAWA	SOR	diag(A)	1e-2	121	34.81 s

In the UZAWA-algorithm A^{-1} has to be evaluated once per iteration. This step is uncritical and can be performed easily and fast by using a CG-solver with ILU(0) preconditioning. In the performed tests, a defect reduction of 1e-8 was achieved with 5 iterations and in $\approx$0.3 s or 4 iterations and $\approx$2.4 s for the meshes *seg_2_res_2* and *seg_1_res_1*, respectively. Therefore, no effort was made to achieve a further optimization of the inner iteration. Instead, for each of the different preconditioners (Table 5.1) and for each different choice of D (Tables 5.2 and 5.4) the influence of the accuracy of the inner solution on computation time and convergence, i.e., the number of necessary iterations, was tested. Between each step in accuracy a factor of

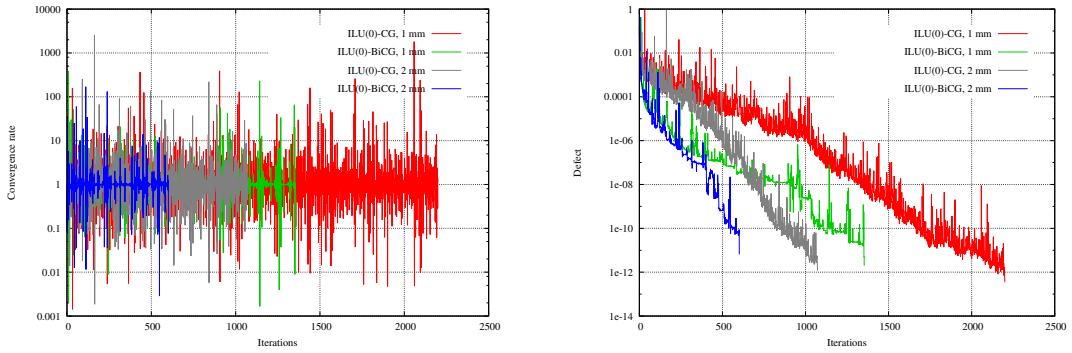

Figure 5.4.: Convergence rate (left) and defect reduction (right) of direct solvers in models *seg_1_res_1* and *seg_2_res_2*.

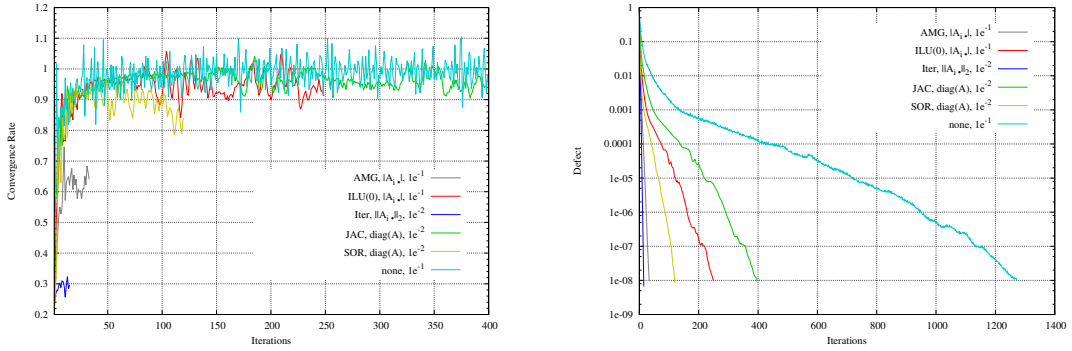

Figure 5.5.: Convergence rate (left) and defect reduction (right) of the UZAWA-algorithm for different preconditioners in model *seg_2_res_2*.

10 was chosen. The results of this evaluation for the two different meshes are given in Tables 5.3 and 5.5, respectively. For the investigated range of values, it was found that the accuracy with which the inner solution is computed does not noticeably influence the convergence of the solution. However, the influence on the speed of the computation is significant. The fastest computation time is reduced by more than 60% for the 2 mm model and nearly 50% for the 1 mm model in comparison to the highest considered relative reduction of 1e-8.
In Table 5.1, the computation times for the different combinations of solver and preconditioner are listed. Only the best choice of preconditioner, and also D in case of the UZAWA-algorithm, is presented. Table 5.1 and Figure 5.4 show that neither the CG- nor the BiCG-solver

Table 5.2.: Timing of UZAWA-algorithm with AMG preconditioner for different choices of D for model *seg_2_res_2*. Only the best performing accuracy for the inner iteration is noted.

D	Accuracy	Iterations	Solving time
$\mathrm{diag}(A)$	1e-2	34	5.97 s
$\lvert A_{i\cdot}\rvert$	1e-1	33	5.79 s
$\sum A_{i\cdot}$	1e-1	35	6.14 s
$\lVert A_{i\cdot}\rVert_2$	1e-1	34	5.97 s

Table 5.3.: Timing of UZAWA-algorithm with AMG preconditioner and $D = |A_{i\cdot}|$ for different choices of accuracy of inner iteration for model *seg_2_res_2*.

Accuracy	Iterations	Solving time
1e0	33	5.79 s
1e-1	33	5.79 s
1e-2	33	5.79 s
1e-3	33	6.11 s
1e-4	33	7.29 s
1e-5	33	8.86 s
1e-6	33	9.61 s
1e-7	33	11.35 s
1e-8	33	13.20 s
1e-9	33	14.71 s

Table 5.4.: Timing of UZAWA-algorithm with AMG preconditioner for different choices of D for model *seg_1_res_1*. Only the best performing accuracy for the inner iteration is noted.

D	Accuracy	Iterations	Solving time
$\lvert A_{i\cdot}\rvert$	1e-1	42	60.42 s
$\sum A_{i\cdot}$	1e-1	42	60.53 s
$\lVert A_{i\cdot}\rVert_2$	1e-1	41	59.24 s

Table 5.5.: Timing of UZAWA-algorithm with AMG preconditioner and $D = \|A_{i\cdot}\|_2$ for different choices of accuracy of inner iteration for model *seg_1_res_1*.

Accuracy	Iterations	Solving time
1e0	41	59.16 s
1e-1	41	59.24 s
1e-2	41	59.28 s
1e-3	41	59.28 s
1e-4	41	72.49 s
1e-5	41	86.23 s
1e-6	41	95.79 s
1e-7	41	110.59 s
1e-8	41	117.78 s

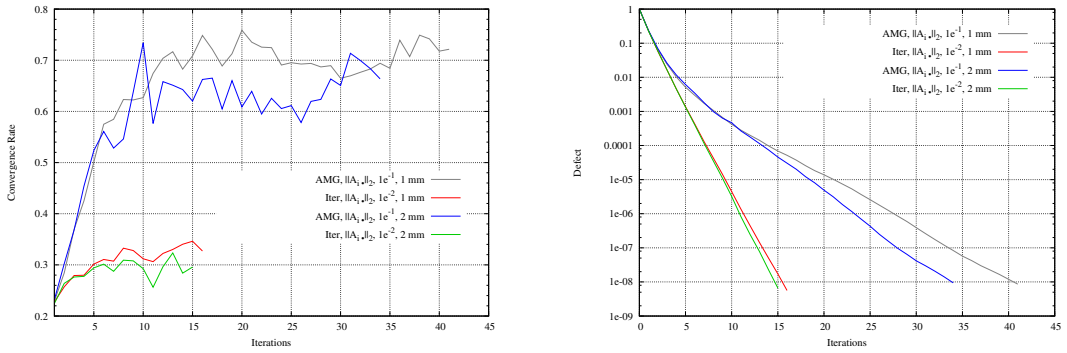

Figure 5.6.: Convergence rate (left) and defect reduction (right) of the UZAWA-algorithm for AMG- and iterative preconditioners in model *seg_1_res_1* and *seg_2_res_2*.

are adequate to solve (5.21). In both cases, after few iterations the convergence rates are fluctuating just under 1 and are partly even above 1. Accordingly, the number of iterations needed is very high and so is the solving time. Comparing the different preconditioners used for the UZAWA-algorithm, the concerns discussed earlier are confirmed, as the ILU(0) as well as the other preconditioners perform suboptimal (Figure 5.5). The best convergence rates are found for the iterative and the AMG-preconditioner. The convergence rates for these two preconditioners for models *seg_1_res_1* and *seg_2_res_2* are shown in Figure 5.6 in more detail. The iterative preconditioner achieves slightly better convergence rates and thus requires less iterations than the AMG-preconditioner. However, due to the lower computational effort per iteration, the AMG-preconditioner leads to a faster solving time (Table 5.1). Therefore, the further evaluations were focussed on the AMG-preconditioner, particularly to find the optimal choice for the approximation of matrix A and to estimate the optimal solving accuracy for the inner iteration.

The computation times in model *seg_1_res_1* (Table 5.4) and *seg_2_res_2* (Table 5.2) yield different optimal choices for approximating A, $\|A_{i\cdot}\|_2$ for model *seg_1_res_1* and $|A_{i\cdot}|$ for *seg_2_res_2*. As the differences for model *seg_2_res_2* are in the range of milliseconds, $\|A_{i\cdot}\|_2$ was chosen for the following computations. For these choices the solving time for different solving accuracies of the inner iteration was evaluated. For model *seg_1_res_1* the fastest solving time was found for an accuracy of 1e0. However, up to an accuracy of 1e-3 the solving time only changes in the range of milliseconds, as only one iteration step is performed for a stopping criterion of 1e-3 and higher. The number of necessary iterations of the UZAWA-algorithm remained constant at 41 for all accuracies (Table 5.5). Also in the coarser model, the fastest solving time is achieved when only one iteration is performed for the inner solver. This is the case for accuracies of 1e0 to 1e-2 (Table 5.3). The number of iterations constantly remained at 33 for all tested accuracies. An accuracy of 1e-2 for the inner iteration was chosen for the following evaluations, corresponding to a single iteration in the inversion of A.

5.7. Numerical Evaluation I: Sphere Studies

In this section, the numerical performance of the M-FEM achieved in solving the EEG forward problem in sphere models is evaluated. First, the numerical accuracy of the M-FEM for the two approaches derived is analyzed and also compared to that of the previously derived Whitney approach (cf. Section 2.4) as it is very similar with regard to source modeling. Thereafter, the accuracy of the M-FEM is compared to that of the partial integration DG approach (cf. Section 4.1.2). Therefore, the previously generated evaluation scenarios (cf. Section 4.2) are used, i.e., first common sphere models and subsequently the models with a reduced skull thickness are used. Finally, the current flow is visualized to help understand the differences of the M-FEM compared to the previously evaluated CG- and DG-FEM.

5.7.1. Methods

In a first comparison, besides the two M-FEM approaches, the Whitney CG-FEM was included, as it relies on the same approximation of the dipole source (cf. Section 2.4). The models *seg_1_res_1* and *seg_2_res_2* were considered. The model *seg_2_res_1* and the coarse models with a geometry resolution of 4 mm were omitted here for reasons of conciseness and due to the limited additional insight they offer, as the results in these models are dominated by the geometry error (cf. Section 4.2). For each model, the source positions already used in Section 4.2 were projected to the closest face center and the source directions were then chosen according to the face normals. Thereby, the result should not be influenced by the interpolation that is needed for arbitrary source directions and positions. Next, the two M-FEM approaches were compared using the models *seg_1_res_1*, *seg_2_res_2*, and *seg_4_res_4* with random source positions and radial source directions. As the interpolation method in hexahedral models is the same for all approaches and the general results should thus not differ strongly from the previous comparison, the Whitney CG-FEM was not included here to allow for a more detailed comparison of projected and direct M-FEM approach. Finally, the two M-FEM approaches were evaluated in the leaky models *seg_2_res_2_r82*, *seg_2_res_2_r83*, and *seg_2_res_2_r84*, again with random positions and radial source directions. As before, no approach based on the CG-FEM was included, since the sensitivity of the CG-FEM to leakages was already shown in the previous chapter and does not differ between the direct source modeling approaches (and as shown not even for the subtraction approach). As in the previous chapter, the solution is evaluated on the whole outer boundary using the measures RDM and lnMAG, so that the results are independent of the choice of the evaluation points.

The studies of the numerical accuracy in sphere models are again complemented by visualizations of the volume currents and of $lnMAG_{\mathbf{j},loc}$ and $totDIFF_{\mathbf{j},loc}$ for a single dipole source in the models *seg_2_res_2_r82*, *seg_2_res_2_r83*, and *seg_2_res_2_r84*. Here, the (projected) M-FEM is compared to both the Whitney CG approach and the partial integration DG approach.

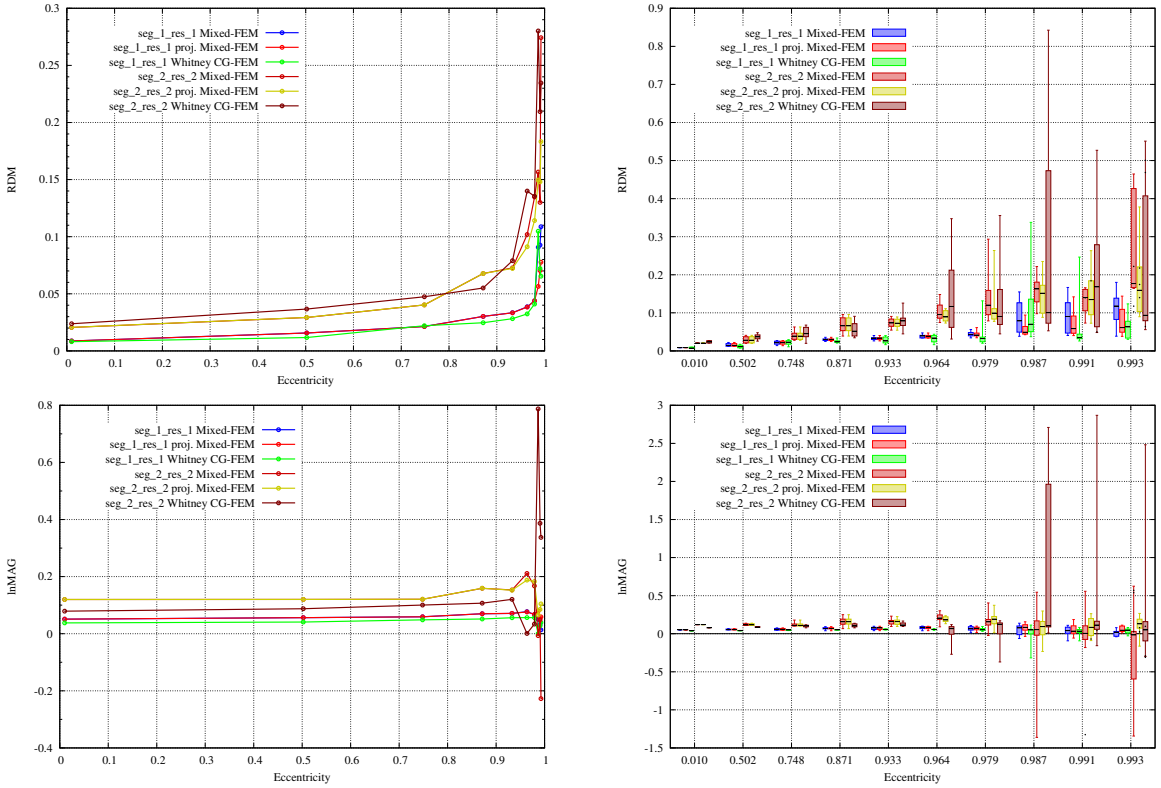

Figure 5.7.: Comparison of direct and projected Mixed-FEM and Whitney CG-FEM in meshes *seg_1_res_1* and *seg_2_res_2*. Results for optimized dipole positions. Visualized are the mean error (left column) and boxplots (right column) of RDM (top row) and lnMAG (bottom row). Dipole positions that are outside the brain compartment in the discretized models are marked as dots. Note the different scaling of the x-axes.

5.7.2. Results

Comparison of Whitney CG-FEM and M-FEM for optimal source positions

Comparing the three approaches considered in Figure 5.7 with regard to the RDM in model *seg_1_res_1*, no remarkable differences are found up to an eccentricity of 0.964 with maximal errors below 0.05 for all approaches (Figure 5.7, top row). At an eccentricity of 0.979 the maximal errors for the M-FEM slightly increase, however, the maximal errors remain below 0.1. The Whitney CG-FEM has a maximal error above 0.1 here, while upper quartile and median are lower than for the M-FEM. For the highest three eccentricities, the RDM clearly increases for all considered approaches. The errors for the M-FEM are constantly increasing with the eccentricity but the variance at the different eccentricities is relatively weak and the maximal errors are below 0.2. The Whitney CG approach shows a high variance with high spread and maximal errors above 0.2 for eccentricities of 0.987 and 0.991. In constrast, it has the lowest maximal error (< 0.15) at the highest eccentricity. Furthermore, the projected M-FEM approach leads to lower errors than the direct approach, with maximal errors and median constantly below 0.15 and 0.1, respectively. In the coarser model *seg_2_res_2*, all approaches perform similar up to an eccentricity of 0.933. For higher eccentricities, the Whitney CG-FEM again shows a high variance and leads to the highest maximal errors of all

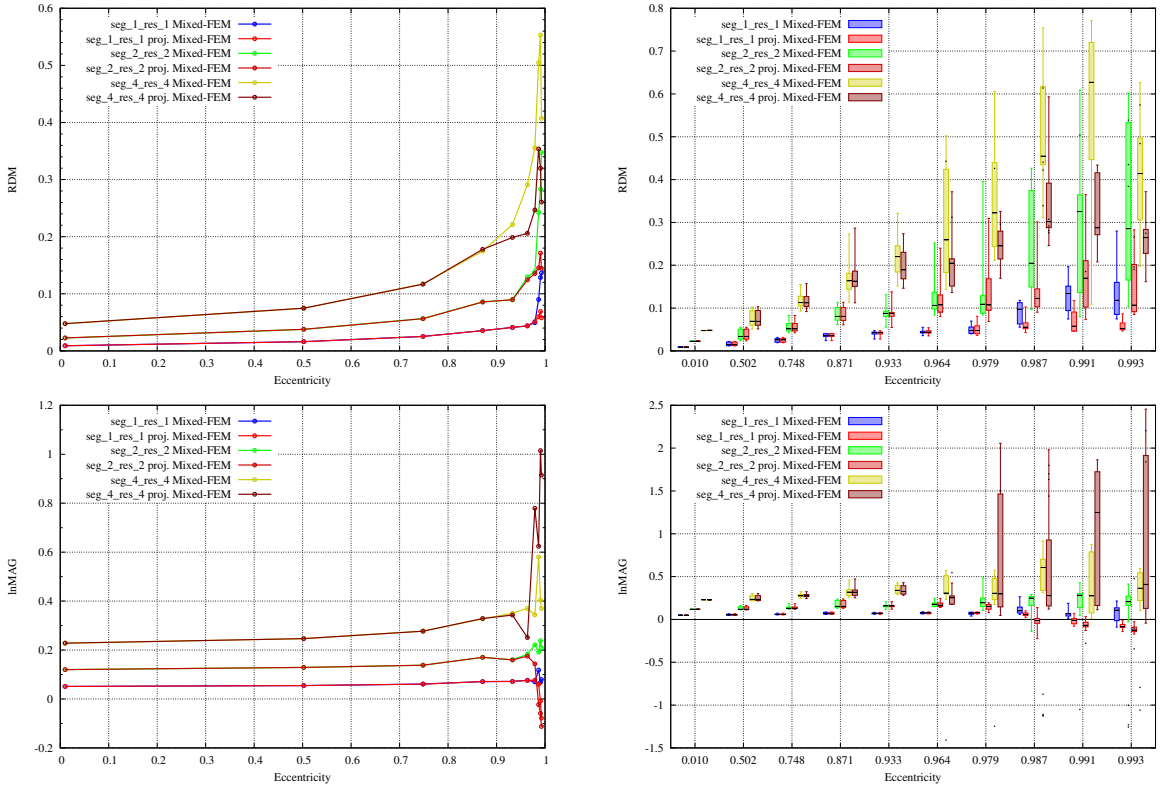

Figure 5.8.: Convergence with increasing mesh and geometrical resolution for Mixed-FEM approaches. Results of radial dipole computations. Visualized are the mean error (left column) and boxplots (right column) of RDM (top row) and lnMAG (bottom row). Dipole positions that are outside the brain compartment in the discretized models are marked as dots. Note the different scaling of the x-axes.

considered approaches with values over 0.8. The projected M-FEM performs better than the direct approach in most instances also in this model.

With regard to the lnMAG (Figure 5.7, bottom row), only minor differences, e.g., an increased spread for the Whitney CG-FEM at an eccentricity of 0.987, are recognizable for model *seg_1_res_1*, while otherwise all approaches mostly achieve very similar accuracies. In model *seg_2_res_2*, the Whitney CG-FEM shows an increased spread for eccentricities of 0.964 and higher. Direct M-FEM and Whitney CG-FEM lead to very high maximal errors for eccentricities of 0.987 and higher with maximal absolute values above 1 and 2.5 and a spread larger than 2 and 2.5, respectively. Here, the projected M-FEM clearly performs best with a maximal spread of about 0.5 and maximal absolute values below 0.25.

Comparison of M-FEM approaches in common sphere models

The next comparison expands the previous results to random source positions. When comparing the two M-FEM approaches with regard to the RDM (Figure 5.8, top row), no major differences are found up to an eccentricity of 0.964 for all models. For model *seg_1_res_1*, the RDM is constantly below 0.05. With increasing eccentricity, the RDM for the projected approach mainly remains below 0.1, while the maximal RDM is at nearly 0.3 for the direct approach and the median is above 0.1. Also in models *seg_2_res_2* and *seg_4_res_4*, the projected approach outperforms the direct approach with regard to the RDM. As previously observed for the

DG-FEM in Chapter 4, the worse approximation of the geometry leads to higher errors in these models, e.g., the minimal RDM at an eccentricity of 0.964 is already at nearly 0.1 for both approaches in model *seg_2_res_2*. At an eccentricity of 0.979, the direct approach has a lower value for the upper quartile and a smaller IQR than the projected approach in this model, while the maximal error is still higher. For more eccentric sources, the projected approach, again, performs clearly better than the direct approach. This is also the case for model *seg_4_res_4*, where minor differences are found up to an eccentricity of 0.933 and larger differences with increasing eccentricity.

The results for the lnMAG (Figure 5.8, bottom row) again do not show remarkable differences for all models up to an eccentricity of 0.933. In model *seg_1_res_1*, the projected approach leads to a lower spread for the three highest eccentricities, however, the lnMAG decreases from positive values for all source positions at low eccentricities to completely negative values at the highest eccentricity. In contrast, the direct approach leads to a higher spread, but the median remains nearly constant up to the highest eccentricity. The same behaviour of both approaches, just at a generally higher error level, i.e., lower spread but general decrease of errors for projected approach and high spread but constant median for direct approach, is found for model *seg_2_res_2*. For the coarsest model, the errors are clearly increased. Here, the direct approach performs better for the four highest eccentricities than the projected approach, especially with regard to the spread (<1 for direct approach, >1.8 for projected approach for eccentricities >0.979).

Comparison of M-FEM approaches in leaky sphere models

As in the common sphere models, also in the models with the thin skull compartment the projected approach mostly outperforms the direct approach (Figure 5.9). However, both with regard to the RDM and the lnMAG, no notable differences between the two approaches are observable at low eccentricities. With regard to the RDM (Figure 5.9, top row), an increase of the errors with increasing eccentricity is found and clearly higher errors with decreasing skull thickness for both approaches (median ≈ 0.15 for model *seg_2_res_2_r84*, ≈ 0.25 for model *seg_2_res_2_r82* at an eccentricity of 0.964). At higher eccentricities, the projected approach shows clearly lower maximal errors for all models (difference >0.075 at 0.979 and clearly increasing for higher eccentricities). Except for an outlier at an eccentricity of 0.979, the projected approach also leads to a lower median of the errors and a smaller IQR.

With regard to the lnMAG (Figure 5.9, bottom row), the maximal errors – and thereby also spread (≈ 0.4) and IQR (≈ 0.1) – for the direct approach increase at an eccentricity of 0.979 for all models, while the spread remains low for the projected approach (≈ 0.1). The spread remains at the same level also for higher eccentricities for the direct approach, while the IQR grows slightly. For the projected approach, growth of spread and IQR are less severe and highest spread and IQR are found at an eccentricity of 0.987. However, as for the common sphere models, a clear decrease of the lnMAG errors is observed for high eccentricities.

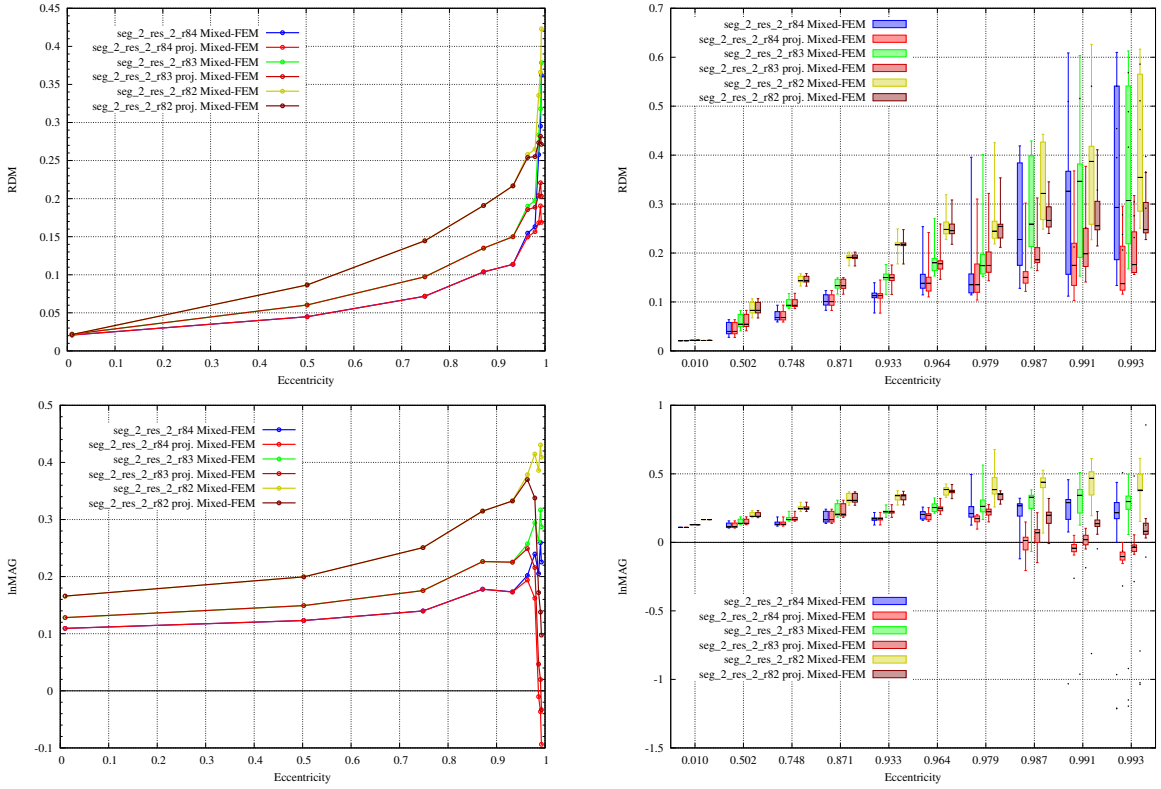

Figure 5.9.: Comparison of increase of errors for decreasing skull thickness between the two Mixed-FEM approaches. Results of radial dipole computations. Visualized are the mean error (left column) and boxplots (right column) of RDM (top row) and lnMAG (bottom row). Dipole positions that are outside the brain compartment in the discretized models are marked as dots. Note the different scaling of the x-axes.

Comparison of projected M-FEM and PI DG approach in sphere models

The studies in sphere models are concluded with a comparison between the projected M-FEM approach and the partial integration DG approach both in common (Figure 5.10) and leaky sphere models (Figure 5.11), as these approaches turned out to be the most accurate ones of the newly introduced approaches. The displayed results are the same as previously presented, just depicted side by side to allow for an easier comparison.

In the common sphere models, the PI DG approach is found to be slightly more accurate with regard to the RDM (Figure 5.10, top row) up to an eccentricity of 0.933, as it leads to lower maximal errors in all considered models. For eccentricities of 0.964 and 0.979 both approaches perform similar especially in model *seg_1_res_1*, while for the highest eccentricities (0.987 and higher) the projected M-FEM performs better than the PI DG approach both with regard to maximal errors and median of the errors. Also with regard to the lnMAG (Figure 5.10, bottom row) the projected M-FEM mainly leads to a slightly smaller IQR and spread, however, most of the differences between the two approaches are rather subtle. An exception are the results for model *seg_4_res_4* at high eccentricities, where the projected M-FEM leads to very high errors as previously recognized (cf. Figure 5.8).

In the sphere models with a thin skull compartment, the DG approach again performs slightly better than the M-FEM approach with regard to the RDM up to an eccentricity

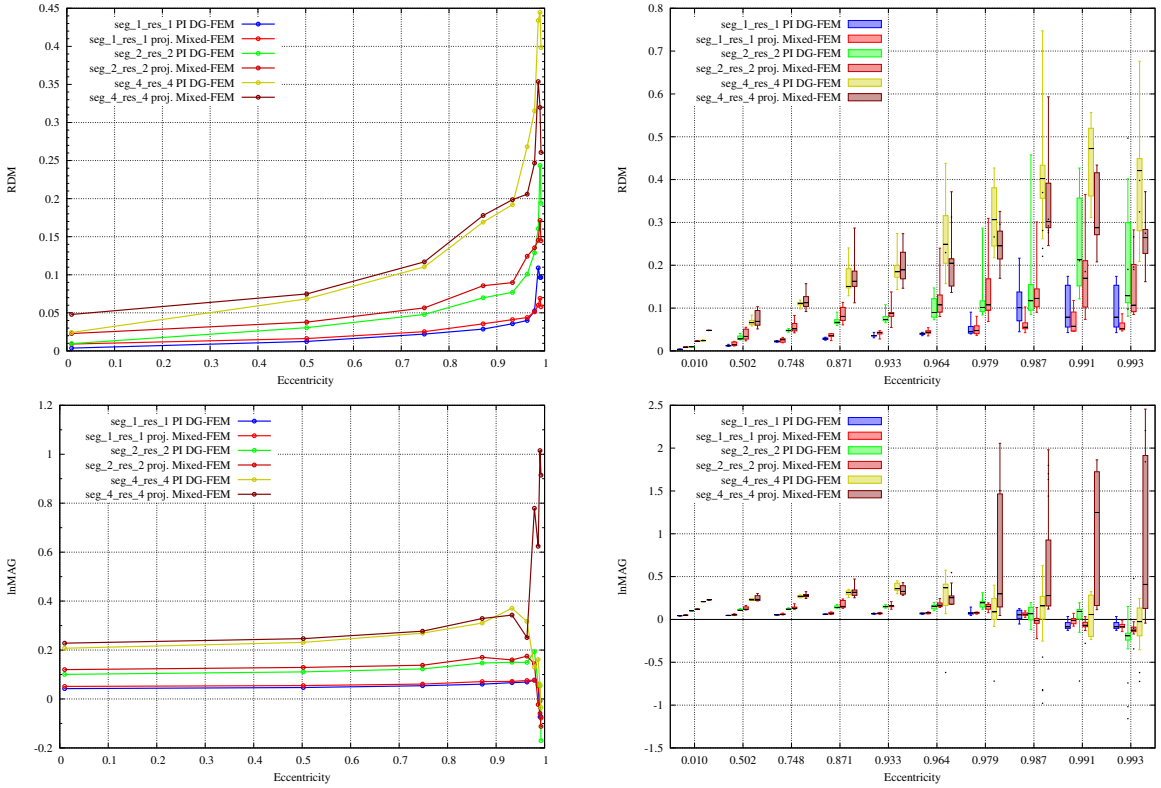

Figure 5.10.: Convergence for projected Mixed-FEM and PI DG approaches with increasing mesh and geometrical resolution. Results of radial dipole computations. Visualized are the mean error (left column) and boxplots (right column) of RDM (top row) and lnMAG (bottom row). Dipole positions that are outside the brain compartment in the discretized models are marked as dots. Note the different scaling of the x-axes.

of 0.979 (Figure 5.11, top row). While the maximal errors are in the same range at this eccentricity, the projected M-FEM clearly leads to a higher IQR and in models *seg_2_res_2_r83* and *seg_2_res_2_r84* also to higher error medians. At the highest eccentricities, the projected M-FEM leads to clearly lower maximal errors than the PI DG-FEM amongst all models and especially for the two highest eccentricities also to a lower median of the errors and a smaller IQR.

With regard to the lnMAG (Figure 5.11, bottom row), no significant differences between the two approaches are visible up to an eccentricity of 0.964. For higher eccentricities, spread and IQR increase for both approaches; the projected M-FEM performs slightly better than the PI DG-FEM. For both approaches the already mentioned decrease of the lnMAG for highest eccentricities is observed. The strength of this effect is similar for both approaches.

Visualization of volume currents in leaky head models

In this section, visualizations of the current flow in the same scenario as in the previous chapter are presented. First, current direction and strength for partial integration DG-FEM and projected M-FEM are shown in models *seg_2_res_2_r82*, *seg_2_res_2*83, and *seg_2_res_2_r84* and also $lnMAG_{\mathbf{j},loc}$ and $totDIFF_{\mathbf{j},loc}$ for partial integration DG in relation to the projected M-FEM are visualized. As a comparison, $lnMAG_{\mathbf{j},loc}$ and $totDIFF_{\mathbf{j},loc}$ are also presented for

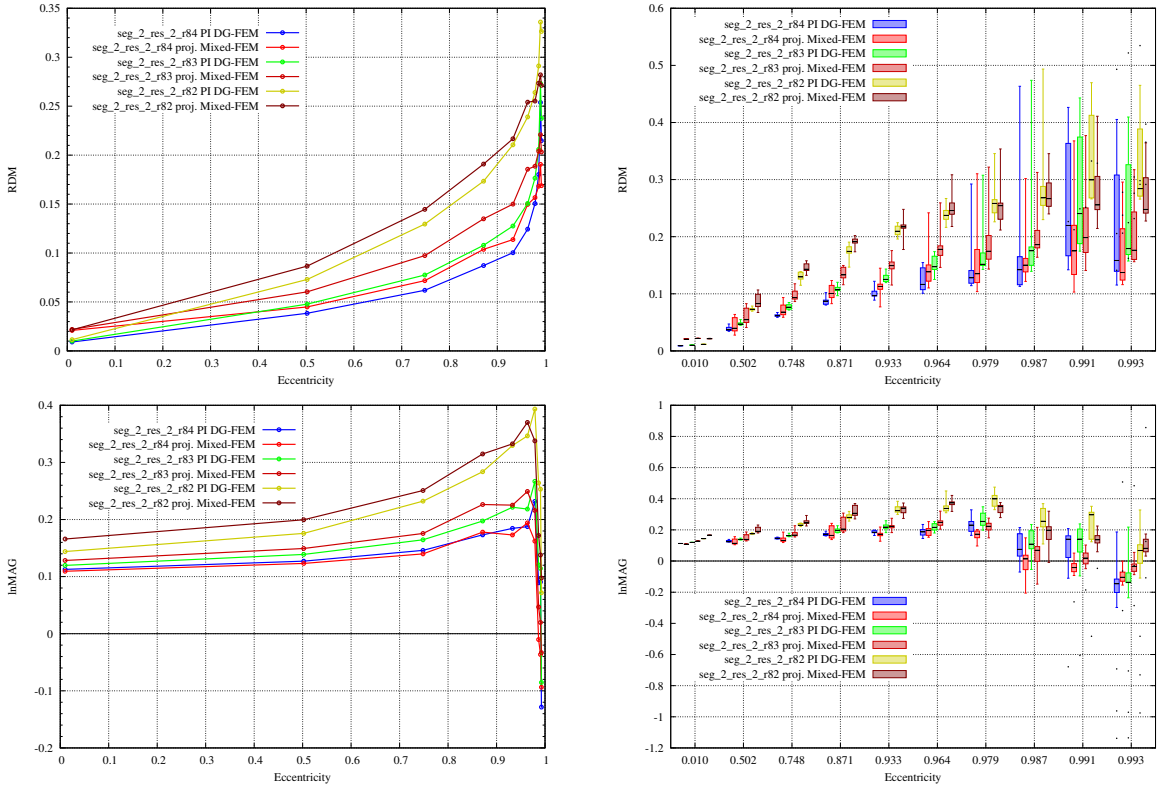

Figure 5.11.: Comparison of increase of errors for decreasing skull thickness between the projected Mixed-FEM and partial integration DG-FEM. Results of radial dipole computations. Visualized are the mean error (left column) and boxplots (right column) of RDM (top row) and lnMAG (bottom row). Dipole positions that are outside the brain compartment in the discretized models are marked as dots. Note the different scaling of the x-axes.

the Whitney CG-FEM in relation to the projected M-FEM.

In Figure 5.12, the current strength and direction for a single dipole simulated using the partial integration DG-FEM and the projected M-FEM are presented side by side. For model *seg_2_res_2_r82* (top row), higher current strengths in the outermost layer of skin elements are found for the PI DG-FEM than for the projected M-FEM. However, for both approaches the maximal current strength is clearly lower than for the CG-FEM approaches (maximum of colorbar at ≈ 40 here, ≈ 137 in Figure 4.13 (partial integration), and ≈ 126 in Figure 4.15 (subtraction)). In contrast to the current strength peaking in two skin elements for the DG-FEM, the distribution is clearly smoother for the M-FEM, where also the current in the skull compartment is clearly recognizable in the visualization as the values are in the middle of the colorbar. Also in model *seg_2_res_2_r83* (middle row) and *seg_2_res_2_r84* (bottom row) the current distribution for the M-FEM is clearly smoother, while it is again peaking in single elements for the DG-FEM. In model *seg_2_res_2_r83* the maximal values for the M-FEM are furthermore clearly lower than for the DG-FEM, while they are at the same level for model *seg_2_res_2_r84*. For the M-FEM, a blurring effect of the low-conducting skull compartment is visible, as the highest current strengths are found in the innermost layer of elements belonging to the skull compartment and smoothly decaying for more superficial elements.

When comparing $lnMAG_{\mathbf{j},loc}$ and $totDIFF_{\mathbf{j},loc}$ for partial integration DG-FEM and projected

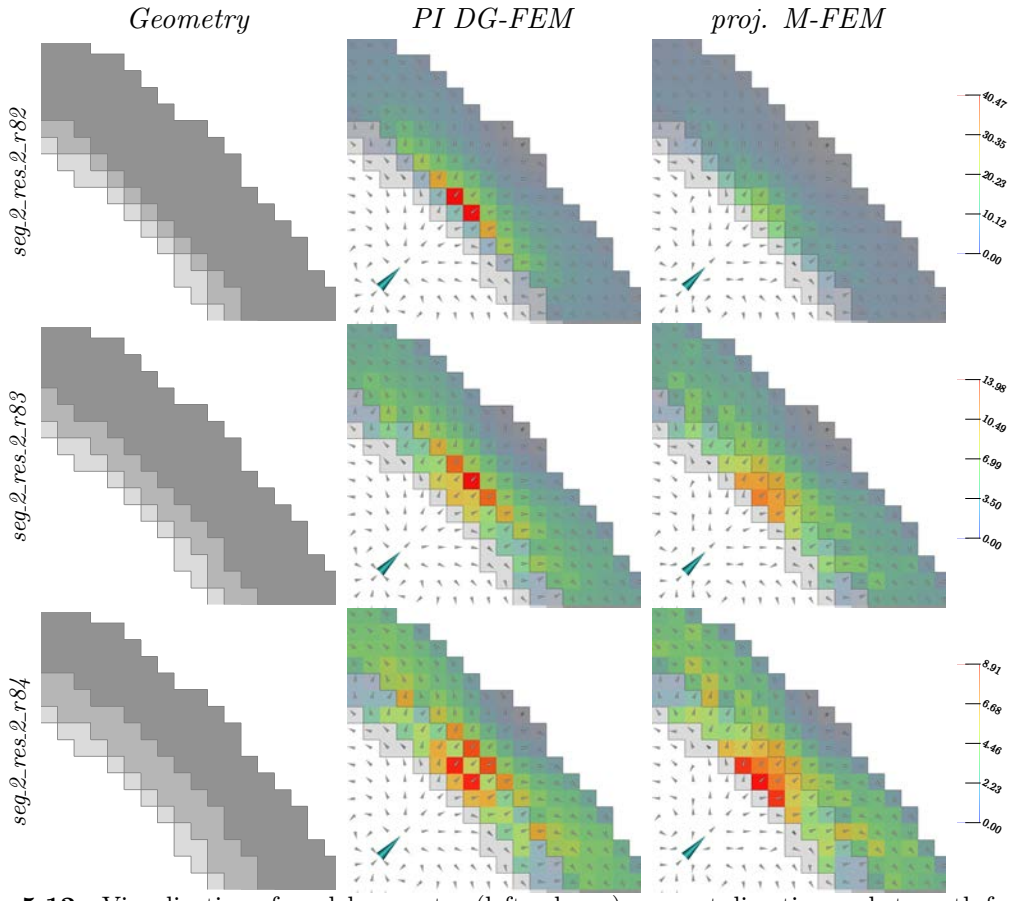

Figure 5.12.: Visualization of model geometry (left column), current direction and strength for partial integration DG approach (middle column) and projected M-FEM approach (right column) for models *seg_2_res_2_r82* (top row), *seg_2_res_2_r83* (middle row), and *seg_2_res_2_r84* (bottom row). The left column shows the model geometry, interior to exterior from bottom left to top right, brain in white, CSF, skull and skin in increasingly dark gray, and air in white. Dark gray lines mark compartment boundaries. In the middle and right columns, the large turquoise cone presents the dipole source. The small and normalized grey cones show the directions of the current flow and, for elements belonging to skull and skin compartments, the coloring indicates the current strength. For each model the color scale is kept constant for both approaches.

M-FEM (Figure 5.13), the strongest differences with regard to the $lnMAG_{\mathbf{j},loc}$ occur in model *seg_2_res_2_r82*, while the distribution of the $totDIFF_{\mathbf{j},loc}$ is very similar for all models and dominated by differences in the CSF compartment. In model *seg_2_res_2_r82* (left), major differences in the skull and the outermost layer of skin elements are observed. Here, as already indicated by Figure 5.12, the current strength for the DG-FEM is higher than for the M-FEM in the skin elements, while it is clearly lower in the skull compartment. This can even be observed when looking at the $totDIFF_{\mathbf{j},loc}$, where the slight absolute differences of the volume currents in these compartments are visible. This indicates a stronger current flow into the skin compartment for the DG-FEM than for the M-FEM, while an opposite effect is found in the skull. However, the highest differences with regard to the $totDIFF_{\mathbf{j},loc}$ are found in the CSF compartment. Furthermore, some high values with regard to the $lnMAG_{\mathbf{j},loc}$ show up at the surface of the skin compartment, these are probably due to the staircase-like geometry. In models *seg_2_res_2_r83* (middle) and *seg_2_res_2_r84* (right), the $lnMAG_{\mathbf{j},loc}$ in skull and

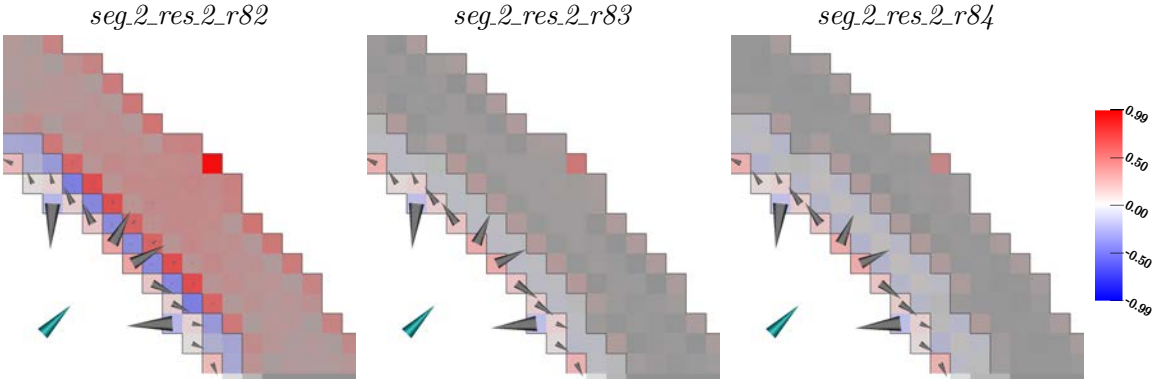

Figure 5.13.: Visualization of current flow differences between PI DG-FEM approach and projected M-FEM approach in models *seg_2_res_2_r82* (left), *seg_2_res_2_r83* (middle), and *seg_2_res_2_r84* (right). The turquoise cone presents the dipole source. The coloring shows the $lnMAG_{\mathbf{j},loc}$ (increase/decrease of the current strength simulated with the CG- compared to the DG-FEM solution). For all models the maximum of the color scale is chosen as the maximal value in the skin and skull compartment. Grey cones, having the same linear scaling for all models, show the $totDIFF_{\mathbf{j},loc}$ (difference in current flow). In models *seg_2_res_2_r83* and *seg_2_res_2_r84* the arrows in skin and skull are not visible due to the relatively small values. Dark gray lines mark compartment boundaries.

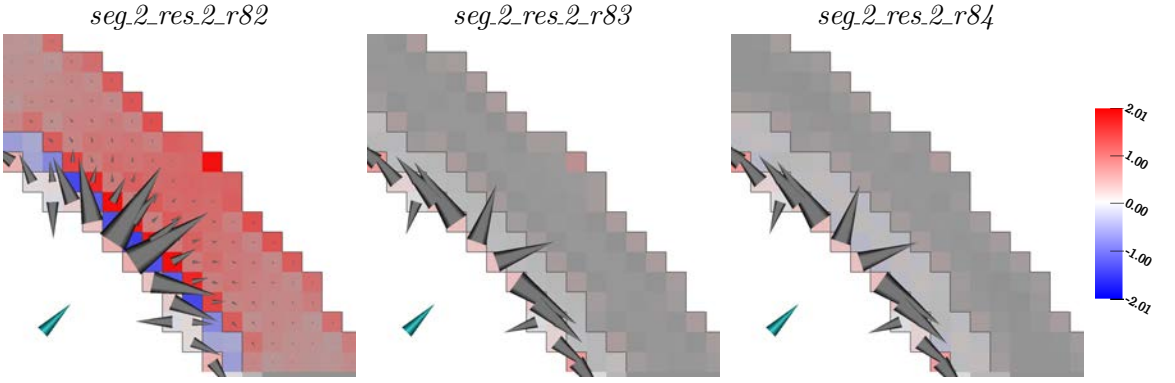

Figure 5.14.: Visualization of current flow differences between Whitney CG-FEM approach and projected M-FEM approach in models *seg_2_res_2_r82* (left), *seg_2_res_2_r83* (middle), and *seg_2_res_2_r84* (right). The turquoise cone presents the dipole source. The coloring shows the $lnMAG_{\mathbf{j},loc}$ (increase/decrease of the current strength simulated with the CG- compared to the DG-FEM solution). For all models the maximum of the color scale is chosen as the maximal value in the skin and skull compartment. Grey cones, having the same linear scaling for all models, show the $totDIFF_{\mathbf{j},loc}$ (difference in current flow). In models *seg_2_res_2_r83* and *seg_2_res_2_r84* the arrows in skin and skull are not visible due to the relatively small values. Dark gray lines mark compartment boundaries.

skin is clearly reduced and no differences with regard to the $totDIFF_{\mathbf{j},loc}$ are visible in these compartments. In contrast, both measures are essentially unchanged in the CSF in comparison to model *seg_2_res_2_r82*.

To be able to estimate the significance of these differences, also $lnMAG_{\mathbf{j},loc}$ and $totDIFF_{\mathbf{j},loc}$ for the Whitney CG-FEM in relation to the projected M-FEM are visualized in Figure 5.14. Here, the maximal $lnMAG_{\mathbf{j},loc}$ is doubled compared to Figure 5.13. This corresponds to a factor of ≈ 2.7 as the $lnMAG_{\mathbf{j},loc}$ scales logarithmically. Also the visualization of the $totDIFF_{\mathbf{j},loc}$ shows that the differences between CG-FEM and M-FEM are clearly stronger than those between DG-FEM and M-FEM. This is especially visible for model *seg_2_res_2_r82*, but

also in models *seg_2_res_2_r83* and *seg_2_res_2_r84* the differences found in the CSF compartment are huge.

5.8. Numerical Evaluation II: Realistic Head Model Study

To augment the studies in the various sphere models, the three approaches Venant CG-FEM, partial integration DG-FEM, and projected M-FEM are compared in a realistic six-compartment hexahedral head model with a mesh width of 2 mm in this section. As a reference the high-resolution tetrahedral head model generated in Section 2.11.2 is used and, as a comparison, the results for the Venant approach in a hexahedral head model with a resolution of 1 mm are shown as well.

5.8.1. Methods

Based on the segmentation also used for the comparisons in Section 2.11.2 and Chapter 3, two realistic six-compartment hexahedral head models with mesh widths of 1 mm and 2 mm were created, resulting in 3,965,968 vertices and 3,871,029 elements and 508,412 vertices and 484,532 elements, respectively. As the model with a mesh width of 2 mm was not corrected for leakages, 1,164 vertices which belong to both CSF and skin elements were found, which is an amount comparable to model *seg_2_res_2_r83*. These were mainly located at the temporal bone. The conductivities were chosen according to Table 3.1. Out of the 18,893 source positions also used in Section 2.11.2, those that were not contained in the gray matter compartment in the hexahedral models were excluded, resulting in 17,870 remaining source positions for the 1 mm model and 17,843 source positions for the 2 mm model. As sensor configuration the 80 channel realistic EEG cap was chosen and as error measures RDM and lnMAG in reference to the solution computed using the Venant CG-FEM in the high-resolution tetrahedral model were calculated.

5.8.2. Results

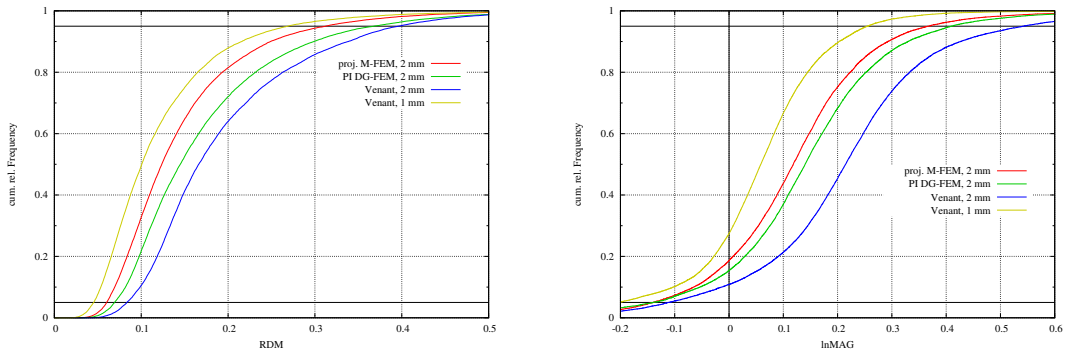

Figure 5.15.: Cumulative relative errors of RDM (left) and lnMAG (right) for EEG in realistic six-layer head model

The cumulative relative frequencies of RDM and lnMAG are displayed in Figure 5.15. Due to the relatively bad approximation of the geometry that is achieved when using a mesh width of 2 mm and regular hexahedra, both RDM and lnMAG are relatively high. Comparing the results in the 2 mm model with regard to the RDM (Figure 5.15, left), the M-FEM performs best with roughly 95% of the errors below 0.31. Thereby, the result is nearly as good as that achieved with the Venant approach in the 1 mm model, where 95% of the errors are below 0.28. The partial integration DG-FEM performs slightly worse than the M-FEM with 95% of the errors reached at about 0.36. For the Venant CG-FEM this mark is reached at an RDM of nearly 0.4.
With regard to the lnMAG, the differences between the results obtained using the different mesh resolutions and also between M- and DG-FEM approaches and the Venant CG-FEM approach are larger than for the RDM (Figure 5.15, right). The projected M-FEM performs best when using the 2 mm model, with 90% of the errors in the range from -0.15 and 0.35. The partial integration DG-FEM performs only slightly worse with 90% of the errors in the range from -0.15 and 0.4. Again, the Venant CG-FEM show the highest errors for the 2 mm model, both with regard to absolute values and spread (90% of the errors in the range from -0.1 to 0.54). The increase in accuracy when using a mesh resolution of 1 mm is clearer for the lnMAG than for the RDM, as for the Venant CG-FEM 90% of the lnMAG-errors are in the range from -0.2 to 0.25, thus showing both a smaller spread than the results in the 2 mm model and also lower absolute values.

5.9. Discussion

In this section, theoretical derivation and numerical experiments in sphere and realistic head models for an approach to solve the EEG forward problem based on the mixed finite element method (M-FEM) were presented. Existence and uniqueness of a solution were proven and a selection of a-priori error measures was stated. Two approaches to model the dipole source were derived, the direct and the projected approach.
The numerical experiments show a high accuracy of the newly introduced method, especially of the projected approach. The comparison with the Whitney CG-FEM approach in models *seg_1_res_1* and *seg_2_res_2* with optimized positions and orientations shows that the M-FEM leads to higher accuracies at high eccentricities, while the differences for lower eccentricities are small (Figure 5.7). The same holds true for arbitrary source directions, where again the projected approach shows higher accuracies than the direct approach, except for model *seg_4_res_4*, and also outperforms the partial integration DG approach that was introduced in the previous chapter (Figures 5.8, 5.10). The M-FEM is by construction charge preserving so that it was expected to prevent leakages (Barrenechea et al., 2007; Ewing et al., 1999). This is confirmed by the comparisons and visualizations in the head models with a thin skull compartment, *seg_2_res_2_r82*, *seg_2_res_2_r83*, and *seg_2_res_2_r84*. These show that, as the DG-FEM, the M-FEM is leakage preventing and leads to higher accuracies and smoother – and thereby more realistic appearing – current distributions than the DG-FEM (Figures 5.11 -

5.14). However, it has to be kept in mind that the DG approach might lead to better results when optimizing the value of η, as discussed in Chapter 4.

The results gained for the realistic six-compartment head model underline the results gained in the sphere studies (Figure 5.15). Again, the projected M-FEM achieves a slightly higher accuracy than the partial integration DG-FEM, while both approaches clearly outperform the Venant CG-FEM. It is difficult to quantify the influence of the leakages on the results obtained here. However, as these were mainly located in the area of the temporal bone, leakage effects do not suffice to explain the higher accuracy of M- and DG-FEM. An overall higher accuracy of these approaches in this kind of model, i.e., regular hexahedral with mesh resolution of 2 mm, can be assumed.

The three main sources of error in the evaluations – inaccurate representation of the geometry, numerical inaccuracies, and leakage effects – were already discussed in Chapter 4 and are still valid here.

No changes occurred for the first point, the errors due to the representation of the geometry. Since again regular hexahedral meshes were used here, the influence of geometry errors remains at a high level, especially for the coarse meshes. No explicit convergence study including results using the models with a coarse representation of the geometry but a higher mesh resolution (*seg_2_res_1*, *seg_4_res_1*, and *seg_4_res_2*) was performed. However, the comparison with the PI DG approach (Figure 5.11) shows that the projected M-FEM approach performs mainly as good and in some cases even better than the DG approach also in the coarse models *seg_2_res_2* and *seg_4_res_4*.

Regarding the second point, the numerical inaccuracy due to the discretization of the equations and the strong singularity, the M-FEM approach allows to increase the regularity of the right-hand side by one degree, since the splitting into two first order PDEs in (5.3) allows to get rid of the derivative applied to the delta distribution included in the primary current $\mathbf{j}^p$. The obtained results show high numerical accuracies, especially at highest eccentricities, and particularly for the projected M-FEM. This comes at the cost of a higher number of degrees of freedom than for the CG-FEM, as also the current $\mathbf{j}$ is considered as an unknown now and has to be discretized. Furthermore, the discrete problem has saddle point structure (5.21) and can no longer be efficiently solved with the previously used AMG-CG solvers. Though the number of unknowns is clearly increased compared to the CG-FEM, it is still lower than for the DG-FEM, e.g., in model *seg_2_res_2* we have $\#\mathrm{DOF}_M = 1,243,716 + 407,904$, $\#\mathrm{DOF}_{DG} = 3,263,232$, and $\#\mathrm{DOF}_{CG} = 428,185$. By introducing a conjugated UZAWA-algorithm with proper preconditioning, the solving time even in the finest model *seg_1_res_1* was reduced to less than a minute, which is only few seconds slower than for the CG-FEM and clearly faster than for the DG-FEM at the moment. Furthermore, as the equation system (5.21) is symmetric, also for the M-FEM the transfer matrix approach can be applied to reduce the number of equation systems that has to be solved to the number of sensors.

As the DG-FEM, also the M-FEM guarantees the conservation of charge and achieved high accuracies also in the sphere models with a thin skull compartment. Therefore, also the M-FEM can be considered as "leakage preventing". Especially at highest eccentricities, it leads

to even higher accuracies than the DG-FEM approaches. The resulting current distribution seems smoother than for the DG-FEM and appeared physically reasonable (Figure 5.13). However, as discussed in the previous chapter, the numerical solution obtained using the DG-FEM can possibly still be improved by optimizing the penalty parameter η. These results encourage the use of the M-FEM also in related applications, such as tDCS or DBS simulations. For the DG-FEM, the use of an unfitted method, the cut-cell DG approach, was discussed in Chapter 4 in order to improve the approximation of the underlying geometry and reduce the geometry error. To the best of the author's knowledge, no comparable method has been proposed for mixed finite elements so far. For the CG-FEM, the use of geometry-adapted meshes to reduce the geometry error was considered and it was shown in a variety of studies that this already clearly improves the representation of the geometry (Camacho et al., 1997; Vorwerk, 2011; Wolters et al., 2007a). However, while the use of non-degenerated parallelepipeds is uncritical for the M-FEM, "some complications may arise for general elements" (Brezzi and Fortin, 1991). At least for the two-dimensional case, error estimates for general quadrilateral grids can be obtained when modifying the lowest-order Raviart-Thomas elements (Chou et al., 2002; Kwak and Pyo, 2011) and for convex quadrilaterals even superconvergence could be shown (Ewing et al., 1999). Therefore, future experiments should investigate the accuracy of the cut-cell DG approach in comparison to the M-FEM using regular or geometry-adapted hexahedral meshes for which the convexity of the elements is ensured. Furthermore, the accuracies in realistic head models with finer mesh widths than the here used 2 mm should be evaluated. This is uncritical for M- and CG-FEM, while the memory demand for the DG-FEM is in this case in a range that would be too high for nowadays common PCs.

A point that was not discussed so far in the past two chapters are the consequences of the obtained results, especially those in the leaky head models, for the MEG forward solution. On the one hand, the simulation of the secondary magnetic flux Φ_s (cf. Sections 1.5 and 2.8) directly depends on an accurate simulation of the volume currents (cf. Equations 1.27, 1.32b, and 2.56). On the other hand, the leakage effects are only local and the currents incorrectly penetrating the skull are relatively weak compared to those in the CSF compartment. This aside, the MEG solution should also in non-leakage scenarios profit from a physically correct and charge preserving simulation of the volume currents, as it is guaranteed by DG- and M-FEM approaches, and the use of DG- and M-FEM for MEG forward simulations should therefore be considered.

6

Summary and Outlook

This thesis was devoted to studying different aspects influencing the accuracy achieved in solving the EEG/MEG forward problem using finite element methods. Both the numerical accuracy of established and newly introduced numerical methods as well as the influence of a differently detailed approximation of the human head by the volume conductor model were investigated.

Summary

After introducing the basic assumptions and equations underlying the forward problem of EEG and MEG (Chapter 1), it was shown that FEM approaches based on a continuous Galerkin formulation (CG-FEM) achieve a high numerical accuracy both in sphere and realistic volume conductor models (Chapter 2) and that the necessary computational effort can be kept in a range that makes a practical application feasible. Based on various comparisons of the different approaches to model the dipole source – Venant, partial integration, subtraction, and Whitney – it was concluded that the Venant approach offers the best compromise between numerical accuracy and computational effort when considering arbitrary source positions and directions. For fixed dipole directions, also the Whitney approach might be considered. Taking the modeling of the CSF as an example it was further shown that the effects of simplifications in the head model generation might be clearly higher than the errors of the numerical methods. This result encouraged the more detailed investigation of the effects of head model simplifications in Chapter 3. Based on the studies by Cho et al. (2015); Vorwerk et al. (2014) the effects of modeling/not modeling different conductive compartments on both the forward and inverse problem of EEG/MEG were investigated. It was shown that distinguishing the conductive compartments CSF, gray matter, and white matter has a huge influence on both EEG and MEG forward solutions with regard to topography and magnitude of the solution. Also the modeling of white matter anisotropy was found to have a considerable effect, while

the distinction of skull compacta and spongiosa only showed recognizable effects for few brain areas and only in the EEG. A MATLAB-based pipeline to perform EEG source analysis with FEM forward solutions including the simple generation of realistic five-compartment head models distinguishing skin, skull, CSF, gray matter, and white matter was presented and evaluated.

Finally, in Chapters 4 and 5 derivation and numerical evaluation for two novel approaches to solve the EEG forward problem were presented, the DG- and the Mixed-FEM. While for the DG-FEM the partial integration and subtraction approach that were previously derived for the CG-FEM could easily be adapted to the new framework, the Mixed-FEM allowed the derivation of two new source modeling approaches, the direct and the projected Mixed-FEM. The introduction of these approaches was motivated by the observation of leakage effects for the CG-FEM, where inaccurate current flow occurs for low-conducting compartments whose thickness is in the range of the mesh width. Both newly introduced approaches fulfill the physical property of conservation of charge and thereby help to prevent leakage effects and achieve a more realistic modeling of the volume currents. This was experimentally confirmed both by statistically evaluating topography and magnitude errors and by visualizing the volume currents. Both in spherical and realistic head models the projected Mixed-FEM achieved the best results for regular hexahedral meshes.

Outlook

Three main sources of errors were identified in the previous discussions following the respective chapters – insufficient resolution of the underlying geometry, numerical inaccuracies due to the discretization of the equations and the modeling of the source, and leakage effects. It was shown that the problem of leakage effects is successfully diminished by the introduction of DG- and Mixed-FEM. Nevertheless, these sources of error give rise to further topics of research.

Some approaches to further increase the numerical accuracy were already discussed in the respective Chapters 2, 4, and 5. One possibility is to try to improve the modeling of the current dipole for the direct approaches such as Venant or Whitney approach, e.g., by achieving a better approximation of the moments of the source distribution or by optimizing the placement of the monopole loads. Some recent improvements for the CG-FEM were proposed by Hanrath et al. (in prep.); Medani et al. (in prep.); Pursiainen et al. (submitted). Such approaches might also be adapted to the DG-framework.

As the up to now performed evaluations using higher order test and trial functions (Grüne, 2014) and adaptive mesh refinement (Meyer, 2013) did not lead to satisfying results especially with regard to the proportion of increase in computational effort and gained numerical accuracy, more sophisticated approaches might be needed, as discussed in Chapter 2. However, due to the large number of sources that has to be calculated for EEG/MEG inverse analysis, these techniques can possibly not be directly used in practical applications, but their results rather allow to draw conclusion for, e.g., the generation of the individual meshes by providing evidence for efficient mesh refinements. One possible outcome – as also discussed in Section

2.7 – might be a global refinement in the source compartment, i.e., the gray matter.

A first step to reduce the geometry error is the use of meshes that approximate the underlying geometry as good as possible. Here, tetrahedral meshes are clearly superior to regular hexahedral meshes. As already mentioned, a simple possibility to overcome this problem when willing to use hexahedral meshes due to their practical advantages, is the use of geometry-adapted hexahedral meshes (Camacho et al., 1997). These were positively evaluated in combination with the CG-FEM (Vorwerk, 2011; Wolters et al., 2007a), but so far not applied in combination with DG- or Mixed-FEM. An even better approximation of the geometry can probably be achieved using unfitted discontinuos Galerkin-methods (UDG) (Bastian and Engwer, 2009; Nüßing et al., 2015). Principally, these allow to directly operate on the output of the segmentation algorithm, e.g., level-set functions, instead of relying on the discretized voxel-based segmentation. Thereby, it is possible to achieve a sub-voxel representation of the geometry. A fundamentally different approach was presented by Koulouri (2015); Stahlhut et al. (2009, 2011). They propose to account for the geometry uncertainties in the computation of the inverse solution by means of Bayesian inversion.

One finding of this thesis was that in many scenarios the effects of model simplifications clearly exceed the numerical inaccuracies. Though the modeling of six conductive compartments and white matter anisotropy as done in Chapter 3 is already a clear improvement compared to three-layer head models, this surely still does not lead to a completely anatomically correct representation of the head's tissues. Further tissues whose influence on EEG forward solutions has yet been investigated are, e.g., blood vessels (Fiederer et al., 2013, to appear) or the dura mater (Ramon et al., 2014), but the accurate (automatic) segmentation of these compartments is still complicated using images obtained with common 3 T MRI scanners. Modern segmentation algorithms are principally able to distinguish eight or more different tissues (Lanfer, 2014), however, the usually achieved image resolutions are insufficient to reasonably resolve these often thin structures, such as the dura mater. Thus, both freely available open-source toolboxes such as FSL or SPM and commercial tools like BESA are usually still restricted to segmenting four or five compartments as it was also done in Section 3.2. Though segmentation was no topic of this thesis, the results gained in Chapter 3 might lead to the conclusion that besides distinguishing further conductive compartments that can hardly be resolved at the current image resolutions, it is also reasonable to spend further efforts on trying to increase the accuracy of the segmentation of important conductive compartments, e.g., the skull or the brain structure. The (strong) effect of a simplified segmentation of the skull on topography and magnitude of EEG forward simulations was involuntarily shown in Section 3.2 (Figure 3.24).

Besides the complex segmentation of the geometry, also the uncertainty about the respective conductivities is problematic. While for example the conductivity of the CSF is well-known and shows only little variance amongst subjects (Baumann et al., 1997), other conductivities such as that of the skull may strongly vary due to age, disease state, and environmental factors (Akhtari et al., 2002). This motivates the use of algorithms for individual conductivity estimation. An algorithm for combined EEG/MEG conductivity calibration was proposed by

Lew et al. (2007, 2009a) and evaluated for skull conductivity calibration by Aydin et al. (2014, 2015). However, this approach seems to be only stable for the simultaneous fitting of a single parameter, for fitting multiple parameters at a time the development of new algorithms would be necessary. Alternatively, just as geometry uncertainties, also conductivity uncertainties might be taken into account by applying Bayesian approaches for the inverse solution (Stahlhut et al., 2009, 2011).

An important point that should always be kept in mind besides the theoretical derivations, numerical evaluations, and simulation studies as they were in the focus of this thesis, is the practical applicability of these findings when using FEM in EEG/MEG source analysis. Here, especially a combined analysis of EEG and MEG data justifies the use of individual and calibrated realistic shaped multi-compartment head models. First examples where combined EEG/MEG source analysis using FEM forward modeling in combination with individual head models was performed and validated in clinical epilepsy diagnosis were published by Aydin et al. (2014, 2015); Rullmann et al. (2009). Though the studies by Aydin et al. (2014, 2015) were based on a quasi-automatic pipeline including individual skull conductivity calibration that is suitable for the use with larger patient groups, the presented results are still single subject studies. Based on these encouraging results, it is desirable that combined EEG/MEG source analysis using calibrated realistic volume conductor models is also performed and validated in group studies.

Finally, it should be mentioned that many of the results presented in this thesis can be directly transferred to other applications. Especially tDCS and DBS are applications for which the more accurate simulation of the electric current and the conservation of charge achieved by DG- and Mixed-FEM as shown in Chapters 4 and 5 is at least as desirable as for EEG and MEG simulations. Thus, the use of DG- and Mixed-FEM for simulating tDCS and DBS should be evaluated.

A

Appendix

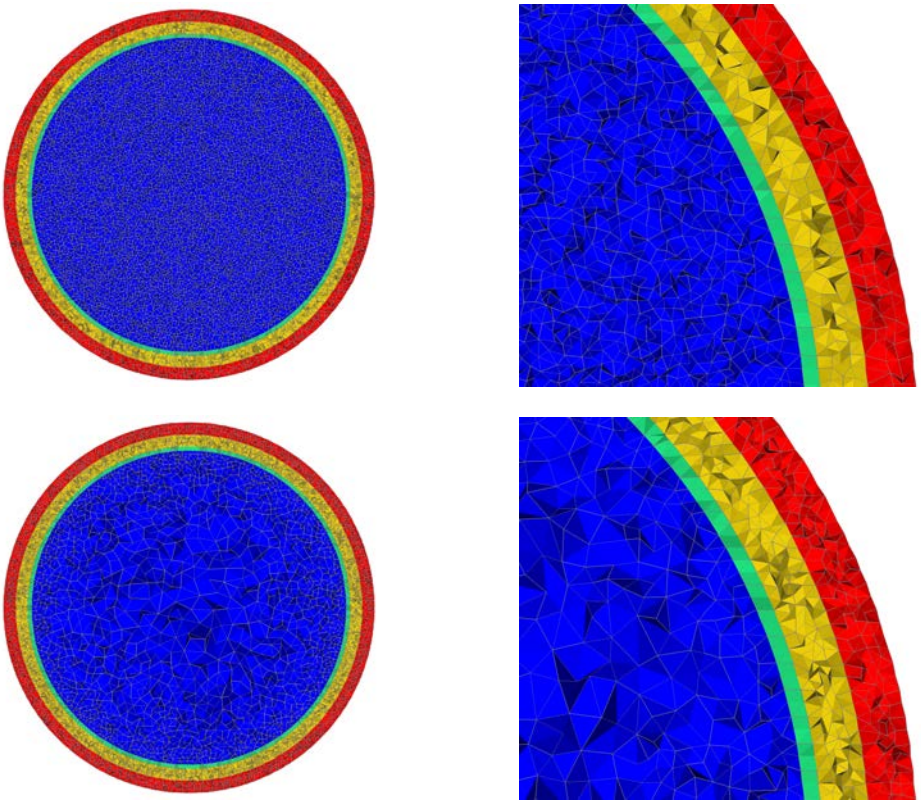

Figure A.1.: The tetrahedral sphere models *4layer-802k* (top row) and *4layer-519k* (bottom row). The cut is made through the $x = 127$ plane.

Table A.1.: (TetGen-) parameters of the tetrahedral sphere models

model	4layer-802k	4layer-519k
# nodes	801,633	518,730
# elements	4,985,234	3,159,575
quality constraint	1.1	1.1
volume constriant	1.12	1 (-1 in brain)
radius (mm)	# nodes per surface	
92	32,674	35,160
86	28,721	31,059
80	25,022	26,477
78	23,616	20,522

Table A.2.: Parameters of the hexahedral sphere models

Model	nodes	elements	edge length / mm	node shift
4layer-hex-1mm	3342701	3262312	1	no
4layer-hex-1mm-ns	3342701	3262312	1	yes

Table A.3.: (TetGen-) Parameters of the Tetrahedral Realistically Shaped Head Models

model	3layer_dir	3layer_sub	3layer_hr	4layer_hr
# nodes	933,038	653,664	2,242,186	2,268,847
# elements	5,891,852	4,075,056	14,223,508	14,353,897
quality constraint	1.1	1.1	1.1	1.1
volume constriant	1.12	1 (-1 in brain)	0.75	1.12
surface	# nodes per surface			
skin	2,219			
outer skull	1,814			
inner skull	2,879			
brain	84,200			

Table A.4.: Computation times of the different CG-FEM forward approaches. Setup measures the time for computing the FE transfer matrix. One forward computation consists of the setup of the right hand side vector and the resulting matrix multiplication. Leadfield indicates the overall time for 19,000 forward computations.

Forward Model	Model	Setup	Forward	Leadfield
Venant	802k-4layer	99 min 26 s	23.4 ms	106 min 51 s
Partial integration	802k-4layer	98 min 58 s	65.1 ms	119 min 34 s
Whitney	802k-4layer	93 min 13 s	39.8 s	107 min 49 s
Subtraction	519k-4layer	76 min 30 s	10.5 s	3394 min 38 s
Venant	4layer-hex-1mm-ns	192 min 57 s	166.2 ms	245 min 34 s
Partial integration	4layer-hex-1mm-ns	183 min 43 s	224.8 ms	254 min 55 s
Subtraction	4layer-hex-1mm	187 min 55 s	12.3 s	4075 min 3 s

B

Publications and Disclosure

Publications and Presentations Related to This Thesis

In this section, the most important publications and presentations related to this thesis are summarized and it is disclosed which passages or results were previously published or presented. Furthermore, the contributions of the author to the respective publications are mentioned.

- The evaluation of the direct approaches partial integration, Venant, and Whitney in Section 2.10.2 is based on Bauer et al. (2015). The author contributed to the implementation of the Whitney approach in the SimBio-toolbox, provided the meshes used for the forward calculations, and contributed in the writing of the publication. The figures were rearranged for this thesis.

- The BEM-FEM comparison study in Section 2.11.1 is based on Vorwerk et al. (2012) to which the author contributed the numerical results and was primarily responsible for writing and publishing as first and corresponding author.

- The evaluation of volume conductor modeling effects on the forward solution (Section 3.1) is based on Vorwerk et al. (2014). The author contributed the results and was primarily responsible for writing and publishing as first and corresponding author.

- The corresponding results for the inverse solution presented in Section 3.1.5 are recited from Cho et al. (2015), where the author provided the necessary EEG/MEG forward solutions, tools for the visualization of the results, and contributed in writing the publication.

- The realistic head model or at least the surfaces used to generate the realistic six-compartment head models used in Sections 2.11.2 and 3.1 was used in several further studies, e.g., Janssen et al. (2013); Lucka et al. (2012); Rampersad et al. (2014).

- The FieldTrip-SimBio pipeline (Section 3.2) was first presented at the *First International Conference on Basic and Clinical Multimodal Imaging* (BaCI) in Geneva, 2013.

- The results for the subtraction DG approach and parts of Theory and Discussion of Chapter 4 are recited from Engwer et al. (submitted), where the author contributed computation and evaluation of the numerical results, the visualizations, and was primarily responsible for writing Introduction, Results, and Discussion as a shared first author.

- Theory and first results for the Mixed-FEM approach (Chapter 5) were first presented at the *First International Conference on Basic and Clinical Multimodal Imaging* (BaCI) in Geneva, 2013.

Software Tools

The software tools used in the creation of scientific results presented in this thesis are listed here.

BrainVISA was used to create inflated surfaces in Section 3.1; *http://www.brainvisa.info*

Curry was used for surface extraction, e.g., in Section 3.1; *http://www.neuroscan.com*

DUNE Finite element toolbox used to implement the DG- and Mixed-FEM approaches; *http://www.dune-project.org*

FreeSurfer was used for brain surface extraction in the creation of the realistic six-compartment head model (Section 3.1); *https://surfer.nmr.mgh.harvard.edu*

FSL was used for image registration (Section 3.1); *http://fsl.fmrib.ox.ac.uk/fsl/fslwiki/FSL*

gnuplot was used to create all line graphs and boxplots; *http://www.gnuplot.info*

MATLAB was used to create heatmaps in Chapter 3, for the implementation of the FieldTrip-SimBio pipeline (Section 3.2), and for further simple calculations; *http://de.mathworks.com/products/matlab*

SCIRun was used to create all 2d- and 3d-visualizations; *http://www.sci.utah.edu/cibc-software/scirun.html*

SimBio Finite element toolbox used to calculate forward solutions presented in Chapter 2; *https://www.mrt.uni-jena.de/simbio/*

TetGen was used to perform all constrained Delaunay tetrahedralizations; *http://tetgen.berlios.de/*

Full List of Publications and Presentations

Peer-Reviewed Publications and Journal Impact Factor (IF)

1. L.D.F. Fiederer, **J. Vorwerk**, F. Lucka, M. Dannhauer, S. Yang, M. Dümpelmann, A. Schulze-Bonhage, A. Aertsen, O. Speck, C.H. Wolters, and T. Ball. The role of blood vessels in high-resolution volume conductor head modeling of EEG. *NeuroImage*, to appear.
   IF: 6.4 (2014)

2. Ü. Aydin, **J. Vorwerk**, M. Dümpelmann, P. Küpper, H. Kugel, M. Heers, J. Wellmer, C. Kellinghaus, J. Haueisen, S. Rampp, and C.H. Wolters. Combining EEG/MEG can outperform single modality EEG or MEG source reconstruction in presurgical epilepsy diagnosis. *PLOS ONE*, 10(3):e0118753, 2015.
   IF: 3.2 (2014)

3. Ü. Aydin, **J. Vorwerk**, P. Küpper, M. Heers, H. Kugel, A. Galka, L. Hamid, J. Wellmer, C. Kellinghaus, S. Rampp, and C.H. Wolters. Combining EEG and MEG for the reconstruction of epileptic activity using a calibrated realistic volume conductor model. *PLOS ONE*, 10(3):e0118753, 2015.
   IF: 3.2 (2014)

4. J.-H. Cho, **J. Vorwerk**, C.H. Wolters, and T.R. Knösche. Influence of the head model on EEG and MEG source connectivity analyses. *NeuroImage*, 110:60-77, 2015.
   IF: 6.4 (2014)

5. **J. Vorwerk**, J.-H. Cho, S. Rampp, H. Hamer, T.R. Knösche, and C.H. Wolters. A guideline for head volume conductor modeling in EEG and MEG. *NeuroImage*, 100:590-607, 2014.
   First and corresponding author, IF: 6.4 (2014)

6. S. Wagner, S.M. Rampersad, Ü. Aydin, **J. Vorwerk**, T.F. Oostendorp, T. Neuling, C.S. Herrmann, D.F. Stegeman, and C.H. Wolters. Investigation of tDCS volume conduction effects in a highly realistic head model. *Journal of Neural Engineering*, 11:016002(14pp), 2014.
   IF: 3.3 (2014)

7. M. Bruchmann, P. Hintze, and **J. Vorwerk**. The time course of feature integration in plaid patterns revealed by meta- and paracontrast masking. *Journal of Vision*, 12(13), 2012.
   IF: 2.5 (2012)

8. **J. Vorwerk**, M. Clerc, M. Burger, and C.H. Wolters. Comparison of boundary element and finite element approaches to the EEG forward problem. *Biomedical Engineering/Biomedizinische Technik*, 57(Suppl. 1), 2012.
   First and corresponding author, IF: 1.2 (2012)

Submitted Publications

1. C. Engwer, **J. Vorwerk**, J. Ludewig, and C.H. Wolters. A discontinuous Galerkin method for the EEG forward problem.
   Shared first author

2. S. Wagner, F. Lucka, **J. Vorwerk**, C.S. Herrmann, G. Nolter, M. Burger, and C.H. Wolters. Using reciprocity for relating the modeling of transcranial current stimulation and the EEG forward problem. *NeuroImage*, invited submission to special issue *Combining Transcranial Electrical Stimulation (tES) and Neuroimaging*

3. S. Pursiainen, **J. Vorwerk**, and C.H. Wolters. Electroencephalography (EEG) forward modeling via synthetic face-intersecting and edgewise finite element sources: Focal interpolated and non-interpolated approaches.

Proceedings with Journal Impact Factor (IF), first author only

1. **J. Vorwerk**, L. Magyari, J. Ludewig, R. Oostenveld, and C.H. Wolters. The FieldTrip-SimBio pipeline for finite element EEG forward computations in MATLAB: Validation and application. *First International Conference on Basic and Clinical Multimodal Imaging (BaCI)*, Geneva, Switzerland, September 5-8, 2013. *Clinical EEG and Neuroscience*, 44(4):E1-E121, (October 2013).
   IF: 3.2

2. **J. Vorwerk**, C. Engwer, J. Ludewig, and C.H. Wolters. A mixed finite element approach to solve the EEG forward problem. *First International Conference on Basic and Clinical Multimodal Imaging (BaCI)*, Geneva, Switzerland, September 5-8, 2013, *Clinical EEG and Neuroscience*, 44(4):E1-E121, (October 2013).
   IF: 3.2

3. **J. Vorwerk**, B. Lanfer, F. Grüne, and C.H. Wolters. Validation and application of realistic head modelling to MEG. *46th DGBMT Annual Conference*, Jena, Germany, September 16-18, 2012. *Biomedical Engineering, 57(Suppl. 1)*, p.794, (2012).
   IF: 1.2

Selection of other Proceedings and Poster Presentations, first author only

1. **J. Vorwerk**, C. Engwer, J. Ludewig, S. Wagner, and C.H. Wolters. A discontinuous Galerkin finite element approach for the EEG forward problem. *International Conference on Basic and Clinical Multimodal Imaging (BaCI)*, Utrecht, The Netherlands, September 1-5, 2015.

2. **J. Vorwerk**, J.-H. Cho, R. Oostenveld, S. Rampp, H. Hamer, T. Knösche, and C.H. Wolters. Influence of realistic head modeling on the EEG forward solution. *20th Annual Meeting of the Organization for Human Brain Mapping*, Hamburg, Germany, June 8-12, 2014, and *Neurovisionen 9*, Cologne, Germany, November 29, 2013.

3. **J. Vorwerk**, C. Engwer, J. Ludewig, and C.H. Wolters. A mixed finite element approach to solve the EEG forward problem. *Innovative Verarbeitung bioelektrischer und biomagnetischer Signale (BBS2014)*, Berlin, Germany, April 10-11, 2014.

4. **J. Vorwerk**, M. Burger, C.H. Wolters, and M. Clerc. Comparison of boundary element and finite element approaches to the EEG forward problem. *46th DGBMT Annual Conference*, Jena, Germany, September 16-18, 2012, and *18th International Conference on Biomagnetism*, Paris, France, August 26-30, 2012.

5. **J. Vorwerk**, B. Lanfer, F. Grüne, and C.H. Wolters. Validation and application of realistic head modelling to MEG. *Neurovisionen 8*, Aachen, Germany, October 26, 2014, and *18th International Conference on Biomagnetism*, Paris, France, August 26-30, 2012.

6. **J. Vorwerk**, F. Grüne, B. Lanfer, F. Lucka, and C.H. Wolters. Comparison of FE-approaches to solve the EEG/MEG forward problem. *Innovative Verarbeitung bioelektrischer und biomagnetischer Signale (BBS2012)*, Berlin, Germany, April 19-20, 2012.

Conference Talks

1. A guideline for volume conductor modeling in EEG and MEG source analysis. *23. Deutsches EEG/EP Mapping Meeting*, Gießen, October 25, 2014.

2. New methodology for the forward problem in EEG/MEG source analysis and in brain stimulation. *48th DGBMT Annual Conference*, Hannover, October 8, 2014.

Master Theses Contributed to Supervision

1. F. Grüne. Validierung von FEM-Ansätzen höherer Ordnung für das EEG-Vorwärtsproblem. Master thesis in Mathematics, Westfälische Wilhelms-Universität Münster, August 2014.

2. J. Ludewig. Discontinuous Galerkin methods for the EEG forward problem. Master thesis in Mathematics, Westfälische Wilhelms-Universität Münster, December 2013.

3. M. Bauer. Special finite elements for dipole modeling. Master thesis in Computer Science, Friedrich-Alexander-Universität Erlangen-Nürnberg, March 2012.

Bibliography

G. Adde, M. Clerc, O. Faugeras, R. Keriven, J. Kybic, and T. Papadopoulo. Symmetric BEM formulation for the M/EEG forward problem. In *Information Processing in Medical Imaging*, pages 524–535. Springer, 2003. 11, 51

J.P. Agnelli, E.M. Garau, and P. Morin. A posteriori error estimates for elliptic problems with dirac measure terms in weighted spaces. *ESAIM: Mathematical Modelling and Numerical Analysis*, 48(06):1557–1581, 2014. 36, 60

S.P. Ahlfors, J. Han, J.W. Belliveau, and M.S. Hämäläinen. Sensitivity of MEG and EEG to source orientation. *Brain Topography*, 23(3):227–232, 2010. 90

A.I. Ahonen, M.S. Hämäläinen, R.J. Ilmoniemi, M.J. Kajola, J.E. Knuutila, J.T. Simola, and V.A. Vilkman. Sampling theory for neuromagnetic detector arrays. *IEEE Transactions on Biomedical Engineering*, 40(9):859, 1993. 91

M. Ainsworth and R. Rankin. Technical note: A note on the selection of the penalty parameter for discontinuous galerkin finite element schemes. *Numerical Methods for Partial Differential Equations*, 28(3):1099–1104, 2012. 137

Z. Akalin-Acar and S. Makeig. Neuroelectromagnetic forward head modeling toolbox. *Journal of Neuroscience Methods*, 190:258–270, 2010. 2

M. Akhtari, H.C. Bryant, A.N. Marmelak, E.R. Flynn, L. Heller, J.J. Shih, M. Mandelkern, A. Matlachov, D.M. Ranken, E.D. Best, M.A. DiMauro, R.R. Lee, and W.W. Sutherling. Conductivities of three-layer live human skull. *Brain Topography*, 14(3):151–167, 2002. 2, 63, 87, 172

P.F. Antonietti and P. Houston. A class of domain decomposition preconditioners for hp-discontinuous Galerkin finite element methods. *Journal of Scientific Computing*, 46(1): 124–149, 2011. doi: 10.1007/s10915-010-9390-1. 114

T. Apel, O. Benedix, D. Sirch, and B. Vexler. A priori mesh grading for an elliptic problem with dirac right-hand side. *SIAM Journal on Numerical Analysis*, 49(3):992–1005, 2011. 36, 60

D.N. Arnold. Mixed finite element methods for elliptic problems. *Computer Methods in Applied Mechanics and Engineering*, 82(1):281–300, 1990. 139

D.N. Arnold and F. Brezzi. Mixed and nonconforming finite element methods: implementation, postprocessing and error estimates. *RAIRO-Modélisation mathématique et analyse numérique*, 19(1):7–32, 1985. 148

D.N. Arnold, F. Brezzi, B. Cockburn, and L.D. Marini. Unified analysis of discontinuous galerkin methods for elliptic problems. *SIAM Journal on Numerical Analysis*, 39(5): 1749–1779, 2002. 2, 105, 106, 108, 112, 118, 119, 137

D.N. Arnold, R.S. Falk, and R. Winther. Finite element exterior calculus, homological techniques, and applications. *Acta Numerica*, 15:1–155, 2006. 144

O. Axelsson. *Iterative solution methods*. Cambridge University Press, New York, 1994. 148

Ü. Aydin, J. Vorwerk, P. Küpper, M. Heers, H. Kugel, A. Galka, L. Hamid, J. Wellmer, C. Kellinghaus, S. Rampp, and C.H. Wolters. Combining EEG and MEG for the reconstruction of epileptic activity using a calibrated realistic volume conductor model. *PLOS ONE*, 9(3):e93154, 2014. 87, 91, 92, 101, 102, 134, 173

Ü. Aydin, J. Vorwerk, M. Dümpelmann, P. Küpper, H. Kugel, M. Heers, J. Wellmer, C. Kellinghaus, J. Haueisen, S. Rampp, and C.H. Wolters. Combined EEG/MEG can outperform single modality EEG or MEG source reconstruction in presurgical epilepsy diagnosis. *PLOS ONE*, 10(3):e0118753, 2015. 91, 92, 101, 173

Ümit Aydin. *Combined EEG and MEG source analysis of epileptiform activity using calibrated realistic finite element head models*. PhD thesis, Fakultät für Informatik und Automatisierung, 2015. URL http://www.db-thueringen.de/servlets/DerivateServlet/Derivate-31566/ilm1-2015000040.pdf. 101, 134

I. Babuška. Error-bounds for finite element method. *Numerische Mathematik*, 16(4):322–333, 1971. 35

I. Babuška, C.E. Baumann, and J.T. Oden. A discontinuous hp finite element method for diffusion problems: 1-D analysis. *Computers & Mathematics with Applications*, 37(9): 103–122, 1999. 109

L.A. Baccald and F. de Medicina. Generalized partial directed coherence. In *15th International Conference on Digital Signal Processing*, pages 163–166. IEEE, 2007. 81, 90

N.B. Bangera, D.L. Schomer, N. Dehghani, I. Ulbert, S. Cash, S. Papavasiliou, S.R. Eisenberg, A.M. Dale, and E. Halgren. Experimental validation of the influence of white matter anisotropy on the intracranial EEG forward solution. *Journal of Computational Neuroscience*, 29(3):371–387, 2010. 85, 88

W. Bangerth and R. Rannacher. *Adaptive Finite Element Methods for Differential Equations*. Springer Science & Business Media, 2003. 60

A.C.L. Barnard, I.M. Duck, M.S. Lynn, and W.P. Timlake. The application of electromagnetic theory to electrocardiology: II. Numerical solution of the integral equations. *Biophysical Journal*, 7(5):463–491, 1967. ISSN 0006-3495. 51

G.R. Barrenechea, L.P. Franca, and F. Valentin. A Petrov-Galerkin enriched method: A mass conservative finite element method for the Darcy equation. *Computer Methods in Applied Mechanics and Engineering*, 196(21):2449–2464, 2007. 138, 167

J.W. Barrett and CC.M. Elliott. Fitted and unfitted finite-element methods for elliptic equations with smooth interfaces. *IMA Journal of Numerical Analysis*, 7(3):283–300, 1987. 32

P. Bastian and C. Engwer. An unfitted finite element method using discontinuous Galerkin. *International Journal for Numerical Methods in Engineering*, 79(12):1557–1576, 2009. 60, 134, 172

P. Bastian, M. Blatt, A. Dedner, C. Engwer, R. Klöfkorn, R. Kornhuber, M. Ohlberger, and O. Sander. A generic grid interface for parallel and adaptive scientific computing. Part II: Implementation and tests in DUNE. *Computing*, 82(2–3):121–138, July 2008a. doi: 10.1007/s00607-008-0004-9. 119, 152

P. Bastian, M. Blatt, A. Dedner, C. Engwer, R. Klöfkorn, M. Ohlberger, and O. Sander. A generic grid interface for parallel and adaptive scientific computing. Part I: Abstract framework. *Computing*, 82(2–3):103–119, July 2008b. doi: 10.1007/s00607-008-0003-x. 119, 152

P. Bastian, F. Heimann, and S. Marnach. Generic implementation of finite element methods in the distributed and unified numerics environment (DUNE). *Kybernetika*, 46(2):294–315, 2010. 119, 152

P. Bastian, M. Blatt, and R. Scheichl. Algebraic multigrid for discontinuous Galerkin discretizations of heterogeneous elliptic problems. *Numerical Linear Algebra with Applications*, 19(2):367–388, 2012. doi: 10.1002/nla.1816. 114

M. Bauer, S. Pursiainen, J. Vorwerk, H. Köstler, and C.H. Wolters. Comparison study for Whitney (Raviart-Thomas)-type source models in finite element method based EEG forward modeling. *IEEE Transactions on Biomedical Engineering*, 62(11):2648–2656, 2015. 19, 24, 25, 26, 39, 41, 57, 177

S.B. Baumann, D.R. Wozny, S.K. Kelly, and F.M. Meno. The electrical conductivity of human cerebrospinal fluid at body temperature. *IEEE Transactions on Biomedical Engineering*, 44 (3):220–223, 1997. 39, 63, 85, 172

L. Bergamaschi, S. Mantica, and F. Saleri. Mixed finite element approximation of Darcy's law in porous media. 1994. 148, 152

O. Bertrand, M. Thévenet, and F. Perrin. 3D finite element method in brain electrical activity studies. In J. Nenonen, H.M. Rajala, and T. Katila, editors, *Biomagnetic Localization and 3D Modelling*, pages 154–171. Report of the Department of Technical Physics, Helsinki University of Technology, 1991. 2, 28

J.D. Bijsterbosch, K.H. Lee, M.D. Hunter, I.D. Wilkinson, T. Farrow, A.T. Barker, and P.W.R. Woodruff. The effect of head orientation on subarachnoid cerebrospinal fluid distribution and its implications for neurophysiological modulation and recording techniques. *Physiological Measurement*, 34(3):N9, 2013. 85

G. Birot, L. Spinelli, S. Vulliemoz, P. Megevand, D. Brunet, M. Seeck, and C.M. Michel. Head model and electrical source imaging: A study of 38 epileptic patients. *NeuroImage: Clinical*, 5:77–83, 2014. 134

M. Blasche, P. Riffel, and M. Lichy. Timtx trueshape and syngo zoomit technical and practical aspects. *Magnetom Flash*, 1:74–84, 2012. 104, 134

M. Braack. Finite elemente. *Lecture Notes, Universität Kiel*, 2012. 141, 148, 150

D. Braess. *Finite elements: theory, fast solvers and applications in solid mechanics.* Cambridge University Press, 2007. 8, 9, 16, 18, 31, 33, 141, 144, 148, 149, 150, 151

R. Brette and A. Destexhe. *Handbook of Neural Activity Measurement.* Cambridge University Press, 2012. ISBN ISBN 978-0-521-51622-8. doi: 10.1017/CBO9780511979958. URL http://www.di.ens.fr/~brette/HandbookMeasurement/. 1, 37, 65

F. Brezzi and M. Fortin. *Mixed and hybrid finite element methods*, volume 15. Springer, 1991. 2, 23, 24, 141, 143, 144, 146, 147, 148, 169

H. Buchner, M. Fuchs, H.-A. Wischmann, O. Dössel, I. Ludwig, A. Knepper, and P. Berg. Source analysis of median nerve and finger stimulated somatosensory evoked potentials: multichannel simultaneous recording of electric and magnetic fields combined with 3D-MR tomography. *Brain Topography*, 6(4):299–310, 1994. 98, 100

H. Buchner, G. Knoll, M. Fuchs, A. Rienäcker, R. Beckmann, M. Wagner, J. Silny, and J. Pesch. Inverse localization of electric dipole current sources in finite element models of the human head. *Electroencephalography and Clinical Neurophysiology*, 102:267–278, 1997. 2, 20, 22

C.R. Butson, S.E. Cooper, J.M. Henderson, and C.C. McIntyre. Patient-specific analysis of the volume of tissue activated during deep brain stimulation. *NeuroImage*, 34(2):661–670, 2007. 64, 88, 98

Z. Cai, X. Ye, and S. Zhang. Discontinuous Galerkin finite element methods for interface problems: a priori and a posteriori error estimations. *SIAM Journal on Numerical Analysis*, 49(5):1761–1787, 2011. 118

D. Calvetti, H. Hakula, S. Pursiainen, and E. Somersalo. Conditionally gaussian hypermodels for cerebral source localization. *SIAM Journal on Imaging Sciences*, 2(3):879–909, 2009. 57

D. Camacho, R. Hopper, G. Lin, and B. Myers. An improved method for finite element mesh generation of geometrically complex structures with application to the skullbase. *Journal of Biomechanics*, 30(10):1067–1070, 1997. 60, 91, 93, 169, 172

E. Casas. L^2 estimates for the finite element method for the Dirichlet problem with singular data. *Numerische Mathematik*, 47(4):627–632, 1985. 10, 33, 34

P. Castillo. Performance of discontinuous Galerkin methods for elliptic PDEs. *SIAM Journal on Scientific Computing*, 24(2):524–547, 2002. 113, 137

A. Chaturvedi, C.R. Butson, S.F. Lempka, S.E. Cooper, and C.C. McIntyre. Patient-specific models of deep brain stimulation: influence of field model complexity on neural activation predictions. *Brain Stimulation*, 3(2):65–77, 2010. 64, 88, 98

K. Chen. *Matrix preconditioning techniques and applications*. Number 19. Cambridge University Press, 2005. 152

J.-H. Cho, J. Vorwerk, C.H. Wolters, and T.R. Knösche. Influence of the head model on EEG and MEG source connectivity analyses. *NeuroImage*, 110:60–77, 2015. 40, 62, 81, 82, 83, 84, 89, 90, 170, 177

S.H. Chou, D.Y. Kwak, and K.Y. Kim. Flux recovery from primal hybrid finite element methods. *SIAM Journal on Numerical Analysis*, 40(2):403–415, 2002. 169

P.G. Ciarlet. *The finite element method for elliptic problems*. North-Holland, 1978. 33

M.J.D Cook and Z.J. Koles. A high-resolution anisotropic finite-volume head model for EEG source analysis. In *Proceedings of the 28th Annual International Conference of the IEEE Engineering in Medicine and Biology Society*, pages 4536–4539, 2006. 2, 135

C. D'Angelo. Finite element approximation of elliptic problems with dirac measure terms in weighted spaces: applications to one-and three-dimensional coupled problems. *SIAM Journal on Numerical Analysis*, 50(1):194–215, 2012. 36, 60

C. D'Angelo and A. Quarteroni. On the coupling of 1d and 3d diffusion-reaction equations: Application to tissue perfusion problems. *Mathematical Models and Methods in Applied Sciences*, 18(08):1481–1504, 2008. 36, 60

M. Dannhauer, B. Lanfer, C.H. Wolters, and T.R. Knösche. Modeling of the human skull in EEG source analysis. *Human Brain Mapping*, 32(9):1383–1399, 2011. doi: 10.1002/hbm.21114. 2, 39, 40, 63, 81, 87, 88, 89

O. David, L. Harrison, and K.J. Friston. Modelling event-related responses in the brain. *NeuroImage*, 25(3):756–770, 2005. 81

J.C. de Munck. The potential distribution in a layered anisotropic spheroidal volume conductor. *Journal of Applied Physics*, 64:465–469, 1988. 13

J.C. de Munck and M.J. Peters. A fast method to compute the potential in the multisphere model. *IEEE Transactions on Biomedical Engineering*, 40(11):1166–1174, 1993. ISSN 0018-9294. 13, 14

J.C. de Munck, B.W. van Dijk, and H. Spekreijse. Mathematical dipoles are adequate to describe realistic generators of human brain activity. *IEEE Transactions on Biomedical Engineering*, 35(11):960–966, 1988. ISSN 0018-9294. 10

D.A. Di Pietro and A. Ern. *Mathematical Aspects of Discontinuous Galerkin Methods*, volume 69. Springer, 2011. 2, 109, 111

D.A. Di Pietro and A. Ern. Analysis of a discontinuous Galerkin method for heterogeneous diffusion problems with low-regularity solutions. *Numerical Methods for Partial Differential Equations*, 28(4):1161–1177, 2012. 109, 111, 118, 137

J. Douglas and J.E. Roberts. Global estimates for mixed methods for second order elliptic equations. *Mathematics of Computation*, 44(169):39–52, 1985. 148

D.A. Drachman. Do we have brain to spare? *Neurology*, 64(12):2004, 2005. ISSN 0028-3878. 5

F. Drechsler, C.H. Wolters, T. Dierkes, H. Si, and L. Grasedyck. A full subtraction approach for finite element method based source analysis using constrained Delaunay tetrahedralisation. *NeuroImage*, 46(4):1055–1065, 2009. doi: 10.1016/j.neuroimage.2009.02.024. 2, 11, 28, 29, 30

R. Durán. Superconvergence for rectangular mixed finite elements. *Numerische Mathematik*, 58(1):287–298, 1990. 148

H.C. Elman and G.H. Golub. Inexact and preconditioned Uzawa algorithms for saddle point problems. *SIAM Journal on Numerical Analysis*, 31(6):1645–1661, 1994. 151, 152

C. Engwer, J. Vorwerk, J. Ludewig, and C.H. Wolters. A discontinuous Galerkin method for the EEG forward problem. submitted. 103, 104, 114, 119, 137, 178

Y. Epshteyn and B. Rivière. Estimation of penalty parameters for symmetric interior penalty galerkin methods. *Journal of Computational and Applied Mathematics*, 206(2):843–872, 2007. 137

A. Ern, A.F. Stephansen, and P. Zunino. A discontinuous Galerkin method with weighted averages for advection-diffusion equations with locally small and anisotropic diffusivity. *IMA Journal of Numerical Analysis*, 29(2):235–256, 2009. 107, 118

L.C. Evans. *Partial differential equations*. Graduate Studies in Mathematics. American Mathematical Society, 1998. 9

R.E. Ewing, M.M. Liu, and J. Wang. Superconvergence of mixed finite element approximations over quadrilaterals. *SIAM Journal on Numerical Analysis*, 36(3):772–787, 1999. 138, 167, 169

L.D.F. Fiederer, F. Lucka, S. Yang, J. Vorwerk, M. Dümpelmann, D. Cosandier Rimélé, A. Schulze-Bonhage, A. Aertsen, O. Speck, C.H. Wolters, and T. Ball. High-resolution forward modeling using finite element method head models based on 7-T MRI data. In *International Conference on Basic and Clinical Multimodal Imaging (BaCI)*, 2013. 172

L.D.F. Fiederer, J. Vorwerk, F. Lucka, M. Dannhauer, S. Yang, M. Dümpelmann, A. Schulze-Bonhage, A. Aertsen, O. speck, C.H. Wolters, and T. Ball. The role of blood vessels in high-resolution volume conductor head modeling of eeg. *NeuroImage*, to appear. 172

M. Fuchs, M. Wagner, H.A. Wischmann, T. Köhler, A. Theißen, R. Drenckhahn, and H. Buchner. Improving source reconstructions by combining bioelectric and biomagnetic data. *Electroencephalography and Clinical Neurophysiology*, 107:93–111, 1998. 87

L. Gastaldi and R.H. Nochetto. Optimal L^∞-error estimates for nonconforming and mixed finite element methods of lowest order. *Numerische Mathematik*, 50(5):587–611, 1987. 148

L. Gastaldi and R.H. Nochetto. Sharp maximum norm error estimates for general mixed finite element approximations to second order elliptic equations. *RAIRO-Modélisation mathématique et analyse numérique*, 23(1):103–128, 1989. 148

N.G. Gencer and C.E. Acar. Sensitivity of EEG and MEG measurements to tissue conductivity. *Physics in Medicine and Biology*, 49:701–717, 2004. 2, 37

D.B. Geselowitz. On bioelectric potentials in an inhomogeneous volume conductor. *Biophysical journal*, 7(1):1–11, 1967. ISSN 0006-3495. 11, 13, 51

S. Giani and P. Houston. Anisotropic hp-adaptive discontinuous Galerkin finite element methods for compressible fluid flows. *International Journal of Numerical Analysis and Modeling*, 9(4):928–949, 2012. 109

G.H. Golub and M.L. Overton. The convergence of inexact Chebyshev and Richardson iterative methods for solving linear systems. *Numerische Mathematik*, 53(5):571–593, 1988. 151

G.H. Golub and C.F. Van Loan. *Matrix computations*. The John Hopkins University Press, Baltimore and London, 2nd edition, 1989. 148

S.I. Gonçalves, J.C. de Munck, and J.P.A. Verbunt. In vivo measurement of skull and brain resistivities with EIT based method and analysis of SEF/SEP data. In *Proceedings of the 23rd Annual International Conference of the IEEE EMBS*, volume 1, pages 1006–1008. IEEE, 2001. 87

S.I. Gonçalves, J.C. de Munck, J. Verbunt, F. Bijma, R.M. Heethaar, and F. Lopes da Silva. In vivo measurement of the brain and skull resistivities using an EIT-based method and

realistic models for the head. *IEEE Transactions on Biomedical Engineering*, 50(6):754–767, 2003. 87

A. Gramfort, T. Papadopoulo, E. Olivi, and M. Clerc. Forward field computation with openmeeg. *Computational Intelligence and Neuroscience*, 2011:1–13, 2011. doi: 10.1155/2011/923703. 2, 19, 51, 59

P.G. Grieve, R.G. Emerson, J.R. Isler, and R.I. Stark. Quantitative analysis of spatial sampling error in the infant and adult electroencephalogram. *NeuroImage*, 21(4):1260–1274, 2004. 91

F. Grüne. Validierung von FEM-Ansätzen höherer Ordnung für das EEG-Vorwärtsproblem. Master thesis in Mathematics, Westfälische Wilhelms-Universität Münster, August 2014. URL http://www.sci.utah.edu/~wolters/PaperWolters/2014/MasterGruene.pdf. 59, 171

F. Grynszpan and D.B. Geselowitz. Model studies of the magnetocardiogram. *Biophysical journal*, 13(9):911, 1973. 14

D. Güllmar, J. Haueisen, and J.R. Reichenbach. Influence of anisotropic electrical conductivity in white matter tissue on the EEG/MEG forward and inverse solution. a high-resolution whole head simulation study. *NeuroImage*, 2010. doi: 10.1016/j.neuroimage.2010.02.014. 2, 40, 88

W. Hackbusch. *Elliptic differential equations: theory and numerical treatment*, volume 18 of *Springer Series in Computational Mathematics*. Springer, 2003. 9, 10, 11, 31, 32

H. Hallez, B. Vanrumste, P. Van Hese, S. Delputte, and I. Lemahieu. Dipole estimation errors due to differences in modeling anisotropic conductivities in realistic head models for EEG source analysis. *Physics in Medicine and Biology*, 53:1877–1894, 2008. 89

M.S. Hämäläinen, R. Hari, R.J. Ilmoniemi, J. Knuutila, and O.V. Lounasmaa. Magnetoencephalography – theory, instrumentation, and applications to noninvasive studies of the working human brain. *Reviews of Modern Physics*, 65(2):413–497, 1993. ISSN 1539-0756. 5, 6, 10, 13, 87

A. Hanrath, J. Vorwerk, C.H. Wolters, and L. Grasedyck. The multipole approach for improving eeg forward simulation accuracy. in prep. 20, 33, 60, 171

K. Harriman, P. Houston, B. Senior, and E. Suli. hp-version discontinuous Galerkin methods with interior penalty for partial differential equations with nonnegative characteristic form. In *Recent Advances in Scientific Computing and Partial Differential Equations. Contemporary Mathematics*, number 330, pages 89–119. AMS, 2003. 108

R. Hartmann. Adjoint consistency analysis of discontinuous Galerkin discretizations. *SIAM Journal on Numerical Analysis*, 45(6):2671–2696, 2007. 108, 112

R. Hartmann. Numerical analysis of higher order discontinuous Galerkin finite element methods. In *VKI Lecture Series 2008-08*, 2008. URL http://ganymed.iwr.uni-heidelberg.de/~hartmann/publications/2008/Har08b.pdf. 105, 110, 111, 119

J. Haueisen, C. Ramon, M. Eiselt, H. Brauer, and H. Nowak. Influence of tissue resistivities on neuromagnetic fields and electric potentials studied with a finite element model of the head. *IEEE Transactions on Biomedical Engineering*, 44(8):727–735, 1997. 86

J. Haueisen, C. Ramon, H. Brauer, and H. Nowak. The influence of local conductivity changes on MEG and EEG. *Biomedizinische Technik*, 45(7-8):211–214, 2000. 86

J. Haueisen, D.S. Tuch, C. Ramon, P.H. Schimpf, V.J. Wedeen, J.S. George, and J.W. Belliveau. The influence of brain tissue anisotropy on human EEG and MEG. *NeuroImage*, 15:159–166, 2002. 88, 89

R.M. Heidemann, D.A. Porter, A. Anwander, T. Feiweier, K. Heberlein, T.R. Knösche, and R. Turner. Diffusion imaging in humans at 7T using readout-segmented EPI and GRAPPA. *Magnetic Resonance in Medicine*, 64(1):9–14, 2010. 64

A. Hillebrand and G.R. Barnes. A quantitative assessment of the sensitivity of whole-head MEG to activity in the adult human cortex. *NeuroImage*, 16(3):638–650, 2002. 90

R.S. Hosek, A. Sances Jr., R.W. Jodat, and S.J. Larson. The contributions of intracerebral currents to the EEG and evoked potentials. *IEEE Transactions on Biomedical Engineering*, 25(5):405–413, 1978. 13

P. Houston and T.P. Wihler. Discontinuous Galerkin methods for problems with Dirac delta source. *ESAIM: Mathematical Modelling and Numerical Analysis*, 46(6):1467–1483, 2012. 117

M.X. Huang, T. Song, D.J. Hagler, I. Podgorny, V. Jousmaki, L. Cui, K. Gaa, D.L. Harrington, A.M. Dale, R.R. Lee, J. Elman, and E. Halgren. A novel integrated MEG and EEG analysis method for dipolar sources. *NeuroImage*, 37:731–748, 2007. 87

J.D. Jackson, C. Witte, and K. Müller. *Klassische Elektrodynamik*. de Gruyter, 2006. ISBN 3110189704. 5, 10, 11, 12, 20, 21

B.H. Jansen and V.G. Rit. Electroencephalogram and visual evoked potential generation in a mathematical model of coupled cortical columns. *Biological Cybernetics*, 73(4):357–366, 1995. 81

A.M. Janssen, S.M. Rampersad, F. Lucka, B. Lanfer, S. Lew, Ü. Aydin, C.H. Wolters, D.F. Stegeman, and T.F. Oostendorp. The influence of sulcus width on simulated electric fields induced by transcranial magnetic stimulation. *Physics in Medicine and Biology*, 58(14): 4881, 2013. 177

A. Johansson. *Duality-based adaptive finite element methods with application to time-dependent problems*. PhD thesis in Mathematics, UmeåUniversity, 2010. 60

K. Kazemi and N. Noorizadeh. Quantitative comparison of SPM, FSL, and Brainsuite for brain MR image segmentation. *Journal of Biomedical Physics & Engineering*, 4(1):13, 2014. 100

R.B. Kellogg. On the Poisson equation with intersecting interfaces. *Applicable Analysis*, 4(2): 101–129, 1974. 118

T. Köppl and B. Wohlmuth. Optimal a priori error estimates for an elliptic problem with dirac right-hand side. *SIAM Journal on Numerical Analysis*, 52(4):1753–1769, 2014. 10, 34, 35

A. Koulouri. *Reconstruction of electric fields and source distributions in EEG brain imaging*. PhD thesis, Imperial College London, August 2015. URL https://spiral.imperial.ac.uk/handle/10044/1/25759. 172

D.Y. Kwak and H.C. Pyo. Mixed finite element methods for general quadrilateral grids. *Applied Mathematics and Computation*, 217(14):6556–6565, 2011. 169

J.-H. Kwon, J.S. Kim, D.-W. Kang, K.-S. Bae, and S.U. Kwon. The thickness and texture of temporal bone in brain CT predict acoustic window failure of transcranial doppler. *Journal of Neuroimaging*, 16:347–52, 2006. 134

J. Kybic, M. Clerc, T. Abboud, O. Faugeras, R. Keriven, and T. Papadopoulo. A common formalism for the integral formulations of the forward EEG problem. *IEEE Transactions on Medical Imaging*, 24(1):12–18, 2005. 11, 51, 52

B. Lanfer. Validation and comparison of realistic head modeling techniques and application to tactile somatosensory evoked EEG and MEG data. Master thesis in Physics, Institut für Biomagnetismus und Biosignalanalyse, Westfälische Wilhelms-Universität Münster, 2007. 36, 58

B. Lanfer. *Automatic Generation of Volume Conductor Models of the Human Head for EEG Source Analysis*. PhD thesis in Mathematics, Westfälische Wilhelms-Universität Münster, July 2014. 172

B. Lanfer, C.H. Wolters, S.O. Demokritov, and C. Pantev. Validating finite element method based EEG and MEG forward computations. In *Proceedings 41. Jahrestagung der DGBMT, Deutsche Gesellschaft für Biomedizinische Technik, Aachen, Germany*, pages 140–141, 2007. URL http://www.bmt2007.de. 58

B. Lanfer, I. Paul-Jordanov, M. Scherg, and C.H. Wolters. Influence of interior cerebrospinal fluid compartments on EEG source analysis. *Biomedical Engineering/Biomedizinische Technik*, 57(Suppl. 1):236–236, 2012a. 2

B. Lanfer, M. Scherg, M. Dannhauer, T.R. Knösche, M. Burger, and C.H. Wolters. Influences of skull segmentation inaccuracies on EEG source analysis. *NeuroImage*, 62(1):418–431, 2012b. doi: 10.1016/j.neuroimage.2012.05.006. 63, 87, 91, 100

G. Lantz, R.G. de Peralta, L. Spinelli, M. Seeck, and C.M. Michel. Epileptic source localization with high density EEG: how many electrodes are needed? *Clinical Neurophysiology*, 114(1): 63–69, 2003. 91

S. Lew, C.H. Wolters, A. Anwander, S. Makeig, and R.S. MacLeod. Low resolution conductivity estimation to improve source localization. *International Congress Series*, 1300:149–152, 2007. doi: 10.1016/j.ics.2006.12.058. 101, 173

S. Lew, C.H. Wolters, A. Anwander, S. Makeig, and R.S. MacLeod. Improved EEG source analysis using low resolution conductivity estimation in a four-compartment finite element head model. *Human Brain Mapping*, 30(9):2862–2878, 2009a. doi: 10.1002/hbm.20714. 101, 173

S. Lew, C.H. Wolters, T. Dierkes, C. Röer, and R.S. MacLeod. Accuracy and run-time comparison for different potential approaches and iterative solvers in finite element method based EEG source analysis. *Applied Numerical Mathematics*, 59(8):1970–1988, 2009b. 18, 19, 30, 39, 40, 50, 53, 58, 102

S. Lew, D.D. Sliva, M.-S. Choe, P.E. Grant, Y. Okada, C.H. Wolters, and M.S. Hämäläinen. Effects of sutures and fontanels on MEG and EEG source analysis in a realistic infant head model. *NeuroImage*, 76:282–293, 2013. doi: 10.1016/j.neuroimage.2013.03.017. 87

J. Li, Jens M. Melenk, B. Wohlmuth, and J. Zou. Optimal a priori estimates for higher order finite elements for elliptic interface problems. *Applied Numerical Mathematics*, 60(1):19–37, 2010. 32, 35

M. Liehr and J. Haueisen. Influence of anisotropic compartments on magnetic field and electric potential distributions generated by artificial current dipoles inside a torso phantom. *Physics in Medicine and Biology*, 53(1):245, 2008. 88

J.L. Lions. Problemes aux limites non homogenesa donées irrégulieres: Une méthode d'approximation. *Numerical Analysis of Partial Differential Equations (CIME 2 Ciclo, Ispra, 1967)*, pages 283–292, 1968. 104, 105

F. Lucka, S. Pursiainen, M. Burger, and C.H. Wolters. Hierarchical bayesian inference for the eeg inverse problem using realistic fe head models: depth localization and source separation for focal primary currents. *NeuroImage*, 61(4):1364–1382, 2012. 177

J. Ludewig. Discontinuous Galerkin methods for the EEG forward problem. Master thesis in Mathematics, Westfälische Wilhelms-Universität Münster, December 2013. URL http://www.sci.utah.edu/~wolters/PaperWolters/2013/Masterarbeit_Ludewig.pdf. 105, 113, 114, 119, 136, 137

G. Marin, C. Guerin, S. Baillet, L. Garnero, and G. Meunier. Influence of skull anisotropy for the forward and inverse problem in EEG: simulation studies using the FEM on realistic head models. *Human Brain Mapping*, 6:250–269, 1998. 2, 87

T. Medani, J. Vorwerk, D. Lautru, D. Schwartz, Z. Ren, G. Sou, and C.H. Wolters. Study, comparison and validation of the Venant method on FEM source modeling applied on spherical and realistic head models. in prep. 25, 60, 171

J.W.H Meijs, O.W. Weier, M.J. Peters, and A. van Oosterom. On the numerical accuracy of the boundary element method. *IEEE Transactions on Biomedical Engineering*, 36: 1038–1049, 1989. 40

F. Meyer. Convergent adaptive finite element methods for the solution of the EEG forward problem with the help of the subtraction method. Master thesis in Mathematics, Westfälische Wilhelms-Universität Münster, May 2013. URL http://www.sci.utah.edu/~wolters/PaperWolters/2013/MasterarbeitMeyer.pdf. 60, 171

V. Montes-Restrepo, P. van Mierlo, G. Strobbe, S. Staelens, S. Vandenberghe, and H. Hallez. Influence of skull modeling approaches on EEG source localization. *Brain Topography*, 27 (1):95–111, 2014. 2, 87, 91

J.C. Mosher and R.M. Leahy. Source localization using recursively applied and projected (RAP) MUSIC. *IEEE Transactions on Signal Processing*, 47(2):332–340, 1999. doi: 10.1109/78.740118. 2

J.C. Mosher, R.M. Leahy, and P.S. Lewis. EEG and MEG: forward solutions for inverse methods. *IEEE Transactions on Biomedical Engineering*, 46(3):245–259, 1999. ISSN 0018-9294. 13

S. Murakami and Y. Okada. Contributions of principal neocortical neurons to magnetoencephalography and electroencephalography signals. *The Journal of Physiology*, 575(3): 925–936, 2006. ISSN 0022-3751. 5

J.-C. Nédélec. Mixed finite elements in $\mathbb{R}^3$. *Numerische Mathematik*, 35(3):315–341, 1980. 23, 24, 143, 144

J.C. Nédélec. *Acoustic and electromagnetic equations: integral representations for harmonic problems*. Springer, 2001. ISBN 0387951555. 11

E. Ng, B. Nitrosso, and B. Peyton. On the solution of Stokes's pressure system within N3S using supernodal Cholesky factorization. *Finite Elements in Fluids: New Trends and Applications*, 1993. 152

S. Nicaise and A.-M. Sändig. General interface problems – I,II. *Mathematical Methods in the Applied Sciences*, 17(6):395–429,431–450, 1994. 118

G. Nolte, O. Bai, L. Wheaton, Z. Mari, S. Vorbach, and M. Hallett. Identifying true brain interaction from EEG data using the imaginary part of coherency. *Clinical Neurophysiology*, 115(10):2292–2307, 2004. 81, 90

A. Nüßing, C.H. Wolters, H. Brinck, and Engwer C. The unfitted discontinuous Galerkin method in brain research. In *International Conference on Basic and Clinical Multimodal Imaging (BaCI)*, 2015. 60, 134, 135, 172

S.H. Oh, S.Y. Lee, M.H. Cho, T.-S. Kim, and I.H. Kim. Electrical conductivity estimation from diffusion tensor and T2: a silk yarn phantom study. In *International Society for Magnetic Resonance in Medicine*, volume 14, page 3034, 2006. 64

Y. Okada. Empirical bases for constraints in current-imaging algorithms. *Brain Topography*, 5 (4):373–377, 1993. ISSN 0896-0267. 5

J. Ollikainen, M. Vauhkonen, P.A. Karjalainen, and J.P. Kaipio. Effects of local skull inhomogeneities on EEG source estimation. *Medical Engineering & Physics*, 21:143–154, 1999. 87

R. Oostenveld and T.F. Oostendorp. Validating the boundary element method for forward and inverse EEG computations in the presence of a hole in the skull. *Human Brain Mapping*, 17 (3):179–192, 2002. 63

R. Plonsey. Action potential sources and their volume conductor fields. *Proceedings of the IEEE*, 65(5):601–611, 2005. ISSN 0018-9219. 5

M. Plum and C. Wieners. Optimal a priori estimates for interface problems. *Numerische Mathematik*, 95(4):735–759, 2003. 32, 33

S. Prudhomme, F. Pascal, J.T. Oden, and A. Romkes. Review of a priori error estimation for discontinuous Galerkin methods. *Technical report 00–27*, 2000. 110

S. Pursiainen, A. Sorrentino, C. Campi, and M. Piana. Forward simulation and inverse dipole localization with the lowest order Raviart-Thomas elements for electroencephalography. *Inverse Problems*, 27(4), 2011. doi: 10.1088/0266-5611/27/4/045003. 2, 24, 25, 41, 59, 138

S. Pursiainen, J. Vorwerk, and C.H. Wolters. Electroencephalography (EEG) forward modeling via synthetic face-intersecting and edgewise finite element sources: focal interpolated and non-interpolated approaches. submitted. 60, 171

E. Ramm, E. Rank, R. Rannacher, K. Schweizerhof, E. Stein, W. Wendland, G. Wittum, P. Wriggers, and W. Wunderlich. *Error-controlled adaptive finite elements in solid mechanics.* John Wiley & Sons, 2003. 60

C. Ramon, P. Schimpf, J. Haueisen, M. Holmes, and A. Ishimaru. Role of soft bone, CSF and gray matter in EEG simulations. *Brain Topography*, 16(4):245–248, 2004. 2, 3, 39, 63, 86

C. Ramon, P. Schimpf, and J. Haueisen. Influence of head models on EEG simulations and inverse source localizations. *BioMedical Engineering OnLine*, 5(10), 2006. doi: 10.1186/1475-925X-5-10. 2

C. Ramon, P. Garguilo, E.A. Fridgeirsson, and J. Haueisen. Changes in scalp potentials and spatial smoothing effects of inclusion of dura layer in human head models for EEG simulations. *Frontiers in Neuroengineering*, 7, 2014. 172

S.M. Rampersad, A.M. Janssen, F. Lucka, Ü. Aydin, B. Lanfer, S. Lew, C.H. Wolters, D.F. Stegeman, and T.F. Oostendorp. Simulating transcranial direct current stimulation with a detailed anisotropic human head model. *IEEE Transactions on Neural Systems and Rehabilitation Engineering*, 22(3):441–452, 2014. 177

P.-A. Raviart and J.-M. Thomas. A mixed finite element method for 2-nd order elliptic problems. In *Mathematical Aspects of Finite Element Methods*, pages 292–315. Springer, 1977. 2, 23

J.K. Rice, C. Rorden, J.S. Little, and L.C. Parra. Subject position affects EEG magnitudes. *NeuroImage*, 64:476–484, 2013. 85, 97, 100

A. Rienäcker, R. Beckmann, J. Pesch, G. Knoll, H. Buchner, and J. Silny. Dipolabbildung im FEM-Netz (III): Berücksichtigung höherer Dipolmomente. Arbeitspapier zum Projekt Anatomische Abbildung elektrischer Aktivität des Zentralnervensystems, RWTH Aachen, November 1994. 21

B. Rivière. *Discontinuous Galerkin methods for solving elliptic and parabolic equations: theory and implementation*. Society for Industrial and Applied Mathematics, 2008. 113

U. Rüde. On the accurate computation of singular solutions of laplace's and poisson's equation. *Multigrid Methods (Copper Mountain, CO., 1987). Lecture Notes in Pure and Applied Mathematics*, 110:517–540, 1988. 36

M. Rullmann, A. Anwander, M. Dannhauer, S. Warfield, F.H. Duffy, and C.H. Wolters. EEG source analysis of epileptiform activity using a 1mm anisotropic hexahedra finite element head model. *NeuroImage*, 44(2):399–410, 2009. doi: 10.1016/j.neuroimage.2008.09.009. 64, 92, 102, 134, 173

L. Ruthotto, H. Kugel, J. Olesch, B. Fischer, J. Modersitzki, M. Burger, and C.H. Wolters. Diffeomorphic susceptibility artefact correction of diffusion-weighted magnetic resonance images. *Physics in Medicine and Biology*, 57(18):1–17, 2012. doi: 10.1088/0031-9155/57/18/5715. 63, 64

R.J. Sadleir and A. Argibay. Modeling skull electrical properties. *Annals of Biomedical Engineering*, 35(10):1699–1712, 2007. 2, 87

J. Sarvas. Basic mathematical and electromagnetic concepts of the biomagnetic inverse problem. *Physics in Medicine and Biology*, 32(1):11–22, 1987. 10, 11, 14, 46

P.H. Schimpf, C.R. Ramon, and J. Haueisen. Dipole models for the EEG and MEG. *IEEE Transactions on Biomedical Engineering*, 49(5):409–418, 2002. 2

C. Schmidt and U. van Rienen. Modeling the field distribution in deep brain stimulation: the influence of anisotropy of brain tissue. *IEEE Transactions on Biomedical Engineering*, 59 (6):1583–1592, 2012. 98

R. Schönen, A. Rienäcker, R. Beckmann, and G. Knoll. Dipolabbildung im FEM-Netz, Teil I. Arbeitspapier zum Projekt Anatomische Abbildung elektrischer Aktivität des Zentralnervensystems, RWTH Aachen, Juli 1994. 2, 20

R. Scott. Finite element convergence for singular data. *Numerische Mathematik*, 21(4): 317–327, 1973. 33, 36

K. Sekihara, M. Sahani, and S.S. Nagarajan. Localization bias and spatial resolution of adaptive and non-adaptive spatial filters for MEG source reconstruction. *NeuroImage*, 25 (4):1056–1067, 2005. 82

K. Shahbazi. An explicit expression for the penalty parameter of the interior penalty method. *Journal of Computational Physics*, 205(2):401–407, 2005. 137

H. Si. TetGen: A quality tetrahedral mesh generator and three-dimensional delaunay triangulator, V1.3, user's manual. Technical Report 9, Weierstrass Institute for Applied Analysis and Stochastics, 2004. http://tetgen.berlios.de. 40

H. Sonntag, J. Vorwerk, C.H. Wolters, L. Grasedyck, J. Haueisen, and B. Maess. Leakage effect in hexagonal FEM meshes of the EEG forward problem. In *International Conference on Basic and Clinical Multimodal Imaging (BaCI)*, 2013. 102

C. Stahlhut, M. Mørup, O. Winther, and L.K. Hansen. SOFOMORE: Combined EEG source and forward model reconstruction. In *IEEE International Symposium on Biomedical Imaging: From Nano to Macro*, pages 450–453. IEEE, 2009. 172, 173

C. Stahlhut, M. Mørup, O. Winther, and L.K. Hansen. Simultaneous EEG source and forward model reconstruction (SOFOMORE) using a hierarchical bayesian approach. *Journal of Signal Processing Systems*, 65(3):431–444, 2011. 172, 173

M. Stenroos and J. Sarvas. Bioelectromagnetic forward problem: isolated source approach revis(it)ed. *Physics in Medicine and Biology*, 57:3517–3535, 2012. 2

M. Stenroos, A. Hunold, and J. Haueisen. Comparison of three-shell and simplified volume conductor models in magnetoencephalography. *NeuroImage*, 94:337–348, 2014. 87

O. Tanzer, S. Järvenpää, J. Nenonen, and E. Somersalo. Representation of bioelectric current sources using whitney elements in finite element method. *Physics in Medicine and Biology*, 50:3023–3039, 2005. 2

G. Taubin. A signal processing approach to fair surface design. In *Proceedings of the 22nd annual conference on Computer graphics and interactive techniques*, pages 351–358. ACM, 1995. 63

M.E. Taylor. *Partial differential equations, basic theory*. Springer-Verlag, New York, 1996. 10

R.F. Thompson. *Das Gehirn*. Spektrum Akadademischer Verlag, 1992. ISBN 3860250639. 4

R. Toupin. Saint-Venant's principle. *Archive for Rational Mechanics and Analysis*, 18(2): 83–96, 1965. doi: 10.1007/BF00282253. 2

D.S. Tuch, V.J. Wedeen, A.M. Dale, J.S. George, and J.W. Belliveau. Conductivity tensor mapping of the human brain using diffusion tensor MRI. *PNAS*, 98(20):11697–11701, 2001. 64, 88, 89

S. Vallaghé and M. Clerc. A global sensitivity analysis of three- and four-layer EEG conductivity models. *IEEE Transactions on Biomedical Engineering*, 56(4):988–995, 2009. 86, 87

S. Vallaghé and T. Papadopoulo. A trilinear immersed finite element method for solving the electroencephalography forward problem. *SIAM Journal on Scientific Computing*, 32(4): 2379–2394, 2010. 2, 60, 135

S. Vallaghé, T. Papadopoulo, and M. Clerc. The adjoint method for general EEG and MEG sensor-based lead field equations. *Physics in Medicine and Biology*, 54:135–147, 2009. 108

S.P. van den Broek, F. Reinders, M. Donderwinkel, and M.J. Peters. Volume conduction effects in EEG and MEG. *Electroencephalography and Clinical Neurophysiology*, 106:522–534, 1998. 63, 87

R. Van Uitert, C. Johnson, and L. Zhukov. Influence of head tissue conductivity in forward and inverse magnetoencephalographic simulations using realistic head models. *IEEE Transactions on Biomedical Engineering*, 51(12):2129–2137, 2004. 82, 86

B.D. Van Veen, W. Van Drongelen, M. Yuchtman, and A. Suzuki. Localization of brain electrical activity via linearly constrained minimum variance spatial filtering. *IEEE Transactions on Biomedical Engineering*, 44(9):867–880, 1997. 81

B. Vanrumste, G. Van Hoey, P. Boon, M. D'Havé, and I. Lemahieu. Inverse calculations in EEG source analysis applying the finite difference method, reciprocity and lead fields. In *Proceedings of the 20th Annual International Conference of the IEEE EMPS, HongKong*, volume 20, 4/6, 1998. 87

F. Vatta, F. Meneghini, F. Esposito, F. Mininel, and F. Di Salle. Solving the forward problem in eeg source analysis by spherical and fdm head modeling: a comparative analysis. *Biomed Sci Instrum*, 45:382–388, 2009. 2

L.A. Vese and T.F. Chan. A multiphase level set framework for image segmentation using the mumford and shah model. *International Journal of Computer Vision*, 50(3):271–293, 2002. 63

J. Vorwerk. Comparison of numerical approaches to the EEG forward problem. Diploma thesis in Mathematics, Institut für Biomagnetismus und Biosignalanalyse, Westfälische Wilhelms-Universität Münster, April 2011. URL http://www.sci.utah.edu/~wolters/PaperWolters/VorwerkDiplom.pdf. 19, 25, 39, 40, 41, 43, 44, 45, 50, 52, 58, 59, 60, 66, 92, 169, 172

J. Vorwerk, M. Clerc, M. Burger, and C.H. Wolters. Comparison of boundary element and finite element approaches to the EEG forward problem. *Biomedical Engineering/Biomedizinische Technik*, 57(Suppl. 1):795–798, 2012. doi: 10.1515/bmt-2012-4152. 2, 39, 51, 54, 58, 59, 90, 177

J. Vorwerk, J.-H. Cho, S. Rampp, H. Hamer, T.R. Knösche, and C.H. Wolters. A guideline for head volume conductor modeling in EEG and MEG. *NeuroImage*, 100:590–607, 2014. 61, 81, 102, 170, 177

S. Wagner. *Optimizing tCS and TMS multi-sensor setups using realistic head models*. PhD thesis in Mathematics, Westfälische Wilhelms-Universität Münster, August 2015. 18

S. Wagner, S.M. Rampersad, Ü. Aydin, J. Vorwerk, T.F. Oostendorp, T. Neuling, C.S. Herrmann, D.F. Stegeman, and C.H. Wolters. Investigation of tDCS volume conduction effects in a highly realistic head model. *Journal of Neural Engineering*, 11:016002, 2014. 92, 98

D. Weinstein, L. Zhukov, and C. Johnson. Lead-field bases for electroencephalography source imaging. *Annals of Biomedical Engineering*, 28(9):1059–1066, 2000. 2, 19, 37

K. Wendel, N.G. Narra, M. Hannula, P. Kauppinen, and J. Malmivuo. The influence of CSF on EEG sensitivity distributions of multilayered head models. *IEEE Transactions on Biomedical Engineering*, 55(4):1454–1456, 2008. 2, 86

C.H. Wolters, M. Kuhn, A. Anwander, and S. Reitzinger. A parallel algebraic multigrid solver for finite element method based source localization in the human brain. *Computing and Visualization in Science*, 5(3):165–177, 2002. doi: 10.1007/s00791-002-0098-0. 18, 50

C.H. Wolters, L. Grasedyck, and W. Hackbusch. Efficient computation of lead field bases and influence matrix for the FEM-based EEG and MEG inverse problem. *Inverse Problems*, 20 (4):1099–1116, 2004. doi: 10.1088/0266-5611/20/4/007. 2, 37

C.H. Wolters, A. Anwander, D. Weinstein, M. Koch, X. Tricoche, and R.S. MacLeod. Influence of tissue conductivity anisotropy on EEG/MEG field and return current computation in a realistic head model: A simulation and visualization study using high-resolution finite element modeling. *NeuroImage*, 30(3):813–826, 2006. doi: 10.1016/j.neuroimage.2005.10.014. 85, 89

C.H. Wolters, A. Anwander, G. Berti, and U. Hartmann. Geometry-adapted hexahedral meshes improve accuracy of finite element method based EEG source analysis. *IEEE Transactions on Biomedical Engineering*, 54(8):1446–1453, 2007a. doi: 10.1109/TBME.2007.890736. 20, 60, 91, 92, 93, 169, 172

C.H. Wolters, H. Köstler, C. Möller, J. Härdtlein, and A. Anwander. Numerical approaches for dipole modeling in finite element method based source analysis. *International Congress Series*, 1300:189–192, 2007b. doi: 10.1016/j.ics.2007.02.014. 58

C.H. Wolters, H. Köstler, C. Möller, J. Härtlein, L. Grasedyck, and W. Hackbusch. Numerical mathematics of the subtraction method for the modeling of a current dipole in EEG source reconstruction using finite element head models. *SIAM Journal on Scientific Computing*, 30(1):24–45, 2007c. doi: 10.1137/060659053. 2, 11, 28, 29, 30, 31, 32, 36, 37

C.H. Wolters, S. Lew, R.S. MacLeod, and M.S. Hämäläinen. Combined EEG/MEG source analysis using calibrated finite element head models. In *Proceedings of the 44th Annual Meeting, DGBMT*, Rostock-Warnemünde, Germany, Oct.5-8, 2010, 2010. URL http://conference.vde.com/bmt-2010. 87

Y. Yan, P.L. Nunez, and R.T. Hart. Finite-element model of the human head: Scalp potentials due to dipole sources. *Medical & Biological Engineering & Computing*, 29:475–481, 1991. 2, 19

F. Zanow. *Realistically shaped models of the head and their application to EEG and MEG.* University of Twente, The Netherlands, 1997. 11, 51

F. Zanow and T.R. Knösche. Asa-advanced source analysis of continuous and event-related EEG/MEG signals. *Brain Topography*, 16(4):287–290, 2004. ISSN 0896-0267. 51

Z. Zhang. A fast method to compute surface potentials generated by dipoles within multilayer anisotropic spheres. *Physics in Medicine and Biology*, 40:335–349, 1995. 13